

秋田県立大学大学院博士学位論文

**Preparation of Carbon-Based Composites and their Application in  
Supercapacitors**

(カーボンベース複合材料の創製およびスーパーキャパシタへの応用)

王 濱

2017年3月

# Abstract

The major objective of this work is to preparation of carbon materials and carbon-based composites targeting the electrode materials of supercapacitors. The advancement of energy storage devices — supercapacitors is importance to the development of many fields that have strong effects on human’s life: renewable energy, portable devices and transportation.

Firstly, graphene oxide/polypyrrole/multi-walled carbon nanotube composites were prepared by in-suit polymerization method. The obtained composites have a special microstructure — polypyrrole chains acted as the “bridge” between multi-wall carbon nanotube and graphene through the amide group and  $\pi$ - $\pi$  stacking, respectively. The composites showed excellent electrochemical performance when used as electrode materials for supercapacitors. However, we also found a reason is that the carbon material (multi-wall carbon nanotube/graphene oxide) showed the poor electrochemical performance.

Secondly, a type of nitrogen-doped carbon nanowires are successfully prepared and used as negative electrode material of supercapacitors. The polypyrrole nanowires were prepared when CTAB as soft template, and then obtained the nitrogen doped carbon nanowires by direct carbonization method when polypyrrole nanowires as the carbon precursor. The carbon nanowires showed good electrochemical performance due to their acceptable nitrogen content and large specific surface area. And then, for further improve the electrochemical performance of carbon nanowires, a kind of porous carbon nanowires are successfully prepared by KOH activation method, and also used as negative electrode material of supercapacitors. The porous carbon nanowires showed the better electrochemical performance than that of carbon nanowires. This is attributed to their adequate nitrogen content and higher specific surface area than that of carbon nanowires.

Thirdly, based on carbon nanowires, various micromorphology  $\text{MnO}_2$ /carbon

nanowires composites were prepared by hydrothermal reaction. The composites possess the special microstructure based on the reaction times, and further effect on the electrochemical performance of themselves. An asymmetric supercapacitor is assembled when the composite as the positive electrode and porous carbon nanowires as the negative electrode, and the supercapacitor exhibited the excellent electrochemical performance.

# Contents

Abstract .....	I
List of Figures .....	VI
List of Tables.....	XI
Chapter 1 Introduction.....	1
1.1 Background .....	1
1.1.1 Electrochemical devices .....	1
1.2 Supercapacitors .....	3
1.2.1 The storage energy principle of EDLCs.....	4
1.2.2 The storage energy principle of pseudocapacitors .....	6
1.3 The electrode materials of supercapacitors .....	7
1.3.1 Carbon-based electrode materials.....	7
1.3.2 Conducting polymer-based electrode materials .....	16
1.3.3 Transition metal oxides-based electrode materials.....	19
1.4 Contribution from this dissertation.....	23
References .....	26
Chapter 2 Materials, experimental and characterizations.....	33
2.1 Materials.....	33
2.1.1 Chemical reagents .....	33
2.1.2 Materials of electrochemical test.....	33
2.2 Experimental methods.....	35
2.2.1 Preparation of polypyrrole (PPy).....	35
2.2.2 Preparation of carbon materials.....	35
2.2.3 Preparation of carbon-based composites .....	36
2.3 Characterization.....	37
2.3.1 Morphological, structure, thermal and component characterizations.....	37
2.3.2 Electrochemical performance characterization .....	38
References:.....	41
Chapter 3 Preparation of graphene oxide/polypyrrole/multi-walled carbon nanotube composite and its application in supercapacitors .....	43
3.1 Introduction .....	43
3.2 Experimental section .....	45
3.2.1 Materials.....	45

3.2.2 Preparation of CM.....	45
3.2.3 Preparation of PCMG composites.....	46
3.2.4 Structure characterization.....	47
3.2.5 Electrochemical tests.....	47
3.2.6 Measurement of conductivity.....	48
3.3 Results and discussion.....	48
3.3.1 Microstructure characterization.....	48
3.3.2 Electrochemical behavior.....	55
3.4. Conculsions.....	62
References:.....	63
Chapter 4 Nitrogen doped carbon nanowires prepared from polypyrrole nanowires for potential application in supercapacitors.....	66
4.1 Introduction.....	66
4.2 Experimental section.....	68
4.2.1 Materials.....	68
4.2.2 Preparation of nanowires polypyrrole.....	68
4.2.3 Preparation of CNW.....	69
4.2.4 Structure characterization.....	69
4.2.5 Electrochemical tests.....	70
4.3 Result and discussion.....	70
4.3.1 Microstructural characterization.....	70
4.3.2 Electrochemical performance.....	79
4.4 Conclusions.....	90
References:.....	91
Chapter 5 KOH-activated nitrogen doped porous carbon nanowires with superior performance in supercapacitors.....	95
5.1 Introduction.....	95
5.2 Experimental section.....	97
5.2.1 Materials.....	97
5.2.2 Preparation of porous N-doped carbon nanowires (PCNW).....	97
5.2.3 Thermal, morphological, structural, and component characterizations.....	97
5.2.4 Electrochemical tests.....	99
5.3 Result and discussion.....	99
5.3.1 Thermal analysis of activation process.....	99

5.3.2. Microstructural characterization.....	101
5.3.3 Electrochemical performance.....	109
5.4 Conclusions.....	121
References:.....	122
Chapter 6 Preparation of MnO <sub>2</sub> /carbon nanowires composites for supercapacitors.....	126
6.1 Introduction.....	126
6.2 Experimental section.....	128
6.2.1 Materials.....	128
6.2.2 Preparation of porous carbon nanowires (PCNW).....	128
6.2.3 Preparation of CNW/MnO <sub>2</sub> composites (CNWMn).....	129
6.2.4 Characterizations.....	129
6.2.5 Electrochemical measurement.....	130
6.3 Results and discussion.....	130
6.3.1 Microstructural characterization.....	130
6.3.2 Growth process of the CNWMn nanostructures.....	139
6.3.3 Electrochemical performance of CNWMn composites.....	143
6.4. Conclusions.....	154
References:.....	156
Chapter 7 Summary and outlook.....	161
7.1. Summary of thesis results.....	161
7.2. Outlook.....	162
Publication.....	164
Acknowledgements.....	166

# List of Figures

<b>Fig. 1.1</b> A fuel cell showing the continuous supply of reactants and redox reactions in the cell .....	2
<b>Fig. 1.2</b> Representation of a battery (Daniell cell) .....	2
<b>Fig. 1.3</b> Representation of a supercapacitor (illustrating the energy storage in the electric double layers at the electrode/electrolyte interfaces) .....	3
<b>Fig. 1.4</b> Models of the electrical double layer at a positively charged surface: (a) the Helmholtz model, (b) the Gouy-Chapman model, and (c) the Stern model [13] .....	5
<b>Fig. 1.5</b> Representation of charged state of a symmetric EDLC using porous material and of the corresponding equivalent circuit. R is resistors, C is capacitors [17].....	6
<b>Fig. 1.6</b> Redox reaction based pseudocapacitance .....	7
<b>Fig. 1.7</b> Carbon materials: a, graphite; b, diamond; c, buckminsterfullerene C <sub>60</sub> ; d, single walled carbon nanotube; e, graphene [21].....	8
<b>Fig. 1.8</b> Macroscopic representation is showing the general concept of the templating technique (a); microscopic synthesis of macroporous carbons using silica spheres as template (b), mesoporous carbons using SBA-15 as template (c) and microporous carbons using zeolite Y as template (d) [13].....	11
<b>Fig. 1.9</b> SAXD patterns of Maxsorb and OMC carbons (left); TEM images and structure models of Maxsorb and OMC carbons (right) [49].....	12
<b>Fig. 1.10</b> Atomic structure of carbon nanotubes: a, schematic diagram showing how a graphene sheet is „rolled“ according to a pair of chiral vectors to form different atomic structures of carbon nanotubes; zig-zag (n, 0) (b), chiral (n,m) (c) and armchair (n,n) (d) carbon nanotubes [13] .....	13
<b>Fig. 1.11</b> Preparation of reduced graphene oxide by Hummer method [65].....	15
<b>Fig. 1.12</b> Various conducting polymer structures .....	17
<b>Fig. 1.13</b> Formation of the bipolaron state in PPy or polythiophene .....	17
<b>Fig. 1.14</b> Conversion between different states of PANI.....	18
<b>Fig. 1.15</b> The typical synthesis processes of RuO <sub>2</sub> [89].....	21
<b>Fig. 1.16</b> crystal structure of $\alpha$ -, $\beta$ -, $\gamma$ -, $\delta$ - and $\lambda$ -MnO <sub>2</sub> [105] .....	23
<b>Fig. 3.1</b> XRD patterns of CM, GO, PPy, PCMG1-1, PCM-1 and PG-1. ....	48
<b>Fig. 3.2</b> TEM image of pure PPy (a), CM (b), PG-1 (c) and PCMG1-1 (d). ....	49
<b>Fig. 3.3</b> SEM image of PG-1 (a, b), PCM-1 (c, d), PCMG1-1 (e, f).....	50
<b>Fig. 3.4</b> FTIR spectra of GO, PCM-1, CM, PPy, PG-1 and PCMG1-1. ....	51
<b>Fig. 3.5</b> N <sub>2</sub> adsorption-desorption isotherms of the PCMG1-1, PG-1 and PCM-1. ....	52
<b>Fig. 3.6</b> XPS spectra of MWCNTs (a, b), CM (c, d), PCM-1(e, f), PG-1 (g, h) and PCMG1-1 (i, j).....	54

<b>Fig. 3.7</b> (a) XPS N 1s spectra of PCMG1-1, PCM-1 and PG-1; (b) XPS Cl 2p spectra of PCMG1-1, PCM-1, PG-1 and CM. ....	55
<b>Fig. 3.8</b> Electrochemical characterization of PCMG, PCM, PG, CMG composites and pure PPy. a (CV), b (GCD), c (EIS) are compared the electrochemical properties of PCMG1-1, PCM and PG composites. d (CV), e (GCD), f (EIS) are compare the electrochemical properties of PCMG composites each other. g (CV), h (GCD), i (EIS) are compare the electrochemical properties of PCMG1-1, PPy and CMG composite. (CV test at a scan rate of $10 \text{ mV S}^{-1}$ , GCD test at a constant current density of $0.5 \text{ A g}^{-1}$ ). ....	56
<b>Fig. 3.9</b> The 3-D graph of the specific capacitance of as-prepared samples. ....	57
<b>Fig. 3.10</b> Electrochemical characterization of PCM-1 and PAM composites (a, b and c showed the CV, GCD and EIS tests, respectively); e, dispersed CM, AM in water after one month. ....	60
<b>Fig. 3.11</b> (a) CV curves of the PCMG1-1 composite at various current density. (b) Specific capacitance as a function of the current density. ....	61
<b>Fig. 3.12</b> Percentage retention of the specific capacitance as a function of GCD cycles at a constant current density of $2 \text{ A g}^{-1}$ . The inset shows the GCD curves of the first and last 4 cycles for PCMG1-1 composite. ....	61
<b>Fig. 4.1</b> SEM image of pure PPy (a), PPy-1 (b), PPy-2 (c), PPy-3 (d), CNW2-1 (e), CNW2-2 (f), CNW2-3 (g), and CNW2-4 (h); TEM image of PPy-2 (i), CNW2-1 (j), CNW2-2 (k), CNW2-3 (l), and CNW2-4 (m). ....	71
<b>Fig. 4.2</b> SEM image of pure PPy (a) and CNW0-2 (b) ....	73
<b>Fig. 4.3</b> XRD patterns of PPy-2, CNW2-1, CNW2-2, CNW2-3, and CNW2-4. ....	73
<b>Fig. 4.4</b> $\text{N}_2$ adsorption-desorption isotherms of CNW2-1, CNW2-2, CNW2-3, and CNW2-4. ....	74
<b>Fig. 4.5</b> XPS survey spectrums of PPy-2, CNW2-1, CNW2-2, CNW2-3, and CNW2-4. ....	75
<b>Fig. 4.6</b> High resolution C 1s, N 1s and O 1s XPS spectrum of PPy-2 (a, f, k), CNW2-1 (b, g, l), CNW2-2 (c, h, m), CNW2-3 (d, i, n), and CNW2-4 (e, j, o) ....	77
<b>Fig. 4.7</b> The types of nitrogen doping of CNW sample. ....	78
<b>Fig. 4.8</b> CV curves of CNW1 (a), CNW2 (c), and CNW3 (e) at a scan rate of $10 \text{ mV s}^{-1}$ ; GCD curves of CNW1 (b), CNW2 (d), and CNW3 (f) at a current density of $1 \text{ A g}^{-1}$ ....	80
<b>Fig. 4.9</b> (a) EIS spectrum of CNW2-1, CNW2-2, CNW2-3, and CNW2-4; (b) The effect of calcination temperature on specific capacitance of CNW (at a current density of $1 \text{ A g}^{-1}$ ). ...	81
<b>Fig. 4.10</b> (a) CV curves of CNW0 at a scan rate of $10 \text{ mV S}^{-1}$ ; (b) GCD curves of CNW0 at a current density of $1 \text{ A g}^{-1}$ ....	82
<b>Fig. 4.11</b> (a) CV curves of CNW2-2 at different scan rates varying from $10$ to $50 \text{ mV s}^{-1}$ ; (b) specific capacitance versus current density of CNW2-2; ....	83
<b>Fig. 4.12</b> Cycling stability of CNW2-2 at a current density of $3 \text{ A g}^{-1}$ . ....	84
<b>Fig. 4.13</b> CV (a, scan rate is $10 \text{ mV s}^{-1}$ ) and GCD (b, current density is $0.5 \text{ A g}^{-1}$ ) curves of CNW2-2 two-electrode system. ....	85

<b>Fig. 4.14</b> Ragone plot of CNW2-2 in two-electrode system at different voltage windows. ...	86
<b>Fig. 4.15</b> GCD curves of CNW2-2 in tow-electrode system at voltage window is 0-0.6 V (a), 0-0.8 V (b), 0-1.0 V (c), 0-1.2 V (d), 0-1.4 V (e) and 0-1.6 V (f). .....	87
<b>Fig. 4.16</b> Cycle stability of CNW2-2 in two-electrode system at a current density is $1 \text{ A g}^{-1}$ , the inset is a ragone plot of CNW2-2 before and after 5000 cycles. ....	88
<b>Fig. 4.17</b> CV (a) and GCD (b) curves of CNW2-2 before and after 5000 cycles in tow-electrode system. ....	88
<b>Fig. 5.1</b> The relationship between activation temperature and time at TGA tests. ....	98
<b>Fig. 5.2</b> TG and DTA curves of the mass ratio of KOH/CNW is 1 (a, b), 2 (c, d) and 3 (e, f) at temperature rising and keeping the temperature process, respectively. ....	101
<b>Fig. 5.3</b> SEM image of CNW (a), PCNW1 (b), PCNW2 (c) and PCNW3 (d). ....	102
<b>Fig. 5.4</b> TEM image of CNW (a), PCNW1 (b), PCNW2 (c) and PCNW3 (d). ....	103
<b>Fig. 5.5</b> XRD patterns of PPy, CNW, PCNW1, PCNW2 and PCNW3. ....	103
<b>Fig. 5.6</b> (a) is $\text{N}_2$ adsorption-desorption isotherms, (b) is pore size distribution of CNW, PCNW1, PCNW2 and PCNW3. ....	104
<b>Fig. 5.7</b> (a) XPS survey spectra of CNW, PCNW1, PCNW2 and PCNW3; (b) high resolution C 1s XPS spectra of CNW, PCNW1, PCNW2 and PCNW3; .....	105
<b>Fig. 5.8</b> High resolution N 1s and O 1s XPS spectrum of CNW (a, e), PCNW1 (b, f), PCNW2 (c, g) and PCNW3 (d, h). ....	107
<b>Fig. 5.9</b> CV curves of CNW, PCNW1, PCNW2 and PCNW3. ....	110
<b>Fig. 5.10</b> GCD curves of CNW, PCNW1, PCNW2 and PCNW3. ....	111
<b>Fig. 5.11</b> (a) EIS curves of CNW, PCNW1, PCNW2 and PCNW3; (b) the Nyquist plots of PCNW2 for raw and fitted data. ....	112
<b>Fig. 5.12</b> CV (a) and GCD (b) curves of PCNW2 at different scan rate and current density; GCD curves of PCNW1 (c) and PCNW3 (d) at different current densities. ....	113
<b>Fig. 5.13</b> Specific capacitance versus current density of CNW, PCNW1, PCNW2 and PCNW3. ....	114
<b>Fig. 5.14</b> (a) Dependence of cycle stability in the current density of PCNW2; (b) cycle stability of PCNW2 at a current density of $3 \text{ A g}^{-1}$ .....	115
<b>Fig. 5.15</b> CV (a, scan rate is $0.01 \text{ V s}^{-1}$ ) and GCD (b, current density is $0.8 \text{ A g}^{-1}$ ) curves of PCNW2 in two-electrode system at different voltage windows. ....	116
<b>Fig. 5.16</b> GCD curves of PCNW2 in two-electrode systems at voltage windows of 0-1.0 V (a), 0-1.2 V (b), 0-1.4 V (c) and 0-1.6 V (d). ....	117
<b>Fig. 5.17</b> (a) Ragone plot of PCNW2 in two-electrode system at different voltage windows; (b) Ragone plot of CNW and PCNW2 in symmetric two-electrode systems; GCD curves of CNW and PCNW2 in two-electrode systems at current density of 0.8 (c), 1.0 (d), 1.4 (e) and 2.4 (f) $\text{A g}^{-1}$ .....	118

<b>Fig. 5.18</b> (a) Cycle stability of PCNW2 in two-electrode system at a current density is $2.4 \text{ A g}^{-1}$ , the inset is a Ragone plot of PCNW2 before and after 5000 cycles; CV (b, scan ratio is $0.01 \text{ V s}^{-1}$ ) and GCD (c, current density is $2.4 \text{ A g}^{-1}$ ) curves of PCNW2 in two-electrode systems before and after 5000 cycles; (d) GCD curves of PCNW2 at different current density in two-electrode systems after 5000 cycles. ....	119
<b>Fig. 6.1</b> SEM image of CNWMn1 (a), CNWMn2 (b), CNWMn3 (c), CNWMn4 (d), $\text{MnO}_2$ 1 (e), $\text{MnO}_2$ 2 (f), $\text{MnO}_2$ 3 (g), and $\text{MnO}_2$ 4 (h). ....	131
<b>Fig. 6.2</b> SEM image of CNW (a) and PCNW (b).....	132
<b>Fig. 6.3</b> (a) XRD patterns of CNWMn1, CNWMn2, CNWMn3 and CNWMn4; (b) XRD patterns of WPPy, CNW and PCNW; (c) XRD patterns of $\text{MnO}_2$ 1, $\text{MnO}_2$ 2, $\text{MnO}_2$ 3 and $\text{MnO}_2$ 4. ....	134
<b>Fig. 6.4</b> $\text{N}_2$ adsorption-desorption isotherms of CNWMn1, CNWMn2, CNWMn3 and CNWMn4 (the inset of b is pore size distribution plots).....	135
<b>Fig. 6.5</b> $\text{N}_2$ adsorption-desorption isotherms of CNW (a) and PCNW (b), and the inset is pore size distribution polts.....	136
<b>Fig. 6.6</b> XPS survey spectra of CNWMn1, CNWMn2, CNWMn3 and CNWMn4;.....	137
<b>Fig. 6.7</b> (a) High resolution Mn 2p XPS spectra of CNWMn2; (b) high resolution of C 1s XPS spectra of CNWMn2; High resolution O 1s XPS spectra of CNWMn1 (c), CNWMn2 (d), CNWMn3 (e) and CNWMn4 (f). ....	138
<b>Fig. 6.8</b> (a) XPS survey spectra of WPPy, CNW and PCNW; high resolution C 1s (b), N 1s (c) and O 1s (d) XPS spectra of WPPy, CNW and PCNW. ....	139
<b>Fig. 6.9</b> Schematic illustrations of the growth process of CNWMn composites controlled by the hydrothermal reaction time.....	140
<b>Fig. 6.10</b> Schematic illustrations of the growth process of pure $\text{MnO}_2$ controlled by the hydrothermal reaction time.....	142
<b>Fig. 6.11</b> CV (scan rate of $0.01 \text{ V s}^{-1}$ ) curves of CNWMn composites in three-electrode system.....	143
<b>Fig. 6.12</b> CV (scan rate of $0.01 \text{ V s}^{-1}$ ) curves of CNW and PCNW in three-electrode system. ....	144
<b>Fig. 6.13</b> GCD curves (current density of $1 \text{ A g}^{-1}$ ) of CNWMn composites in three-electrode system.....	145
<b>Fig. 6.14</b> EIS curves of CNWMn composites in three-electrode system.....	146
<b>Fig. 6.15</b> Specific capacitance versus current density of CNWMn composites in three-electrode system. ....	147
<b>Fig. 6.16</b> GCD curves of CNWMn1 (a), CNWMn2 (b), CNWMn3 (c) and CNWMn4 (d) at different current densities in three-electrode system. ....	148
<b>Fig. 6.17</b> CV (a, scan rate of $0.01 \text{ V s}^{-1}$ ) and GCD (b, current density of $1 \text{ A g}^{-1}$ ) curves of CNWMn2 and $\text{MnO}_2$ 2 in three-electrode system.....	148
<b>Fig. 6.18</b> Dependence of cycle stability in the current density of CNWMn2. ....	149

<b>Fig. 6.19</b> CV curves of PCNW and CNWMn2 in three-electrode system at 0.01 V s <sup>-1</sup> .....	150
<b>Fig. 6.20</b> CV (a, scan rate of 0.01 V s <sup>-1</sup> ) and GCD (b, current density of 2 A g <sup>-1</sup> ) curves of two-electrode asymmetric system (using CNWMn2 and PCNW as the positive and negative electrode, respectively) at different potential windows.....	150
<b>Fig. 6.21</b> CV (a) and GCD (b) curves of asymmetric system measured at different scan rates and current densities in a potential window of 1.5 V, respectively.....	151
<b>Fig. 6.22</b> (a) EIS curve of asymmetric system (the inset is electrical equivalent circuit); (b) EIS curves of two-electrode asymmetric system for raw and fitted data (the table is equivalent circuit parameters).....	152
<b>Fig. 6.23</b> Cycle stability of asymmetric system. ....	153
<b>Fig. 6.24</b> Ragone plot of asymmetric system. ....	154

# List of Tables

<b>Table 1.1</b> Different carbon structures used in supercapacitors electrodes with active carbon, template carbon, carbon nanotube and graphene [32].	10
<b>Table 2.1</b> Physical and chemical properties of reagents	34
<b>Table 3.1</b> Grouping of the samples	46
<b>Table 3.2</b> N 1s core level peak analyses. Each peak corresponds to a specific type of nitrogen: N-1, pyrrolic nitrogen; N-2, quaternary nitrogen; N-3, oxidized nitrogen.	55
<b>Table 4.1</b> The preparation condition of pure PPy and PPy-x.	68
<b>Table 4.2</b> The preparation condition of CNW and CNG	69
<b>Table 4.3</b> The Specific Surface Area, Pore Width and Micropore Volume of CNW2 samples	74
<b>Table 4.4</b> Chemical compositions of samples as obtained by XPS	75
<b>Table 4.5</b> N 1s and O 1s core level peak analyses	78
<b>Table 4.6</b> The specific capacitance and energy density of CNW2-2 in tow-electrode system	89
<b>Table 5.1</b> Pore properties and specific capacitances of CNW and PCNW samples	106
<b>Table 5.2</b> XPS analysis of the CNW and PCNW samples	106
<b>Table 5.3</b> Equivalent circuit parameters fitted from Nyquist plots for PCNW1, 2 and 3.	112
<b>Table 5.4</b> The specific capacitance and energy density of PCNW2 in two-electrode systems	120
<b>Table 5.5</b> The specific capacitance and energy density of PCNW2 before and after 5000 cycles in two-electrode systems	120
<b>Table 6.1</b> Pore volume, specific surface area and pore size of samples	136
<b>Table 6.2</b> XPS spectrum analysis of samples	137

# Chapter 1 Introduction

## 1.1 Background

Energy is one of the most important factors for the development of modern society. Till now, the non-renewable fossil fuels are still the main energy sources in people's lives, and we depend on fossil fuels with two serious consequences: exhaustion of reserves and worsening of the greenhouse effect caused by the emission of carbon dioxide (CO<sub>2</sub>) from their combustion. Moreover, energy demands will increase with the increase of world population and economic development, which will increase the atmospheric concentration of CO<sub>2</sub> if no action is taken, and the result will be ever greater climate warming. Thus, all global organizations agree that energy is the main challenge of this century that our habitat must overcome.

Currently, many researchers want to reverse this trend through renewable energies, for example, the solar [1, 2], wind [3], biomass [4], geothermal [5] and so on. However, for these energies to be successful application, it is important to consider how they can be used more efficiently and find innovative management solutions, reliable conversion and storage of energy, which are low cost and widely applicable. For this, we need: (1) efficient photovoltaic and thermoelectrical systems to convert light and heat into electricity, respectively; (2) electronic conductors such as superconductors to minimize the Joule effect; and (3) storage systems such as batteries, supercapacitors to store energy in chemical energy and convert it back to electricity when required [6]. Among of them, the storage of electrical energy plays a vital role in sectors such as transport, telecommunications, medicine and other sectors.

### 1.1.1 Electrochemical devices

Systems for electrochemical energy storage and conversion include fuel cells, batteries and electrochemical capacitors (ECs). More specifically:

Fuel cell, it operate based on the working principle to the electrolysis of water (as shown in Fig. 1.1), i.e. the electricity is produced by oxidation on a di-hydrogen ( $H_2$ ) electrode coupled with reduction on another electrode of an oxidant such as oxygen from the air, together producing water. Moreover, this is an “open” system, that is to say, directly supply externally, and hence not directly electrically rechargeable [6].

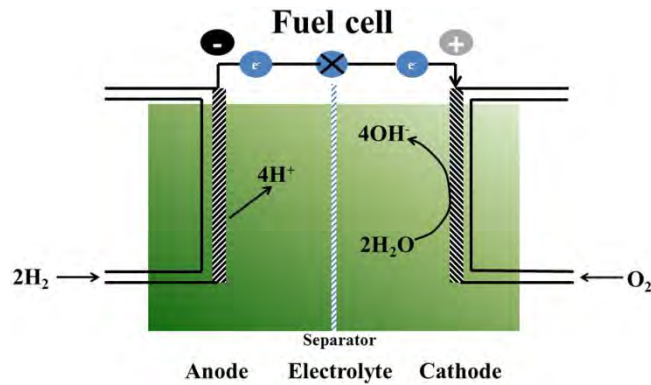


Fig. 1.1 A fuel cell showing the continuous supply of reactants and redox reactions in the cell.

Battery, it is a closed system, with the anode and cathode being the charge-transfer medium and taking an active role in the redox reaction as “active masses” [7]. In other words, it can deliver/store electrical energy generated from reversible redox reactions that may occur in the constituent materials of their electrodes (as shown in Fig. 1.2).

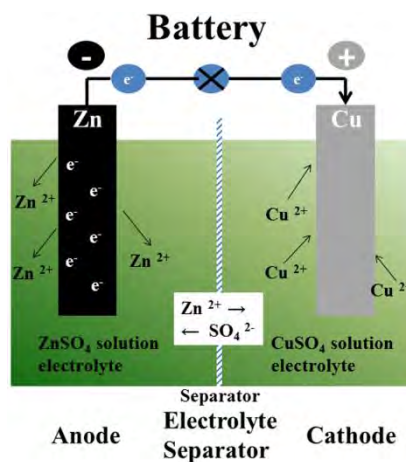


Fig. 1.2 Representation of a battery (Daniell cell).

In supercapacitor, energy may not be delivered via redox reactions, it is based on capacitive properties of an electrical double layers at the electrode/electrolyte interfaces (as shown in Fig. 1.3) with a capacity per unit mass or area expressed in  $F g^{-1}$  and  $F cm^{-3}$ , respectively. EDLs results in a parallel movement of electrons in the external wire, that is, in the energy delivering process.

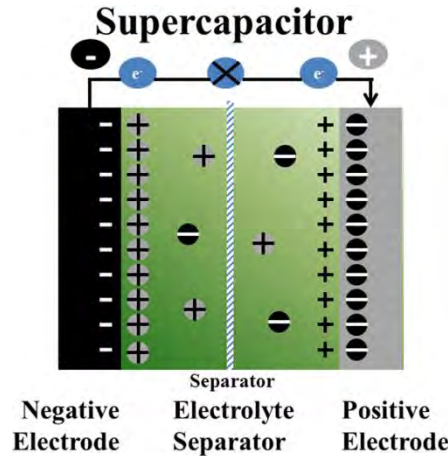


Fig. 1.3 Representation of a supercapacitor (illustrating the energy storage in the electric double layers at the electrode/electrolyte interfaces).

## 1.2 Supercapacitors

Supercapacitors (SCs), we also know as electrochemical capacitors or ultracapacitors. They have caused widespread concern due to their long cycle life ( $> 500,000$  cycles), rapid charge/discharge rate, high power density ( $> 10 kW kg^{-1}$ ) and small environment impact [8-10]. A typical supercapacitor usually contains four parts: electrode, electrolyte, separators and current collectors [11]. SCs can be divided into two types based on their energy storage principles: the electrical double layers capacitors (EDLCs) and the pseudocapacitor [12]. For convenience, we explain the two energy storage principles separately, though they usually function together in a supercapacitor.

### 1.2.1 The storage energy principle of EDLCs

As mentioned 1.1.1 and as shown in Fig. 1.3, the working principle of EDLCs is electrical double layers (EDLs) theory. EDLCs are ideally suited to the rapid storage and release of energy. They can store much energy due to the large interfacial area and the atomic range of charge separation distances. As illustrated in Fig. 1.4a, the idea of the EDLs was first proposed by Helmholtz in the 19<sup>th</sup> century [13]. The Helmholtz double layer model expound that two layers of opposite charge form at the interface of electrode/electrolyte and are separated by an atomic distance [13]. This simple model was further modified by Gouy and Chapman [14, 15] based on the continuous distribution of ions in the electrolyte solution, and they proposed the diffuse layer (as shown in Fig. 1.4b). Based on the Helmholtz and Gouy-Chapman model, stern [16] clearly stated that the ion distribution includes two regions: the inner region called the compact layer or stern layer and the diffuse layer [13] (as shown in Fig. 1.4c). In the stern layer, the ions of solution are strongly adsorbed by the electrode, thus it is also called compact layer. Furthermore, the compact layer consists of specifically adsorbed ions and non-specifically adsorbed counterions. The two types of adsorbed ions are distinguished by the inner Helmholtz plane (IHP) and outer Helmholtz plane (OHP) [13]. Thus, the capacitance of EDLs ( $C_{dl}$ ) can be expressed by the following equation (Eq. 1.1):

$$\frac{1}{C_{dl}} = \frac{1}{C_H} + \frac{1}{C_{diff}} \quad (\text{Eq. 1.1})$$

where  $C_H$  and  $C_{diff}$  are the capacitance of compact double layer and diffusion region, respectively.

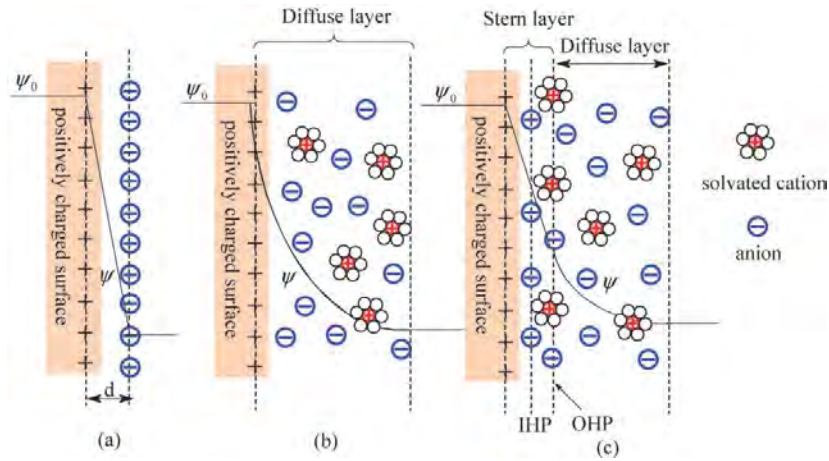


Fig. 1.4 Models of the electrical double layer at a positively charged surface: (a) the Helmholtz model, (b) the Gouy-Chapman model, and (c) the Stern model [13].

An EDLCs consists of two electrode, generally the material of electrode is active carbon (AC). The material of electrode is direct contact with the current collector, and the electrode separated by a porous film impregnated with an electrolyte solution (as shown in Fig. 1.5). When an electric potential difference is applied between the electrodes, the negative charge carriers, electrons, in the negatively polarized electrode are balanced by an equal number of positive cations at the electrode/electrolyte interface, while at the positively polarized electrode are electrically balanced by anions [17]. Therefore, a supercapacitor includes two electrodes is equivalent to two capacitors in series and the resulting capacitance (C) can be expressed by Eq. 1.2:

$$\frac{1}{C} = \frac{1}{C_+} + \frac{1}{C_-} \quad (\text{Eq. 1.2})$$

where C, C<sub>+</sub> and C<sub>-</sub> are the capacitance of the whole supercapacitors, positive electrode and negative electrode, respectively. In case of a symmetric system, both electrodes employ by the equal in materials, mass and size, the Eq. 2 can be simplified to Eq. 1.3 [17]:

$$C = 4 \times \frac{C_E}{m_{AM}} \quad (\text{Eq. 1.3})$$

where C<sub>E</sub> and m<sub>AM</sub> are the capacitance of electrode and the total mass of active materials.

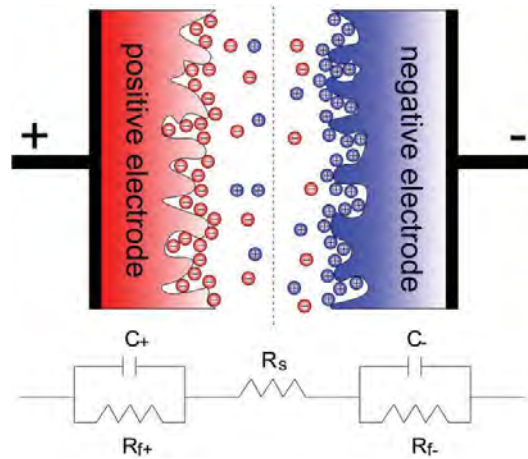


Fig. 1.5 Representation of charged state of a symmetric EDLC using porous material and of the corresponding equivalent circuit. R is resistors, C is capacitors [17].

### 1.2.2 The storage energy principle of pseudocapacitors

Pseudocapacitors, they are distinctly different from EDLCs. Because EDLCs follow purely electrostatic phenomena and their energy storage is completely reversible. However, pseudocapacitors utilize the fast redox reactions occurring at the surface and bulk of the electrode materials are able to give a much large energy density when compared with EDLCs [18, 19] (as shown in Fig. 1.6). As we all know, the chemical reactions are not completely reversible ever for the best effort reversible combination of electrode and electrolyte. Therefore, pseudocapacitors are always have some residual electrode materials cannot take part in the reversible chemical reaction process, even after complete discharge [20]. This phenomenon leads to the loss of active materials, which further reduces the value of the maximum specific capacitance with increasing the cycle numbers, and the affects the cycle stability of the pseudocapacitors. In addition, pseudocapacitors have the highest charge-transfer rate at a special potential. Sometime delay is required to overcome this potential barrier, and this time is responsible for the delayed response of pseudocapacitors relative to EDLCs, which have instantaneous electrostatic responses [20]. Although, pseudocapacitors have the dispute of cycle stability and response-time, they are still aroused researcher's interesting owing to their high ability of storage energy based on the chemical reaction. Thence, overcome the above mentioned problems have been

the topic of scientific investigation in recent years.

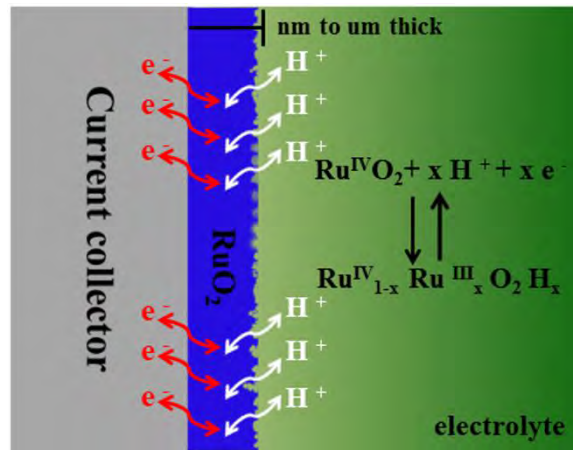


Fig. 1.6 Redox reaction based pseudocapacitance.

## 1.3 The electrode materials of supercapacitors

As described above, a typical supercapacitor contains four parts: electrode, electrolyte, separators and current collector. The core part is electrode material, which directly determines the capacitance, delivery rate and efficiency of a supercapacitor.

### 1.3.1 Carbon-based electrode materials

Carbon, as we all know, it exists in three forms, namely, amorphous carbon, graphite and diamond (as shown in Fig. 1.7) [21]. Their properties have many changes based on the arrangement of carbon atoms. For instance, graphite is soft, stable and blank. There are due to its form of carbon with strong covalent bonding in the carbon plane and the much weaker van der Waals interaction in the transverse direction between the layers (as shown in Fig. 1.7a). The each carbon atoms of diamond bound to four other carbon atoms in a regular lattice, and this is lead to the diamond hard and transparent (as shown in Fig. 1.7b).

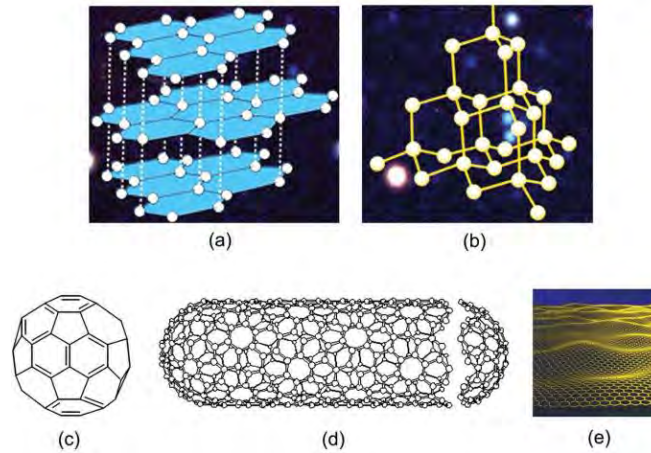


Fig. 1.7 Carbon materials: a, graphite; b, diamond; c, buckminsterfullerene C<sub>60</sub>; d, single walled carbon nanotube; e, graphene [21].

The attraction of carbon as the supercapacitor electrode material arises from the unique chemical and physical properties, as following [22]:

- high specific surface area range (1 to > 2000 m<sup>2</sup> g<sup>-1</sup>),
- high conductivity,
- controlled pore structure,
- processability and compatibility in composite materials,
- high temperature stability,
- relatively low cost.

Especially, the high surface area and conductivity are critical factors for carbon materials as the supercapacitors electrodes. Furthermore, the surface area of carbon materials will be deeply impact by the pore structures. Thus, the pore structures of carbon materials are other key factor for carbon materials electrodes.

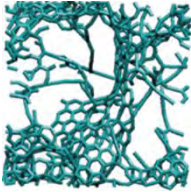
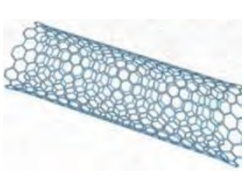
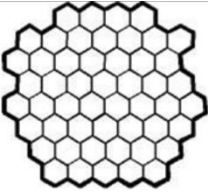
### 1) Active carbon (AC)

AC is the most common supercapacitors electrodes materials owing to its high surface area, high conductivity and low cost (as shown in Table. 1.1). AC is generally produced from physical (thermal) and/or chemical activation of various types of carbonaceous materials, for example, biomass (rice husk [23], ramie [24], sorghum pith [25]), polymer (Resin [26], polypyrrole [27, 28]), chemical reagent (furfuryl alcohol [29]), and etc. The chemical activation is usually carried out at a lower

temperature with activation agents, such as potassium hydroxide (KOH) [30], sodium hydroxide (NaOH) [31], zinc chloride (ZnCl) [24], and etc. AC can obtain the 3-dimensional (3-D) porous network and high surface area in the bulk of carbon materials through the activation process. As we all know, AC can obtain a broad pore size distribution consisting of micropores ( $< 2$  nm), mesopores (2~50 nm) and macropores ( $> 50$  nm) still through the activation process. Recently, many researchers have pointed out that the relationship of capacitance and surface area of AC are not proportional. For example, with a high surface area reached up to  $3000 \text{ m}^2 \text{ g}^{-1}$ , but the corresponding specific capacitance  $< 10 \text{ } \mu\text{F cm}^{-2}$ , much smaller than the theoretical value ( $15\text{-}25 \text{ } \mu\text{F cm}^{-2}$ ) [13], suggesting that not all pores are benefit for charge accumulation [33]. Therefore, although the surface area is an important factor for the capacitance performance of AC, the other aspects of the AC, such as pore size distribution, type and structure of pore, and surface functionality can also impact the capacitance performance of AC.

3-D AC has been developed for high rate electrochemical capacitive energy storage. This kind of 3-D AC is characterized by four typical features at different dimensions: firstly, micropores, some studies have showed that they contribute mostly to the specific surface area [22, 34]. Initially, the micropores size smaller than 0.5 nm were investigated and the result suggested that this kind of micropores were not accessible to hydrated ions [35, 36]. The effect of the micropore size on the capacitance of AC was further investigated by carbon materials with controllable micropore size. The AC can have a narrow pore size distribution with a mean value that is tunable in the range of 0.5~3 nm [37]. Secondly, mesopores, they can allow the rapid transport of ions from the electrolyte to the entire surface of the electrodes and make them quickly available for electric charge exchange [38]. Finally, macropores and localized graphitic structure, they can serve as ion-buffering reservoirs and enhances the electrical conductivity, respectively [38]. Especially, the macro and mesopores are a prerequisite for the transport of the electrolyte to the micropores in many ACs.

Table 1.1 Different carbon structures used in supercapacitors electrodes with active carbon, template carbon, carbon nanotube and graphene [32].

Materials	Active carbon	Template carbon	Carbon nanotubes	Graphene
Dimensionality	3-D	3-D	1-D	2-D
Conductivity	Low	Low	High	High
Volumetric capacitance	High	Low	Low	Moderate
Cost	Low	High	High	Moderate
Structure				

Besides control the surface area and pore size of the AC, the achievable maximum capacitance of EDLCs remains limited, and high energy density supercapacitors require more excellent electrochemical performance of AC electrode materials. A strategy to increase the capacitance is introduced pseudocapacitive phenomena at the electrode and electrolyte interface, and the usual practice is substituting some atoms in AC by heteroatoms (such as N [39], O [40], boron (B) [41]). These heteroatoms are derived from the carbon sources and transform into a part of the chemical structure as a result of incomplete carbonization. They are also derived from the dopant during subsequent doping process. In addition, we also note that the electronic properties of AC depend strongly on size and chirality, and the properties cannot be easily tailored [42]. The electronic properties of these AC also can be improved by incorporating heteroatoms. But, it is not always energetically favorable for most of the heteroatoms to reside in the network of AC. The most of these doping, the usual choice is B or N, owing to the following: firstly, B and N are the nearest neighbors of the C in the periodic table. The C atom of AC replaced by B or N, the total number electrons in the system remains unchanged. Secondly, the atomic radius of B and N are similar to

C. Thirdly, the B or N doped AC similar to the usual semi-conduction materials, and this is benefit for their application in electronic devices [42].

## 2) Template carbon

Template carbons (as shown in Table 1.1), they are produced by the carbonization of an organic compound in nanospace of a template inorganic substance (such as mesopores silica or aluminosilicate [38]), and then the resulting carbon is obtained by removing the template [13, 43]. Fig. 1.8 shows the schematic representation of general concept of the templating technique and the porous carbons obtained from different templates. Compared with AC, template carbon possess the controllable narrow pore size distributions, ordered pore structure, large specific surface area and an interconnected pore network. These advantages of template carbon result them promising candidates for supercapacitor electrode materials.

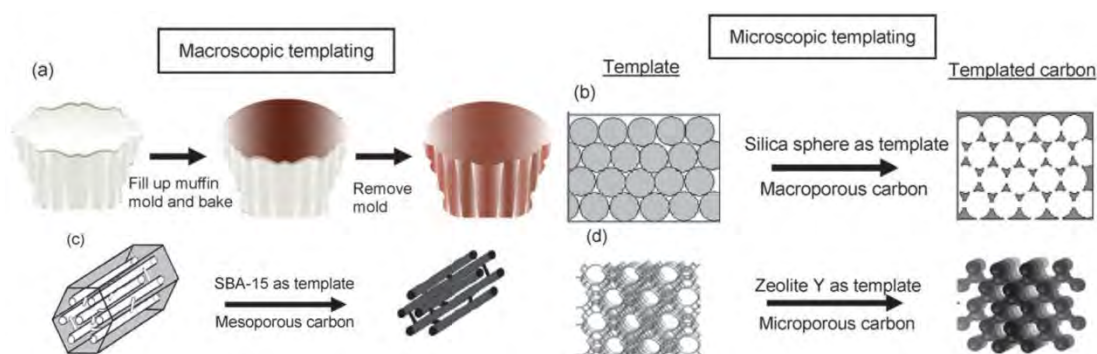


Fig. 1.8 Macroscopic representation is showing the general concept of the templating technique (a); microscopic synthesis of macroporous carbons using silica spheres as template (b), mesoporous carbons using SBA-15 as template (c) and microporous carbons using zeolite Y as template (d) [13].

Many carbon structures with well controlled micropores, mesopores and macropores produced by different types of template and carbon have been studied for supercapacitor applications [44, 45]. For example, a microporous carbon was obtained by using zeolite Y as the template and the resultant carbon possessed a high specific capacitance of about  $340 \text{ F g}^{-1}$  [45]. The template microporous carbon possessed a narrow pore size distribution, suitable pore size to the electrolyte ions and the ordered

straight pore channels. Compared with disordered and broad pore size distribution of microporous of AC, the template microporous carbon is better for use as high energy density electrode materials.

Compared with microporous carbon, mesoporous carbon has larger porous size, and this advantage is expected to favor fast ionic transport in mesoporous channels, resulting in a good rate performance [46]. Some researchers also have been proposed that the presence of mesoporous (usually 2~8 nm) can accelerate the kinetic process of the ion diffusion in the electrodes and improve the power density at high current densities, but the microporous structure is accessible to the electrolyte ions are essential for high energy storage [47, 48]. For example, W. Xing et al. [49] reported that they prepared a mesoporous carbons were template from mesoporous silica SBA-15, the mesoporous carbon possess the varying ordered pore symmetries such as P6mm and Ia3d (as shown in Fig. 1.9). The unique pore structure of mesoporous carbon resulted in the superior electric double layer capacitive performance. In short, the unique ordered pore structure of template carbon very conducive to it applied to supercapacitors.

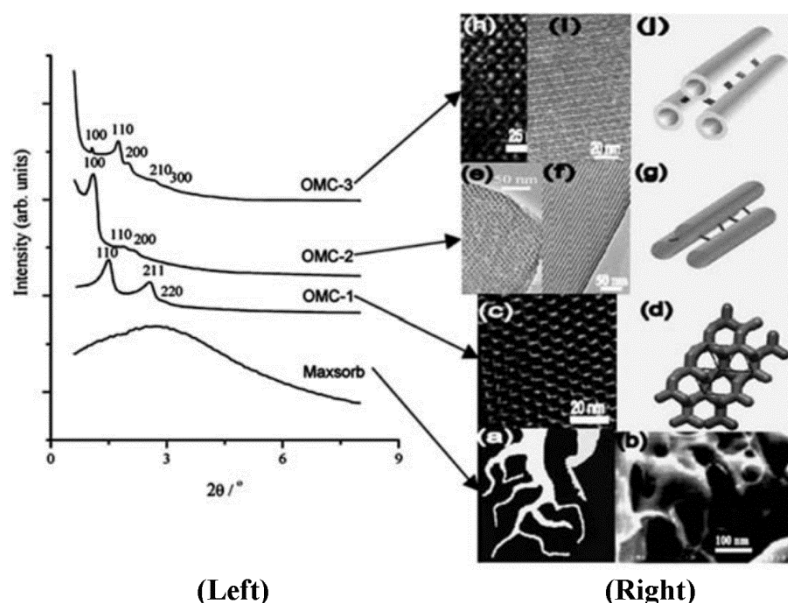


Fig. 1.9 SAXD patterns of Maxsorb and OMC carbons (left); TEM images and structure models of Maxsorb and OMC carbons (right) [49].

### 3) Carbon nanotubes (CNTs)

CNTs, its discovery has significantly advanced the science and engineering of carbon materials. Iijima using transmission electron microscope to examine carbon samples by an arc-discharge method (this method similar to that used for the fullerene synthesis), he found the needlelike tubes now popularly known as carbon nanotubes [50]. As we all know, CNTs possess the high conductivity, unique mechanical properties, high chemical stability, high aspect ratios and high activated surface areas (as shown in Table 1), and they have been widely studied for supercapacitors within the past decade [51, 52]. Right now, CNTs are produced by the catalytic decomposition of certain hydrocarbons. By control manipulation of various parameters, it is possible to generate nanostructures in assorted conformations and also control their crystalline order [53], and Fig. 1.10 shows the atomic structures of different types of carbon nanotubes. CNTs can be classified as single-walled carbon nanotube (SWCNT) and multi-walled carbon nanotube (MWCNT) [13, 42]. The diameter and length of SWCNT lie in the range of 0.4~2 nm and 1~100  $\mu\text{m}$ , respectively. For MWCNT, it can contain 2~50 SWCNTs having inner diameters 1.5~20 nm while outer diameters 2.5~30 nm [42].

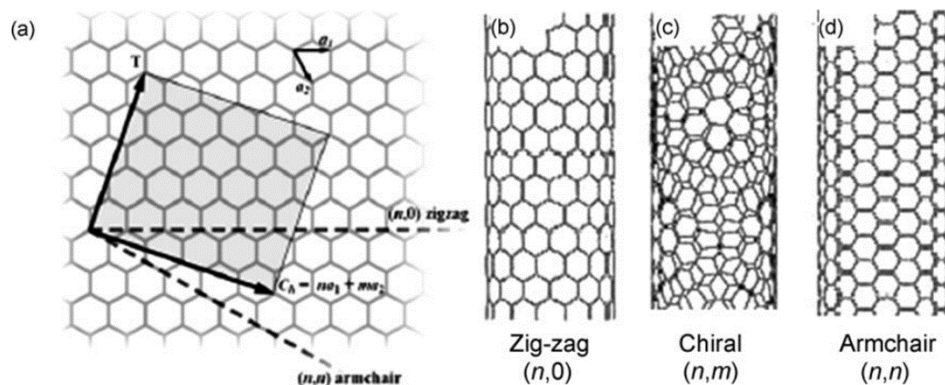


Fig. 1.10 Atomic structure of carbon nanotubes: a, schematic diagram showing how a graphene sheet is ‘rolled’ according to a pair of chiral vectors to form different atomic structures of carbon nanotubes; zig-zag  $(n, 0)$  (b), chiral  $(n,m)$  (c) and armchair  $(n,n)$  (d) carbon nanotubes [13].

Electrolyte ions can be stored in CNTs electrodes via the following ways:

adsorption and accumulation on the outer surface, adsorption and accumulation in the inner channel when CNTs are open and storage in the void space between bundles of tubes [38]. Owing to the above merits, CNTs are a good choice as high power electrode materials. Some researchers have shown that the specific capacitance of CNTs is highly dependent on their morphology and purity [54]. For pure CNTs, the specific capacitance in the range of 15~80 F g<sup>-1</sup>, and correspond specific surface area in the range of 120~400 m<sup>2</sup> g [54, 55]. C.M. Niu [56] et al. have reported a MWCNT electrode shows a high specific capacitance of 113 F g<sup>-1</sup> with surface area of 430 m<sup>2</sup> g<sup>-1</sup> and a power density of 8 kW kg<sup>-1</sup>. And even, studies have pointed out that the highest specific capacitance of pure CNTs electrode is found to be ~100 F g<sup>-1</sup>, and the energy density is smaller than that of AC [57, 13]. These disadvantages attributed to that their relatively small specific surface area (generally < 500 m<sup>2</sup> g<sup>-1</sup> [13, 58]) restricts their usage in high energy supercapacitors. Moreover, the other difficulties are retaining the intrinsic properties of individual CNTs on the macroscopic scale [59] and the high cost of purification [58]. Therefore, modifications and incorporation with other active materials have been proposed to overcome the above drawbacks.

#### **4) Graphene**

Graphene, a new star in nanoscience and nanomaterial, it is a one-atom-thick 2D sheet of sp<sup>2</sup>-bonded carbon, the carbon atoms arranged in a honeycomb lattice (as shown in Table. 1.1), and exhibits many advantages, such as high electrical and thermal conductivity, great mechanical strength and high surface area (theoretically 2630 m<sup>2</sup> g<sup>-1</sup>), has attracted great interest during the past decade for application in supercapacitors [60-62]. Graphene was first discovered by Andre Geim and Konstantin Novoselov in 2004. They obtained graphene sheets by using cohesive tape to repeatedly split graphite crystals into increasingly thinner pieces until individual atomic planes were reached [21, 60]. As we all know, one of the critical challenges in the synthesis and application of graphene sheets is to overcome the strong cohesive van der Waals energy of the  $\pi$ -stacked layers in graphite [58, 63, 64]. Currently, the most comment method is exfoliation of GO followed by reduction to give the final product, reduced graphite oxide (Hummer's method, as shown in Fig. 1.11) [20, 65].

Furthermore, the other methods are assembling graphene sheets into graphene-based materials with ordered 2D or 3D microstructures and separating graphene sheets with other nanomaterials [66, 67].

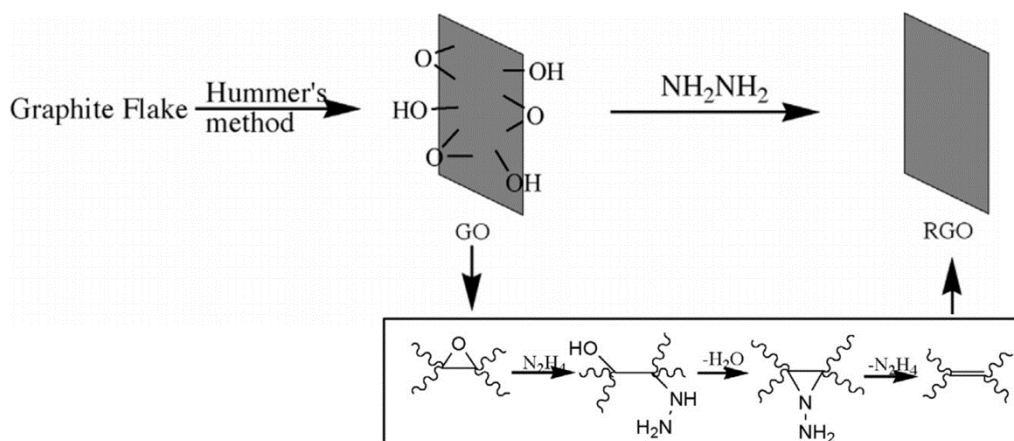
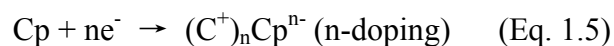
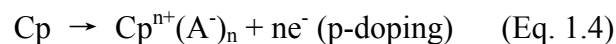


Fig. 1.11 Preparation of reduced graphene oxide by Hummer method [65].

The excellent electric conductivity and mechanical flexibility of graphene enable its electrodes to undergo fast electron transfer without any significant volume expansion/shrinking during charging-discharging [46]. Moreover, graphene sheets irreversibly aggregate due to the  $\pi$ - $\pi$  interactions and van der Waals forces, and make most pores. Therefore, graphene displays a moderate specific capacitance of  $\sim 110 \text{ F g}^{-1}$  [11]. There are many reports aiming to directly utilize the 2D structure of graphene for supercapacitors. S.R.C. Vivekchand et al. prepared reduced graphene with a specific surface area as high as  $925 \text{ m}^2 \text{ g}^{-1}$  by exfoliation at  $1050 \text{ }^\circ\text{C}$ , and exhibited specific capacitance of  $117 \text{ F g}^{-1}$  [68]. But the high temperature exfoliation process is energy consuming and difficult to control. X. Yang et al. prepared a hydrated graphene film for inhibited the restacking of graphene sheets, and this film exhibited a high specific capacitance ( $215 \text{ F g}^{-1}$ ) and excellent cycle stability [69]. In addition, J.J. Yoo assembled vertically aligned graphene electrodes which showed a high specific capacitance up to  $250 \text{ F g}^{-1}$ , and suggesting this in-plane design can utilize the maximum electrochemical surface area of graphene sheets [70].

### 1.3.2 Conducting polymer-based electrode materials

Conducting polymers, their each atom along the backbone is involved in a  $\pi$  bond, which is much weaker than the  $\sigma$  bonds that hold the atoms in the polymer chain together, and they characteristically have a conjugated backbone with a high degree of  $\pi$ -orbital overlap [71]. Hence, they can render conductive through the conjugated bond system along the polymer backbone [10]. In 1977, American scientists Heeger, MacDiarmid and their Japanese colleague Shirakawa discovered that the doping polyacetylene (PA) with iodine exhibited the metal-like properties [72, 73], and since then people have begun to study of conducting polymers. Most conducting polymers were synthesized by modification of the structure shown in Fig. 1.12. Conducting polymers show a low conductivity in the neutral state. Their conductivity can improve by the formation of charge carriers upon oxidizing (p-doping) or reducing (n-doping) their conjugated backbone [74]. The simplified reaction (Eq. 1.4 and 1.5) for these two charging processes are as follows [10]:



The typical n-doping conducting polymer are PA and poly(paraphenylene), and these polymers have high impedances. Polypyrrole (PPy) and polyaniline (PANI), they are the typical p-doping conducting polymers [75]. Neutral PPy or polythiophene is oxidized, and then, a relaxation process causes the generation of localized electronic state, and this state is called polaron. If an additional electron is removed, it is very conducive to remove the second electron from the polaron than from another part of the polymer chain. And this leads to the formation of one bipolaron rather than two polarons (as shown in Fig. 1.13) [74, 76]. Another unique doping process is the doping of PANI by protonation. This process leads to an internal redox reaction converting the semiconducting form of PANI (emeraldine base) to a “metallic” form (emeraldine salt). The reaction between the different forms of PANI is shown in the Fig. 1.14 [74].

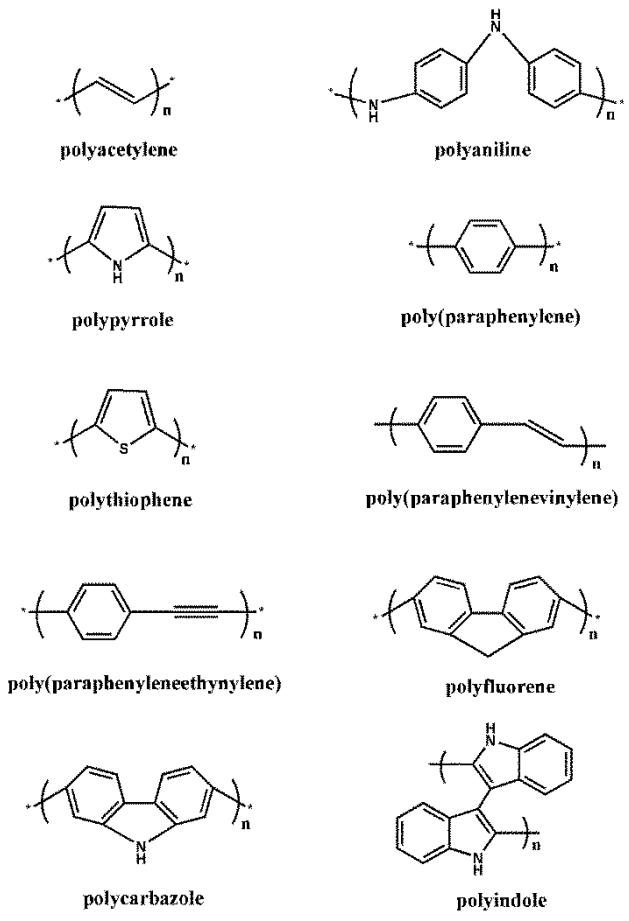


Fig. 1.12 Various conducting polymer structures.

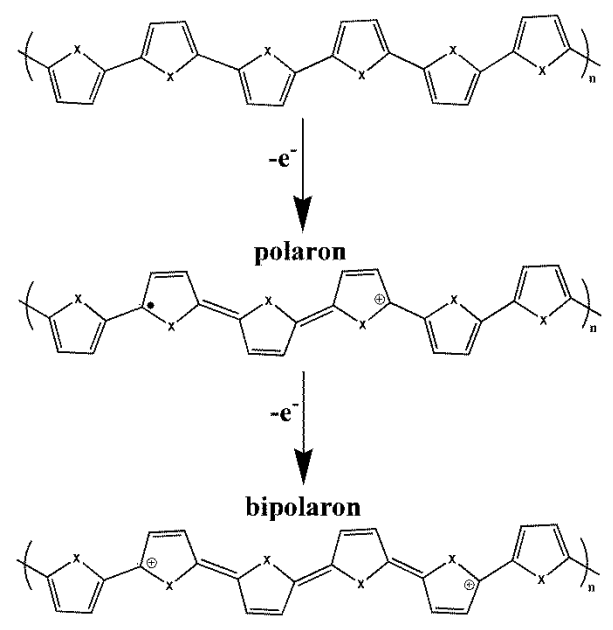


Fig. 1.13 Formation of the bipolaron state in PPy or polythiophene.

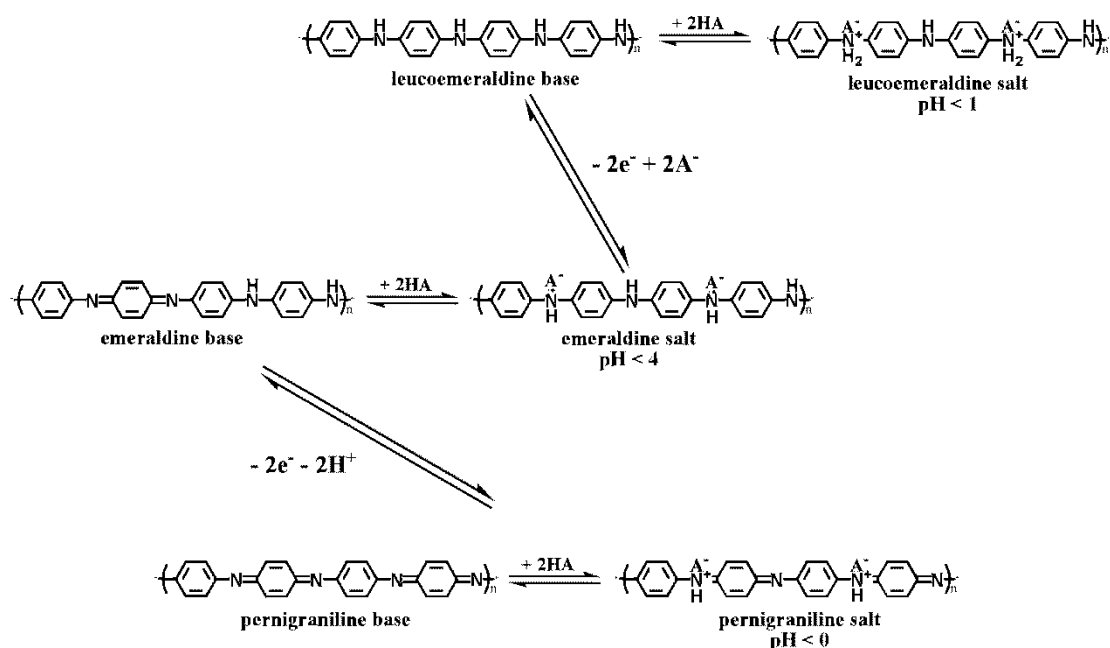


Fig. 1.14 Conversion between different states of PANI

Conducting polymers possess many advantages, such as high conductivity in a doped state, high storage capacity/reversibility, adjustable redox activity through chemical modification, and low cost/environment impact. These advantages make them suitable materials for supercapacitors [77, 78]. The common conducting polymer in supercapacitor applications are PANI [79], PPy [80], polythiophene [81] and their derivatives. PANI and PPy often use as cathode materials due to they can only be p-doped. There are many reports on applying the above conducting polymer to supercapacitors. For examples, H.L Li et al. have reported a pure PANI modification electrode exhibited a high specific capacitance and which reach up to  $815 \text{ F g}^{-1}$  [82]. A kind of 3D polyaniline have prepared by Y. Gawli et al. by inorganic and organic acid co-doping, and it possesses a nearly constant high specific capacitance of  $350 \text{ F g}^{-1}$  at the current density range of  $1\sim 40 \text{ A g}^{-1}$ . At same time, it exhibits good cycle stability at the current density of  $40 \text{ A g}^{-1}$  [83]. Even, Y. Huang et al. have prepared a kind of polypyrrole from the molecular ordering, and this kind of polypyrrole exhibited the excellent cycle stability (the capacitance retentions of over 97, 91 and 86 % after 15000, 50000 and 100000 charging/discharging cycles, respectively), and can sustain over 230000 charging/discharging cycles with still

about half of initial capacitance retained [84]. Unfortunately, swelling and shrinking of conducting polymer unavoidable occur during the charging/discharging process (due to the intercalating/deintercalating function). This problem will further lead to mechanical degradation of the electrode and fading electrochemical performance during cycling, and then limit the conducting polymer applied to supercapacitors.

### 1.3.3 Transition metal oxides-based electrode materials

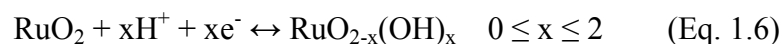
Transition metal oxides, they can provide higher energy density for supercapacitors than that of carbon materials and better cycle stability than that of conducting polymers. They store energy not only through the electrical double layer capacitance (like carbon materials) but also by the faradaic reactions between electrode materials and electrolyte ions at a suitable potential window [85]. The normal conditions for transition metal oxides in supercapacitors application are [86]:

- the metal can exist in two or more oxidation states that coexist over a continuous range with no phase changes involving irreversible modifications of a 3D structure;
- the protons can freely intercalate into the oxide lattice on reduction and out of the lattice on oxidation, allowing facile interconversion of  $O^{2-} \leftrightarrow OH^-$ ;
- the oxide should be electronically conductive.

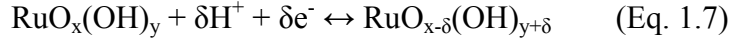
In current, the common transition metal oxides are ruthenium oxide, manganese oxide, cobalt oxide and nickel oxide.

#### 1) $RuO_2$

Among the transition metal oxides,  $RuO_2$  has been widely investigated due to its highly reversible redox reactions, three distinct oxidation states accessible within a 1.2 V voltage window, high proton conductivity, remarkably high specific capacitance and high rate capability [87, 88]. The pseudocapacitive behaviors of  $RuO_2$  in acid and alkali electrolyte exhibit different reactions. In acid electrolyte, the mechanism was suggested to be as follow (Eq. 1.6 and 1.7):



or



The rapid reversible electron transfer is accompanied by adsorption of protons on the surface of RuO<sub>2</sub> particles, and the oxidation state of Ru can change from II to IV [86, 89-91]. In alkali electrolyte, the changes in the valency state of RuO<sub>2</sub> also has been suggested that in the carbon/ruthenium composite is charged state, the RuO<sub>2</sub> in the composite will be oxidized to RuO<sub>4</sub><sup>2-</sup>, RuO<sub>4</sub><sup>-</sup> and RuO<sub>4</sub>, and when it discharged the high valency state compounds will be reduced to RuO<sub>2</sub> [86, 92].

It is worth noting, the crystallinity of RuO<sub>2</sub> is the key parameter in determining the value of specific capacitance. The amorphous structure of RuO<sub>2</sub> is benefit for the proton intercalate into the bulk of RuO<sub>2</sub> but not into the crystalline phase [93]. For example, the amorphous ruthenium oxide materials in the acid electrolyte exhibited a maximum specific capacitance of 720 F g<sup>-1</sup> upon calcination at 150 °C [91]. It is also noting that hydrous RuO<sub>2</sub> possess the better capacitive performance than that of anhydrous RuO<sub>2</sub>. This is owing to the hydrous regions are more permeable to protons and proton conduction inside RuO<sub>2</sub> is dominant compared with the electron conduction [94, 95]. Such as, in the literature [96], hydrous RuO<sub>2</sub> (RuO<sub>2</sub>·0.5H<sub>2</sub>O) showed a specific capacitance as high as 900 F g<sup>-1</sup>. The microstructure of RuO<sub>2</sub> is determined by the preparation method. Generally, the methods of preparation of RuO<sub>2</sub> are hydrothermal synthesis and sol-gel synthesis [97], and these synthesis methods as shown in Fig. 1.15. The results showed that the amorphous and crystalline phase RuO<sub>2</sub> can be obtained at low and high temperature, respectively [98]. Although amorphous RuO<sub>2</sub> can provide excellent capacitive performance, its drawbacks, such as the high cost and environment impact, hinder it from being used in the commercialization of supercapacitors [99].

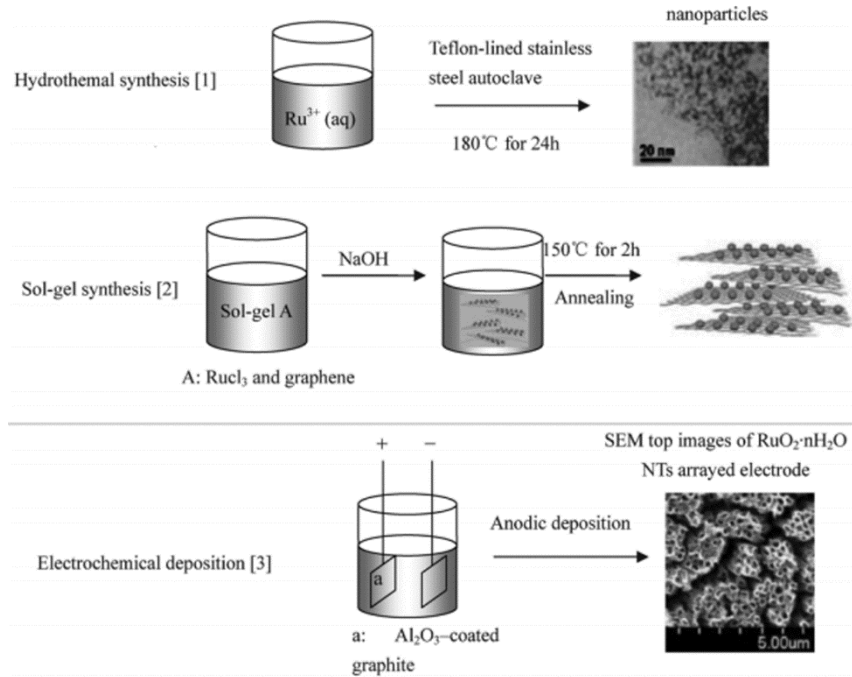
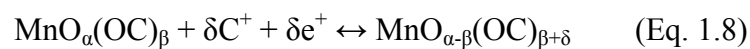


Fig. 1.15 The typical synthesis processes of  $\text{RuO}_2$  [89].

## 2) $\text{MnO}_2$

Manganese oxides, they present low cost, low toxicity, environment safety and high theoretical capacities (ranging from 1100 to 1300  $\text{F g}^{-1}$ ), and have acted as the alternative materials for  $\text{RuO}_2$  [100, 101]. In 1999, Lee and Goodenough reported that the amorphous  $\text{MnO}_2$  could be used as an excellent electrode material for faradaic electrochemical capacitor [102]. Since then, the manganese oxides have attracted major attention and is considered a promising alternative of materials for supercapacitors application.

Manganese oxides also have pluralism valence states, and their capacitance come mainly from faraday reaction based on these valence states. Some reversible redox transitions involving the exchange of protons or cations would occurs between manganese oxides and electrolyte, as well as the transitions between  $\text{Mn(III)/Mn(II)}$ ,  $\text{Mn(IV)/Mn(III)}$ , and  $\text{Mn(VI)/Mn(IV)}$  [103]. The proposed mechanism of redox process is expressed in Eq. 1.8 [86, 104]:



where  $\text{C}^+$  signifies the protons and alkali metal cations (such as  $\text{Li}^+$ ,  $\text{Na}^+$ ,  $\text{K}^+$ ) in the electrolyte, the  $\text{MnO}_\alpha(\text{OC})_\beta$  and  $\text{MnO}_{\alpha-\beta}(\text{OC})_{\beta+\delta}$  indicate  $\text{MnO}_2 \cdot \text{H}_2\text{O}$  in high and low

oxidation states, respectively. Similar to  $\text{RuO}_2$ , the capacitive performance of manganese oxides also heavily depend on their crystalline structures. Manganese oxides have many crystalline structures, including  $\alpha$ -,  $\beta$ -,  $\gamma$ -,  $\delta$ - and  $\lambda$ - $\text{MnO}_2$ , the different structures can be described by the size of their tunnels determined by the number of octahedral subunits ( $n \times m$ ), as shown in Fig. 1.16 [105]. The  $\alpha$ - $\text{MnO}_2$  consists of double chains of edge-sharing  $\text{MnO}_6$  octahedra, which are linked at corners to form 1D ( $2 \times 2$ ) and ( $1 \times 1$ ) tunnels in the tetragonal unit cell [106].  $\beta$ - $\text{MnO}_2$  is composed of single strands of edge-sharing  $\text{MnO}_6$  octahedra to form a 1D ( $1 \times 1$ ) tunnel [107].  $\gamma$ - $\text{MnO}_2$  is composed of ramsdellite ( $1 \times 2$ ) and pyrolusite ( $1 \times 1$ ) domains.  $\delta$ - $\text{MnO}_2$  is a 2D layered structure with an interlayer separation of  $\sim 7 \text{ \AA}$ . It has a significant amount of water and stabilizing cations such as  $\text{Na}^+$  or  $\text{K}^+$  between the sheets [108].  $\lambda$ - $\text{MnO}_2$  is a 3D spinel structure.

For  $\alpha$ - $\text{MnO}_2$ , it has synthesized by a hydrothermal reaction of  $\text{KMnO}_4$  under acidic conditions exhibited a specific capacitance of only  $71.1 \text{ F g}^{-1}$  at a current density of  $0.3 \text{ A g}^{-1}$  [109]. With  $\gamma$ - $\text{MnO}_2$ , some studies have reported that the specific capacitance of it only  $20\text{-}30 \text{ F g}^{-1}$  [110, 111]. For 2D layered structure of  $\delta$ - $\text{MnO}_2$ , several methods for synthesizing it have been developed.  $\delta$ - $\text{MnO}_2$  obtained by hydrothermal synthesis process exhibited a much higher specific capacitance [112].  $\delta$ - $\text{MnO}_2$  also obtained through a redox reaction between  $\text{MnSO}_4$  and  $\text{KMnO}_4$ , and this kind of  $\delta$ - $\text{MnO}_2$  exhibited excellent capacitive performance (its specific capacitance is  $236 \text{ F g}^{-1}$ ) in  $0.1 \text{ mol L}^{-1} \text{ NaSO}_4$  electrolyte [105]. In addition, C.T. Sun et al. have prepared all kinds of ( $\alpha$ -,  $\beta$ -,  $\gamma$ - and  $\delta$ -) crystalline structure  $\text{MnO}_2$  by similar methods [113]. Their research also showed that the  $\delta$ - $\text{MnO}_2$  possess more outstanding capacitive performance (the specific capacitance is  $190 \text{ F g}^{-1}$ ) than the other  $\text{MnO}_2$ , this is owing to the interlayer spacing of  $\delta$ - $\text{MnO}_2$  ( $0.54 \text{ nm}$ ) is larger than the size of the cations (such as  $\text{K}^+$ ,  $\text{Na}^+$  and  $\text{Li}^+$ , their size are  $0.33$ ,  $0.36$  and  $0.38 \text{ nm}$ , respectively), providing enough space for cations to move in and out within the layers. Also attributed to the Mn centers of  $\delta$ - $\text{MnO}_2$  located at the surface, and the Mn centers could contribute to the faradaic charge storage [113].

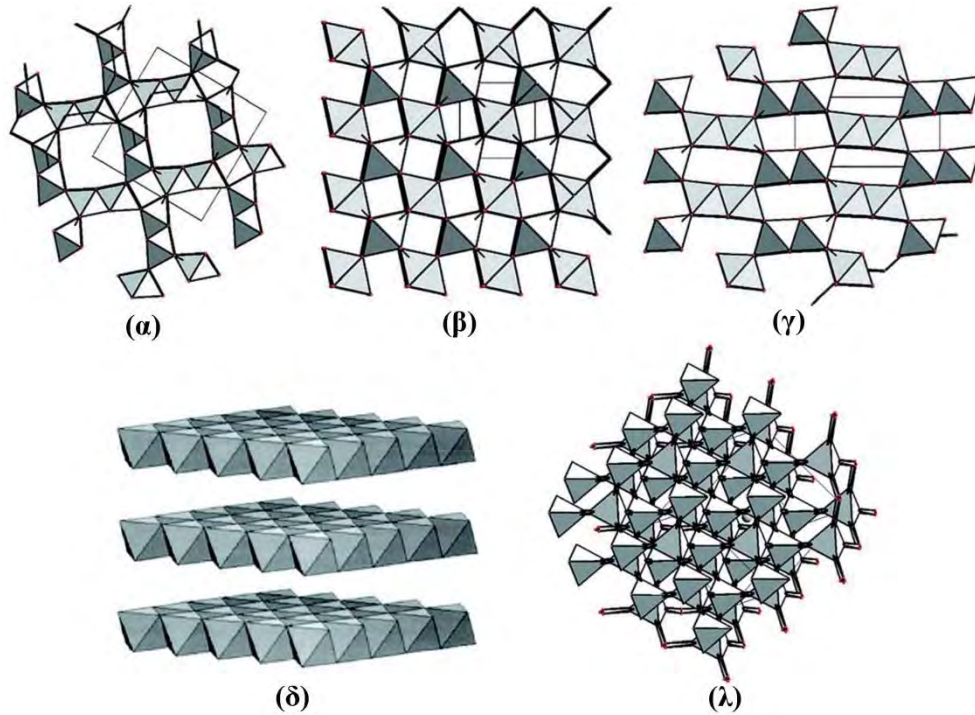


Fig. 1.16 crystal structure of  $\alpha$ -,  $\beta$ -,  $\gamma$ -,  $\delta$ - and  $\lambda$ - $\text{MnO}_2$  [105].

Unfortunately, Mn oxides applied in supercapacitors still have several challenges. The first challenge is the dissolution problem.  $\text{MnO}_2$  electrode will be suffer capacitance degradation during cycling, and this is due to the partial dissolution of  $\text{MnO}_2$  [114]. The dissolution reaction can be expressed as Eq. 1.9 [115]:



Many researchers have been carried out prevent Mn oxides from the dissolution during cycling. For instance, some new kind electrolytes have been developed to avoid forming acidic environment in solution [116]. The other challenges are the low specific surface area and poor electronic conductivity. To improve the specific surface area of Mn oxides, many researchers doping other metals into Mn oxides [117] or introducing multilayered film electrodes [118]. To enhance the electronic conductivity of Mn oxides, researchers often doping the highly conductive supports into Mn oxides, such as conducting polymer, active carbon, CNTs and graphite [86].

## 1.4 Contribution from this dissertation

Supercapacitors have attracted a lot of attention due to they can complement or

replace batteries in electrical energy storage. The core issue of research on supercapacitors is preparation of electrode materials. In this thesis, chapter 3 describes the preparation of graphene oxide/polypyrrole/multi-walled carbon nanotube composite by in-suit polymerization method, and further systematically explored the effect of the three componets' mass ratio on the property of microstructure and electrochemical performance of composites. The obtained composites have a special microstructure (polypyrrole chains acted as the "bridge" between multi-walled carbon nanotube and graphene oxide), and they showed excellent electrochemical performance when used as electrode materials for supercapacitors. However, the preparation method is complexity, and we also found a reason is that the binary carbon material (multi-wall carbon nanotube/graphene oxide) showed the poor electrochemical performance.

In chapter 4, in order to solve the problem of chapter 3, a type of nitrogen-doped carbon nanowires are successfully synthesized and used as negative electrode material of supercapacitors. The carbon nanowires were facilely prepared through direct carbonization method using polypyrrole nanowires (prepared when hexadecyl trimethyl ammonium bromide as soft template) as the carbon precursor. The carbon nanowires have the acceptable nitrogen content and large specific surface area. These features cause the kind of carbon nanowires showed good electrochemical performance. For further improve the electrochemical performance of carbon nanowires, in chapter 5, a kind of porous carbon nanowires are successfully prepared and also used as negative electrode material of supercapacitors. The porous carbon nanowires with high specific surface area and adequate nitrogen content are prepared by KOH activation of nonporous nitrogen doped carbon nanowires. Moreover, the porous carbon nanowires showed the better electrochemical performance than that of carbon nanowires.

The above studies focused on the development of negative electrode materials. In chapter 6, based on chapter 4, describes the preparation of MnO<sub>2</sub>/carbon nanowire composites (a kind of positive electrode material) by hydrothermal method under different reaction times. The composites possess the special microstructure based on

the reaction times, and the special microstructures have a profound effect on their electrochemical performance. The composites and porous carbon nanowires (prepared in chapter 5) acted as the positive and negative electrode materials of asymmetric supercapacitors, respectively. The asymmetric supercapacitor showed the high energy density, excellent rate capability and high cycle stability.

## References

- [1] G. Yan, T. Bai, J.L. Yu, *Sol. Energy* 125 (2016) 243-255.
- [2] B. Cárdenas, N. León, J. Pye, H.D. García, *Sol. Energy* 126 (2016) 32-43.
- [3] A. Dabbaghiyan, F. Fazelpour, M.D. Abnavi, M.A. Rosen, Iran, *Renew. Sust. Energ. Rev.* 55 (2016) 455-466.
- [4] A. Kumar, N. Kumar, P. Baredar, A. Shukla, *Renew. Sust. Energ. Rev.* 45 (2015) 530-539.
- [5] Nasruddin, M.I. Alhamid, Y. Daud, A. Surachman, A. Sugiyono, H.B. Aditya, T.M.I. Mahlia, *Renew. Sust. Energ. Rev.* 53 (2016) 733-740.
- [6] J.M. Tarascon, P. Simon, *Electrochemical Energy Storage*, Vol. 1, Wiley, 2015, p. viii.
- [7] M. Winter, R.J. Brodd, *Chem. Rev.* 104 (2004) 4245-4270.
- [8] P. Simon, Y. Gogotsi, *Nat. Mater.* 7 (2008) 845-854.
- [9] J.R. Miller, A.F. Burke, *Electrochem. Soc. Interface* 17 (2008) 53-57.
- [10] G.A. Snook, P. Kao, A.S. Best, *J. Power Sources* 196 (2011) 1-12.
- [11] M.D. Stoller, S. Park, Y. Zhu, J. An, R.S. Ruoff, *Nano Lett.* 8 (2008) 3498-3502.
- [12] Y. Huang, J.J. Liang, Y.S. Chen, *Small* 8 (2012) 1805-1834.
- [13] L.L. Zhang, X.S. Zhao, *Chem. Soc. Rev.* 38 (2009) 2520-2531.
- [14] G Gouy, *J. Phys.* 4 (1910) 457.
- [15] DL Chapman, LI, *Philos. Mag.* 6 (1913) 475.
- [16] O. Stern, *Z. Electrochem.* 30 (1924) 508.
- [17] F. Béguin, V. Presser, A. Balducci, E. Frackowiak, *Adv. Mater.* 26 (2014) 2219-2251.
- [18] M.J. Zhi, C.C. Xiang, J.T. Li, M. Li, N.Q. Wu, *Nanoscale* 5 (2013) 72-88.
- [19] J.Y. Cao, X.H. Li, Y.M. Wang, F.C. Walsh, J.H. Ouyang, D.C. Jia, Y. Zhou, *J. Power Sources* 293 (2015) 657-674.
- [20] A. Ghosh, Y.H. Lee, *ChemSusChem* 5 (2012) 480-499.
- [21] L. Dai, D.W. Chang, J.B. Baek, W. Lu, *Small* 8 (2012) 1130-1166.
- [22] A.G. Pandolfo, A.F. Hollenkamp, *J. Power Sources* 157 (2006) 11-27.

- [23] D.L. Zeng, Q. Zhang, S.Y. Chen, S.L. Liu, G.H. Wang, *Micropor. Mesopor. Mat.* 219 (2016) 54-58.
- [24] X. Du, W. Zhao, Y. Wang, C.Y. Wang, M.M. Chen, T. Qi, C. Hua, *Mingguo Ma, Bioresource Technol.* 149 (2013) 31-37.
- [25] S.T. Senthilkumar, B. Senthilkumar, S. Balaji, C. Sanjeeviraja, R.K. Selvan, *Mater. Res. Bull.* 46 (2011) 413-419.
- [26] N. Nishiyama, T. Zheng, Y. Yamane, Y. Egashira, K. Ueyama, *Carbon* 43 (2005) 269-274.
- [27] L. Qie, W.M. Chen, Z.H. Wang, Q.G. Shao, X. Li, L.X. Yuan, X.L. Hu, W.X. Zhang, Y.H. Huang, *Adv. Mater.* 24 (2012) 2047-2050.
- [28] X.Y. Zhou, J.J. Tang, J. Yang, J. Xie, B. Huang, *J. Mater. Chem. A* 1 (2013) 5037-5044.
- [29] L. Sun, C.J. Yan, Y. Chen, H.Q. Wang, Q.Y. Wang, *J. Non-Cryst. Solids* 358 (2012) 2723-2726.
- [30] R. Ubago-Perez, F. Carrasco-Marín, D. Fairen-Jimenez, *Micropor. Mesopor. Mat.* 92 (2006) 64-70.
- [31] B. Xu, Y.F. Chen, G. Wei, G.P. Cao, H. Zhang, Y.S. Yang, *Mater. Chem. Phys.* 124 (2010) 504-509.
- [32] P. Simon, Y. Gogotsi, *Acc. Chem. Res.* 46 (2013) 1094-1103.
- [33] K. Kierzek, E. Frackowiak, G. Lota, G. Gryglewicz, J. Machnikowski, *Electrochim. Acta* 49 (2004) 515-523.
- [34] J Gamby, P.L Taberna, P Simon, J.F Fauvarque, M Chesneau, *J. Power Sources* 101 (2001) 109-116.
- [35] D.Y. Qu, *J. Power Sources* 109 (2002) 403-411.
- [36] H. Shi, *Electrochim. Acta* 41 (1996) 1633-1639.
- [37] Y. Gogotsi, A. Nikitin, H. Ye, W. Zhou, J. E. Fischer, B. Yi, H. C. Foley, M. W. Barsoum, *Nat. Mater.* 2 (2003) 591-594.
- [38] D.S. Su, R. Schlögl, *ChemSusChem* 3 (2010) 136-168.
- [39] D. Hulicova-Jurcakova, M. Kodama, S. Shiraishi, H. Hatori, Z.H. Zhu, G.Q. Lu, *Adv. Funct. Mater.* 19 (2009) 1800-1809.

- [40] E. Raymundo-Piñero, M. Cadek, F. Béguin, *Adv. Funct. Mater.* 19 (2009) 1032-1039.
- [41] Q.L. Hao, X.F. Xia, W.J. W.Lei, J.S. Wang, *Carbon* 81 (2015) 552-563.
- [42] D. Jana, C.L. Sun, L.C. Chen, K.H. Chen, *Prog. Mater. Sci.* 58 (2013) 565-635.
- [43] S. Jun, S.H. Joo, R. Ryoo, M. Kruk, M. Jaroniec, Z. Liu, T. Ohsuna, O. Terasaki, *J. Am. Chem. Soc.* 122 (2000) 10712-10713.
- [44] W. Li, D. Chen, Z. Li, Y. Shi, Y. Wan, G. Wang, Z. Jiang, D. Zhao, *Carbon* 45 (2007) 1757-1763.
- [45] C.O. Ania, V. Khomenko, E. Raymundo-Pinero, J.B. Parra, F. Beguin, *Adv. Funct. Mater.* 17 (2007) 1828-1836.
- [46] S. Chen, W. Xing, J.J Duan, X.J Hu, S.Z. Qiao, *J. Mater. Chem. A* 1 (2013) 2941-2954.
- [47] E. Frackowiak, *Phys. Chem. Chem. Phys.* 9 (2007) 1774-1785.
- [48] J.S. Huang, B.G. Sumpter, V. Meunier, *Chem. Eur. J.* 14 (2008) 6614-6626.
- [49] W. Xing, S.Z. Qiao, R. G. Ding, F. Li, G.Q. Lu, Z.F. Yan, H.M. Cheng, *Carbon* 44 (2006) 216-224.
- [50] S. Iijima, *Nature* 354 (1991) 56-58.
- [51] P.J. Hall, M. Mirzaeian, S.I. Fletcher, F.B. Sillars, A.J.R. Rennie, G.O. Shitta-Bey, G. Wilson, A. Cruden, R. Carter, *Energy Environ. Sci.*, 2010, 3, 1238-1251.
- [52] T. Bordjiba, M. Mohamedi, L.H. Dao, *Adv. Mater.* 20 (2008) 815-819.
- [53] N.M. Rodriguez, *J. Mater. Res.* 8 (1993) 3233-3250.
- [54] E. Frackowiak, K. Jurewicz, K. Szostak, S. Delpeux, F. Beguin, *Fuel Process. Technol.* 77/78 (2002) 213-219.
- [55] E. Frackowiak, S. Delpeux, K. Jurewicz, K. Szostak, D. CazorlaAmoros, F. Beguin, *Chem. Phys. Lett.* 361 (2002) 35-41.
- [56] C.M. Niu, E.K. Sichel, R. Hoch, D. Moy, H. Tennent, *Appl. Phys. Lett.* 70 (1997) 1480-1482.
- [57] H. Pan, J.Y. Li, Y.P. Feng, *Nanoscale Res. Lett.* 5 (2010) 654-668.
- [58] H. Jiang, P.S. Lee, C.Z. Li, *Energy Environ. Sci.* 6 (2013) 41-53.
- [59] D.N. Futaba, K. Hata, T. Yamada, T. Hiraoka, Y. Hayamizu, Y. Kakudate, O.

- Tanaike, H. Hatori, M. Yumura, S. Iijima, *Nat. Mater.* 5 (2006) 987-994.
- [60] K. Novoselov, A. Geim, S. Morozov, D. Jiang, Y. Zhang, S. Dubonos, I. Grigorieva, A. Firsov, *Science* 306 (2004) 666-669.
- [61] J.L. Xia, F. Chen, J.H. Li, N.J. Tao, *Nat. Nanotechnol.* 4 (2009) 505-509.
- [62] P. Avouris, Z.H. Chen, V. Perebeinos, *Nat. Nanotechnol.* 2 (2007) 605-615.
- [63] Y. Sun, Q. Wu, G. Q. Shi, *Energy Environ. Sci.* 4 (2011) 1113-1132.
- [64] B. Luo, S.M. Liu, L.J. Zhi, *Small* 8 (2012) 630-646.
- [65] X. Wang, C. Yang, H.D. Li, P. Liu, *Electrochimica Acta* 111 (2013) 729-737.
- [66] Y. Xu, K. Sheng, C. Li, G. Shi, *ACS Nano* 4 (2010) 4324-4330.
- [67] W. Lv, D.M. Tang, Y.B. He, C.H. You, Z.Q. Shi, X.C. Chen, C.M. Chen, P.X. Hou, C. Liu, Q. H. Yang, *ACS Nano* 3 (2009) 3730-3736.
- [68] S.R.C. Vivekchand, C.S. Rout, K.S. Subrahmanyam, A. Govindaraj, C.N.R. Rao, *J. Chem. Sci.* 120 (2008) 9-13.
- [69] X. Yang, J. Zhu, L. Qiu, D. Li, *Adv. Mater.* 23 (2011) 2833-2838.
- [70] J.J. Yoo, K. Balakrishnan, J. Huang, V. Meunier, B.G. Sumpter, A. Srivastava, M. Conway, A.L. Reddy, J. Yu, R. Vajtai, P.M. Ajayan, *Nano Lett.* 11 (2011) 1423-1427.
- [71] L. Ghasemi-Mobarake, M.P Prabhakaran, M. Morshed, M.H. Nasr-Esfahani, H. Baharvand, S. Kiani, S.S Al-Deyab, S. Ramakrishna, *J. Tissue Eng. Regen. Med.* 5 (2011), e17-e35.
- [72] Y.W. Park, A. Denenstien, C.K. Chiang, A.J. Heeger, A.G. MacDiarmid, *Solid State Commun.* 29 (1979) 747-751.
- [73] H. Shirakawa, E.L. Louis, A.G. MacDiarmid, C.K. Chiang, A.J. Heeger, *J. Chem. Soc. Chem. Commun.* (1977) 578- 580.
- [74] U. Lange, N.V. Roznyatovskaya, V.M. Mirsky, *Anal. Chim. Acta.* 614 (2008) 1-26.
- [75] K. Naoi, S. Suematsu, A. Manago, *J. Electrochem. Soc.* 147 (2000) 420-426.
- [76] J.L. Bredas, G.B. Street, *Acc. Chem. Res.* 18 (1985) 309-315.
- [77] V. Gupta, N. Miura, *Mater. Lett.* 60 (2006) 1466-1469.
- [78] L. Fan, J. Maier, *Electrochem. Commun.* 8 (2006) 937-940.
- [79] J.H. Liu, J.W. An, Y.C. Zhou, Y.X. Ma, M.L. Li, M. Yu, S.M. Li, *ACS Appl.*

- Mater. Interfaces 4 (2012) 2870-2876.
- [80] T.Y. Liu, L. Finn, M.H. Yu, H.Y. Wang, T. Zhai, X.H. Lu, Y.X. Tong, Y. Li, Nano Lett. 14 (2014) 2522-2527.
- [81] A. Alabadi, S. Razzaque, Z.H. Dong, W.X. Wang, B. Tan, J. Power Sources 306 (2016) 241-247.
- [82] H.L. Li, J.X. Wang, Q.X. Chu, Z. Wang, F.B. Zhang, S.C. Wang, J. Power Sources 190 (2009) 578-586.
- [83] Y. Gawli, A. Banerjee, D. Dhakras, M. Deo, D. Bulani, P. Wadgaonkar, M. Shelke, S. Ogale, Sci. Rep. 2016 DIO 10.1038/srep21002.
- [84] Y. Huang, M.S. Zhu, Z.X. Pei, Y. Huang, H.Y. Geng, C.Y. Zhi, ACS Appl. Mater. Interfaces 8 (2016) 2435-2440.
- [85] D.D. Zhao, S.J. Bao, W.J. Zhou, H.L. Li, Electrochem. Commun. 9 (2007) 869-874.
- [86] G.P. Wang, L. Zhang, J.J. Zhang, Chem. Soc. Rev. 41 (2012) 797-828.
- [87] H. Lee, M.S. Cho, I.H. Kim, J.D. Nam, Y. Lee, Synth. Met. 160 (2010) 1055-1059.
- [88] I.H. Kim, K.B. Kim, J. Electrochem. Soc. 153 (2006) A383-A389.
- [89] W.T. Deng, X.B. Ji, Q.Y. Chen, C.E. Banks, RSC Adv. 1 (2011) 1171-1178.
- [90] S. Ferro, A. De Battisti, J. Phys. Chem. B 106 (2002) 2249-2254.
- [91] J.P. Zheng, P.J. Cygan, T.R. Jow, J. Electrochem. Soc. 142 (1995) 2699-2703.
- [92] Y. Su, F. Wu, L. Bao, Z. Yang, New Carbon Mater. 22 (2007) 53-57.
- [93] J.P. Zheng, T.R. Jow, J. Electrochem. Soc. 142 (1995) L6-L8.
- [94] W. Sugimoto, K. Yokoshima, Y. Murakami, Y. Takasu, Electrochim. Acta 52 (2006) 1742-1748.
- [95] W. Sugimoto, H. Iwata, K. Yokoshima, Y. Murakami, Y. Takasu, J. Phys. Chem. B 109 (2005) 7330-7338.
- [96] J.W. Long, K.E. Swider, C.I. Merzbacher, D.R. Rolison, Langmuir 15 (1999) 780-785.
- [97] X. Zhang, W. Shi, J. Zhu, W. Zhao, J. Ma, S. Mhaisalkar, T.L. Maria, Y. Yang, H. Zhang, H.H. Hng, Nano Res. 3 (2010) 643-652.

- [98] Y. Liu, W. Zhao, X. Zhang, *Electrochim. Acta* 53 (2008) 3296-3304.
- [99] Y.S. Hu, L.Z. Fan, J. Maier, P. Adelhelm, B. Smarsly, M. Antonietti, *Adv. Funct. Mater.* 17 (2007) 3083-3087.
- [100] J.K. Chang, M.T. Lee, W.T. Tsai, *J. Power Sources* 166 (2007) 590-594.
- [101] S. Devaraj, N. Munichandraiah, *Electrochem. Solid-State Lett.* 8 (2005) A373-A377.
- [102] H.Y. Lee, J.B. Goodenough, *J. Solid State Chem.* 144 (1999) 220-223.
- [103] C.C. Hu, T.W. Tsou, *Electrochem. Commun.* 4 (2002) 105-109.
- [104] S.C. Pang, M.A. Anderson, T.W. Chapman, *J. Electrochem. Soc.* 147 (2000) 444-450.
- [105] S. Devaraj, N. Munichandraiah, *J. Phys. Chem. C* 112 (2008) 4406-4417.
- [106] S.L. Brock, N.G. Duan, Z.R. Tian, O. Giraldo, H. Zhou, S.L. Suib, *Chem. Mater.* 10 (1998) 2619-2628.
- [107] M.M. Thackeray, *Prog. Solid State Chem.* 25 (1997) 1-71.
- [108] R.H. Ma, Y. Bando, L.Q. Zhang, T. Sasaki, *Adv. Mater.* 16 (2004) 918-922.
- [109] H.G. Wang, Z.G. Lu, D. Qian, Y.J. Li, W. Zhang, *Nanotechnology* 18 (2007) 115616.
- [110] E. Macheaux, T. Brousse, D. Belanger, D. Guyomard, *J. Power Sources* 165 (2007) 651-655.
- [111] T. Brousse, M. Toupin, R. Dugas, L. Athouel, O. Crosnier, D. Belanger, *J. Electrochem. Soc.* 153 (2006) A2171-A2180.
- [112] S.W. Donne, A.F. Hollenkamp, B.C. Jones, *J. Power Sources* 195 (2010) 367-373.
- [113] C.T. Sun, Y.J. Zhang, S.Y. Song, D.F. Xue, *J. Appl. Cryst.* 46 (2013) 1128-1135.
- [114] Y.C. Hsieh, K.T. Lee, Y.P. Lin, N.L. Wu, S.W. Donne, *J. Power Sources* 177 (2008) 660-664.
- [115] S.C. Pang, M.A. Anderson, T.W. Chapman, *J. Electrochem. Soc.* 147 (2000) 444-450.
- [116] K. Xu, S. Zhang, B.A. Poesse, T.R. Jow, *Electrochem. SolidState Lett.* 5 (2002) A259-A262.

[117] H. Zheng, F. Tang, M. Lim, J. Power Sources 195 (2010) 680-683.

[118] E.H. Liu, W. Li, J. Li, X.Y. Meng, R. Ding, S.T. Tan, Mater. Res. Bull. 44 (2009) 1122-1126.

# Chapter 2 Materials, experimental and characterizations

## 2.1 Materials

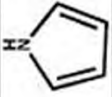
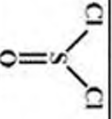
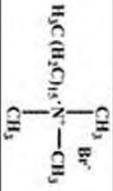
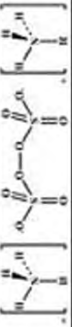
### 2.1.1 Chemical reagents

In this research, pyrrole (Py) monomer was purified by distillation under reduced pressure before use. Graphite powder (325 mesh) was purchased from Kaitiong Co. Ltd. (Tianjin, China). MWCNTs powder was purchased from Institute of Chemical Physics (Chengdu, China). Other reagents were commercially available and analytically graded, and the physical and chemical properties of them are shown in Table 2.1. All solutions were prepared with distilled water.

### 2.1.2 Materials of electrochemical test

For electrochemical testing, we choose nickel foam or stainless mesh (300 mesh) as the current collector. Before use, nickel foam and stainless mesh are trimmed to strips (3×1 cm), and then the strips immersed in acetone and ethanol, respectively, and with the sonication. Finally, the strips were dried under vacuum at 50 °C for 12 h. We chose the polytetrafluoroethylene (PTFE) as the binder between active materials and current collector [1, 2], and we also chose the acetylene black as the conductive agent [3].

Table 2.1 Physical and chemical properties of reagents

Name	Molecular formula	Structural formula	Density (g cm <sup>-3</sup> )	Molecular weight	Melting point (°C)	Boiling point (°C)
Pyrrrole	C <sub>4</sub> H <sub>5</sub> N		0.967	67.09	-23	129-131
Thionyl chloride	SOCl <sub>2</sub>		1.638	118.97	-105	78.8
Cetrimonium bromide	C <sub>19</sub> H <sub>42</sub> BrN		---	364.45	237~250	---
Iron (III) chloride hexahydrate	FeCl <sub>3</sub> ·6H <sub>2</sub> O	---	---	270.29	37	280-285
Ammonium persulphate	(NH <sub>4</sub> ) <sub>2</sub> S <sub>2</sub> O <sub>8</sub>		---	228.18	120	---
Potassium hydroxide	KOH	---	2.044	56.11	360.4	1327
Potassium permanganate	KMnO <sub>4</sub>	---	2.703	158.04	240	---
Concentrated sulfuric acid	H <sub>2</sub> SO <sub>4</sub>	---	1.84	98.04	10	337
Hydrochloric acid	HCl	---	1.18	36.46	-27.32	48

## 2.2 Experimental methods

### 2.2.1 Preparation of polypyrrole (PPy)

#### 1) Preparation of globular PPy

Globular PPy was prepared by the chemical oxidation method [4]. In a typical experiment, 1 mL Py monomer was dispersed in 50 mL distilled water at ambient temperature. Then, under nitrogen protection, 0.8148 g sulfamic acid (SA) and 50 mL 0.3 M FeCl<sub>3</sub> solution was added slowly to the mixture. After magnetic stirring for 0.5 h, the resultant product was dried under vacuum at 40 °C for 12 h to obtain a black powder of PPy.

#### 2) Preparation of nanowires PPy (WPPy)

Nanowires PPy also prepared by the chemical oxidation method, and Cetrimonium Bromide (CTAB) as the soft template [5, 6]. In a typical process, In a typical process, 0.758 g CTAB and 10.5 mL HCl (12 mol L<sup>-1</sup>) were added in 52 mL deionized water and stirred for 0.5 h. 0.5 mL Py was added into the mixture with vigorous stirring and stirred for 2 h. Afterwards, 10 mL 0.83 M (NH<sub>4</sub>)<sub>2</sub>S<sub>2</sub>O<sub>8</sub> solution was added drop by drop to the above mixture to start the polymerization. The reaction was performed under room temperature for 1 h. Finally, the product was removed from solution, copiously washed with deionized water, and dried in vacuum at 5 °C for 12 h to obtain the WPPy as a black powder.

### 2.2.2 Preparation of carbon materials

#### 1) Preparation of graphene oxide (GO)

GO was prepared from natural graphite via a modified Hummers method [7, 8]. Firstly, preoxidized graphite powder was synthesized through reaction of natural graphite (3 g), sulfuric acid (12 mL), K<sub>2</sub>S<sub>2</sub>O<sub>8</sub> (2.5 g), and P<sub>2</sub>O<sub>5</sub> (2.5 g). The reaction mixture was maintained at 80 °C for 5 h and terminated by adding 500 mL deionized water. This preoxidized graphite powder (600 mg) was further oxidized by sulfuric acid (24 mL) and KMnO<sub>4</sub> (3 g), and maintained at room

temperature for 2 h and then at 35 °C for 2 h. After that, the reaction mixture was maintained at 98 °C for 0.5 h and terminated by adding 50 mL deionized water. After the dilution with deionized water (150 mL) and decomposition of excessive  $\text{KMnO}_4$  by  $\text{H}_2\text{O}_2$  (30 wt%, 6 mL), the resulting GO solution was filtered and washed with deionized water for 3 times, and removed metal ions by dialysis membranes for a week. GO film was obtained after drying in a vacuum for 24 h.

## **2) Preparation of carbon nanowires (CNW)**

CNW was prepared via direct carbonization method [9]. In a typical process, 0.2 g WPPy was carbonized under flowing  $\text{N}_2$  at 750 °C for 2 h with a heating rate of  $10\text{ °C min}^{-1}$ , and obtained the CNW sample as a black powder.

## **3) Preparation of porous carbon nanowires (PCNW)**

PCNW sample was obtained by KOH activation method [10, 11]. In a typical process, KOH was directly mixed with CNW in an agate mortar, and then the mixture was carried out at 800 °C for 1 h under  $\text{N}_2$  atmosphere with a heating rate of  $10\text{ °C min}^{-1}$ , followed by washing with HCl and deionized water and drying at 80 °C for 12 h.

### **2.2.3 Preparation of carbon-based composites**

#### **1) Preparation of polypyrrole/MWCNTs/GO composites (PCMG)**

PCMG composite was prepared via in situ chemical oxidative polymerization method [12]. In a typical experiment, 19.4 mg GO was dispersed in 50 mL of deionized water with 0.5 h sonication, followed by the addition of 19.4 mg MWCNTs with vigorous stirring for 10 min. And then, 1.118 g sulfamic acid (SA) and 1 mL Py were added into the mixture and stirred at room temperature for 10 min. Afterwards, 50.00 mL 0.30 M  $\text{FeCl}_3$  solution was added drop by drop to the mixture to start the polymerization. The reaction was performed under nitrogen protection for 0.5 h. The final product was dried under vacuum at 50 °C for 12 h to obtain the PCMG composite as a black powder.

## **2) Preparation of CNW/MnO<sub>2</sub> composites (CNWMn)**

CNWMn composite was prepared by hydrothermal method and directly reacting KMnO<sub>4</sub> with CNW [13]. Briefly, 0.110 g KMnO<sub>4</sub> dissolved in 200 mL deionized water, and then 0.055 g CNW added the above solution under sonication. After 1 h for sonication, the solution was transferred to a Teflon-lined stainless steel autoclave (capacity of 200 mL) and heated at 140 °C in an electric oven for a certain time. The autoclave was cooled naturally to room temperature, and the products were filtered, washed by water to remove the residual reactants. Finally, the products were dried in an oven at 80 °C.

## **2.3 Characterization**

### **2.3.1 Morphological, structure, thermal and component characterizations**

#### **1) Scanning electron microscope (SEM)**

The morphologies of samples were characterized by SEM (S-4300, Hitachi Co., Ltd., Tokyo, Japan). The sample was sputter-coated by gold with Ion sputter (E-1030, Hitachi Co., Ltd., Tokyo, Japan) for 2 min to provide enhanced conductivity. The test voltage was 15 KV, and electric current was 10 μA.

#### **2) Transmission electron microscopy (TEM)**

The morphologies of samples were further characterized by TEM (Hitachi H-8100, Tokyo, Japan). For TEM observations, samples were dispersed in ethanol and then a small drop of the suspension was spread onto a 400 mesh copper grid.

#### **3) X-ray diffraction (XRD)**

The crystallographic structure of samples was tested by X-ray diffraction system in range of  $2\theta=5\sim 90^\circ$  by step scanning with a diffractometer (XRD-6000, Shimadzu Co., Ltd., Kyoto, Japan). Nickel-filter Cu K $\alpha$  radiation ( $\lambda=0.15417$  nm) was used with a generator voltage of 40 kV and a current of 30 mA.

#### **4) Fourier transforms infrared spectroscopy (FTIR)**

The molecular structure of samples was identified by FTIR (JRT-7000, JASCO,

Japan) with the KBr pellet method. The The wavelength range was between 4000 and 600  $\text{cm}^{-1}$ , and the resolution was 4  $\text{cm}^{-1}$ . Fifty scans were averaged for each sample.

### **5) Thermal Gravimetric Analyzer (TGA)**

TGA (DTA-60, shimadzu Co., Ltd., Kyoto, Japan) was carried out in the experimental temperature range at a ramp setting of 10  $^{\circ}\text{C min}^{-1}$  from room temperature to 800  $^{\circ}\text{C}$ , and then retained 800  $^{\circ}\text{C}$  for 1 h in flowing nitrogen.

### **6) Nitrogen adsorption-desorption isotherms**

The specific surface area and porosity of samples were proved using nitrogen adsorption-desorption isotherms which were performed using an ASAP 2020 apparatus (Micromeritics, USA) at -196  $^{\circ}\text{C}$ . All samples were outgassed under vacuum at 80  $^{\circ}\text{C}$  overnight prior to measurement. The specific surface area was calculated according to the Brunauer-Emmett-Teller (BET) equation, and the pore size distribution was derived from the adsorption branches of the isotherms.

### **7) X-ray photoelectron spectroscopy (XPS)**

The chemical composition of samples was identified by X-ray photoelectron spectroscopy (PHI-5000, Perkin-Elmer Corp., USA) in a range of 0~1000 eV.

## **2.3.2 Electrochemical performance characterization**

### **1) Preparation of working electrode**

The fabrication of working electrodes was carried out as follows. The sample, polytetrafluoroethylene (PTFE, the mass ratio of the sample and PTFE is 95:5), and ethanol, and grinding adequately to obtained a paste [14]. Then the paste was coated onto the nickel foam or stainless mesh, which was followed by drying under vacuum at 80  $^{\circ}\text{C}$  for 24 h and then compressed at 10 MPa for 5 min.

### **2) Electrochemical tests**

The electrochemical tests were measured with an electrochemical workstation (CHI 660D, Shanghai Chenhua, China) in the three or two-electrode system in electrolyte. For three-electrode system, saturated calomel electrode and platinum foil were used as reference and counter electrode, respectively. The working electrode as mentioned

above. Cyclic voltammetry (CV) and galvanostatic charge/discharge (GCD) were conducted in a potential window at different scan rates and current densities, respectively. Electrochemical impedance spectroscopy (EIS) was carried out in the frequency range from  $10^5$  to  $10^{-2}$  Hz at open circuit potential with an ac perturbation of 5 mV. The two-electrode system was assembled with two working electrodes (the active material of two electrodes were same or different samples). The CV and GCD tests were run at different voltage windows.

### 3) Determination of capacitive performance

#### ① Specific capacitance (SC)

SC is an important basis for the judgment of capacitive performance of samples. The SC of the sample can be obtained from the CV curve in three-electrode system and the equation as follows:

$$C = \frac{\int I(V)dV}{mv\Delta V} \quad (\text{Eq. 2.1})$$

where  $I$  is the response current density ( $\text{A cm}^{-2}$ ),  $v$  is the potential scan rate ( $\text{V s}^{-1}$ ),  $m$  is the mass of the active material and  $V$  is the potential (V) [15, 16]. It can also be obtained from the GCD curve in three-electrode system and the following equation:

$$C_m = \frac{I*t}{\Delta V*m} \quad (\text{Eq. 2.2})$$

where  $I$  is the discharge current (A),  $t$  is the discharge time (s),  $\Delta V$  is the potential window (V) and  $m$  is the mass of active material (g) [17]. In two-electrode system, the SC still can be obtained by Eq. 2.1 and 2.2, expect that the  $m$  is the total mass of active material on two working electrodes (g) [18].

#### ② Energy and power density

For supercapacitors with excellent performance, the high power and energy density are expected. The energy density ( $E$ ,  $\text{Wh kg}^{-1}$ ) and power density ( $P$ ,  $\text{W kg}^{-1}$ ) were calculated from the GCD curves of two-electrode system according to the following equations [19, 20]:

$$E = \frac{1}{2} C_m (\Delta V)^2 \quad (\text{Eq. 2.3})$$

$$P = \frac{E}{t} \quad (\text{Eq. 2.4})$$

where  $C_m$ ,  $t$  and  $\Delta V$  are the specific capacitance, discharge time (h) and voltage window (V) in two-electrode system, respectively.

## References:

- [1] A. Laforgue, P. Simon, C. Sarrazin, J.F. Fauvarque, *J. Power Sources* 80 (1999) 142-148.
- [2] L. Bonnefoi, P. Simon, J.F. Fauvarque, C. Sarrazin, J.F. Sarrau, A. Dugast, *J. Power Sources* 80 (1999) 149-155.
- [3] T. cottineau, M. toupin, T. delahaye, T. brousse, D. belanger, *Appl. Phys. A* 82 (2006) 599-606.
- [4] F. Yakuphanoglu, I.S. Yahia, B.F. Senkal, G.B. Sakr, W.A. Farooq, *Synthetic Met.* 161 (2011) 817-822.
- [5] X.T. Zhang, J. Zhang, W.H. Song, Z.F. Liu, *J Phys Chem B* 110 (2006) 1158-1165.
- [6] A.M. Wu, H. Kolla, S. K, Manohar, *Macromolecules* 38 (2005) 7873-7875.
- [7] H.F. Yang, Q.X. Zhang, C.S. Shan, F.H. Li, D.X. Han, L. Niu, *Stable, Langmuir* 26 (2010) 6708-6712.
- [8] Y.J. Park, S.Y. Park, I. In, *J. Ind. Eng. Chem.* 17 (2011) 298-303.
- [9] H.M. Luo, Y.F. Yang, YX Sun, D.J. Chen, X. Zhao, D.Y. Zhang, J.Q. Zhang, *J. Appl. Electrochem.* 45 (2015) 839-848.
- [10] M. Zhou, F. Pu, Z. Wang, S.Y. Guan, *Carbon* 68 (2014) 185-194.
- [11] J. Gorka, A. Zawislak, J. Choma, M. Jaroniec, *Carbon* 46 (2008) 1159-1174.
- [12] P. Liu, X. Wang, H.D. Li, *Synthetic Met.* 181 (2013) 72-78.
- [13] K. Dai, L.H. Lu, C.H. Liang, J.M. Dai, Q.Z. Liu, Y.X. Zhang, G.P. Zhu, Z.L. Liu, *Electrochim. Acta* 116 (2014) 111-117.
- [14] J. Yan, T. Wei, B. Shao, F.Q. Ma, Z.J. Fan, M.L. Zhang, C. Zheng, Y.C. Shang, W.Z. Qian, F. Wei, *Carbon* 48 (2010) 1731-1737.
- [15] C.J. Hung, P. Lin, T.Y. Tseng, *J. Power Sources* 259 (2014) 145-153.
- [16] S.X. Denga, D. Sun, C.H. Wua, H. Wang, J.B. Liua, Y.X. Sun, H. Yan, *Electrochim. Acta.* 111 (2013) 707-712.
- [17] R. Ramya, R. Sivasubramanian, M.V. Sangaranarayanan, *Electrochim. Acta.* 101 (2013) 109-129.

- [18] C. Johne, R. Fritsch, A. Ignaszak, *Electroanal.* 26 (2014) 1560-1572.
- [19] S.A. El-Khodary, G.M. El-Enany, M. El-Okr, M. Ibrahim, *Electrochim. Acta.* 150 (2014) 269-278.
- [20] B. Ma, X. Zhou, H. Bao, X.W. Li, G.C. Wang, *J. Power Sources* 215 (2012) 36-42.

# **Chapter 3 Preparation of graphene oxide/polypyrrole/multi-walled carbon nanotube composite and its application in supercapacitors**

## **3.1 Introduction**

Supercapacitors have attracted enormous attention in recent years due to their great advantages including high power density, long cycle life, reversibility, and small environmental impact [1-3]. At present, carbon-based materials (e.g., active carbon [3], carbon nanotubes [6, 7], and graphene [5, 8]) are widely applied as electrode materials for supercapacitors because of their excellent conductivity, huge surface area, and robust mechanical strength. However, as a kind of double-layer capacitance electrode materials, the specific capacitance of carbon-based materials is lower than those of other materials, such as metal oxides and hydroxide [9]. As a counterpart, conducting polymers possess many advantages (e.g., high conductivity, large storage capacity, and reversibility [10, 11]) that make them promising materials for supercapacitors. Unfortunately, their electrochemical performances tend to fade for swelling and shrinking during cycling [9]. Given the complementary profiles of carbon-based materials and conducting polymers in terms of specific capacitance and mechanical strength, numbers of researchers have been focusing on developing electrode materials based on their composites to better the performance of supercapacitors [3-5].

Graphene oxide (GO), a significant carbon-based material, has attracted extensive attention for its unique 2-D structure and properties. GO contains ample oxygen functional groups on their sheets and edges. These oxygen groups act as active spots, providing strong reactivity of GO sheets with polymers and thus making it easy fabricating GO-based 2-D composites [12]. For instance, recently, Wang et al

fabricated GO/polyaniline (PANI) composites with high specific capacitance by in situ polymerization [12, 13]. The maximum specific capacitance reached up to  $746 \text{ F g}^{-1}$  when the mass ratio of graphene oxide and aniline was 1:200 [12]. However, GO is less self-conductive [14], which is disadvantageous for supercapacitors. Another carbon-based material, carbon nanotube (CNT) is a traditional 1-D electrode material for supercapacitors. Since agglomeration and insolubility of CNTs in water restrict their homogeneous dispersion in polymer matrix [16], much research is concentrated on the modification of CNTs and the application on supercapacitors thereafter [15]. For instance, sulfonated multi-walled carbon nanotubes (MWCNTs)/PANI nanorods 1-D composites have been prepared by Zhu et al [17]. Apart from the specific capacitance as high as  $515.2 \text{ F g}^{-1}$ , this composites showed a good cycling stability (below 10% capacity loss after 1000 cycles). This was attributed to functionalized CNTs that afforded the huge specific area and suitable pore size for electrolyte ion transport [9].

Compared with 1-D or 2-D composites, 3-D composites possess many advantages when applied in supercapacitors, such as hierarchical porosity, high contacting efficiency, and ease of handling [18]. In recent reports, researchers are trying to fabricate the CNTs/graphene (GS)/polymer 3-D composites. The GS/CNTs/PANI composites have been successfully prepared by Yan et al [19]. The specific capacitance of this composites reached up to  $1035 \text{ F g}^{-1}$ , just a little lower than that of GS/PANI composites ( $1046 \text{ F g}^{-1}$ ), but much higher than that of pure PANI ( $115 \text{ F g}^{-1}$ ). At the same time, this composite showed good cycling stability (after 1000 cycles, the capacitance decreased by only 6%). Sandwiched nanostructure PANI/multi-walled carbon nanotubes (MWCNTs)/GS composites have been prepared by Zhou et al [20]. The specific capacitance of these composites was up to  $259.4 \text{ F g}^{-1}$  in an organic electrode and  $490.1 \text{ F g}^{-1}$  in  $1 \text{ M H}_2\text{SO}_4$ . In addition, other conducting polymer/carbon material 3-D composites have been prepared, for example, PPy/carbon, PANI/cross-linked carbon network and graphene/CNT-PANI, and all of them possess high specific capacitance and cycle stability [21-23]. In particular, the GS/PPy/CNT composites have been prepared by Lu [24] and Peng [25], the specific capacitance of

this composites reached up to 361 and 178 F g<sup>-1</sup>, respectively. However, the effects of mass ratios of polymer, GS and CNTs on the electrochemical properties of such composites have not been investigated intensively.

In this work, we report the synthesis of a novel three-component composite, polypyrrole (PPy)/chlorinated-MWCNTs (CM)/GO composites (PCMG), for the first time to the best of our knowledge. The composite was prepared through in-suit polymerization method and we further systematically explored the effect of the three componets' mass ratio on the property of electrochemical capacitance and chemical structure of PCMG composites. We find that the introduction of fewer amounts of GO and CM into PPy will greatly improve the electrochemical performance of PPy.

## **3.2 Experimental section**

### **3.2.1 Materials**

Graphite powder (325 mesh) was purchased from Kaitong Co.LtD. (Tianjin, China). MWCNTs powder was purchased from Institue of Chemical Physics (Chengdu, China). Py monomer was purified by distillation under reduced pressure before use. Other reagents were commercially available and analytically graded. Solutions were prepared with distilled water.

### **3.2.2 Preparation of CM**

CM was prepared from MWCNTs via the following method M [26, 27]. Firstly, preoxidized MWCNTs powder was synthesized through reaction of pristine MWCNTs (2 g), sulfuric acid (300 mL) and nitric acid (100 mL). The reaction mixture was maintained at 70 °C for 2 h, filtrated, washed with HCl solution (5%), dried in air, and generated the acid-treated MWCNTs (AM). After that, the AM were refluxed in 200 mL thionyl chloride at 70 °C for 12 h. Finally, removing thionyl chloride by distillation and drying in a vacuum for 24 h.

### 3.2.3 Preparation of PCMG composites

GO was prepared according to the previous report [28]. PCMG composites were prepared by in-suit polymerization. In a typical experiment, 19.4 mg GO was dispersed in 50 mL of deionized water with 0.5 h sonication, followed by the addition of 19.4 mg CM ( $m_{GO}:m_{CM}=1:1$ ,  $m_{GO+CM}:m_{Py}=1:25$ ) with vigorous stirring for 10 min. And then, 1.118 g sulfamic acid (SA) and 1 mL Py were added into the mixture and stirred at room temperature for 10 min. Afterwards, 50.00 mL 0.30 M  $FeCl_3$  solution was added drop by drop to the mixture to start the polymerization. The reaction was performed under nitrogen protection for 0.5 h. The final product was dried under vacuum at 50 °C for 12 h to obtain the PCMG1-1 composites as a black powder. PPy/CM (PCM, without GO), PPy/GO (PG, without CM), pure PPy (without GO and CM) and CM/GO (CMG, without Py) samples were also prepared for comparison. According to the difference of proportions, the samples are referred to different groups shown in Table 3.1. In addition, we also prepared of PPy/AM composites (PAM, the mass ratio of AM and Py was same to PCM-1, just CM was replaced by AM) for comparison.

Table 3.1 Grouping of the samples

Name	$m_{GO+CM}:m_{Py}$ <sup>a</sup>	$m_{GO}:m_{CM}$ <sup>b</sup>
PCMG1-1	1:25	1:1
PCMG1-2	1:50	1:1
PCMG2-1	1:25	2:1
PCMG2-2	1:50	2:1
PCMG3-1	1:25	1:2
PCMG3-2	1:50	1:2
PCMG1-3	1:12.5	1:1
PCM-1	1:25	Without GO
PCM-2	1:50	Without GO
PG-1	1:25	Without CM
PG-2	1:50	Without CM
CMG	Without Py	1:1

<sup>a</sup> the mass ratio of CM+GO and Py; <sup>b</sup> the mass ratio of GO and CM.

### 3.2.4 Structure characterization

The morphology of samples was observed by a scanning electron microscopy (SEM, S-4300, Hitachi Co., Ltd., Tokyo, Japan) and transition electron microscopy (TEM, H-8110, Hitachi Co., Ltd., Tokyo, Japan). The crystallographic structures of the samples were observed by a powder X-ray diffraction system (XRD, XRD-6000, Shimadzu Co., Ltd., Kyoto, Japan) equipped with Cu K $\alpha$  radiation. The molecular structure of the composites was identified by Fourier transform infrared spectroscopy (FTIR, JRT-7000; JASCO, Japan). Nitrogen adsorption/desorption isotherms were collected at liquid-nitrogen temperature (-196°C) with a Micromeritics ASAP 2020. All samples were outgassed under vacuum at 80°C overnight prior to measurement. The specific surface area was calculated according to the BET method. The molecular structure of the composites was identified by X-ray photoelectron spectroscopy (XPS, PHI-5000, Perkin-Elmer Corp., USA).

### 3.2.5 Electrochemical tests

The test electrodes were prepared by mixing the samples, polytetrafluoroethylene (10  $\mu$ L), and ethanol (50  $\mu$ L), and grinding adequately to form a slurry. The slurry was coated onto a surface of nickel foam, which was followed by drying under vacuum at 60 °C for 24 h and then compressed at 10 MPa for 5 min.

All electrochemical measurements were performed by a three-electrode system, platinum foils, saturated calomel electrode and Ni foam coated with samples were used as counter, reference and working electrodes, respectively. The measurements were carried out in a 1M NaNO<sub>3</sub> aqueous electrolyte at room temperature. Cyclic voltammetry (CV), galvanostatic charge/discharge (GCD) and electrochemical impedance spectroscopy (EIS) were measured by a CHI 660D electrochemical workstation. CV tests were processed at scan rate of 10 mV S<sup>-1</sup>. GCD curves were measured at current density of 0.5 A g<sup>-1</sup>. EIS measurements were carried out in the frequency range from 10<sup>5</sup> to 10<sup>-2</sup> Hz at open circuit potential with an ac perturbation of 5 mV. The voltage windows of CV and GCD tests were set in the range from -0.8

to 0 V.

### 3.2.6 Measurement of conductivity

The conductivity of sample was measured according to the previous report.<sup>28</sup> As follows, the test sample were prepared in a pellet form (diameter: 13 mm, thickness: 0.6 mm) at a pressure of 40 MPa. Four probes method was used to measure the conductivity of the obtained sample by a four-probe resistivity/square resistance tester (Kund Technology Co. Ltd., Guangzhou, China).

## 3.3 Results and discussion

### 3.3.1 Microstructure characterization

Fig. 3.1 shows the XRD patterns of CM, GO, pure PPy, PCMG1-1, PCM-1 and PG-1. CM exhibits a sharp and high intensity peak at  $25.9^\circ$  and a lower intensity peak at  $44.4^\circ$ , which attributes to the diffraction signature of the distance between the walls of CM and the interwall spacing [20]. For GO, the diffraction peak appears at  $11.3^\circ$ , which is ascribed to the oxygen-containing functional groups and water molecule insertion between the GO layers [28]. The only broad characteristic peak at about  $25.6^\circ$  of pure PPy exhibits that pure PPy is amorphous [29]. The XRD patterns of the another three composites presents characteristic peaks similar to the pure PPy and no additional peak has been introduced into the patterns.

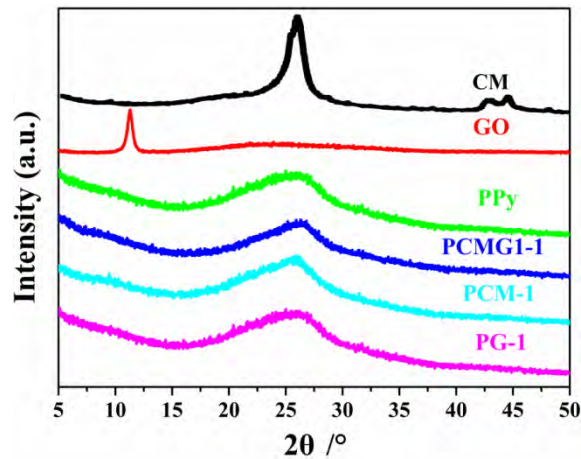


Fig. 3.1. XRD patterns of CM, GO, PPy, PCMG1-1, PCM-1 and PG-1.

Fig. 3.2 and 3.3 show the TEM and SEM images of prepared samples. As shown in fig. 3.2a, pure PPy particles exhibit a globular structure (with diameters ranging between 150 and 200 nm), forming agglomerates. A network of interconnected CM with about 25 nm diameter was observed in fig. 3.2b. In addition, a little fragment of MWCNTs was observed and which is attributed to the MWCNTs by the acid and chloration treatment. Once PPy composited with GO, the layered of GO was observed from the fig. 3.3a (low magnification in fig. 3.3a) and PPy particles was not observed, this is maybe because the PPy particles inset the interlayer of GO.

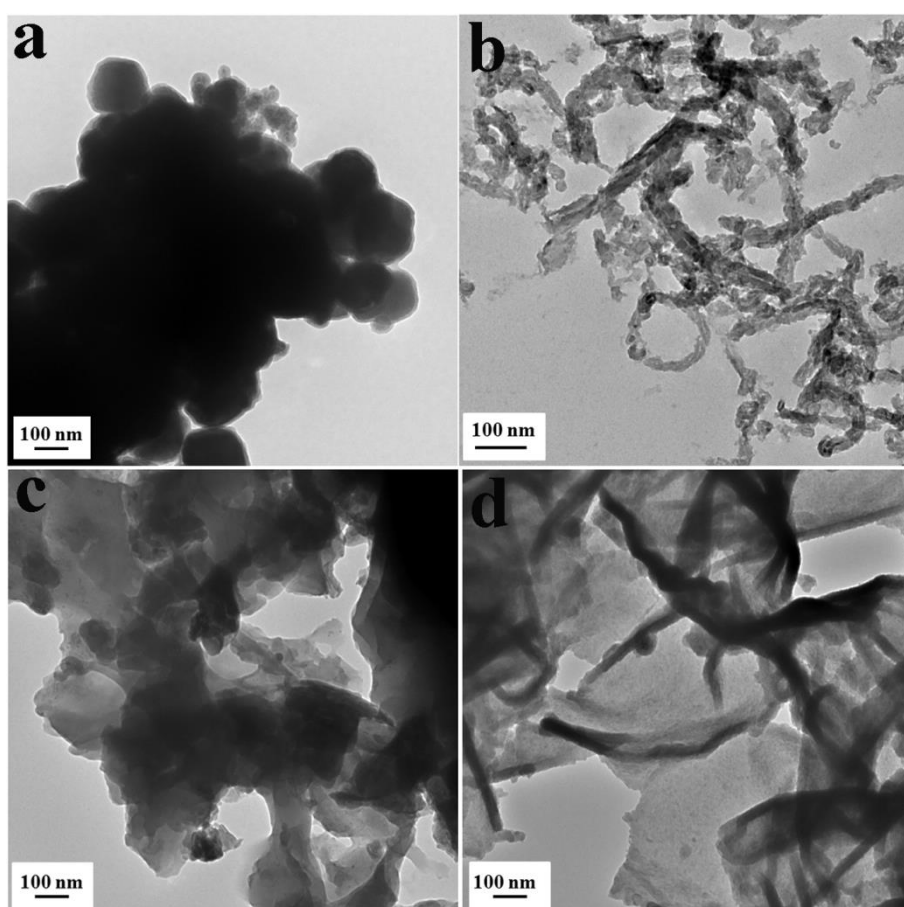


Fig. 3.2 TEM image of pure PPy (a), CM (b), PG-1 (c) and PCMG1-1 (d).

The PPy particles were observed on the edge of the sheets of GO (fig. 3.3b), and relatively homogeneous coated on the surface of GO (fig. 3.2c), which is due to the high chemical activity and surface area of GO [30]. It proves our inference from fig. 3.3a. In case of PPy composited with CM, the PPy particles coated on the surface of

CM (fig. 3.3d), but many particles form agglomerates outside CM (fig. 3.3c). If PPy composited with GO and CM at the same time, the same as the PG-1 composite, we just observed the sheets of the GO (low magnification in fig. 3.3e), this is may be like with the PG-1, the CM and PPy particles inset the interlayer of GO. CM and PPy particles were observed on the edge of the GO sheets (fig. 3.3f), homogeneously distributed on the surface of GO (fig. 3.2d). Compared of PCMG1-1 with PCM-1 composites, PPy particles relatively homogeneous distributed on the surface of GO in PCMG1-1. In addition, some PPy particles coated on the surface of CM and may be acted as connected of GO and CM. This structure may benefit for the electric capacity of PCMG composites.

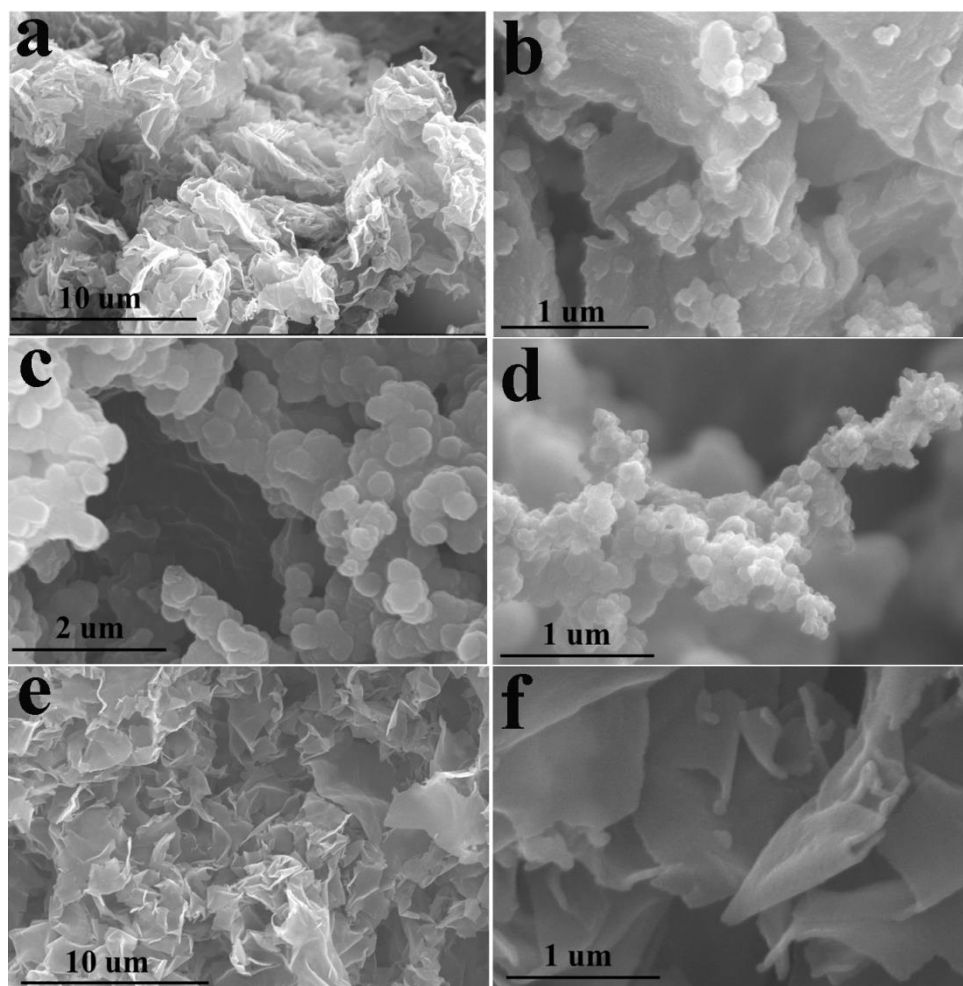


Fig. 3.3 SEM image of PG-1 (a, b), PCM-1 (c, d), PCMG1-1 (e, f).

Fig. 3.4 showed the FTIR spectra of the samples. In the spectra of PPy, the peak at

1156  $\text{cm}^{-1}$  assigned to the C-N stretching, and =C-H peaked at 1030  $\text{cm}^{-1}$ , at 1530 and 1453  $\text{cm}^{-1}$  were attributed to stretching vibrations of the pyrrole ring [31]. In the spectra of CM, the peak at 1779  $\text{cm}^{-1}$  was for Cl-C=O group [27]. Once CM composited with PPy, the peak of O=C-Cl disappeared, and a new peak was found at 1650  $\text{cm}^{-1}$  attributed to the N-C=O group (fig. 3.4, the FTIR spectra of PCM-1). The feature peak of PPy still existed and just had some redshift. The same situation was found in the FTIR spectra of PCMG1-1. It is suggested that PPy chains combined with CM through the O=C-Cl groups and finally got the amide groups. In the spectra of GO, the peak at 1623  $\text{cm}^{-1}$  might be due to the unoxidized graphitic domains [28], and the peak appeared at the spectra of PG-1 also. In the spectra of PCMG1-1, the feature peaks of PCM-1, PPy and GO were observed. However, a slight difference in the intensity and position of these peaks could be found in the PCMG1-1. Compared with neat PPy, the peak attributed to the stretching vibration of the pyrrole rings for the PCMG1-1 composite shifted to a low frequency region (the peaks at 1530 and 1453  $\text{cm}^{-1}$  for neat PPy were shifted to 1505 and 1420  $\text{cm}^{-1}$ , respectively), and this is due to  $\pi$ - $\pi$  interaction between PPy and GO, CM [31]. These indicated that the composite of PCMG1-1 were successfully prepared.

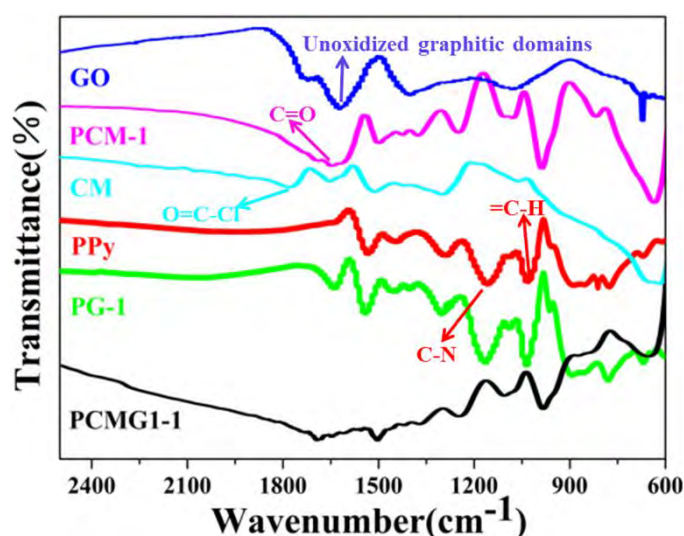


Fig. 3.4 FTIR spectra of GO, PCM-1, CM, PPy, PG-1 and PCMG1-1.

Fig. 3.5 showed the  $\text{N}_2$  adsorption-desorption isotherms of PCMG1-1, PG-1, and

PCM-1. All samples exhibited type II (nonporous type) nitrogen adsorption isotherm. The amount of N<sub>2</sub> adsorbed on the PCMG1-1 was higher than those of PG-1 and PCM-1 at the same pressure. In addition, the surface area of PCMG1-1, PG-1 and PCM-1 is 53.1, 36.9 and 18.8 m<sup>2</sup> g<sup>-1</sup> (the specific surface area calculated using the BET equation), respectively. These results suggest that the PCMG1-1 may possess the excellent electrochemical properties than other samples.

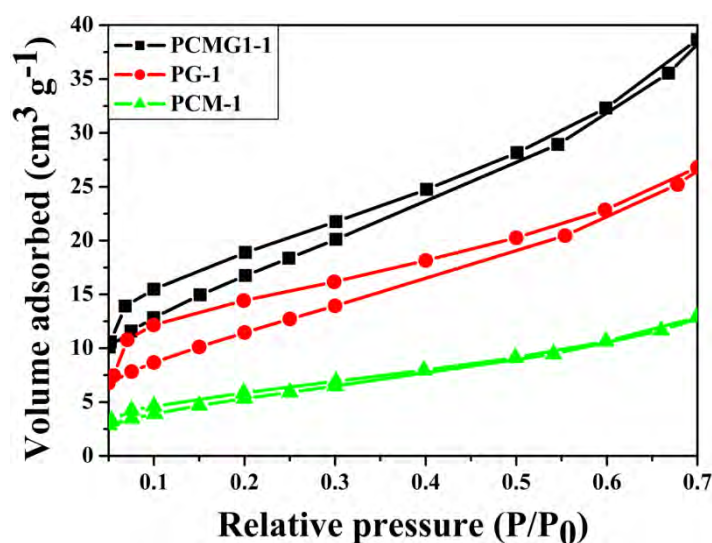


Fig. 3.5. N<sub>2</sub> adsorption-desorption isotherms of the PCMG1-1, PG-1 and PCM-1.

We also performed XPS examination on MWCNTs, CM, PCM-1, PG-1 and PCMG1-1 (fig. 3.6). Fig. 3.6a reveals that the amount ratio of C:O in MWCNTs is 94.60:4.73, corresponding to carbon atoms in different functional groups (fig. 3.6b): the non-oxygenated ring C (285.2 eV) and the C in C-O bond (286.4 eV). Once MWCNTs was treated by acid and thionyl chloride, the amount ratios of C:O:Cl is 83.80:11.62:4.26 (fig. 3.6c) and the amount of chloride and oxygen atoms is higher than that of MWCNTs. Two new peaks appeared and centered at 287.6 and 289.6 eV (fig. 3.6d), which were assigned to O=C-Cl and HO-C=O groups, respectively. For PCM-1 composites, the amount ratios of C:N:O:Cl is 77.66:14.47:6.72:1.15 (fig. 3.6e), and the amount of nitrogen is higher than that of CM, but chloride atoms is lower. For the C 1s spectrum of the PCM-1 composites in fig. 3.6f, the peak centered at 287.5 eV is attributed to amide groups [27]. It is suggested that PPy chains joined with CM via

O=C-Cl groups. Fig. 3.6g and h show the XPS and C 1s spectrum of PG-1 composites. The amount ratios of C:N:O is 79.24:13.33:6.90 and the amount of chloride atoms is very low, off the record (fig. 3.6g). It is worth noting that a small peak was observed in fig. 3.6h and the peak centered at 291.5 eV, which is assigned to  $\pi$ - $\pi$  stacking effect between PPy and GO [12, 32]. Finally, PPy composited with CM and GO, got the PCMG1-1 composites. The characteristic peaks of amide groups and  $\pi$ - $\pi$  stacking effect were observed in C 1s spectrum of PCMG1-1 composites (fig. 3.6j), which is suggested that PPy chains acted as the "bridge" between CM and GO through the amide groups and  $\pi$ - $\pi$  stacking effect for formed the PCMG1-1 composites.

The XPS N 1s spectra of PG-1, PCM-1 and PCMG1-1 could be deconvoluted into three peaks (Fig. 3.7a) with binding energies of  $400.2 \pm 0.2$  eV (N-1),  $401.2 \pm 0.2$  eV (N-2), and  $402.7 \pm 0.2$  eV (N-3). These peaks could be assigned to pyrrolic nitrogen (N-1), quaternary nitrogen (N-2), and oxidized nitrogen (N-3), respectively [33, 34]. The pyrrolic nitrogen was ascribed to the PPy chains of samples; the quaternary nitrogen was attributed to the O=C-NH groups; the oxidized nitrogen was due to the PPy chains combined with CM and GO through the oxygen-containing functional groups. The ratios of pyrrolic, quaternary and oxidized nitrogen for samples are summarized in Table 3.2. The main conclusion of the peak deconvolution analysis is that all samples have the largest amount of pyrrolic nitrogen. PG-1 possessed the largest amount of oxidized nitrogen due to the GO possessed most oxygen-containing functional groups in these samples. In addition, PCM-1 had the largest amount of quaternary nitrogen owing to the CM possessed many O=C-Cl groups. These results showed that PPy chains combined with GO through oxygen-containing functional groups except the  $\pi$ - $\pi$  stacking effect. Fig. 3.7b shows the Cl 2p XPS spectra of CM, PG-1, PCM-1 and PCMG1-1. As shown in fig. 3.7b, the Cl 2p XPS spectra of PCM-1 and PCMG1-1 could be deconvoluted into two peaks with binding energies of  $198.4 \pm 0.2$  eV and  $200.2 \pm 0.2$  eV. These peaks could be attributed to  $\text{Cl}^+$  of oxidant ( $\text{FeCl}_3$ ), and the O=C-Cl groups, respectively. Compared with them, the Cl 2p XPS spectra of CM and PG-1 just had one peak, the peak centered at 198.6 and 200.4 eV, corresponding to  $\text{Cl}^+$  of oxidant ( $\text{FeCl}_3$ ), and the O=C-Cl groups, respectively.

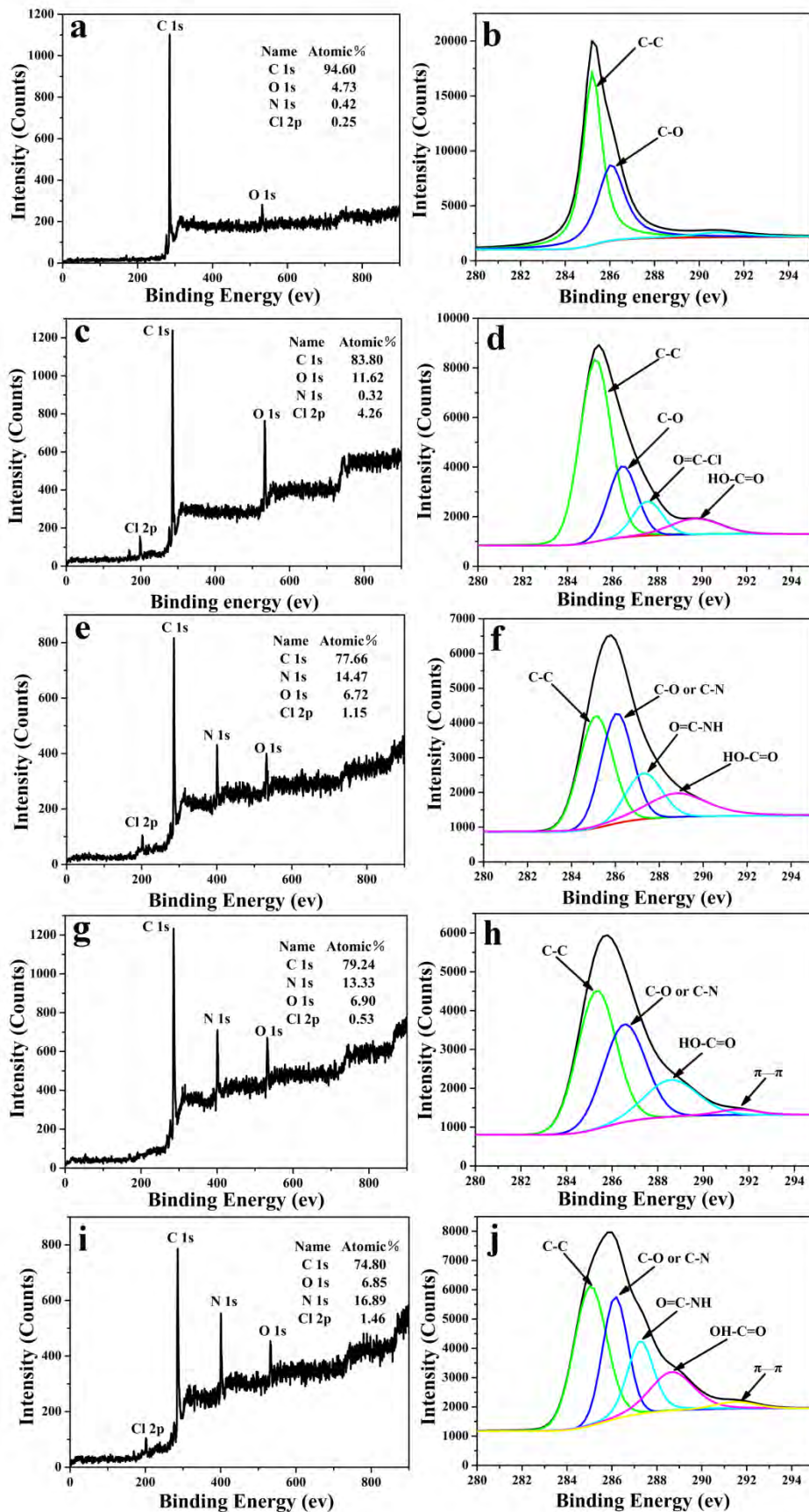


Fig. 3.6 XPS spectra of MWCNTs (a, b), CM (c, d), PCM-1 (e, f), PG-1 (g, h) and PCMG1-1 (i, j).

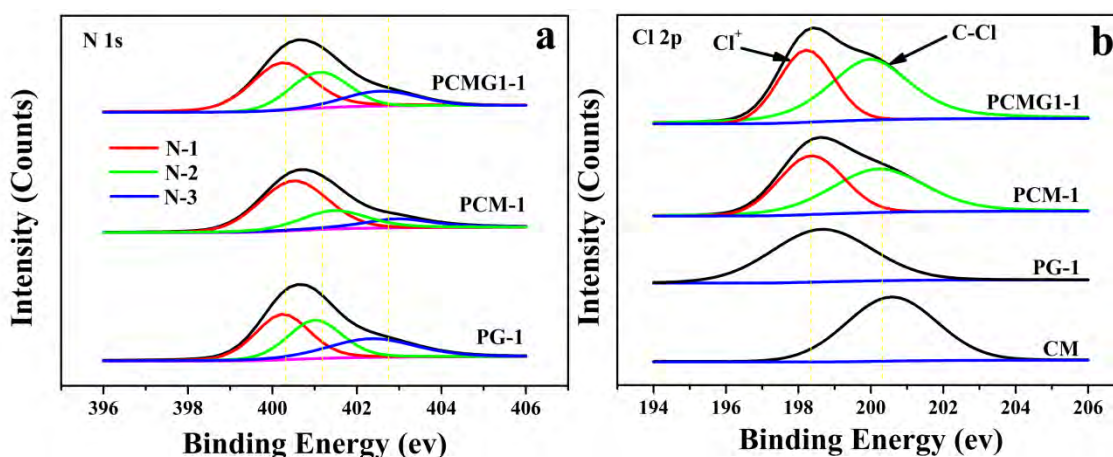


Fig. 3.7 (a) XPS N 1s spectra of PCMG1-1, PCM-1 and PG-1; (b) XPS Cl 2p spectra of PCMG1-1, PCM-1, PG-1 and CM.

Table 3.2 N 1s core level peak analyses. Each peak corresponds to a specific type of nitrogen: N-1, pyrrolic nitrogen; N-2, quaternary nitrogen; N-3, oxidized nitrogen.

	N-1 (%)	N-2 (%)	N-3 (%)
Sample	400.2±0.2 eV	401.2±0.2 eV	402.7±0.2 eV
PCMG1-1	52.1	28.9	19.0
PCM-1	57.6	31.9	10.5
PG-1	53.2	25.8	21

### 3.3.2 Electrochemical behavior

Electrochemical test were carried out using CV, GCD and EIS techniques to measure the electrochemical behavior of the prepared samples in three-electrode system. Fig. 3.8a showed the CV curves of PCMG1-1, PG-1, PG-2, PCM-1 and PCM-2 composites. The specific capacitance of the electrode can be calculated from the CV curve according to Eq. 2.1 [35, 36]. This equation indicates that, the samples possessing the maximum response current will possess the maximum specific capacitance under the other parameters are constant. PCMG1-1 composites possess the maximum response current is obvious and corresponds to a higher specific capacitance, compared with other samples. As we all know, high response current of

electrode requires high surface area and conductivity [37]. The conductivity of PCMG1-1 ( $62.5 \text{ S cm}^{-1}$ ) is higher than PG-1 ( $36.3 \text{ S cm}^{-1}$ ), PG-2 ( $33.3 \text{ S cm}^{-1}$ ), PCM-1 ( $20.6 \text{ S cm}^{-1}$ ) and PCM-2 ( $17.4 \text{ S cm}^{-1}$ ). In addition, the specific surface area of PCMG1-1 is higher than the other samples (fig. 5) due to the special 3-D structure (the special 3-D structure was formed by point (PPy nanoparticle), line (CM nanoparticle) and plane (GO layer), and PPy chain acted as the “bridge” between CM and GO, which was beneficial for improving the conductivity of composites, and thus important for increasing the specific capacitance).

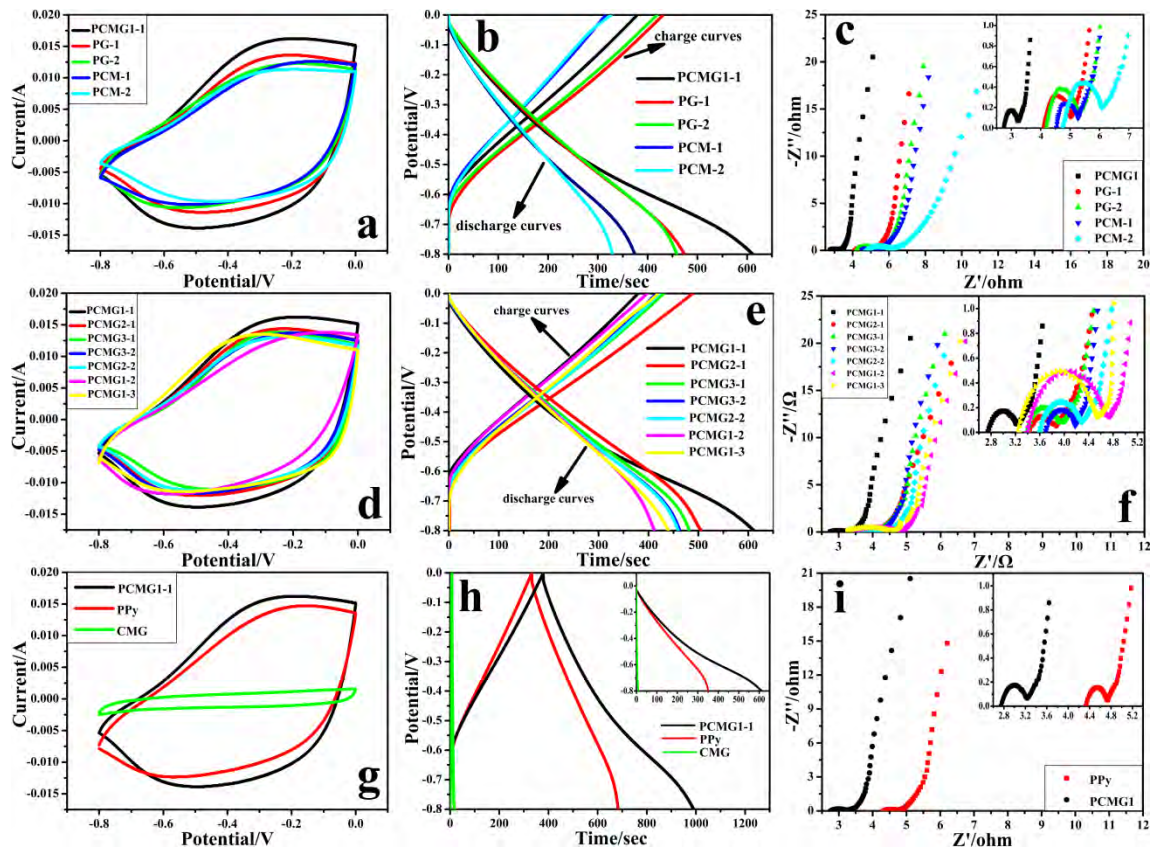


Fig. 3.8. Electrochemical characterization of PCMG, PCM, PG, CMG composites and pure PPy. a (CV), b (GCD), c (EIS) are compared the electrochemical properties of PCMG1-1, PCM and PG composites. d (CV), e (GCD), f (EIS) are compare the electrochemical properties of PCMG composites each other. g (CV), h (GCD), i (EIS) are compare the electrochemical properties of PCMG1-1, PPy and CMG composite. (CV test at a scan rate of  $10 \text{ mV S}^{-1}$ , GCD test at a constant current density of  $0.5 \text{ A g}^{-1}$ ).

Fig. 3.8b showed the GCD curves of PCMG1-1, PG-1, PG-2, PCM-1 and PCM-2 composites. From these curves, we could get the specific capacitance of samples according to Eq. 2.2 [38]. From Eq. 2.2, the specific capacitance of PCMG1-1, PG-1, PG-2, PCM-1 and PCM-2 are found 406.7, 296.3, 286.3, 234.4 and 205.0  $\text{F g}^{-1}$ , respectively. These results are in accordance with those deduced from CV curves. Should be noted is that the specific capacitance of PG composites is higher than PCM composites (obvious displayed in fig. 3.9). This is due to that the high specific surface area of GO is benefit for increasing the material-electrolyte interfacial area.

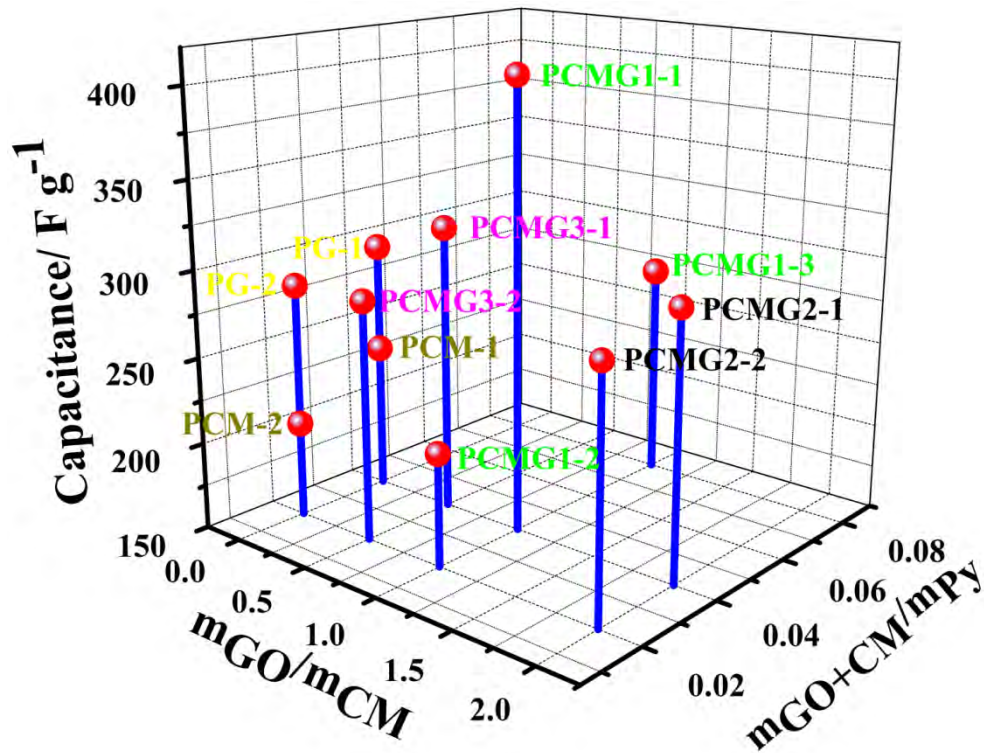


Fig. 3.9 The 3-D graph of the specific capacitance of as-prepared samples.

In EIS curves, the internal resistance ( $R_s$ ) can be obtained from the point intersecting with the real axis in the region of high frequency, the semicircle is due to the charge transfer and which will affect capacitive behavior at high current loading [39, 40]. Fig. 3.8c shown the EIS curves of PCMG1-1, PG-1, PG-2, PCM-1 and PCM-2 composites and their  $R_s$  is 2.7, 4.1, 4.2, 4.5 and 4.7  $\Omega$ , respectively (as shown in fig. 3.8c, the inset enlarged view in the region of high frequency). It is worth noting

that the internal resistance of PG composites is lower than those of the PCM composites, which is in consistence with the observations in GCD testing. The semicircle radius of PCMG1-1 is lower than the other samples, which may be due to the special 3-D structure of PCMG1-1 is benefit for the ions migration. In addition, the vertical shapes at lower frequency in EIS curve of PCMG1-1 indicate pure capacitor behavior as an ideal capacitor [41].

Fig. 3.8d, e and f show the CV, GCD and EIS curves of PCMG composites, respectively. In fig. 3.8d, PCMG1-1 possesses the higher response current than the other samples. On the one hand, the conductivity of PCMG1-1 is higher than the other samples (the conductivity of PCMG2-1, PCMG3-1, PCMG3-2, PCMG2-2, PCMG1-2 and PCMG1-3 is 53.3, 50.1, 48.5, 45.5, 37.7 and 43.4 S cm<sup>-1</sup>, respectively). On the other hand, may-be the surface area of PCMG1-1 is higher than the other samples, which is due to PCMG1-1 possess the perfect 3-D structure when the mass ratio of GO and CM is 1, mass ratio of GO+CM and Py is 0.04. From fig. 3.8e and Eq. 2.2, the specific capacitance of PCMG2-1, PCMG3-1, PCMG3-2, PCMG2-2, PCMG1-2 and PCMG1-3 is 316.2, 301.2, 289.4, 287.5, 214.4 and 274.9 F g<sup>-1</sup>, respectively. All of the values were smaller than PCMG1-1 (406.7 F g<sup>-1</sup>). Notably, the specific capacitance of PCMG<sub>x</sub>-1 (x=1, 2, 3, the mass ration of GO+CM and Py is 0.04) is higher than that of PCMG<sub>x</sub>-2 (x=1, 2, 3, the mass ratio of GO+CM and Py is 0.02) and it is easy to get through observation of fig. 3.9. Furthermore, the specific capacitance of PCMG1-3 (the mass ratio of GO+CM and Py is 0.08) is smaller than that of PCMG1-1. This suggests that when the mass ratio of GO+CM and Py is 0.04, formation of PCMG composite 3-D structure is most benefit for electrochemical property of it. Moreover, the specific capacitance of PCMG composite is higher or corresponds than that of PG and PCM composites (obvious displayed in fig. 3.9). This indicates that the 3-D structure of PCMG composite benefits for the electrochemical capacitance performance.

From the point intersecting of EIS curve of PCMG with the real axis in the region of high frequency (as shown in fig. 3.8f, the inset enlarged view in the region of high frequency), we got the internal resistance of PCMG2-1, PCMG3-1, PCMG3-2,

PCMG2-2, PCMG1-2 and PCMG1-3 is 3.4, 3.4, 3.7, 3.6, 3.4 and 3.3  $\Omega$ , respectively. The  $R_s$  of PCMG $x$ -1 ( $x=1, 2, 3$ ) is lower than that of PCMG $x$ -2 ( $x=1, 2, 3$ ), and the  $R_s$  of PCMG is lower than that of PG and PCM. It is worth noting, although the internal resistance of PCMG1-3 is lower than that of PCMG2-1 and PCMG3-1, but its charge transfer resistance is larger than that of PCMG $x$ -1. These results are in accordance with those deduced from GCD curves. In addition, the semicircle radius of PCMG1-1 is lower than the other samples and the PCMG1-2 possess the largest semicircle radius. It means that PCMG1-2 possesses the maximum charge transfer resistance, and this can explain the specific capacitance of PCMG1-2 is the lowest in all PCMG composites.

Fig. 3.8g, h and i show the electrochemical performance of PCMG1-1, PPy and CMG compared with one another. In fig. 3.8g, the response current of PCMG1-1 is higher than those of PPy and CMG, the CV curve of CMG is closer to rectangle in shape and which can be attributed to its EDL energy storage mechanism [42]. From fig. 3.8h and Eq. 2.2, the specific capacitance of PPy and CMG is 173.7 and 19.8  $F g^{-1}$ , respectively. Fig. 3.8i shown the EIS curves of PCMG1-1 and PPy, the internal resistance of PPy is 4.3  $\Omega$ , higher than that of PCMG1-1 (2.7  $\Omega$ ). In addition, the length of 45° segment (Warburg region) of EIS curve at high frequency is related to the ion diffusion in the electrolyte to the electrode interface [43]. The Warburg curve of PCMG1-1 is quite shorter than that of PPy, which indicates the short ion diffusion path of PCMG1-1. This promotes the efficient access of electrolyte ions to the PCMG1-1 electrode surface.

We also compared the electrochemical behavior of PCM-1 and PAM composites, the results were shown in the fig. 3.10. The response current of PCM-1 is much larger than that of PAM. The specific capacitance of PCM-1 and PAM was 234.4 and 160.2  $F g^{-1}$ , respectively (fig. 3.10b). The internal resistance of PAM was 5.6  $\Omega$  (fig. 3.10c), much higher than that of PCM-1 (4.5  $\Omega$ ). In addition, the semicircle radius of PAM was higher than that of PCM-1 (fig. 3.10c), which meant that the PAM possess the higher charge transfer resistance than PCM-1. This is because MWCNTs were treated by thionyl chloride and resulted CM. CM could be well dispersed in water (as shown

in fig. 3.10e), well improving the contact rate of composites and electrolyte.

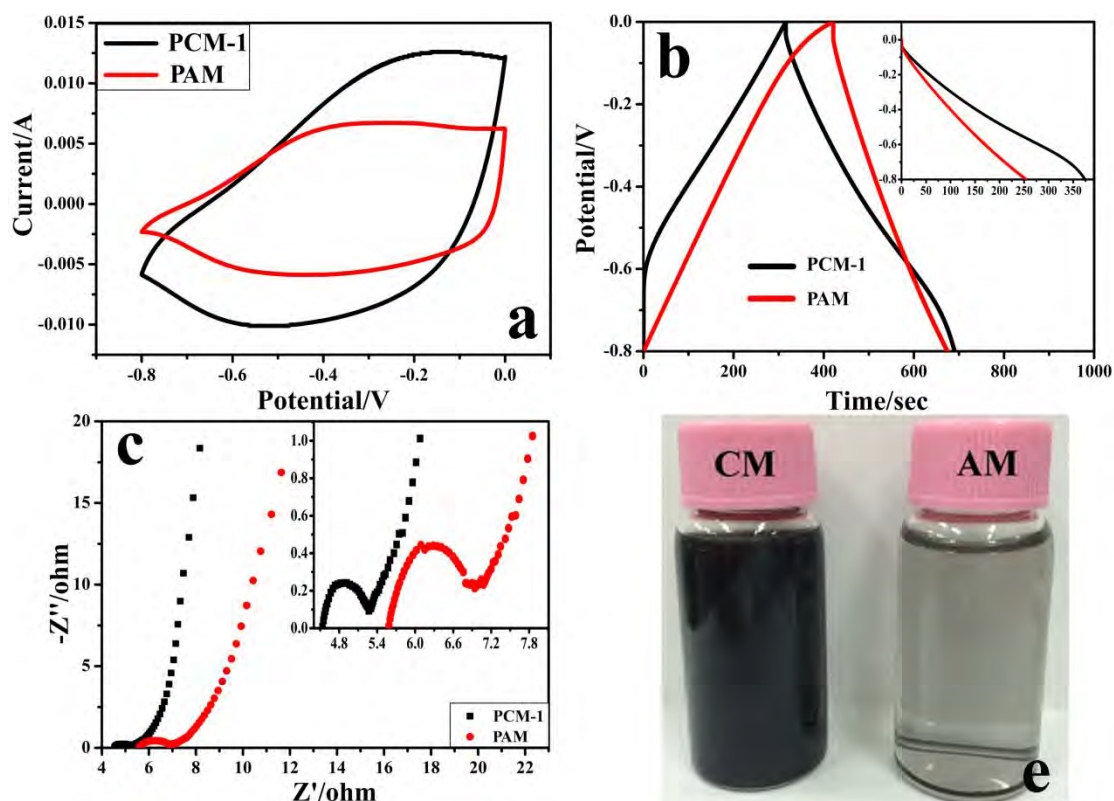


Fig. 3.10 Electrochemical characterization of PCM-1 and PAM composites (a, b and c showed the CV, GCD and EIS tests, respectively); e, dispersed CM, AM in water after one month.

Fig. 3.11a showed the CV curves of PCMG1-1 sample at different scan rates ranging from 5 to 30  $\text{mV s}^{-1}$ . Generally, the response current of PCMG1-1 increased with increasing scan rate. It is worthy to mention, distortion of CV curve was observed until the scan rate up to 30  $\text{mV s}^{-1}$ . Fig. 11b shows the specific capacitance of PCMG1-1 composite at different charging current densities from 0.5 to 3  $\text{A g}^{-1}$ . The specific capacitance reached 400.6 and 245.2  $\text{F g}^{-1}$  at the current density of 0.5 and 3  $\text{A g}^{-1}$ , respectively. The PCMG1-1 sample preserved 61.2% of its specific capacitance when the current density increased from 0.5 to 3  $\text{A g}^{-1}$ . These results suggest that the PCMG1-1 composite possesses the fast charge-discharge properties.

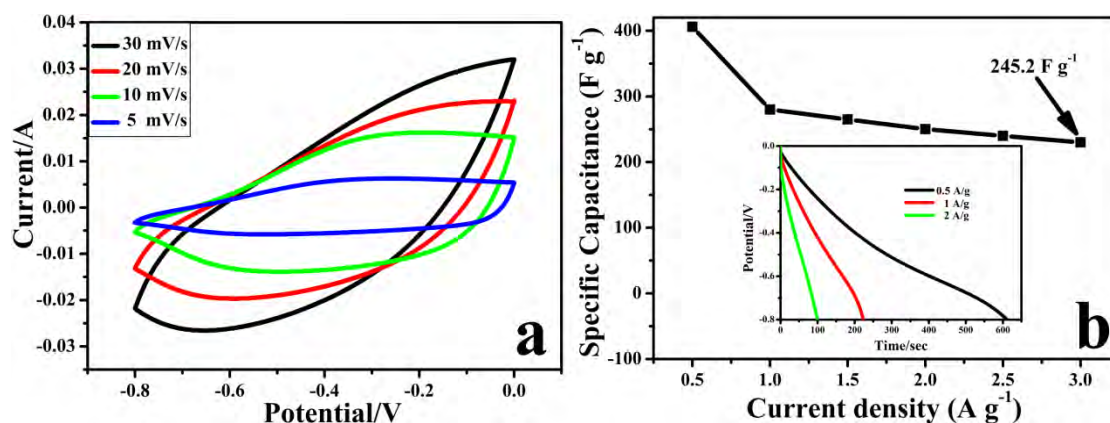


Fig. 3.11. (a) CV curves of the PCMG1-1 composite at various current density. (b) Specific capacitance as a function of the current density.

The cycle stability of the prepared samples was evaluated by repeating the GCD test (fig. 3.12). The capacitance retention after 1000 cycles of PCMG1-1, PG-1, PCM-1 and PPy is 92 %, 73 %, 85 % and 62 %, respectively. Moreover, the capacitance retention after 250 cycles of PCMG1-1 is a constant, while the capacitance retention of PG-1, PCM-1 and PPy continued to decline. These are the illustration of excellent cycling stability and reversibility in the repetitive cycling for PCMG1-1.

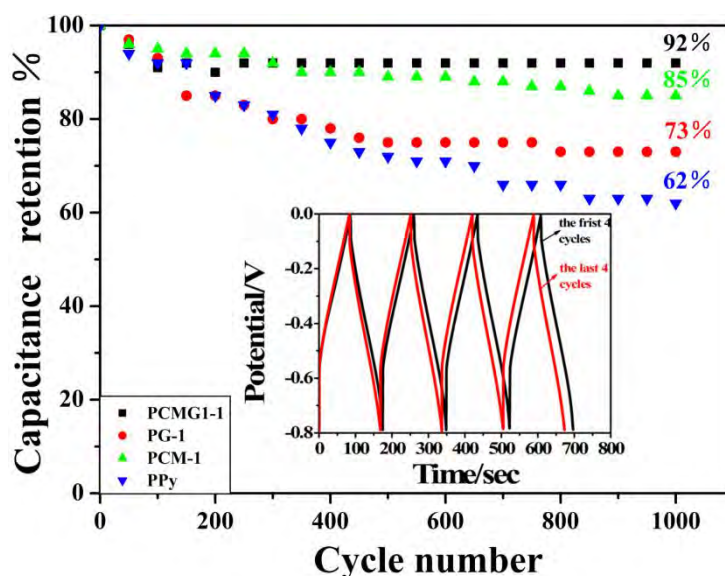


Fig. 3.12. Percentage retention of the specific capacitance as a function of GCD cycles at a constant current density of  $2 \text{ A g}^{-1}$ . The inset shows the GCD curves of the first and last 4 cycles for PCMG1-1 composite.

### 3.4. Conclusions

In this paper, PCMG composites were synthesized via in situ polymerization. In the 3-D structure of PCMG composites, the PPy chains act as the “bridge” between GO and CM. The maximum specific capacitance of PCMG composite is  $406.7 \text{ F g}^{-1}$  (at the current density of  $0.5 \text{ A g}^{-1}$ ) when the mass ratio of GO and CM is 1 and the mass ratio of GO+CM and Py is 0.04 (PCMG1-1). The cycling stability of electrode materials was remarkably improved by the introduction of GO and CM to form the 3-D structure. After 1000 cycles, the retention capacitance of PCMG1-1 is 92% at a current density of  $2 \text{ A g}^{-1}$ , considerably higher than those of PG, PCM and PPy. However, the preparation method of PCMG is complex, and PCMG is difficult to apply to reality.

## References:

- [1] L.L.Zhang, X.S.Zhao, *Chem. Soc. Rev.* 38 (2009) 2520-2531.
- [2] M.E. Roberts, D.R. Wheeler, B.B. McKenzie, B.C. Bunker, *J. Mater. Chem.* 19 (2009) 6977-6979.
- [3] Y.G. Wang, H.Q. Li, Y.Y. Xia, *Adv. Mater.* 18 (2006) 2619-2623.
- [4] Y. Sun, Q. Wu, G.Q. Shi, *Energy Environ. Sci.* 4 (2011) 1113-1132.
- [5] C.Z. Zhu, J.F. Zhai, D. Wen, S.J. Dong, *J. Mater. Chem.* 22 (2012) 6300-6306.
- [6] V. Gupta, N. Miura, *Electrochim. Acta.* 52 (2006) 1721-1726.
- [7] M. Baibarac, I. Balto, C. Godon, S. Lefrant, O. Chauvet, *Carbon* 42 (2004) 3143-3152.
- [8] Y.S. Luo, D.Z. Kong, Y.L. Jia, J.S. Luo, Y. Lu, D.Y. Zhang, K.W. Qiu, C.M. Li, T. Yu, *RSC Adv.* 3 (2013) 5851-5859.
- [9] G.P. Wang, L. Zhang, J.J. Zhang. *Chem. Soc. Rev.* 41 (2012) 797-828.
- [10] L.Z. Fan, J. Maier. *Electrochem. Commun.* 8 (2006) 937.
- [11] C. Arbizzani, M. Mastragostino, L. Meneghello, *Electrochim. Acta.* 41 (1996) 21-26.
- [12] H.L. Wang, Q.L. Hao, X.J. Yang, L.D. Lu, X. Wang, *Appl. Polym. Sci.* 2 (2010) 821-828.
- [13] C.Z. Yuan, B. Gao, L.F. Shen, S.D. Yang, L. Hao, X.J. Lu, F. Zhang, X.G. Zhang, *Nanoscale* 3 (2011) 529-545.
- [14] L. Tan, B. Wang, H.X. Feng, *RSC Adv.* 3 (2013) 2561-2565.
- [15] Z. Spitalsky, D. Tasis, K. Papagelis, C. Galiotis, *Progr. Polym. Sci.* 35 (2010) 357-401.
- [16] S. Bose, T. Kuila, A.K. Mishra, R.. Rajasekar, N.H. Kim, J.H. Lee, *J. Mater. Chem.* 22 (2012) 767-784.
- [17] Z.Z. Zhu, G.C. Wang, M.Q. Sun, X.W. Li, C.Z. Li, *Electrochim. Acta.* 56 (2011) 1366-1372.
- [18] A.H. Lu, G.P. Hao, Q. Sun, X.Q. Zhang, W.C. Li, *Macromol. Chem. Phys.* 213 (2012) 1107-1131.

- [19] J. Yan, T. Wei, Z.J. Fan, W.Z. Qian, M.L. Zhang, X.D. Shen, F. Wei, *J. Power Sources* 195 (2010) 3041-3045.
- [20] S.P. Zhou, H.M. Zhang, X.H. Wang, J. Li, F.S. Wang, *RSC Adv.* 3 (2013) 1797-1807.
- [21] M. Beidaghi, C.L. Wang, *Electrochim. Acta.* 56 (2011) 9508-9514.
- [22] H. Hu, S.W. Liu, M. Hanif, S.L. Chen, H.Q. Hou, *J. Power Sources.* 268 (2014) 451-458.
- [23] Q. Cheng, J. Tang, N. Shinya, L.C. Qin, *J. Power Sources.* 241 (2013) 423-428.
- [24] X.J. Lu, F. Zhang, H. Dou, C.Z. Yuan, S.D. Yang, L. Hao, L.F. Shen, L.J. Zhang, X.G. Zhang, *Electrochimica Acta.* 69 (2012) 160-166.
- [25] Y.J. Peng, T.H. Wu, C.T. Hsu, S.M. Li, M.G. Chen, C.C. Hu, *J. Power Sources* 272 (2014) 970-978.
- [26] H.R. Byon, S.W. Lee, S. Chen, P.T. Hammond, S.H. Yang, *Carbon* 49 (2011) 457-467.
- [27] J.H. Liu, J.W. An, Y.C. Zhou, Y.X. Ma, M.L. Li, M. Yu, S.M. Li, *ACS Appl. Mater. Interfaces* 4 (2012) 2870-2876.
- [28] H.X. Feng, B. Wang, L. Tan, N.L. Chen, N.X. Wang, B.Y. Chen, *J. Power Sources* 246 (2014) 621-628.
- [29] J. Liu, M.X. Wan, *J. Mater. Chem.* 11 (2001) 404-407.
- [30] S. M. Paek, E.J. Yoo, I. Honma, *Nano Lett.* 9 (2009) 72-75.
- [31] B.L. Liang, Z.Y. Qin, J.Y. Zhao, Y. Zhang, Z. Zhou, Y.Q. Lu, *J. Mater. Chem.* 2 (2014) 2129-2135.
- [32] X.B. Fan, W.C. Peng, Y. Li, X.Y. Li, S.L. Wang, G.L. Zhang, F.B. Zhang. *Adv. Mater.* 20 (2008) 4490-4493.
- [33] J. Zhu, A. Holmen, D. Chen, *ChemCatChem* 5 (2013) 378-401.
- [34] D. Hulicova, J. Yamashita, Y. Soneda, H. Hatori, M. Kodama, *Chem. Mater.* 17 (2005) 1241-1247.
- [35] C.J. Hung, P. Lin, T.Y. Tseng, *J. Power Sources* 259 (2014) 145-153.
- [36] S.X. Denga, D. Sun, C.H. Wua, H. Wang, J.B. Liua, Y.X. Sun, H. Yan, *Electrochim. Acta.* 111 (2013) 707-712.

- [37] H. Jiang, P.S. Lee, C.Z. Li, *Energy Environ. Sci.* 6 (2013) 41-53.
- [38] J. Hu, Z. Kang, F. Li, X. Huang, *Carbon* 67 (2014) 221-229.
- [39] J. T. Zhang, X. S. Zhao, *ChemSusChem* 5 (2012) 818-841.
- [40] L.F. Lai, H.P. Yang, L. Wang, B.K. Teh, J.Q. Zhong, H. Chou, L.W. Chen, W. Chen, Z.X. Shen, R.S. Ruoff, J.Y. Lin, *ACS Nano*. 6 (2012) 5941-5951.
- [41] C. Zheng, X.F. Zhou, H.L. Cao, G.H. Wang, Z.P. Liu, *J. Power Sources* 258 (2014) 290-296.
- [42] M. Rose, Y. Korenblit, E. Kockrick, L. Borchardt, M. Oschatz, S. Kaskel, G. Yushin, *Small* 7 (2011) 1108-1117.
- [43] Jaidev, R.I. Jafri, A.K. Mishra, S. Ramaprabhu, *J. Mater. Chem.* 21 (2011) 17601-17605.

# **Chapter 4 Nitrogen doped carbon nanowires prepared from polypyrrole nanowires for potential application in supercapacitors**

## **4.1 Introduction**

In order to solve the problem of chapter 3 (the preparation method of electrode material is complexity), the study was transferred to the development of carbon materials. At present, many carbon materials have been widely applied as electrode materials for supercapacitors due to their double-layer capacitance, long cycle life and low cost [1-4]. However, it has been demonstrated that the specific capacitances of carbon materials (e.g., carbon nanotubes [5, 6] and graphene [7, 8]) are lower than those of other materials (e.g., metal oxides [9, 10] and hydroxide [11]). To improve the electrical and chemical performance of carbon materials, an effective way is to engineer carbon nanomaterials by substituting some atoms with heteroatoms, such as nitrogen (N) [12], sulphur (S) [13], phosphorus (P) [14], and boron (B) [15], to tailor their electron donor or acceptor properties [16, 17].

Many researchers have dedicated to the rational design and fabrication of heteroatom-doped carbon nanomaterials, and applied them on supercapacitors. For instance, rich N-doped ordered mesoporous carbon has been prepared by Chen et al [18]. Apart from the specific capacitance as high as  $216 \text{ F g}^{-1}$  at the current density of  $0.1 \text{ A g}^{-1}$ , this N-doped mesoporous carbon showed a good cycle stability (after 10000 cycles, a slight increase of about 7.5% in specific capacitance); Zhang et al [19] prepared N, S co-doped ordered mesoporous carbon, whose specific capacitance retention reached 97% after 2000 cycles at a current density of  $2 \text{ A g}^{-1}$ . In addition, the N, P co-doped carbon nanofibers prepared by Chen et al [16], had a specific capacitance of  $204.9 \text{ F g}^{-1}$  with the specific capacitance retention up to 97% after

4000 cycles. Nitrogen doping is an effective method to improve the capacitance of carbon materials, which is attributed to the introduction of pseudocapacitance through redox reaction. It will increase the surface wettability of carbon materials to electrolyte and the electric conductivity [20, 21].

The pyrrole (Py) is often used as a nitrogen source for N-doping carbon material prepared by chemical vapor deposition (CVD) method [22]. For example, a high specific surface area ( $1560 \text{ m}^2 \text{ g}^{-1}$ ) N-doped mesoporous carbon was prepared by Yang [22] and Fulvio [23] using Py as carbon and nitrogen source at the same time via CVD method. However, the CVD process is complicated, easily leading to environmental pollution, which impedes the application of this method in practical use. To address this problem, simple and environment-friendly methods have been employed for preparation of N-doping carbon materials, in which direct carbonized method is a promising one. For example, Ma et al [24] utilized Py as both the carbon and nitrogen source, to obtain N-doping carbon materials by direct carbonized method, but the final usage of the material is catalyst support; Wang [25] and Zhou [26] also prepared N-doped carbon materials by same method, and used it for lithium ion batteries. Because the process of Py steaming is harsh and can be omitted, the direct carbonized method is an effective way to avoid the complicated process and environmental pollution it causes. Furthermore, their studies suggest that the carbon materials possess high specific surface area and certain nitrogen content, which therefore may be suitable for supercapacitors. However, at present, there are still rare reports on applying N-doped carbon prepared from direct carbonized polypyrrole on supercapacitors. Moreover, the aforementioned studies have focused only on the effect of carbonization temperature or time on the structure and performance of carbon materials, but ignored the influence of amount of surfactant on performance of carbon materials. In the current study, we use the simple and environmental-friendly method for preparation of N-doped carbon nanowires (CNW), and applied it in supercapacitors. After investigating the effect of amounts of surfactant and carbonization temperature on capacitance performance of CNW in details, we find that the CNW possess excellent capacitance performance due to its unique nanowire

structure and apposite nitrogen content. The results indicate a promising candidate in the supercapacitors field

## 4.2 Experimental section

### 4.2.1 Materials

Py monomer was purified by distillation under reduced pressure before use. Other reagents, such as hexadecyl trimethyl ammonium bromide (CTAB), ammonium persulphate (APS), hydrochloric acid (HCl) and concentrated sulfuric acid (H<sub>2</sub>SO<sub>4</sub>), were all locally commercially available and of analytical grade, and used without further purification. All solutions were prepared with distilled water.

### 4.2.2 Preparation of nanowires polypyrrole

Nanowires polypyrrole was prepared by chemical oxidation. In a typical process, 0.758 g CTAB and 10.5 mL HCl (12 mol L<sup>-1</sup>) were added in 52 mL deionized water and stirred for 0.5 h. 0.5 mL Py was added into the mixture with vigorous stirring and stirred for 2 h. Afterwards, 10 mL 0.83 M (NH<sub>4</sub>)<sub>2</sub>S<sub>2</sub>O<sub>8</sub> solution was added drop by

Table 4.1 The preparation condition of pure PPy and PPy-x

Samples	Py (mL)	n <sub>Py</sub> /n <sub>CTAB</sub> <sup>a</sup>	CTAB (g)
Pure PPy	0.5	--	0
PPy-1	0.5	1.7	1.515
PPy-2	0.5	3.4	0.758
PPy-3	0.5	6.8	0.379

<sup>a</sup> The molar ratio of Py and CTAB.

drop to the above mixture to initiate the polymerization. The reaction was performed at room temperature for 1 h. Finally, the product was removed from solution, copiously washed with deionized water, and dried in vacuum at 5 °C for 12 h to obtain the product (named as PPy-1) as a black power. The condition of the PPy-x (x=1, 2 and 3) preparation is given in Table 4.1. For comparison, we also prepared pure PPy, the preparation process was the same as the PPy-x except of CTAB addition.

### 4.2.3 Preparation of CNW

In a typical process, 0.2 g PPy-2 was carbonized under flowing N<sub>2</sub> at 750 °C for 2 h with a heating rate of 10 °C min<sup>-1</sup>, and obtained the CNW2-2 sample as a black power. Pure PPy, PPy-1, PPy-2 and PPy-3 were also carbonized under other temperatures. According to the difference of preparation conditions, the samples are referred to different groups shown in Table 4.2.

Table 4.2 The preparation condition of CNW and CNG

Carbon precursor	Carbonization temperature (°C)			
	650	750	850	950
Pure PPy	CNG0-1	CNG0-2	CNG0-3	CNG0-4
PPy-1	CNW1-1	CNW1-2	CNW1-3	CNW1-4
PPy-2	CNW2-1	CNW2-2	CNW2-3	CNW2-4
PPy-3	CNW3-1	CNW3-2	CNW3-3	CNW3-4

### 4.2.4 Structure characterization

The morphology of samples was observed by transmission electron microscopy (TEM, h-8110, Hitachi Co., Ltd. Tokyo, Japan) and scanning electron microscopy (SEM, S-4300, Hitachi Co., Ltd. Tokyo, Japan). The molecular structure of the samples was identified by Fourier transform infrared spectroscopy (FTIR, JRT-7000; JASCO, Japan). Nitrogen adsorption-desorption isotherms were measured at -196 °C on a Micromeritics ASAP 2020 apparatus. The specific surface area was calculated according to the Brunauer-Emmett-Teller (BET) equation. All samples were outgassed under vacuum at 80 °C overnight prior to measurement. The crystallographic structure of the samples was observed by X-ray diffraction (XRD, XRD-6000, Shimadzu Co., Ltd. Kyoto, Japan) equipped with Cu K $\alpha$  radiation. X-ray photoelectron spectroscopy (XPS) analysis was performed on the PHI Quantum 5000 equipped with an Al K $\alpha$  radiation source.

### 4.2.5 Electrochemical tests

The test electrodes were prepared by mixing the samples, polytetrafluoroethylene

(10  $\mu\text{L}$ ), and ethanol (50  $\mu\text{L}$ ), and grinding adequately to obtain a homogeneous paste. Then the paste was coated onto the stainless steel mesh (300 mesh), which was followed by drying under vacuum at 80  $^{\circ}\text{C}$  for 24 h and then compressed at 10 MPa for 5 min. For three-electrode systems, Platinum foil, saturated calomel electrode and test electrode were used as counter, reference and working electrode, respectively. Cyclic voltammetry (CV), galvanostatic charge/discharge (GCD) and electrochemical impedance spectroscopy (EIS) were measured by a CHI 660D electrochemical workstation. The measurements were carried out in 1 M  $\text{H}_2\text{SO}_4$  aqueous electrolyte at room temperature, and the voltage windows of CV and GCD tests were set in -0.4~0.6 V. EIS measurements were carried out in the frequency range from  $10^5$  to  $10^{-2}$  Hz at open circuit potential with an ac perturbation of 5 mV. The symmetric two-electrode system was assembled with two almost identical test electrodes (active material is CNW2-2 sample) and the measurements were also carried out in 1 M  $\text{H}_2\text{SO}_4$  aqueous electrolyte at room temperature. The CV and GCD tests were run at different voltage windows.

## 4.3 Result and discussion

### 4.3.1 Microstructural characterization

Fig. 4.1 shows the typical SEM and TEM images of pure PPy, PPy-x, and the carbonized samples. In Fig. 4.1a, the pure PPy particles exhibit a globular structure forming agglomerates, and its carbonization product still remains the globular structure (see Fig. 4.2b). Shown in Fig. 4.1b, c and d are SEM images of PPy-x prepared in the presence of CTAB with different concentrations (from 4.1b to 4.1d, the concentration of CTAB increases). It should be noted that nanowires of PPy are obtained only in the presence of CTAB, and the nanowire structure is the governing structure with the increase of the concentration of CTAB within a certain range.

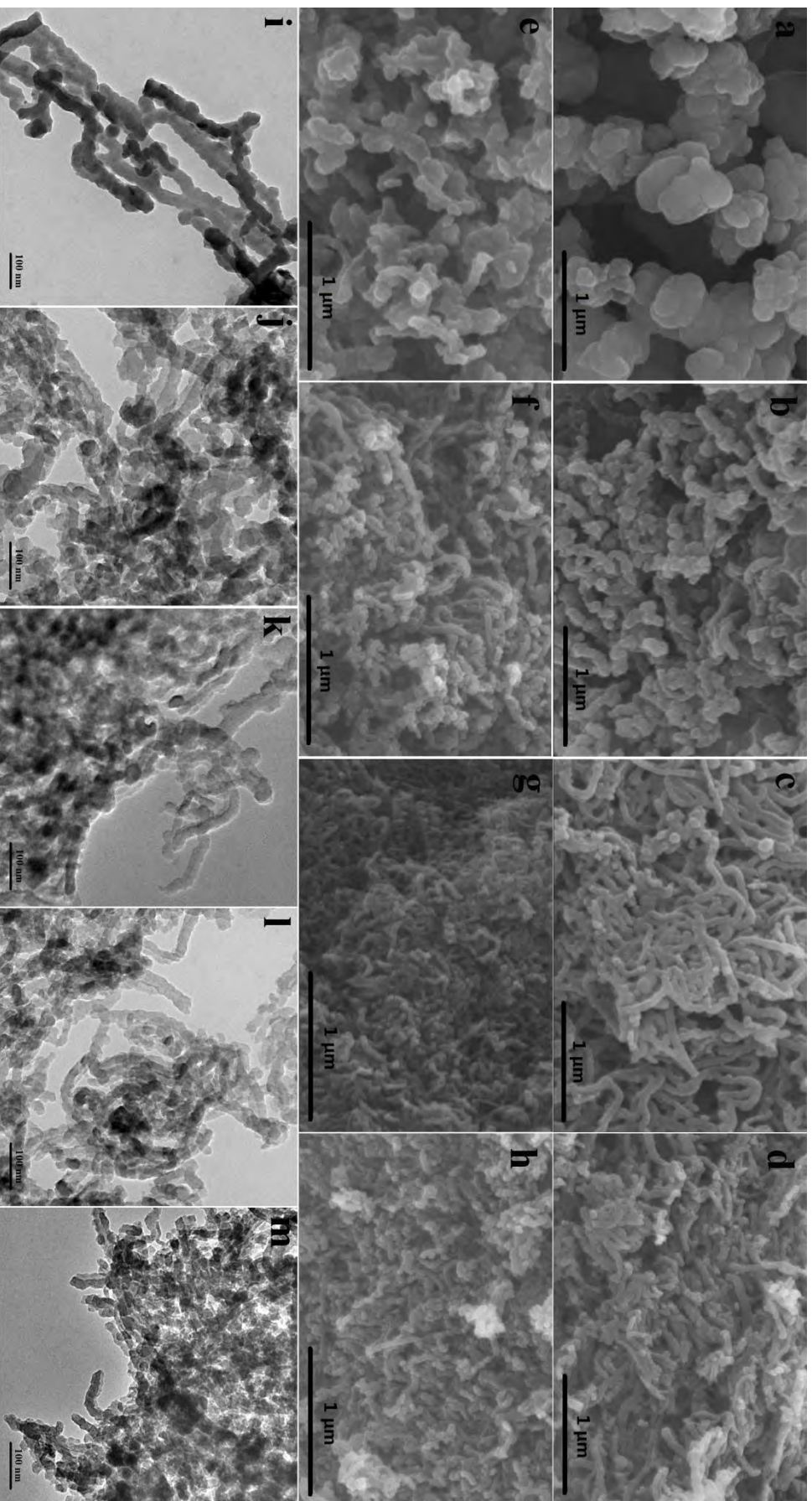


Fig. 4.1 SEM image of pure PPy (a), PPy-1 (b), PPy-2 (c), PPy-3 (d), CNW2-1 (e), CNW2-2 (f), CNW2-3 (g), and CNW2-4 (h); TEM image of PPy-2 (i), CNW2-1 (j), CNW2-2 (k), CNW2-3 (l), and CNW2-4 (m).

This is due to CTAB can form rod-like micelles in aqueous solution, which can direct the formation of nanowires of polypyrrole in the preparation step [30]. In addition, shown in Fig. 4.1b, is the hybrid structure of nanoparticles and nanowires of PPy-1 prepared when the molar ratio of Py and CTAB is 1.7. PPy-2 (Fig. 4.1c) prepared when the molar ratio of Py and CTAB is 3.4, shows entire interconnected nanowires. It is found in Fig. 1d that PPy-3 prepared when the molar ratio of Py and CTAB is 6.8 shows the vast majority of interconnected nanowires, and there are also some nanoparticles attached on PPy nanowires. These phenomenon can be explained as follows: when the molar ratio of Py and CTAB is 1.7, the excess CTAB can increase the charge repulsion and restrict growth of nanowires polypyrrole [31, 32]; with the amount decrease of CTAB, the restriction effect also gradually decreases and thus the nanowire polypyrrole becomes the governing structure; however, when the molar ratio of Py and CTAB reaches to 6.8, the excess pyrrole outside the micelle templates and resulting nanoparticle polypyrrole output [33]. Once PPy-2 is carbonized, we can find that CNW2 samples (Fig. 4.1e, f, g, and h) are still maintained the nanowire structure of PPy-2. However, the diameter of nanowires gradually decreases with the gradual increase of carbonized temperature, which can result in the increase of surface area of CNW2. In addition, we find that the fragment of nanowires is gradually increased with the carbonized temperature. This phenomenon can lead to the stacking mesoporous structure collapse of CNW2. In TEM images, the PPy-2 nanowires (Fig. 4.1i) have a diameter of about 50-70 nm and the lengths extend to several micrometers. The diameter of CNW2-1 nanowires (Fig. 4.1j) is about 25 nm and those of CNW2-2, CNW2-3, and CNW2-4 (Fig. 4.1k, l, and m) are all about 20 nm. Furthermore, the fragments of nanowires are still observed in CNW2 samples, and those belonging to CNW2-4 are more than the other samples. These results may affect the surface area and pore volume of CNW2 samples.

Fig. 4.3 shows the XRD curves of PPy-2, pure PPy, and the carbonized samples CNW2. For pure PPy, a broad characteristic peak at about  $25.6^{\circ}$  reveals that it is amorphous [34, 35]. Compared with pure PPy, a broad characteristic peak in PPy-2 sample is also observed but the peak position moves to  $23.6^{\circ}$ , which suggests that

PPy-2 is amorphous but has some regular arrays to some extent [36]. In the spectra of CNW2, the peak moves to  $24.1^\circ$ , arising from the (002) plane of graphite [37]. Furthermore, a weak peak can be observed at  $44.0^\circ$  corresponding to graphite (101), which might be a sign of the complete transformation of PPy to another kind of carbon-based nanowires [24]. We can find that the intensity of the weak peak of CNW2-3 is larger than the other samples, which suggests that PPy-2 has been completely transformed into carbon-based nanowires when the carbonized temperature is  $850^\circ\text{C}$ .

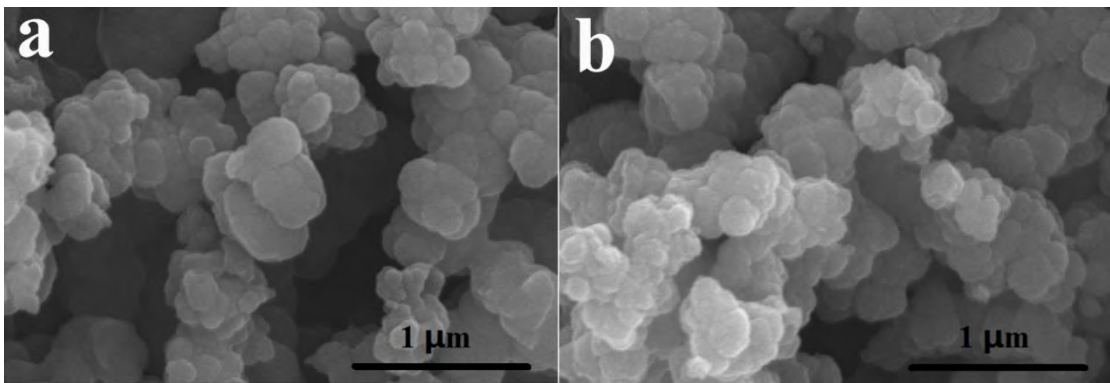


Fig. 4.2 SEM image of pure PPy (a) and CNW0-2 (b)

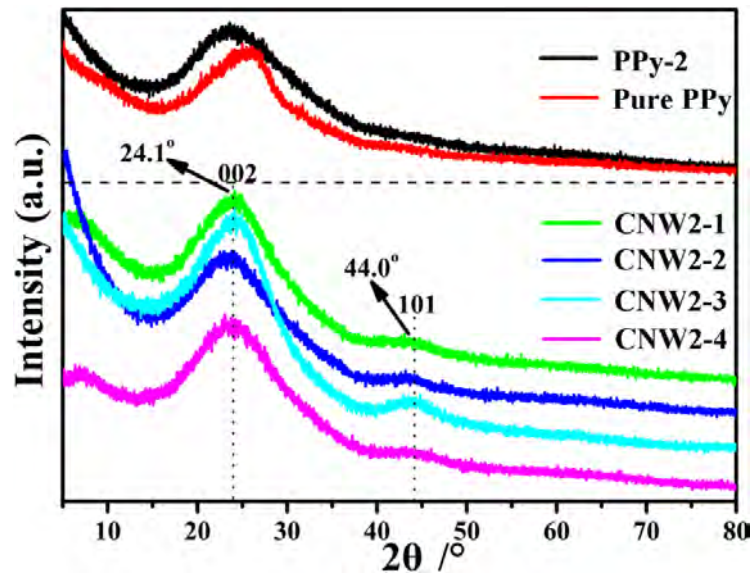


Fig. 4.3 XRD patterns of PPy-2, CNW2-1, CNW2-2, CNW2-3, and CNW2-4.

The pore-size and specific surface area characterizations of CNW2 samples were performed by measuring  $\text{N}_2$  adsorption/desorption isotherms. These isotherms are shown in Fig. 4.4. CNW2 samples exhibit hybrid IUPAC Type-III and Type-IV shapes,

indicating the existence of stacking mesoporous structures [5]. The specific surface area of CNW2 increases with the increase of carbonized temperature. CNW2-4 has the highest specific surface area ( $580.2 \text{ m}^2 \text{ g}^{-1}$ , Table 4.3). The inset of Fig. 4.4 shows the pore-size distribution of CNW2, which is mainly distributed in 10-50 nm. The average pore width and pore volume of CNW2 obtained by BJH method are shown in Table III. Opposite to specific surface area, CNW2-4 has the lowest pore volume ( $0.39 \text{ cm}^3 \text{ g}^{-1}$ ) and pore width (25.6 nm). These may be attributed to that the stacking mesoporous structure collapse with the increase of the carbonized temperature, and this inference has been proofed by SEM and TEM images.

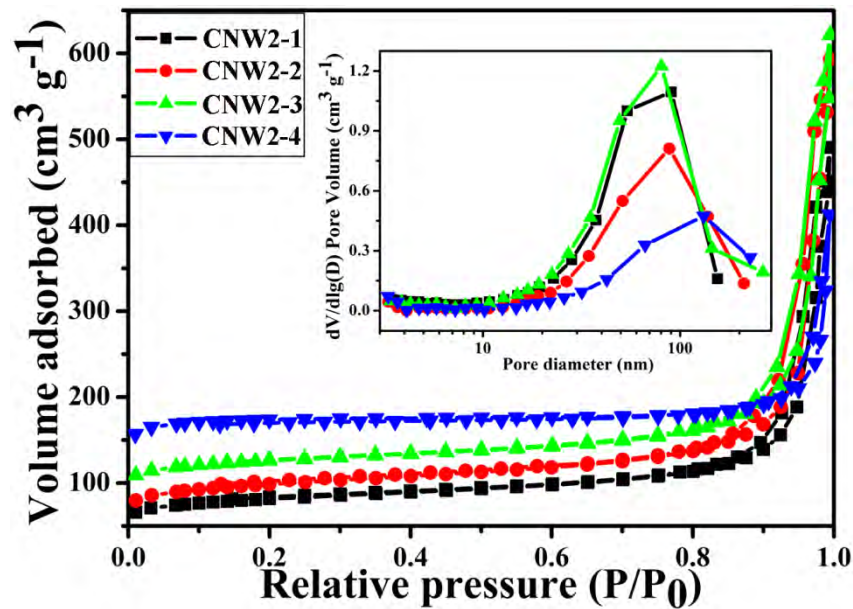


Fig. 4.4  $\text{N}_2$  adsorption-desorption isotherms of CNW2-1, CNW2-2, CNW2-3, and CNW2-4.

Table 4.3 The Specific Surface Area, Pore Width and Micropore Volume of CNW2 samples

Samples	$S_{\text{BET}} [\text{m}^2 \text{ g}^{-1}]^{\text{a}}$	$D_{\text{BJH}} [\text{nm}]^{\text{b}}$	$V_{\text{BJH}} [\text{cm}^3 \text{ g}^{-1}]^{\text{b}}$
CNW2-1	306.9	70.0	0.75
CNW2-2	405.6	40.1	0.51
CNW2-3	482.5	49.4	0.71
CNW2-4	580.2	25.6	0.39

<sup>a</sup> The specific surface area calculated using the BET equation.

<sup>b</sup> The pore width and micropore volume calculated according to the BJH method.

Fig. 4.5 shows the XPS spectra of PPy-2 and CNW2 samples, which display that besides carbon and oxygen, nitrogen signals can be simultaneously observed. We obtained the chemical compositions of samples by XPS analysis and the results are shown in table 4.4. It is noteworthy that the nitrogen content decreases from 6.62 to 1.55 at. % as the carbonization temperature increases from 650 to 950 °C. This result indicates that nitrogen is oxidized and can be more easily removed during the carbonization process [38]. Remarkably, a reduction is especially drastic from 750 to 850 °C. Samples CNW2-1 and CNW2-2 contain larger amount of N (6.62 and 5.59 at. %, respectively). This result suggests that the appropriate carbonized temperature should be less than 850 °C.

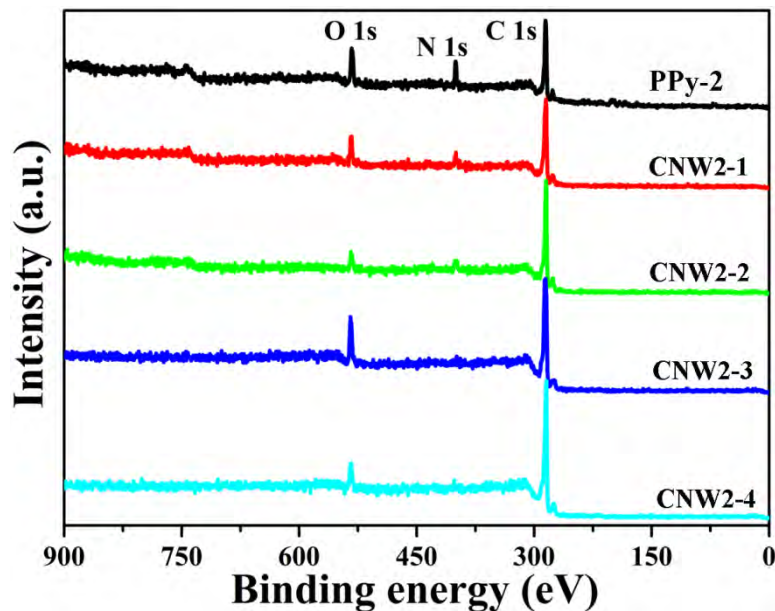


Fig. 4.5 XPS survey spectrums of PPy-2, CNW2-1, CNW2-2, CNW2-3, and CNW2-4.

Table 4.4 Chemical compositions of samples as obtained by XPS

Samples	C/at. %	N/at. %	O/at. %	N/C	O/C
PPy-2	75.70	11.70	12.60	0.155	0.166
CNW2-1	84.66	6.62	8.72	0.078	0.103
CNW2-2	88.69	5.59	5.72	0.063	0.064
CNW2-3	87.03	2.03	10.89	0.023	0.125
CNW2-4	92.40	1.55	6.05	0.017	0.065

More information about the change of surface chemistry has been obtained from the deconvoluted high-resolution XPS spectra of three regions (C, N, and O, shown in Fig.

4.6). The C1s spectra of PPy-2 and CNW2 in Fig. 4.6a-e can be deconvoluted into four components. The carbon species correspond to aromatic or other sp<sup>2</sup>-hybridised carbon atoms bound to neighbouring carbon atoms (C-C) or hydrogen (C-H) (284.5 eV); carbon in C-O (285.4 eV); carbon in C-N/C=N (286.6 eV); and carbon in C=O (289.4 eV) [39, 40, 22]. Obviously, compared to PPy-2 (Fig. 4.6a), CNW2 samples possess more C-C bond corresponding to the graphite carbon at 284.5 eV as the carbonization temperature increases. This indicates that the degree of graphitization of CNW2 rises with the carbonization temperature increases. The N1s spectra of PPy-2 and CNW2 could be deconvoluted into three peaks (Fig. 4.6f-j) with binding energies of  $398.4 \pm 0.2$  eV,  $400.6 \pm 0.2$  eV and  $401.6 \pm 0.2$  eV. These peaks could be assigned to pyridinic nitrogen (N-1), pyrrolic nitrogen (N-2), and quaternary nitrogen (N-3), respectively [41-43]. The contents of the three types of nitrogen atoms are listed in the table 4.5. This suggests that all samples have the largest amount of N-2 except CNW2-4; also, the content of N-1 has a significant increase after PPy-2 is carbonized except CNW2-4. Interestingly, in contrast with PPy-2, nitrogen atoms in CNW2-4 mainly exist in the form of N-3, suggesting that the CNW2-4 sample has been basically graphitized and most of N atoms have been doped into the graphite-like framework at 950 °C. It also suggests that the N-1 is just a transition state for N-3 as the carbonization temperature increases. This may be because N-3 species own higher binding energy than N-1 species, thus higher thermal stability is reasonable to be expected [19]. In addition, the resolution spectra of O 1s can be fitted into three peaks and the results are given in Fig. 4.6k-o. In detail, these three peaks at  $531.7 \pm 0.2$  eV,  $533.5 \pm 0.2$  eV, and  $534.9 \pm 0.2$  eV represent OH/C-O (O-1), C=O (O-2), and C-O-OH (O-3) groups, respectively [44, 45]. These results indicate that there are some lactone, carboxyl and quinone groups on the surface of CNW2 [46]. The contents of the three types of oxygen atoms are also listed in table 4.5. We can find that after PPy-x is carbonized, the content of O-1 significantly decreases but O-3 significantly increases. These oxygen-containing functional groups would have a profound impact on the capacitive performance of CNW2. Overall, the XPS spectra indicate that the N-doped carbon nanowires have been obtained by carbonized PPy

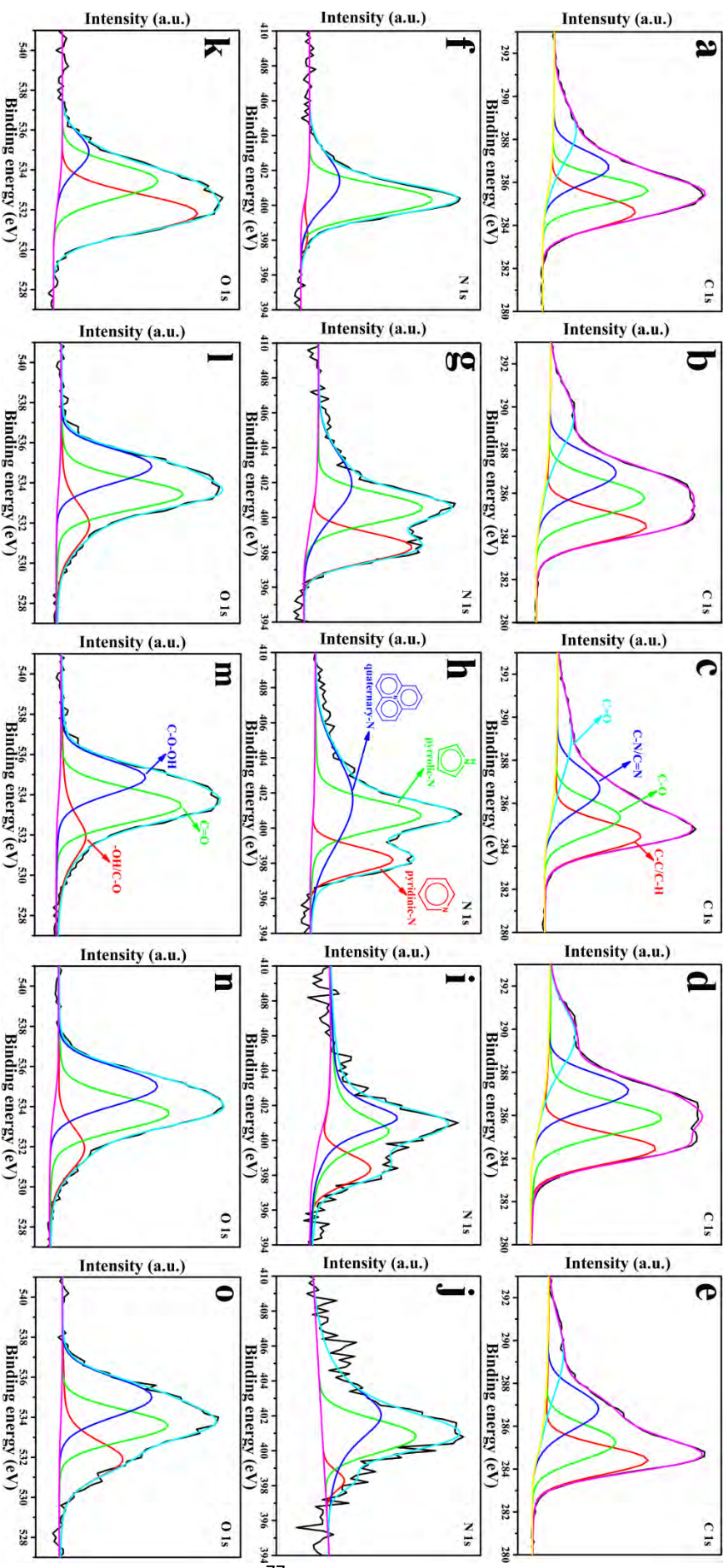


Fig. 4.6 High resolution C 1s, N 1s and O 1s XPS spectrum of PPy-2 (a, f, k), CNW2-1 (b, g, l), CNW2-2 (c, h, m), CNW2-3 (d, i, n), and CNW2-4 (e, j, o).

nanowires; the doping level and graphitization level of CNW2 is lower but rises with the carbonization temperature.

Table 4.5 N 1s and O 1s core level peak analyses

Samples	N-1 (%)	N-2 (%)	N-3 (%)	O-1 (%)	O-2 (%)	O-3 (%)
	398.4 ± 0.2	400.6 ± 0.2	401.6 ± 0.2	531.7 ± 0.2	533.5 ± 0.2	534.9 ± 0.2
PPy-2	4	67	29	56	34	10
CNW2-1	34	39	27	17	48	35
CNW2-2	22	39	39	15	49	36
CNW2-3	23	39	38	21	42	37
CNW2-4	4	33	63	26	39	35

Fig. 4.7 shows the types of nitrogen doping of CNW sample. As illustrated, CNW is obtained by PPy-x direct carbonization method. Pyrrolic nitrogen incorporates into a five membered ring and connects with two neighboring carbon atoms, which contributes two p-electrons to  $\pi$  system. Pyridine nitrogen at the edge of carbon plane incorporates into a six membered ring and also connects with two neighboring carbon atoms, donating one p-electron to the aromatic  $\pi$  system [44]. Quaternary nitrogen provides the nitrogen atoms to replace carbon atom in the carbon lattice, and this leads to its connecting and sp<sup>3</sup> hybridizing with three neighboring carbon atoms, which has a significant effect on the electrochemical performance of the carbon material [44, 47].

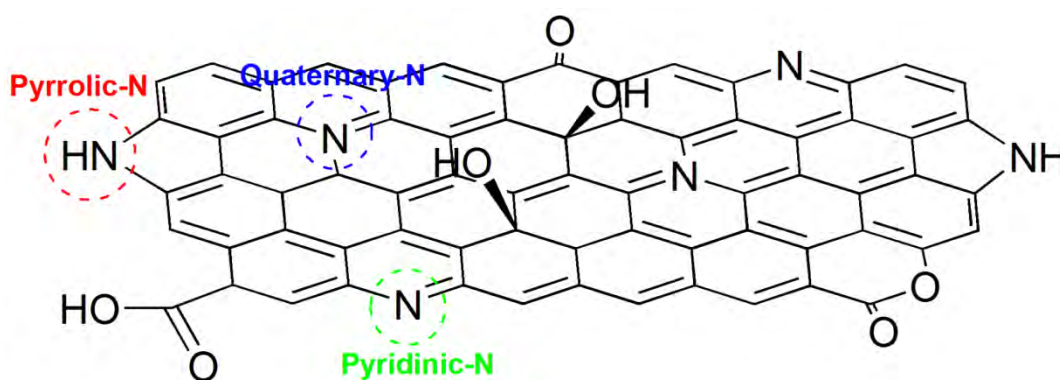
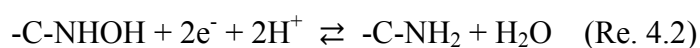
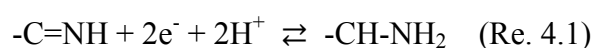


Fig. 4.7 The types of nitrogen doping of CNW sample.

### 4.3.2 Electrochemical performance

In order to evaluate the electrochemical characteristics of CNW samples, CV, GCD, and EIS measurements were employed to characterize the capacitive properties in 1 M H<sub>2</sub>SO<sub>4</sub> aqueous solution. Fig. 4.8 shows the CV and GCD curves of CNW. The scan rate of CV is 10 mV s<sup>-1</sup>, and the current density of GCD is 1 A g<sup>-1</sup>. In Fig. 4.8a, c, and e, we can find that all samples exhibit a typical capacitive behavior with quasi-rectangular shape, indicating ideal capacitance behavior. Also notably, a pair of weak and broad peaks can be observed in the CV curve of CNW in a wide voltage range of -0.1-0.4 V, which proves the presence of typical pseudocapacitance effects in the H<sub>2</sub>SO<sub>4</sub> electrolyte [48]. Nitrogen has higher electronegativity than carbon and can provide a lone electron pair for the carbon with the π-conjugated rings, which makes the surface of the carbon materials more active electrochemically [18]. Some researchers have proposed the pseudocapacitance of the nitrogen doped carbon in acidic medium probably due to the following electrochemical reactions on the surface of carbon [49, 50]:



Furthermore, the oxygen-containing groups (quinone groups bring pseudocapacitance through redox reaction, and lactone groups introduce electron-acceptor property on the carbon surface) on the surface of CNW also contribute to the overall capacitance through pseudocapacitance [51]. However, these contribution resulting from quinone and lactone groups will be weakened by the carboxyl groups through its hindering and retarding the electrolyte contact the carbon surface [46]. From table 4.5, we can see that the content sum of O-1 and O-2 is more than the content of O-3 in all CNW2 samples, this suggesting that the contribution of quinone and lactone groups predominates in these samples. In addition, the pair of peaks gradually weakens as the carbonization temperature rises, and disappears when the temperature reaches 950 °C. This is attributed to that the nitrogen content decreases as the carbonization temperature increases. However, CNW2-1 has weaker peaks than CNW2-2 and

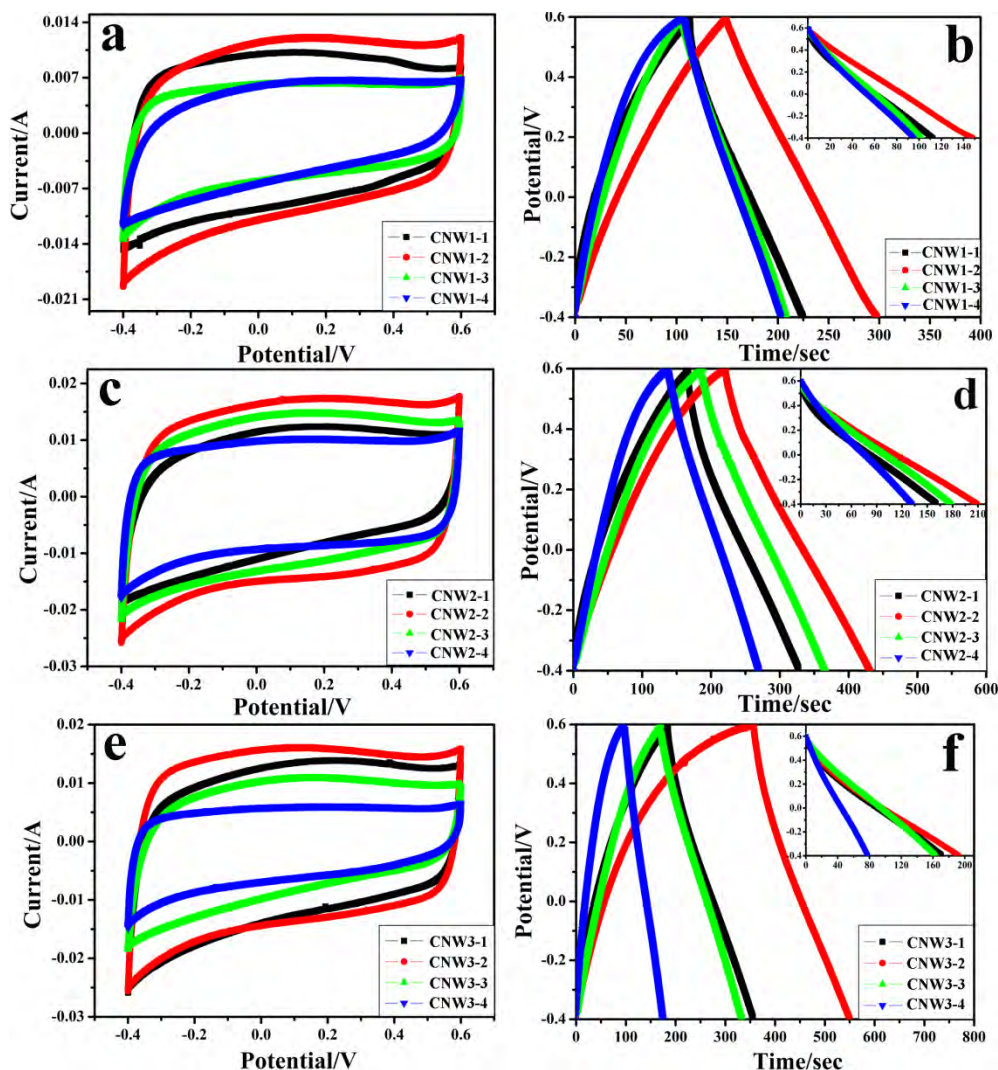


Fig. 4.8 CV curves of CNW1 (a), CNW2 (c), and CNW3 (e) at a scan rate of  $10 \text{ mV s}^{-1}$ ; GCD curves of CNW1(b),CNW2 (d), and CNW3 (f) at a current density of  $1 \text{ A g}^{-1}$ .

CNW2-3, though it has the highest nitrogen content. This is due to that the specific surface area of CNW2-1 is smaller than those of CNW2-2 and CNW2-3. This result reflects that all involved reactions (the faradaic redox and the charge separation reactions) are interface-bound [49, 52]. CNW2-2 has the relatively significant peaks than the other samples, and may have the highest capacitance. We ascribe this to the following factors: (1) although the nitrogen content of CNW2-1 (6.62 %) is higher than those of CNW2-2 (5.59 %) and CNW2-3 (2.03 %), the specific surface areas of CNW2-2 ( $405.6 \text{ m}^2 \text{ g}^{-1}$ ) and CNW2-3 ( $482.5 \text{ m}^2 \text{ g}^{-1}$ ) are higher than that of CNW2-1 ( $306.9 \text{ m}^2 \text{ g}^{-1}$ ); (2) although the specific surface area of CNW2-2 is smaller than those

of CNW2-3 and CNW2-4 ( $580.2 \text{ m}^2 \text{ g}^{-1}$ ), the nitrogen content of CNW2-2 is much higher than those of CNW2-3 and CNW2-4 (1.55 %).

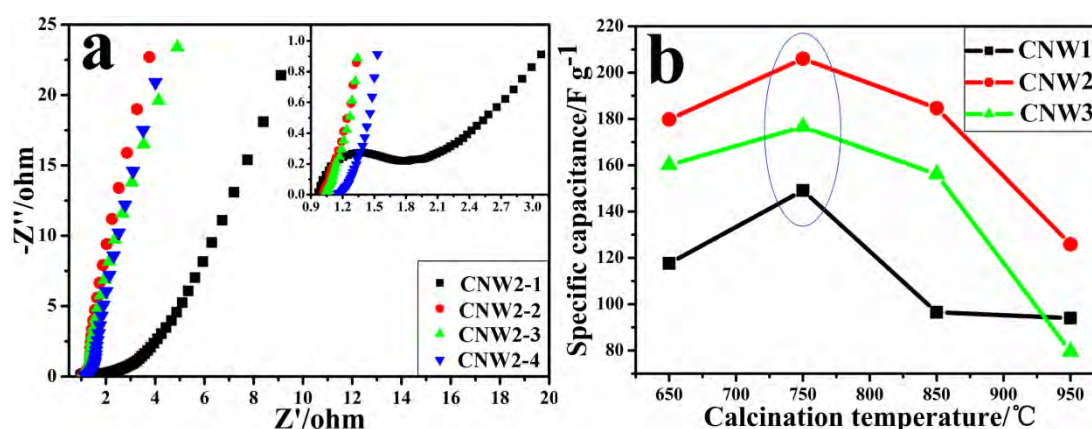


Fig. 4.9 (a) EIS spectrum of CNW2-1, CNW2-2, CNW2-3, and CNW2-4; (b) The effect of calcination temperature on specific capacitance of CNW (at a current density of  $1 \text{ A g}^{-1}$ ).

The above phenomenon can also be confirmed by the GCD curve (Fig. 4.8b, d and f). From Eq. 2.2, the specific capacitances of all samples are obtained and the results are shown in fig. 4.9b. The CNW2-2 achieves the highest specific capacitance of  $207 \text{ F g}^{-1}$  at a current density of  $1 \text{ A g}^{-1}$ , consistent with our inference. For comparison, we also examined the capacitive performance of CNW0 (see supporting information Fig. 4.10). The results show that the specific capacitance of CNW0 is far less than CNW1, 2, and 3. This indicates that the wire morphology is better than globular morphology for capacitive performance of CNW. Furthermore, specific capacitance of CNW2 is higher than those of CNW1 and 3, and the specific capacitance of CNW $_x$ -2 is higher than those of CNW $_x$ -1, 3, and 4 ( $x=1, 2, 3$ ). The specific capacitance of N-doped carbon depends on two factors: (1) the high double-layer capacitance attributed to its high surface area; (2) the special pseudocapacitance mainly caused by its nitrogen content [49]. Hence, the balance of specific surface area and nitrogen content is a decisive factor for these N-doped carbon nanowires to obtain an excellent electrochemical capacitive performance. The results of GCD testing show that CNW2 (carbonization temperature is  $750 \text{ }^{\circ}\text{C}$ ) samples strike the balance and possess the better electrochemical performance than the other samples.

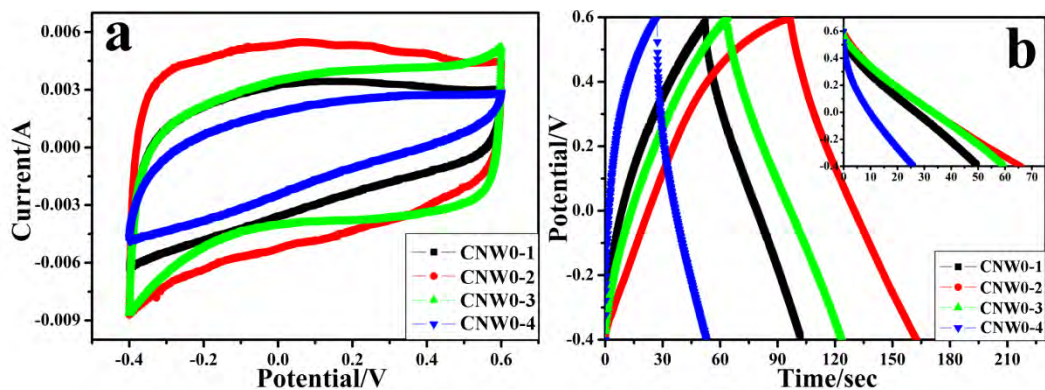


Fig. 4.10 (a) CV curves of CNW0 at a scan rate of  $10 \text{ mV S}^{-1}$ ; (b) GCD curves of CNW0 at a current density of  $1 \text{ A g}^{-1}$ .

To further study the capacitance behavior of CNW2 samples, EIS was used to measure the charge transport and ion diffusion. The Nyquist plots were generated, as shown in Fig. 4.9a. Except CNW2-1, the other samples present a similar Nyquist plots shape, composed of two regions: a nearly vertical line at low frequency assigned to the characterized capacitive behavior [53, 54], and a sloping lines at intermediate frequency related to the ion diffusion in the electrolyte to the electrode interface [55, 56]. It is clear that, the line at low frequency of CNW2-2 is much more vertical than the other samples; the sloping line at intermediate frequency of CNW2-2, CNW2-3, and CNW2-4 are all shorter than that of CNW2-1. Compared to the other samples, CNW2-1 has a semicircle at high frequency attributed to the charge transfer resistance [57]. Moreover, the Fig. 4.9a inset shows that the intercept at the real part ( $Z'$ ) is related to the internal resistance, including the intrinsic resistance of the sample, the contact resistance between the sample and stainless steel mesh current collector, and the resistance of bulk electrolyte [58]. The internal resistances of CNW2-1, CNW2-2, CNW2-3, and CNW2-4 are  $0.97$ ,  $1.02$ ,  $1.03$ , and  $1.16 \text{ } \Omega$ , respectively, which indicates that the internal resistances of the samples are gradually increasing with the carbonization temperature. To sum up, the result of EIS testing shows that the CNW2-2 possesses an excellent electrochemical capacitive performance, which is consistent with the CV and GCD analysis.

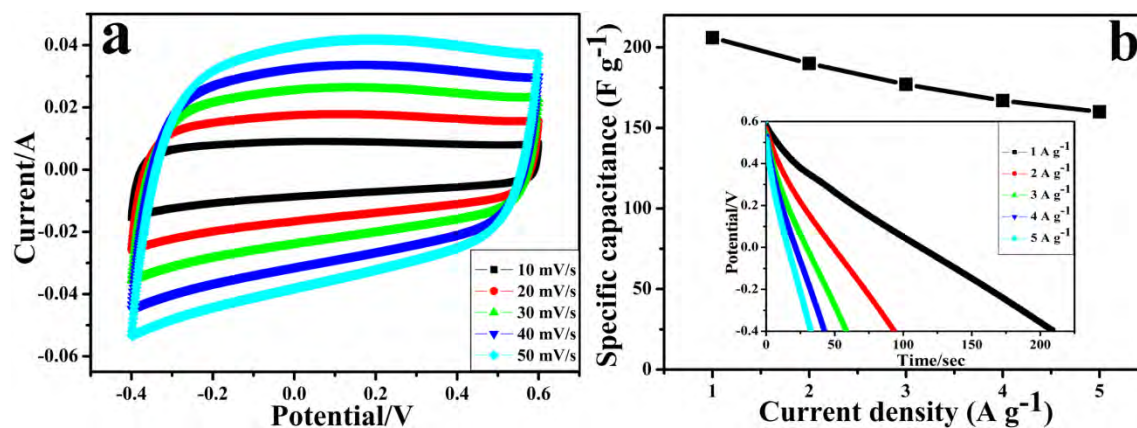


Fig. 4.11 (a) CV curves of CNW2-2 at different scan rates varying from 10 to 50  $\text{mV s}^{-1}$ ; (b) specific capacitance versus current density of CNW2-2;

Fig. 4.11a shows the CV curves of CNW2-2 samples at different scan rates ranging from 10 to 50  $\text{mV s}^{-1}$ . Generally, the response current of CNW2-2 gradually increases when increasing the scan rate. The CV curve has maintained the rectangular shape, and a rapid current response on voltage reversal at each end potential at the scan rates ranging from 10 to 50  $\text{mV s}^{-1}$ . These reveal its good electrochemical capacitive performance at high scan rates. Also note that, the pair of weak peaks almost disappears at the scan rate of 50  $\text{mV s}^{-1}$ , which may be because there is not enough time for electrochemical reaction, thus making the specific capacitance of CNW2-2 decline. Fig. 4.11b shows the specific capacitances of CNW2-2 at different current densities from 1 to 10  $\text{A g}^{-1}$ . Clearly, the downward trend of specific capacitance of CNW2-2 is nonlinear, which suggests that the pseudocapacitive behavior happens at the electrode-electrolyte interface [48]. From Eq. 2.2, the specific capacitances reach 207 and 150  $\text{F g}^{-1}$  at the current density of 1 and 10  $\text{A g}^{-1}$ , respectively, and the capacitance retention of CNW2-2 is 72.5 %. These results indicate that the CNW2-2 possesses the fast charge-discharge properties, which is very important for supercapacitors application.

Cycle stability is another important factor for supercapacitor application. In order to evaluate the cycle stability of CNW2-2, repeated the GCD test were measured at a current density of 3  $\text{A g}^{-1}$  for 5000 cycles, as shown in Fig. 4.12. The specific capacitance of CNW2-2 is very stable after 5000 cycles, suggesting excellent cycle

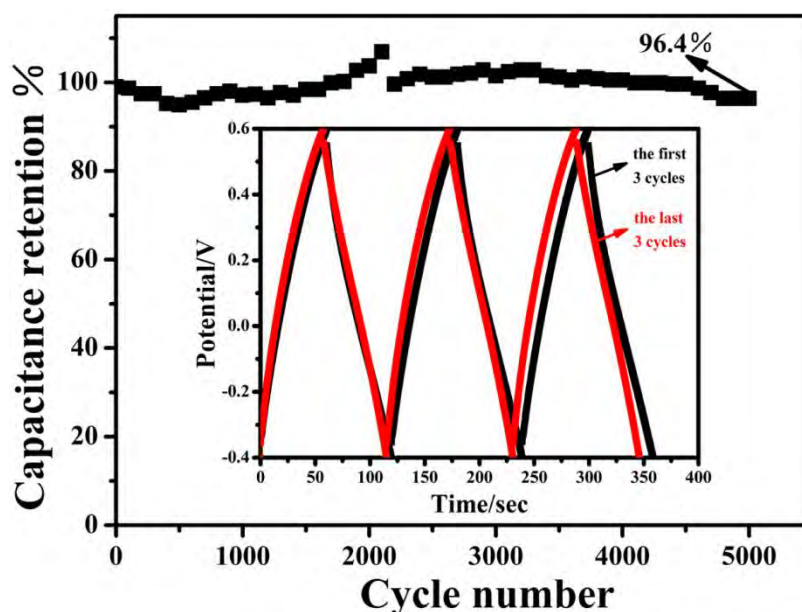


Fig. 4.12 Cycling stability of CNW2-2 at a current density of  $3 \text{ A g}^{-1}$ .

stability. The specific capacitance has a slight decline of about 3.6 % (in the first cycle, it is  $178 \text{ F g}^{-1}$ , and after the 5000th cycle, it is  $172 \text{ F g}^{-1}$ ). Notably, the specific capacitance has a slight increase in 1500-4500 cycles, this is attributed to the following factors: (1) the nitrogen-containing functional groups are firmly incorporated into the carbon framework; (2) a continuous activation takes place in the surface of CNW2-2; (3) the oxidation-reduction reaction based on nitrogen functional groups are reversible [18, 59, 60].

In order to confirm the excellent capacitive performance of CNW2-2 from the three-electrode system, we also carried out the CV, GCD and cycle stability tests in symmetric two-electrode systems, and the results are shown in Fig. 4.13. The voltage window is a key factor which directly impacts the specific capacitance and energy density of supercapacitors. CV tests were performed in different voltage windows to define the best operating voltage window (as shown in Fig. 4.13a) [61]. From Fig. 4.13a, we can find that all CV curves exhibit quasi-rectangular shapes when the voltage windows are below 1.5 V. Furthermore, there is no significant increase of anodic current even when the voltage window is 0-1.5 V, which means that the electrolyte is not decomposed due to the storage of nascent hydrogen on the electrode below the thermodynamic potential for water decomposition [62]. However, the

anodic current sharply increases when the voltage window increases to 1.6 V, which means that the electrolyte is decomposed with hydrogen and/or oxygen evolution [61]. These results suggest that the best voltage window of two-electrode system is 0-1.5 V. In addition, the response current of CV curve gradually increases with the increase of voltage window, which means that the specific capacitance of symmetric capacitor gradually increases. Fig. 4.13b shows the GCD tests in two-electrode systems at different voltage windows. All GCD curves show an equilateral triangle shape, which reflects its ideal capacitive behavior. We can obtain the specific capacitance of different voltage windows from these GCD curves by Eq. 2.2. The specific capacitances are 30.2, 30.7, 31.6, 35.3, 38.1 and 40.2  $\text{F g}^{-1}$  at 0-0.6, 0-0.8, 0-1.0, 0-1.2, 0-1.4 and 0-1.5 V, respectively. These results also prove the inference from CV test.

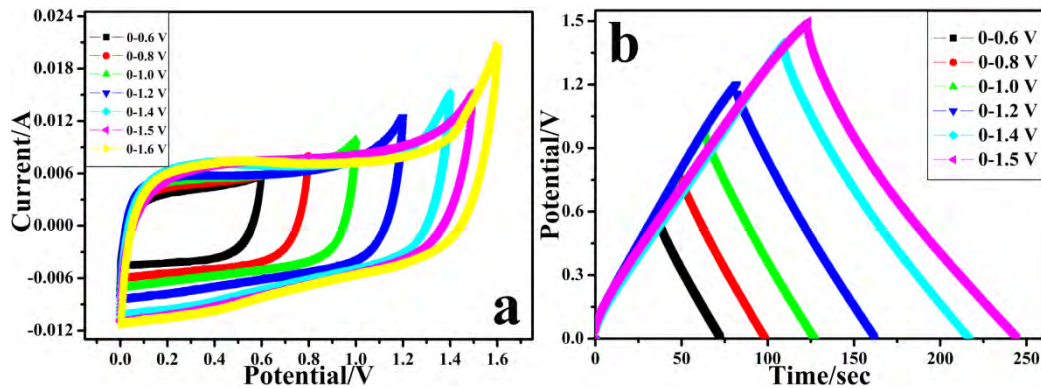


Fig. 4.13 CV (a, scan rate is  $10 \text{ mV s}^{-1}$ ) and GCD (b, current density is  $0.5 \text{ A g}^{-1}$ ) curves of CNW2-2 two-electrode system.

In electrochemical capacitors with excellent performance, the high power density and energy density are expected. The energy and power density of the samples are calculated from the GCD curves according to Eq. 2.3 and 2.4, and the Ragone plots of different voltage windows at a series of charge-discharge rates for CNW2-2 (as shown in Fig. 4.15) are shown in Fig. 4.14. Overall, the energy density decreases gradually with the increase of power density, and under the same charge-discharge rate, the energy density and power density increase gradually with the increase of voltage window. In the two-electrode system with a voltage window of 0-1.5 V, the sample exhibits a maximum energy density of  $13.2 \text{ Wh kg}^{-1}$  and a power density of  $257 \text{ W}$

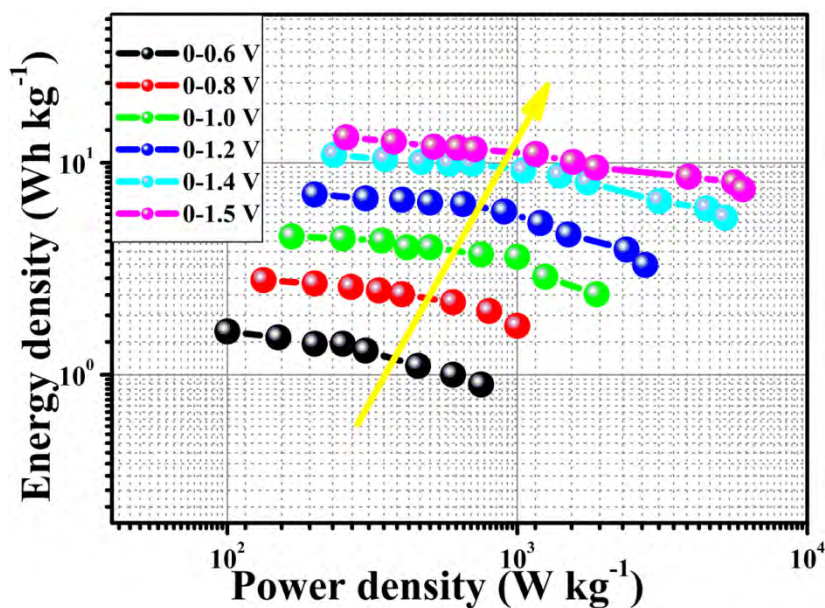


Fig. 4.14 Ragone plot of CNW2-2 in two-electrode system at different voltage windows.

$\text{kg}^{-1}$  at the current density of  $0.33 \text{ A g}^{-1}$ . At the current density of  $2.5 \text{ A g}^{-1}$  and voltage window of  $0\text{-}1.5 \text{ V}$ , the power density reaches to  $1869 \text{ W kg}^{-1}$ ; the corresponding energy density is  $9.5 \text{ Wh kg}^{-1}$ , and the energy density retention is  $71.9 \%$  compared with the current density of  $0.33 \text{ A g}^{-1}$ . At the same current density and voltage window, the energy density retentions are  $56.3 \%$ ,  $60.7 \%$ ,  $64.4 \%$ ,  $64.8 \%$  and  $65.1 \%$  at  $0\text{-}0.6 \text{ V}$ ,  $0\text{-}0.8 \text{ V}$ ,  $0\text{-}1.0 \text{ V}$ ,  $0\text{-}1.2 \text{ V}$  and  $0\text{-}1.4 \text{ V}$ , respectively (as shown in table 4.6). The maximum energy density and energy density retention obtained at a voltage window of  $0\text{-}1.5 \text{ V}$  are much higher than those of other voltage windows. In addition, at the current density of  $10 \text{ A g}^{-1}$  and voltage window of  $0\text{-}1.5 \text{ V}$ , the energy density still reaches to  $7.5 \text{ Wh kg}^{-1}$ , much higher than that of voltage window of  $0\text{-}1.4 \text{ V}$  (at current density of  $10 \text{ A g}^{-1}$ , the energy density is  $5.5 \text{ Wh kg}^{-1}$ ). This further shows that the voltage window is a key factor for supercapacitors. Compared with previously reported energy density of carbon materials in two-electrode systems, commercial activated carbon ( $< 10 \text{ Wh kg}^{-1}$ ) [6], activated carbon ( $< 10 \text{ Wh kg}^{-1}$ ) [63, 64], carbon nanotube ( $< 10 \text{ Wh kg}^{-1}$ ) [65, 66] and graphene ( $< 4 \text{ Wh kg}^{-1}$ ) [67] in aqueous electrolyte, CNW2-2 sample shows outstanding performance. In summary, these

above analyses indicate that the optimal voltage window of the CNW2-2 sample in two-electrode systems is 0-1.5 V, a very suitable range for supercapacitors.

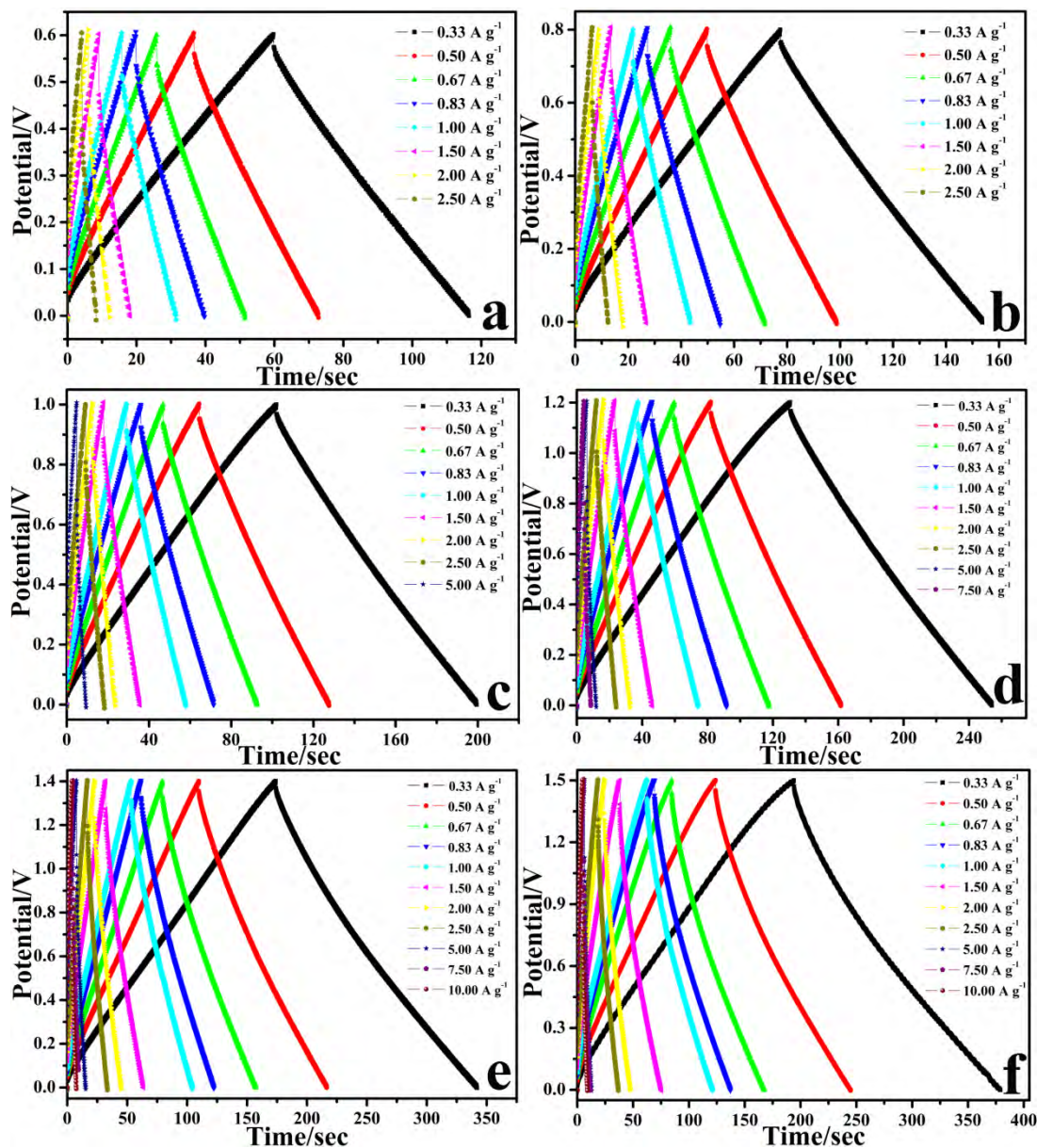


Fig. 4.15 GCD curves of CNW2-2 in two-electrode system at voltage window is 0-0.6 V (a), 0-0.8 V (b), 0-1.0 V (c), 0-1.2 V (d), 0-1.4 V (e) and 0-1.6 V (f).

We also evaluated the cycle stability of CNW2-2 in two-electrode systems by repeating the GCD test at the voltage window of 0-1.5 V, and the results are shown in Fig. 4.16. The specific capacitance of CNW2-2 in two-electrode systems shows a 1.5 % variation after 5000 cycles (as shown in Fig. 4.17), indicating the excellent cycle stability. To further understand the superior electrochemical stability of CNW2-2,

energy and power density of CNW2-2 electrodes before and after the cycling were measured at different current densities as shown in the inset of Fig. 4.16. CNW2-2 sample also exhibits a high energy density of 13.0 Wh kg<sup>-1</sup> at a current density of 0.33 A g<sup>-1</sup> after 5000 cycles. Compared with before cycling, the energy density retention is 98.5 %. Even when the current density is 10 A g<sup>-1</sup>, the energy density still reaches to 7.3 Wh kg<sup>-1</sup> after 5000 cycles. These results further evidence the excellent cycle stability of CNW2-2.

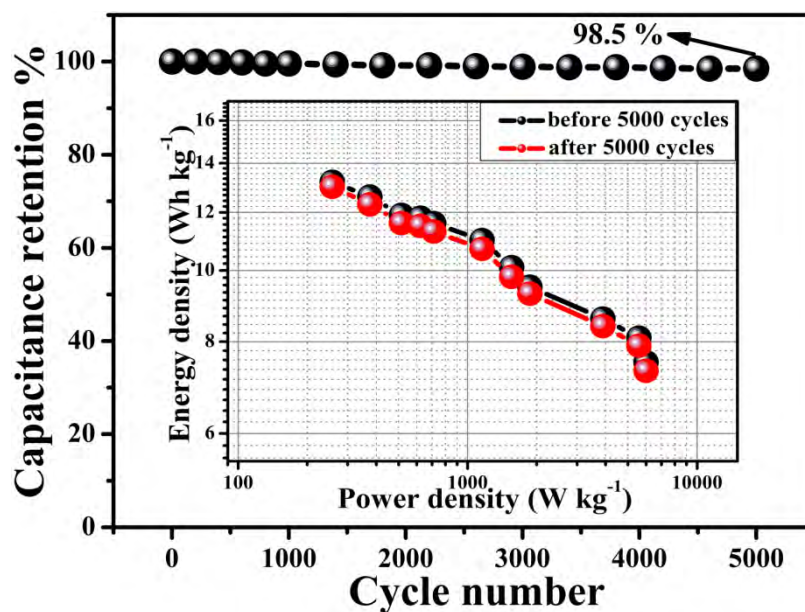


Fig. 4.16 Cycle stability of CNW2-2 in two-electrode system at a current density is 1 A g<sup>-1</sup>, the inset is a ragone plot of CNW2-2 before and after 5000 cycles.

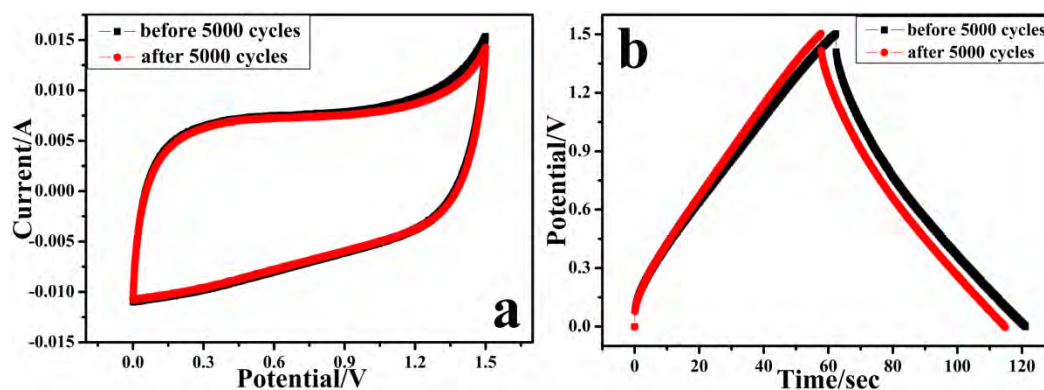


Fig. 4.17 CV (a) and GCD (b) curves of CNW2-2 before and after 5000 cycles in two-electrode system.

Table 4.6 The specific capacitance and energy density of CNW2-2 in low-electrode system

Current density/ $A\ g^{-1}$ Voltage window/V	0.33		0.50		0.67		0.83		1.00		1.50		2.00		2.50		5.00		7.50		10.00		EDR (%) <sup>c</sup>
	C <sup>a</sup>	E <sup>b</sup>	C	E	C	E	C	E	C	E	C	E	C	E	C	E	C	E	C	E	C	E	
0-0.6	31.5	1.6	30.2	1.5	28.6	1.4	27.6	1.4	26.3	1.3	22.3	1.1	20.7	1.0	17.5	0.9	--	--	--	--	--	--	56.3
0-0.8	31.8	2.8	30.7	2.7	29.8	2.6	28.6	2.5	27.0	2.4	25.1	2.2	22.8	2.0	18.8	1.7	--	--	--	--	--	--	60.7
0-1.0	32.5	4.5	31.6	4.4	31.2	4.3	29.5	4.0	28.9	4.0	26.6	3.7	23.0	3.6	22.0	2.9	20.1	2.4	--	--	--	--	64.4
0-1.2	36.8	7.1	35.3	6.8	34.8	6.7	34.3	6.5	33.1	6.4	28.3	5.9	27.5	5.2	25.8	4.6	24.3	3.9	22.1	3.3	--	--	64.8
0-1.4	41.0	10.9	38.1	10.4	37.1	10.1	36.6	9.9	36.3	9.9	33.9	9.2	31.9	8.7	28.2	7.1	26.5	6.6	24.6	6.1	22.5	5.5	65.1
0-1.5	42.1	13.2	40.2	12.6	38.0	11.9	37.7	11.8	37.2	11.6	35.1	11.0	32.1	10.1	29.8	9.5	27.4	8.6	25.8	8.1	23.6	7.5	71.9

<sup>a</sup> The specific capacitance (F g<sup>-1</sup>) of CNW2-2 sample in low-electrode system

<sup>b</sup> The energy density (Wh kg<sup>-1</sup>) of CNW2-2 sample in low-electrode system.

<sup>c</sup> The energy density retention, the energy density at current density is 2.5 A g<sup>-1</sup> divided by that of at current density is 0.33 A g<sup>-1</sup>.

## 4.4 Conclusions

In conclusion, the nitrogen doped carbon nanowires CNW2-2 were facilely prepared through direct carbonization method at a carbonization temperature of 750 °C using polypyrrole nanowires as the carbon precursor. CNW2-2 possesses high nitrogen content (5.59 at. %) and large specific surface area (405.6 m<sup>2</sup> g<sup>-1</sup>). In three electrode systems, the co-contribution of double-layer capacitance and pseudocapacitance makes CNW2-2 exhibit a high capacitance (207 F g<sup>-1</sup> at 1 A g<sup>-1</sup>), excellent rate capability (150 F g<sup>-1</sup> remained at 10 A g<sup>-1</sup>), as well as good cycle stability (96.4 % capacitance retention after 5000 cycles). In the symmetric two-electrode systems, CNW2-2 indicates a high energy density of 13.2 Wh kg<sup>-1</sup> at a high power density of 257 W kg<sup>-1</sup> at the current density of 0.33 A g<sup>-1</sup>, and the energy density retention is 71.9 % at the current density of 2.5 A g<sup>-1</sup>. However, the electrochemical performance of CNW2-2 is still not very satisfactory.

## References:

- [1] L.M. Dai, D.W. Chang, J.B. Baek, W. Lu, *Small* 8 (2012) 1130-1166.
- [2] D. Banham, F.X. Feng, J. Burt, E. Alsayheen, V.B. Bimodal, *Carbon* 48 (2010) 1056-1063.
- [3] Y. Zhang, H. Feng, X.B. Wu, L.Z. Wang, A.Q. Zhang, T.C. Xia, *Int. J. Hydrogen Energy* 34 (2009) 4889-4899.
- [4] L.L. Zhang, X.S. Zhao, *Chem. Soc. Rev.* 38 (2009) 2520-2531.
- [5] Y.S. Yun, G.B. Yoon, K.K. Kang, H.J. Jin, *Carbon* 80 (2014) 246-254.
- [6] Q. Wang, J. Yan, Y.B. Wang, G.Q. Ning, Z.J. Fan, T. Wei, *Carbon* 52 (2013) 209-218.
- [7] C. Zheng, X.F. Zhou, H.L. Cao, G.H. Wang, Z.P. Liu, *J. Power Sources* 258 (2014) 290-296.
- [8] J. Hu, Z. Kang, F. Li, X. Huang, *Carbon* 67 (2014) 221-229.
- [9] T.Y. Wei, C.H. Chen, H.C. Chien, S.Y. Lu, C.C. Hu, *Adv. Mater.* 22 (2010) 347-351.
- [10] Q. Li, Z.L. Wang, G.R. Li, R. Guo, L.X. Ding, Y.X. Tong, *Nano Lett.* 12 (2012) 3803-3807.
- [11] G.G. Zhang, W.F. Li, K.Y. Xie, F. Yu, H.T. Huang, *Adv. Funct. Mater.* 23 (2013) 3675-3681.
- [12] H. Zhao, K.S. Hui, K.N. Hui, *Carbon* 76 (2014) 1-9.
- [13] Y. Shin, G. E. Fryxell, W. Um, K. Parker, S. V. Mattigod, R. Skaggs, *Adv. Funct. Mater.* 17 (2007) 2897-2901.
- [14] Z. Liu, J.H. Mi, Y. Yang, X.L. Tan, C. Lv, *Electrochim. Acta* 115 (2014) 206-215.
- [15] D. Jana, C.L. Sun, L.C. Chen, K.H. Chen, *Prog. Mater. Sci.* 58 (2013) 565-635.
- [16] L.F. Chen, Z.H. Huang, H.W. Liang, H.L. Gao, S.H. Yu, *Adv. Funct. Mater.* 24 (2014) 5104-5111.
- [17] L.F. Chen, Z.H. Huang, H.W. Liang, W.T. Yao, Z.Y. Yu, S.H. Yu, *Energy Environ. Sci.* 6 (2013) 3331-3338.
- [18] H. Chen, M. Zhou, Z. Wang, S.Y. Zhao, S.Y. Guan, *Electrochim. Acta* 148 (2014)

187-194.

[19] D.Y. Zhang, Y. Hao, L.W. Zheng, Y. Ma, H.X. Feng, H.M. Luo, *J. Mater. Chem. A* 1 (2013) 7584-7591.

[20] A. Stein, Z.Y. Wang, M.A. Fierke, *Adv. Mater.* 21 (2009) 265-293.

[21] J.P. Paraknowitsch, A. Thomas, M. Antonietti, *J. Mater. Chem.* 20 (2010) 6746-6758.

[22] C.M. Yang, C.D. Weidenthaler, B. Spliethoff, M. Mayanna, F. Schuth, *Chem. Mater.* 17 (2005) 355-358.

[23] P.F. Fulvio, M. Jaroniec, C.D. Liang, S. Dai, *J. Phys. Chem. C* 112 (2008) 13126-13133.

[24] Y.W. Ma, S.J. Jiang, G.Q. Jian, H.S. Tao, L.S. Yu, X.B. Wang, *Energy Environ. Sci.* 2 (2009) 224-229.

[25] Z.H. Wang, X.Q. Xiong, L. Qie, Y.H. Huang, *Electrochimica Acta* 106 (2013) 320-326.

[26] X.Y. Zhou, J.J. Tang, J. Yang, J. Xie, B. Huang, *J. Mater. Chem. A* 1 (2013) 5037-5044.

[27] L. B. Xing, S.F. Hou, J. Zhou, J.L. Zhang, W.J. Si, Y.H. Dong, S.P. Zhuo, *J. Solid State Chem.* 230 (2015) 224-232.

[28] D.D. Han, X.Y. Jing, P.C. Xu, Y.S. Ding, J.Y. Liu, *J. Solid State Chem.* 218 (2014) 178-183.

[29] H. Akbi, L. Yu, B. Wang, Q. Liu, J. Wang, J.Y. Liu, D.L. Song, Y.B. Sun, L.H. Liu, *J. Solid State Chem.* 221 (2015) 338-344.

[30] M.M. Sun, S.C. Zhang, T. Jiang, L. Zhang, J.H. Yu, *Electrochem. Commun.* 10 (2008) 1819-1822.

[31] W. Lei, P. He, Y.H. Wang, S.S. Zhang, F.Q. Dong, H.T. Liu, *Electrochim. Acta* 132 (2014) 112-117.

[32] L.F. Gou, C.J. Murphy, *Nano Lett.* 3 (2003) 231-234.

[33] X.T. Zhang, J. Zhang, W.H. Song, Z.F. Liu, *J. Phys. Chem. B* 110 (2006) 1158-1165.

[34] B. Wang, J.H. Qiu, H.X. Feng, E. Sakai, *Electrochim. Acta* 151 (2015) 230-239.

- [35] J. Liu, M.X. Wan, *J. Mater. Chem.* 11 (2001) 404-407.
- [36] J. Upadhyay, A. Kumar, *Mater. Sci. Eng. B* 178 (2013) 982-989.
- [37] M. Seredych, R.C. Enrique, M.J. Biggs, W. Skinner, T.J. Bandoz, *Carbon* 78 (2014) 540-558.
- [38] M. Sevilla, V.V. Patricia, A.B. Fuertes, *Adv. Funct. Mater.* 21 (2011) 2781-2787.
- [39] K.Y. Chun, H.S. Lee, C.J. Lee, *Carbon* 47 (2009) 169-177.
- [40] H.L. Wang, Q.L. Hao, X.J. Yang, L.D. Lu, X. Wang, *ACS Appl. Mater. Interfaces* 2 (2010) 821-828.
- [41] S.N. Talapaneni, G.P. Mane, A. Mano, C. Anand, D.S. Dhawale, T. Mori, *ChemSusChem* 5 (2012) 700-708.
- [42] G.P. Mane, S.N. Talapaneni, C. Anand, S. Varghese, H. Iwai, Q.M. Ji, *Adv. Funct. Mater.* 22 (2012) 3596-3604.
- [43] J. Wei, D.D. Zhou, Z.K. Sun, Y.H. Deng, Y.Y. Xia, D.Y. Zhao, *Adv. Funct. Mater.* 23 (2013) 2322-2328.
- [44] J. Pu, C.W. Li, L. Tang, T.T. Li, L. Ling, K. Zhang, Y.C. Xu, Q.W. Li, Y.G. Yao, *Carbon* 94 (2015) 650-660.
- [45] V. Datsyuk, M. Kalyva, K. Papagelis, J. Parthenios, D. Tasis, A. Siokou, I. Kallitsis, C. Galiotis, *Carbon* 46 (2008) 833-840.
- [46] Z.B. Zulamita, C.M. Francisco, M.C. Carlos, *J. Power Sources* 219 (2012) 80-88.
- [47] S.P. Wang, J.N. Zhang, P. Shang, Y.Y. Li, Z.M. Chen, Q. Xu, *Chem. Commun.* 50 (2014) 12091-12094.
- [48] L.R. Hou, L. Lian, D.K. Li, G. Pang, J.F. Li, X.G. Zhang, *Carbon* 64 (2013) 141-149.
- [49] M. Zhou, F. Pu, Z. Wang, S.Y. Guan, *Carbon* 68 (2014) 185-194.
- [50] W.R. Li, D.H. Chen, Z. Li, Y.F. Shi, Y. Wan, J.J. Huang, *Electrochem. Commun.* 9 (2007) 569-573.
- [51] C. Vagner, G. Fingueneisel, T. Zimny, P. Burg, B. Grzyb, J. Machnikowski, J.V. Weber, *Carbon* 41 (2003) 2847-2853.
- [52] L. Zhao, L.Z. Fan, M.Q. Zhou, H. Guan, S.Y. Qiao, M. Antonietti, M.M. Titirici, *Adv. Mater.* 22 (2010) 5202-5206.

- [53] X.M. Fan, C. Yu, J. Yang, Z. Ling, J.S. Qiu, *Carbon* 70 (2014) 130-141.
- [54] M.D. Stoller, S. Park, Y.W. Zhu, J.H. An, R.S. Ruoff, *Nano Lett.* 8 (2008) 3498-3502.
- [55] V. Ruiz, C. Blanco, R. Santamaria, J.M. Ramos-Fernández, M. Martínez-Escandell, A.S. Iveda-Escribano, *Carbon* 47 (2009) 195-200.
- [56] H.X. Feng, B. Wang, L. Tan, N.L. Chen, N.X. Wang, *J. Power Sources* 246 (2014) 621-628.
- [57] N.D. Kim, D.B. Buchholz, G. Casillas, M. José-Yacamán, Robert P. H. Chang, *Adv. Funct. Mater.* 24 (2014) 4186-4194.
- [58] T.W. Cai, M. Zhou, D.Y. Ren, G.S. Han, S.Y. Guan, *J. Power Sources* 231 (2013) 197-202.
- [59] E. Raymundo-Pinero, F. Leroux, F. Beguin, *Adv. Mater.* 18 (2006) 1877-1882.
- [60] W. Lee, J.H. Moon, *ACS Appl. Mater. Interfaces* 6 (2014) 13968-13976.
- [61] K. Fic, G. Lota, M. Meller, E. Frackowiak, *Energy Environ. Sci.* 5 (2012) 5842-5850.
- [62] X. Yang, Y.S. He, G. Jiang, X.Z. Liao, Z.F. Ma, *Electrochem. Commun.* 13 (2011) 1166-1169.
- [63] D.W. Wang, F. Li, M. Liu, G.Q. Lu, H.M. Cheng, *Angew. Chem. Int. Ed.* 47 (2008) 373-376.
- [64] C.W. Huang, C.T. Hsieh, P.L. Kuo, H. Teng, *J. Mater. Chem.* 22 (2012) 7314-7322.
- [65] K.H. An, W.S. Kim, Y.S. Park, J.M. Moon, D.J. Bae, S.C. Lim, Y.S. Lee, Y.H. Lee, *Adv. Funct. Mater.* 11 (2001) 387-392.
- [66] Y. Honda, T. Haramoto, M. Takeshige, H. Shiozaki, T. Kitamura, M. Ishikawa, *Electrochem Solid-State Lett.* 10 (2007) A106-A110.
- [67] J.T. Zhang, J.W. Jiang, H.L. Li, X.S. Zhao, *Energy Environ. Sci.* 4 (2011) 4009-4015.

# **Chapter 5 KOH-activated nitrogen doped porous carbon nanowires with superior performance in supercapacitors**

## **5.1 Introduction**

For further improve the electrochemical performance of carbon nanowires (in chapter 4), the study was transferred to the development of porous carbon materials. Nowadays, carbon materials are often used in electrical double-layer capacitor owing to the low cost [1, 2], high cycle stability [3, 4] and excellent conductivity [5, 6]. Unfortunately, the low specific capacitance of carbon material greatly limited their application in a wider range. Pseudocapacitors often employ conducting polymers and metal oxides as the electrode material, but their poor cycle stability and high price are detrimental to their application in supercapacitors [7].

Recently, many researchers showed that substituting some atoms in carbon nanomaterials by heteroatoms (such as N [8], S [9] and B [10]) is an effective way to improve the specific capacitance. This is owing to the fact that heteroatoms can introduce pseudocapacitive effects and improve the wettability of carbon materials in electrolyte solution [6, 11]. However, the specific capacitance of doped carbon was observed to have a significant decrease at high current densities, limiting their further applications [5]. Because of its high specific capacitance at high current densities, heteroatom-doped porous carbon was applied to address the challenge. In the traditional approach, porous carbon is usually prepared by template methods, and then treated by heteroatom sources to obtain heteroatom-doped porous carbon. For instance, Chen [12] and Xu [13] have showed that the N-doped porous carbon possessed excellent capacitive performance at high current densities. However, their preparation methods are complicated and high-cost. Compared with the template method, KOH activation method is a simpler one for preparing porous carbon, which

is more suitable for large-scale production. It has been reported that the KOH activation of porous carbon shows the improvement on specific surface area and capacitive performance [14-16]. For instance, KOH-activated ordered mesoporous carbon possesses high specific surface area of  $1410 \text{ cm}^2 \text{ g}^{-1}$  and high specific capacitance of  $200 \text{ F g}^{-1}$  at a current density of  $0.5 \text{ A g}^{-1}$  [5]; under the condition of KOH/carbon mass ratio of 2.5, the activation temperature of  $800 \text{ }^\circ\text{C}$  and the activation time of 1 h, the mesoporous carbon is obtained, and its specific capacitance is  $218 \text{ F g}^{-1}$  at a current density of  $1 \text{ A g}^{-1}$  [17].

Pyrrole is a kind of significant nitrogen source of N-doping porous carbon. Its doping process is often performed via chemical vapor deposition. However, the doping condition is normally rather harsh and easily leads to environmental pollution [18]. Hence, it is urgently needed a facile and environment-friendly method for preparation of N-doped porous carbon. Recently, some studies showed that polypyrrole nanowires could act simultaneously as both the nitrogen source and the carbon source, which facilitates the simplification of the preparation, and the product exhibited the excellent performance in lithium ion battery. [19-21] However, it is known that there is much difference between the energy storage mechanisms of lithium ion battery (through the lithium ion intercalation-deintercalation, which is a chemical process [22]) and supercapacitors (through the charge separation in the interface of electrode/electrolyte, which is a physical process). The N-doped porous carbon nanowires prepared by polypyrrole nanowires may be very suitable for supercapacitors due to its plentiful pore structure, high surface area and some nitrogen content. We have noticed that the performance of these N-doped porous carbon nanowires in supercapacitors has never been systematically investigated. In this paper, we prepared the N-doped porous carbon nanowires by the similar method, and applied it in supercapacitors. We find that the capacitive performance of N-doped porous carbon nanowires is closely related to the mass ratio of KOH and carbon. This is due to the fact that the pore size distribution, specific surface area and nitrogen content of N-doped porous carbon nanowires would be greatly affected by the mass ratio of KOH and carbon.

## **5.2 Experimental section**

### **5.2.1 Materials**

Py monomer was purified by distillation under reduced pressure before use. The other reagents, such as KOH, ammonium persulphate (APS), CTAB and concentrated sulfuric acid, all were locally commercially available and of analytical grade, were used without further purification. All solution was prepared with distilled water.

### **5.2.2 Preparation of porous N-doped carbon nanowires (PCNW)**

PNCW samples were obtained by KOH activation method. Different amounts of KOH were directly mixed with CNW (prepared in chapter 4) in an agate mortar. KOH and CNW mixtures with mass ratios of 1/1, 2/1 and 3/1 were used, and the activation resulting products were denoted PCNW1, PCNW2 and PCNW3, respectively. After mixing, the samples were carried out at 800 °C for 1 h under N<sub>2</sub> atmosphere with a heating rate of 10 °C min<sup>-1</sup>, followed by washing with HCl and deionized water until the pH of the filtrate was 7.0 and drying at 80 °C for 12 h.

### **5.2.3 Thermal, morphological, structural, and component characterizations**

Thermal Gravimetric Analyzer (TGA, DTA-60, shimadzu Co., Ltd., Kyoto, Japan) was carried out in the experimental temperature range at a ramp setting of 10 °C min<sup>-1</sup> from room temperature to 800 °C, and then retained 800 °C for 1 h (as shown in Fig. 5.1) in flowing nitrogen. The morphology of samples was observed by scanning electron microscopy (SEM, s-4300, Hitachi Co., Ltd. Tokyo, Japan) and transmission electron microscopy (TEM, h-8110, Hitachi Co., Ltd. Tokyo, Japan). The crystallographic structure of the samples was observed by a power X-ray diffraction

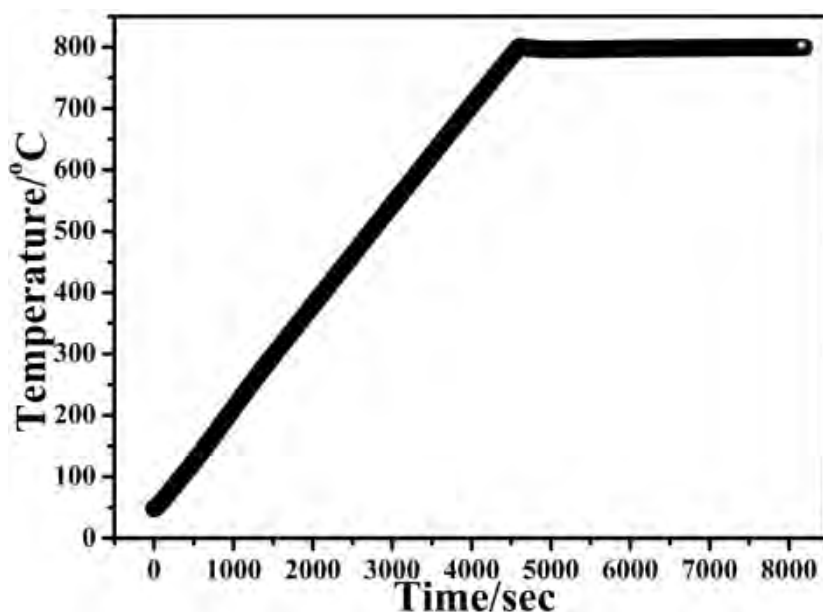


Fig. 5.1 The relationship between activation temperature and time at TGA tests.

system (XRD, XRD-6000, Shimadzu Co., Ltd. Kyoto, Japan) equipped with Cu K $\alpha$  radiation. The porosity of carbons was proved using nitrogen adsorption-desorption isotherms which were performed using an ASAP 2020 apparatus (Micromeritics, USA) at -196 °C. All samples were outgassed under vacuum at 80 °C overnight prior to measurement. The specific surface area was calculated according to the Brunauer-Emmett-Teller (BET) equation, and the pore size distribution was derived from the adsorption branches of the isotherms. X-ray photoelectron spectroscopy (XPS) analysis was performed on PHI Quantum 5000 equipped with an Al K $\alpha$  radiation source.

#### 5.2.4 Electrochemical tests

The electrochemical tests were measured with an electrochemical workstation (CHI 660D, Shanghai Chenhua, China) in the three or two-electrode system in 1 M H<sub>2</sub>SO<sub>4</sub> electrolyte. For three-electrode system, saturated calomel electrode and platinum foil were used as reference and counter electrode, respectively. The working electrode was prepared by mixing the samples, polytetrafluoroethylene (PTFE, the mass ratio of the sample and PTFE is 95:5), and ethanol, and grinding adequately to obtained a paste

[23]. Then the paste was coated onto the stainless mesh (300 mesh), which was followed by drying under vacuum at 80 °C for 24 h and then compressed at 10 MPa for 5 min (the density of electrode is 1.86 g cm<sup>-3</sup>). Cyclic voltammetry (CV) and galvanostatic charge/discharge (GCD) were conducted in a potential window from -0.4 to 0.6 V. Electrochemical impedance spectroscopy (EIS) were carried out in the frequency range from 10<sup>5</sup> to 10<sup>-2</sup> Hz at open circuit potential with as ac perturbation of 5 mV. The symmetric two-electrode system was assembled with two almost identical working electrodes (the active material was PCNW2 sample). The CV and GCD tests were run at different voltage windows.

## 5.3 Result and discussion

### 5.3.1 Thermal analysis of activation process

In order to evaluate the activation process of CNW, the mass loss (TG) and different thermal analysis (DTA) curves of both KOH treated CNW were measured, as shown in Fig. 5.2. From Fig. 5.2a, c and e (the TG/DTA curves of activation process at from the room temperature to 800 °C), it is obvious that the activation process is carried out in four stages: in the first stage, an evident mass loss in TG and a sharp peak in DTA involve the dehydration of CNW and KOH in the range of room temperature to 150 °C; in the second stage, a meaningful mass loss takes place at 150-300 °C; in the third stage, no significant mass loss is observed at 300-700 °C; in the final stage, the important mass loss turns out above 700 °C. Some researchers have proposed that the phenomenon in the second stage attributes to the degradation of KOH and the degradation process shown in Eq. 5.1 [24, 35]. In the third stage, the small mass loss is assigned to the depletion of carbon by the reaction of carbon and H<sub>2</sub>O with the release of H<sub>2</sub> (Eq. 5.2, 5.3) [24, 26]. In addition, K<sub>2</sub>CO<sub>3</sub> forms from the reaction of CO<sub>2</sub> and K<sub>2</sub>O (Eq. 5.4) [27]. In the final stage, the activation temperature above 700 °C, the K<sub>2</sub>CO<sub>3</sub> (formed in Eq. 5.4) is decomposed into CO<sub>2</sub> and K<sub>2</sub>O (Eq. 5.5), and disappears at 800 °C. The production of CO<sub>2</sub> from Eq. 5.5 can be contributed

to further porosity development by carbon gasification (Eq. 5.6) [28]. Moreover,  $K_2O$  and  $K_2CO_3$  can be further reduced by carbon to bring metallic K at around 800 °C (Eq. 5.7, 5.8), and the metallic K will be inserted in the graphitic layers [24, 27]. In summary, KOH activates carbon through three aspects: firstly, the formation of  $H_2O$  and  $CO_2$  can contribute to porosity development by carbon gasification; then, the formation of  $K_2O$  and  $K_2CO_3$  can etch the carbon framework by redox reactions, which is beneficial to form the pore structure; finally, the formation of metallic K is an important factor for developing the pore structure by inserting into the graphitic layers.

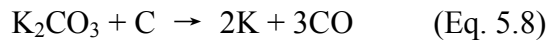
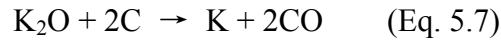
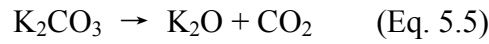
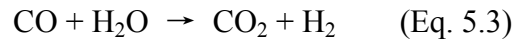
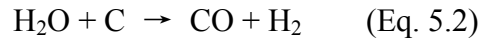
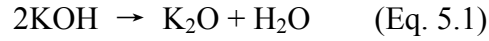


Fig. 5.2b, d and f show the TG/DTA curves of activation process when the temperature remain 800 °C for 1 h. We can find that, the mass loss still exists at the temperature of 800 °C. It is evident that the activation reaction is still continuing. Furthermore, after a comparison of Fig. 5.2b, d and f, it can be noticed that, the DTG curves of Fig. 5.2d and f have a weak peak at 300-1100 s. This may be owing to that excessive  $K_2O$  and  $K_2CO_3$  (for Fig. 5.2d and f, the mass ratio of KOH and CNW is 2 and 3, respectively) are still etching carbon framework and will contribute to pore structure again. However, in Fig. 5.2b, the DTA curve does not have this peak. This is due to the fact that no excessive potassium compounds (for Fig. 5.2b, the mass ratio of KOH and CNW is 1) reacts with carbon. This phenomenon will have a profound impact on specific surface area and electrochemical performance of PCNW.

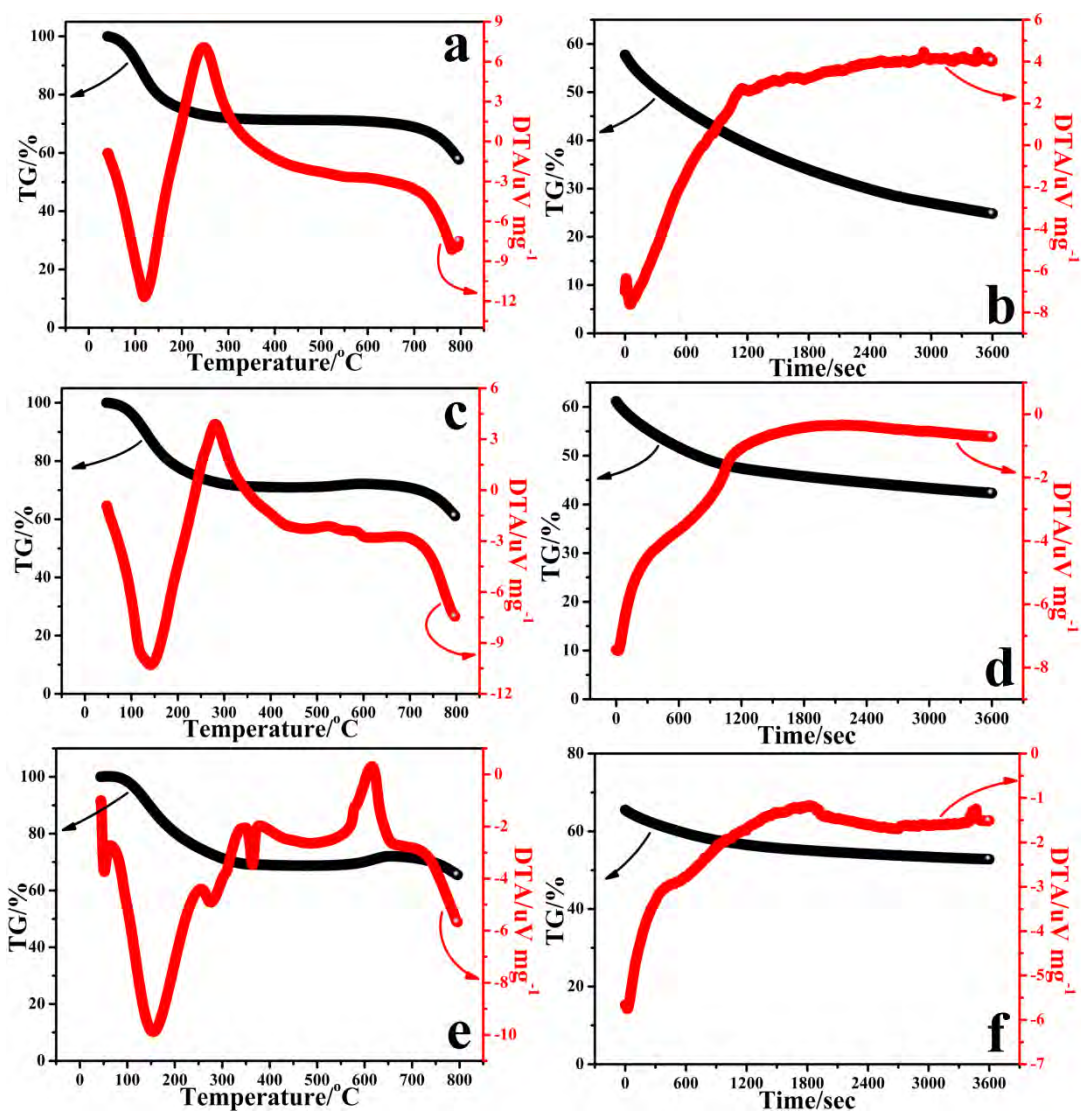


Fig. 5.2 TG and DTA curves of the mass ratio of KOH/CNW is 1 (a, b), 2 (c, d) and 3 (e, f) at temperature rising and keeping the temperature process, respectively.

### 5.3.2. Microstructural characterization

SEM and TEM were used to examine the morphology of as-prepared PPy and PCNW. As shown in Fig. 5.3a, the PPy displays nanowires structure when introducing CTAB at polymerization process of pyrrole molecule. After the carbonization and activation of PPy, the nanowires structure was destroyed and many fragments were observed. Moreover, with the increases of the mass of KOH, the fragment structure gradually became the governing structure. As shown in Fig. 5.3b (PCNW1) and c (PCNW2), the fragments and nanowires structure exist at the same

time. It is found in Fig. 5.3d (PCNW3) that entire fragments structure appears when the mass ratio of KOH and CNW is 3. These fragments structure may be beneficial for the specific surface area of PCNW sample. In TEM images (Fig. 5.4), we also find many fragments structure in PCNW samples. In addition, the partially enlarged views (in Fig. 5.4b, c and d) of TEM images reveal the amorphous porous structure. This porous structure will play a positive role on electrochemical performance of PCNW sample, and will further be characterized by porous size distribution.

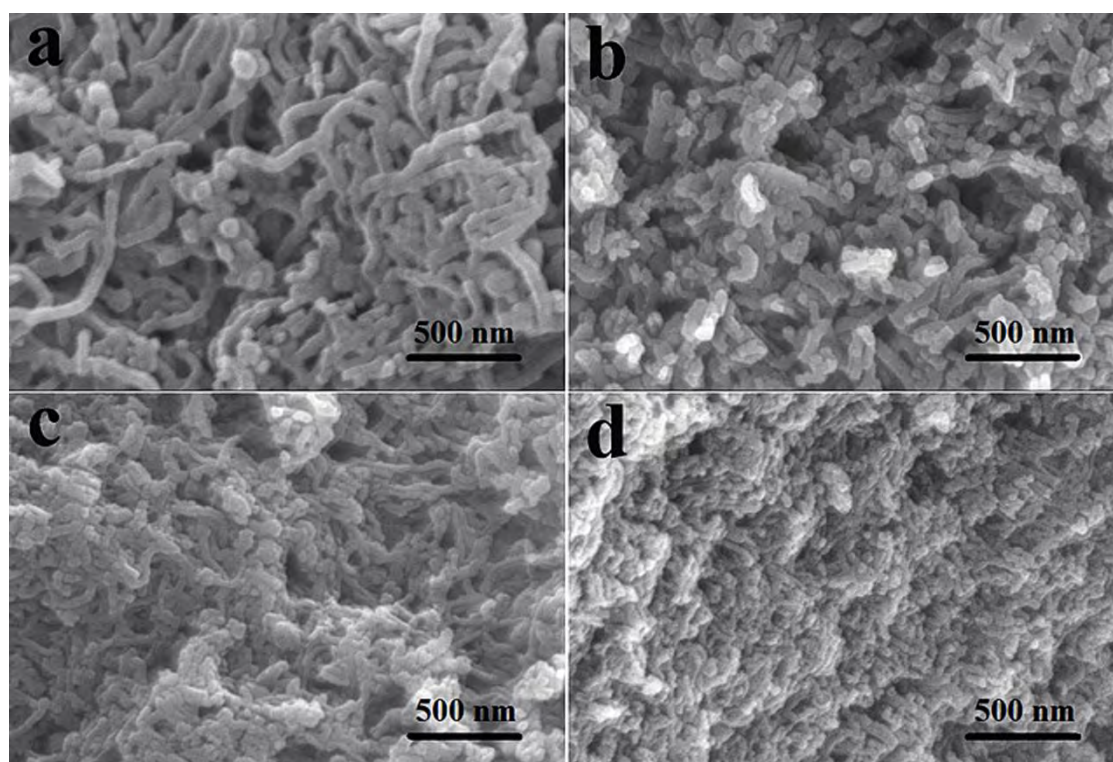


Fig. 5.3 SEM image of CNW (a), PCNW1 (b), PCNW2 (c) and PCNW3 (d).

The XRD patterns of PPy nanowires, CNW and PCNW samples are shown in Fig. 5.5. About PPy nanowires, a broad peak at  $25^{\circ}$  reveals that PPy is amorphous. After carbonization process (CNW), the peak moves to  $24.1^{\circ}$ , resulted from the (002) plane of graphite [29]. Additionally, a weak peak at  $42.7^{\circ}$  corresponding to graphite (101) plane is observed [30]. Compared with CNW, the intensities of (002) and (101) plane peaks increase and the peak positions have a slight shift after activation process. These results are attributed to that the graphitization degree of PCNW samples is

enhanced at the activation temperature of 800 °C.

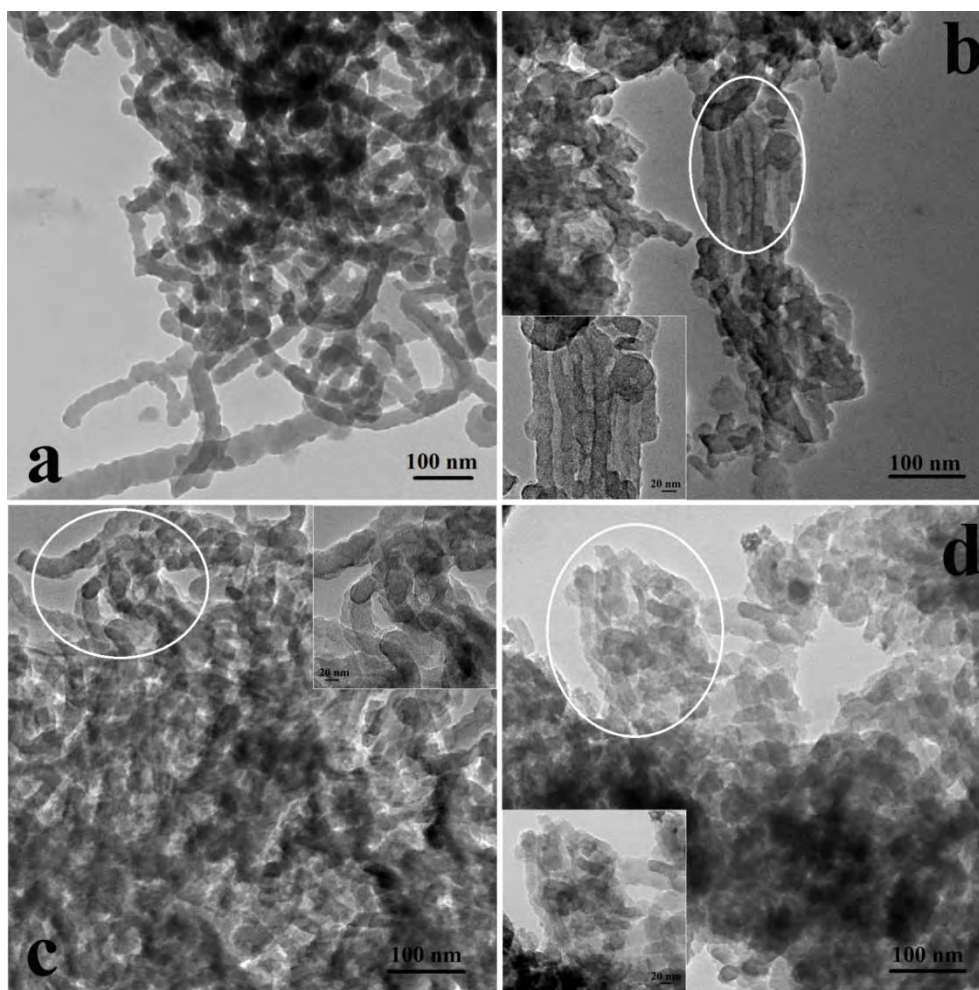


Fig. 5.4 TEM image of CNW (a), PCNW1 (b), PCNW2 (c) and PCNW3 (d).

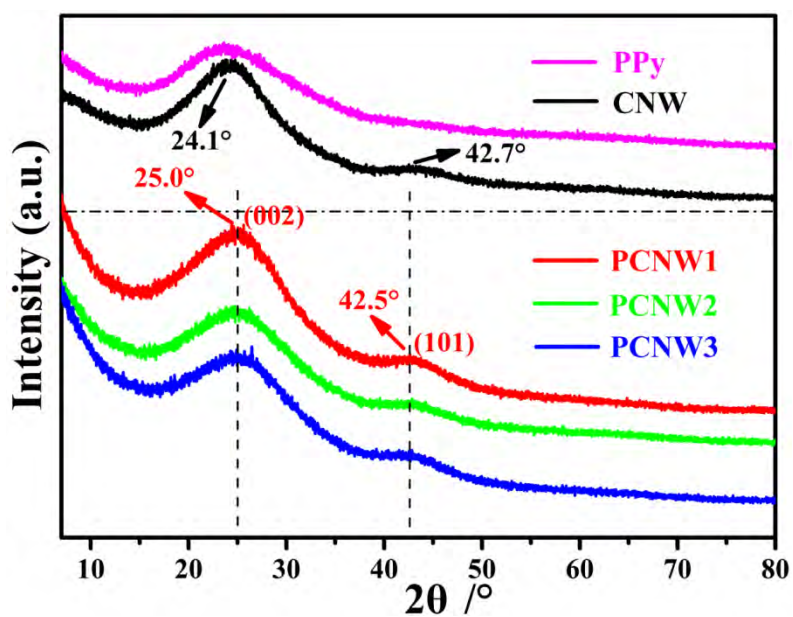


Fig. 5.5 XRD patterns of PPy, CNW, PCNW1, PCNW2 and PCNW3.

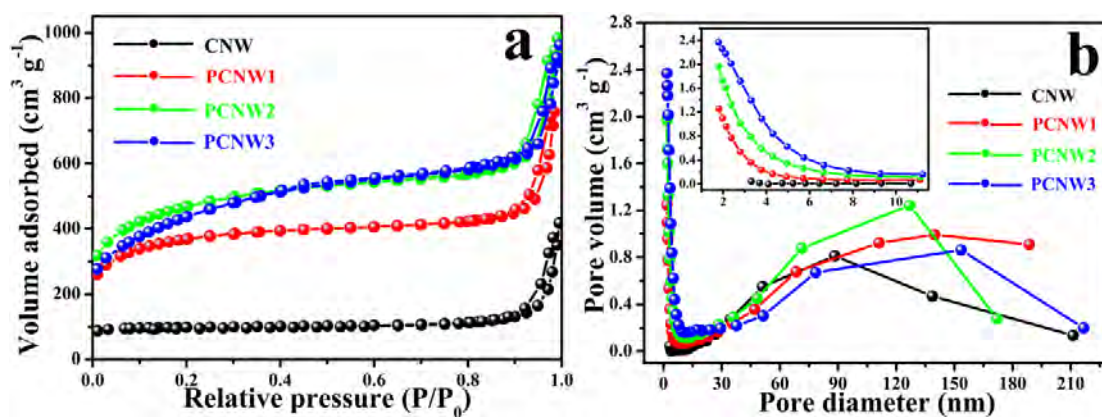


Fig. 5.6 (a) is  $N_2$  adsorption-desorption isotherms, (b) is pore size distribution of CNW, PCNW1, PCNW2 and PCNW3.

In order to investigate the pore properties of CNW samples after KOH activation, the nitrogen adsorption-desorption isotherms of CNW and PCNW were performed, and the results were shown in Fig. 5.6a. It is clear that the CNW shows the type-II sorption isotherm, suggesting the non-porous structure [6], while, the PCNW samples display type-I sorption isotherms and possess a much higher nitrogen sorption capacity, indicating the polyporous structure [17]. With the increase of the mass ratio of KOH and CNW, the remarkably increased pore volume and microporous volume ratio (shown in Table 5.1) reveal a more developed porous structure of PCNW samples. Moreover, H3 hysteresis loops are observed at  $0.9 < P/P_0 < 1$  in all samples, reflecting the existence of stacking porous structure by carbon nanowires. It should be noted that, as shown in Table 5.1, the specific surface area of PCNW increases from 1284 to 1656  $m^2 g^{-1}$  with the increase of KOH/CNW mass ratio from 1 to 2, but decreases to 1568  $m^2 g^{-1}$  when KOH/CNW mass ratio is 3, while, the microporous area ratio continuously decreases with the increase of KOH/CNW mass ratio. This may be due to the more developed microporous structure formed with the increase of KOH/CNW mass ratio from 1 to 2, but some micropores were gradually transformed into mesoporous when KOH/CNW mass ratio was 3. Fig. 5.6b shows the pore size distribution curves recorded from the adsorption process of the isotherms. It obviously proves the trimodal distribution pore structures of PCNW samples, the prolific microporous by KOH activation, a little mesoporous by KOH activation or carbon

nanowires stack, and some macroporous by carbon nanowires stack. Compared with PCNW, CNW sample just contains mesoporous and macroporous by carbon nanowires stack, and macropores make a great contribution to the pore volume and specific surface area. However, the contribution gradually decreases with the increase of KOH/CNW mass ratio, and this is owing to the fact that the carbon nanowires structure is destroyed (as shown in Fig. 5.3 and 5.4) by KOH.

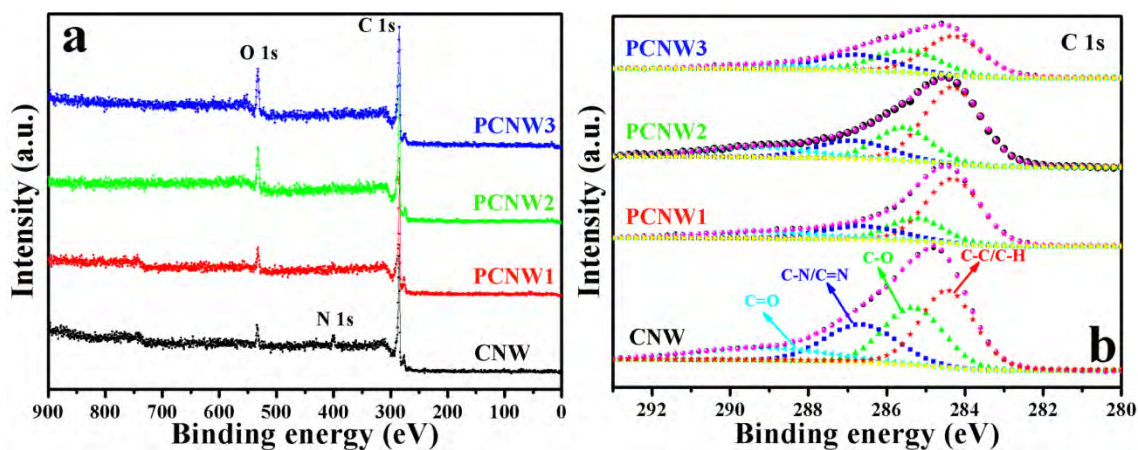


Fig. 5.7 (a) XPS survey spectra of CNW, PCNW1, PCNW2 and PCNW3; (b) high resolution C 1s XPS spectra of CNW, PCNW1, PCNW2 and PCNW3.

The KOH activation can also affect the nitrogen content and the nitrogen chemical state in PCNW samples. XPS analysis was employed on the CNW and PCNW, and the results are shown in Fig. 5.7a. As shown in table 5.2, the nitrogen content decreases with the increase of KOH/CNW mass ratio in the activation process. The nitrogen content of CNW, PCNW1, 2 and 3 are 5.59, 2.54, 2.41 and 0.84 at. %, respectively. This suggests that it is difficult to obtain carbon materials with high porosity and high nitrogen content in the meantime. This is due to the fact that the nitrogen-containing functional groups are oxidized at the activation process [6, 31]. To further understand the chemical state of nitrogen in samples, we analyzed the high-resolution C 1s and N 1s peaks in details. The C 1s spectra of CNW and PCNW in Fig. 5.7b can be further deconvoluted into four different peaks, at 284.5, 285.4, 286.6 and 289.4 eV, corresponding to C-C/C-H, C-O, C-N/C=N and C=O, respectively [32, 33].

Table 5.1 Pore properties and specific capacitances of CNW and PCNW samples

Sample	Pore volume (cm <sup>3</sup> g <sup>-1</sup> )					S <sub>BET</sub> (m <sup>2</sup> g <sup>-1</sup> )					D <sub>Micro</sub> <sup>b</sup> (nm)	Specific capacitance (F g <sup>-1</sup> )		
	Total	Micro	Meso	Macro	Ratio <sup>a1</sup>	Total	Micro	Meso	Macro	Ratio <sup>a2</sup>		1 A g <sup>-1</sup>	3 A g <sup>-1</sup>	5 A g <sup>-1</sup>
CNW	0.52	--	0.16	0.36	--	406	--	223	183	--	--	206	177	160
PCNW1	0.76	0.33	0.15	0.28	43.7	1298	1053	200	45	81.1	1.70	220	130	70
PCNW2	1.08	0.56	0.31	0.21	52.2	1642	1277	334	31	77.8	1.71	291	230	190
PCNW3	1.13	0.63	0.38	0.12	55.6	1568	1179	381	8	75.2	1.70	180	110	63

<sup>a1</sup> the micropore volume to total pore volume ratio, <sup>a2</sup> the micropore area to total pore area;

<sup>b</sup> micropore width at the pore volume maximum.

Table 5.2 XPS analysis of the CNW and PCNW samples

Sample	C/at. %	N/at. %	O/at. %	N/C	O/C	O-1	O-2	O-3
						531.7 ± 0.2	533.5 ± 0.2	534.9 ± 0.2
CNW	88.69	5.59	5.72	0.063	0.064	15	49	36
PCNW1	91.09	2.54	6.38	0.028	0.070	47	35	18
PCNW2	91.08	2.41	6.51	0.026	0.071	43	36	21
PCNW3	87.19	0.84	11.97	0.010	0.137	41	33	26

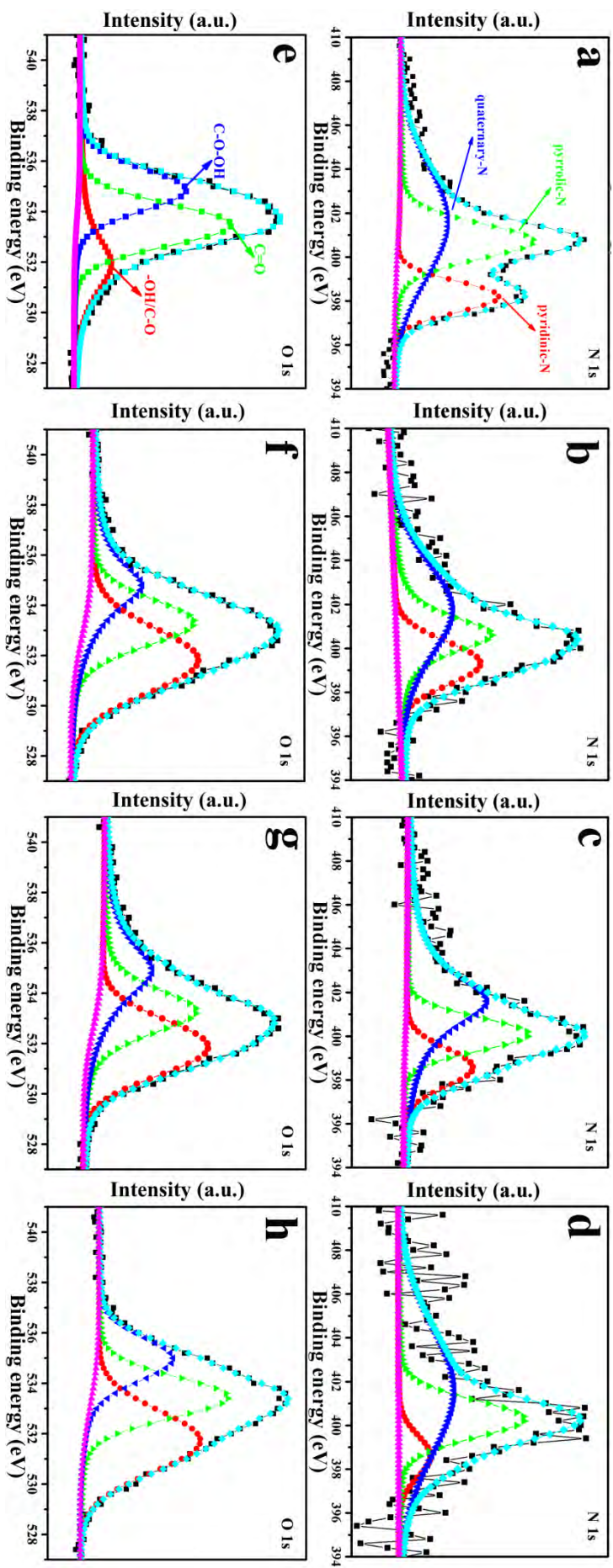


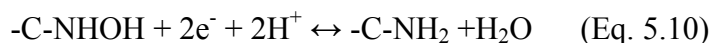
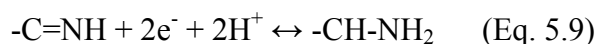
Fig. 5.8 High resolution N 1s and O 1s XPS spectrum of CNW (a, e), PCNW1 (b, f), PCNW2 (c, g) and PCNW3 (d, h).

Obviously, the intensity of the four peaks affected by the KOH/CNW mass ratio, and the intensity of C-N/C=N peak in PCNW samples are weaker than that of CNW. This phenomenon is attributed to the fact that the nitrogen content decreases in the KOH activation process. Fig. 5.8a, b, c and d shows the deconvolution of the high-resolution N 1s peaks of CNW, PCNW1, 2 and 3, respectively. The deconvolution of the N 1s spectra yields three peaks: 398.4 eV, pyridinic nitrogen; 400.6 eV, pyrrolic nitrogen; and 401.6 eV, quaternary nitrogen [34, 35]. The highest energy contribution of all samples at 400.6 eV is attributed to pyrrolic nitrogen, whereas the energy contribution of pyridinic nitrogen (at 398.4 eV) gradually decreases with the increase of KOH/CNW mass ratio, until turns into the lowest energy contribution peak (as shown in Fig. 5.8d). This is may be due to the fact that the pyridinic nitrogen can be more easily oxidized than the other types of nitrogen in activation process. In addition, the resolution spectra of O 1s can also be fitted into three peaks and the results are shown in Fig. 5.8e-h. In detail, they are oxygen in –OH/C-O (O-1,  $531.7 \pm 0.2$  eV), oxygen in C=O (O-2,  $533.5 \pm 0.2$  eV), and oxygen in C-O-OH (O-3,  $534.9 \pm 0.2$  eV) [36]. These results indicate that the surface of PCNW has some lactone, carboxyl and quinone groups [37]. The content of the three types of oxygen atoms are listed in table 5.2. It is easy to find that after CNW is activated, the content of O-3 significantly decrease and O-1 significantly increase. These oxygen containing functional groups will have an interesting impact on the capacitive performance of PCNW.

In short, a series of nitrogen doped porous carbon nanowires with high specific surface area and temperate content of nitrogen doped into carbon framework are prepared by KOH activated of a nonporous nitrogen-enriched carbon nanowires. Owing to the unique features, the nitrogen-doped porous carbon nanowires are expected to possess the superior electrochemical capacitive performance as the electrode material for supercapacitors.

### 5.3.3 Electrochemical performance

The electrochemical performances of the CNW and PCNW samples were detected by the techniques of CV, GCD and EIS in the 1 M H<sub>2</sub>SO<sub>4</sub> aqueous solution. Fig. 5.9 illustrates CV curves of the CNW and PCNW at a scan rate of 0.01 V s<sup>-1</sup>. CNW exhibits a typical capacitive behavior with a quasi-rectangular shape, indicating its ideal capacitance behavior [38]. Furthermore, a pair of weak and broad peaks can be observed at a voltage range of 0-0.4 V, indicating that the capacitance results from the combination of EDLC and pseudocapacitance corresponds to redox reaction (as shown in Eq. 5.9 and 5.10 of the nitrogen content in samples [34, 12]).



Compared with CNW, PCNW exhibits a special leaf-shaped of CV curve, which is attributed to the porous structure of PCNW. Especially, on the CV curve of PCNW2, a pair of more obvious peaks is found, which is owing to the fact that the highest specific surface area of PCNW2 improves the contact area between PCNW2 and electrolyte, though the nitrogen content of PCNW2 is less than that of CNW. Furthermore, the oxygen containing groups on the surface of PCNW also contribute to the overall capacitance through pseudocapacitance [39]. For example, quinone groups bring pseudocapacitance through redox reaction; lactone groups introduce electron-acceptor property in the carbon surface. However, these contributions stemming from quinone and lactone groups will be impaired by the carboxyl groups by its hindering and retarding the electrolyte contact the carbon surface [37]. From table 5.2, the content of O-3 significantly decreases, which will benefit for the capacitive performance of PCNW. Finally, the area enclosed by the CV curves of PCNW, which is proportional to the capacitance [40, 41], increases first and then decrease with the increase of the KOH/CNW mass ratio. These results indicate that PCNW2 sample possesses an excellent electrochemical capacitive performance.

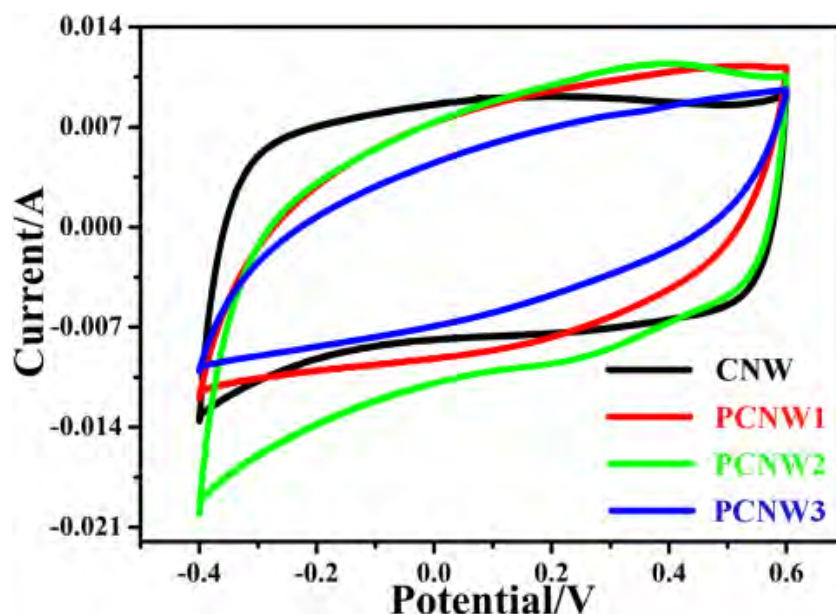


Fig. 5.9 CV curves of CNW, PCNW1, PCNW2 and PCNW3.

The electrochemical performance of as-prepared samples was further analyzed by the GCD method and the results are shown in Fig. 5.10. The discharge time of PCNW2 is markedly longer than those of other samples, suggesting that the PCNW2 possesses further more excellent electrochemical capacitive performance than the other samples. We can get the specific capacitance by these curves [42]. From Eq. 2.2, the specific capacitances of CNW, PCNW1, 2 and 3 are 206, 220, 291 and 180  $\text{F g}^{-1}$ , respectively, at a current density is  $1 \text{ A g}^{-1}$ , and the specific capacitance of PCNW increases first and then decreases with the increase of the KOH/CNW mass ratio. These results are in accordance with those deduced from CV curves. Furthermore, more interesting is that in the PCNW samples, it appears a sudden potential drop (IR drop), and the IR drop increases with the increase of KOH/CNW mass ratio. This can be attributed to the resistance of electrolyte and the inner resistance of ion diffusion in micropores [43, 44].

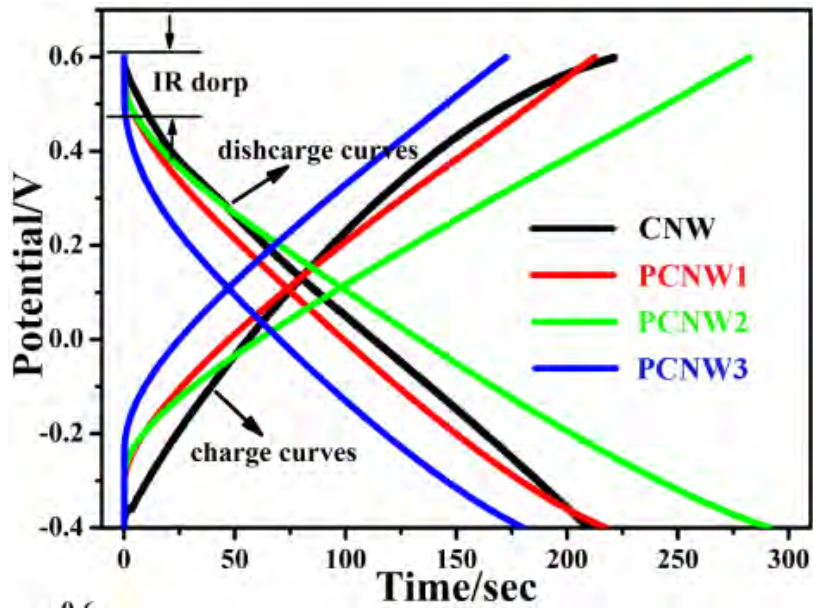


Fig. 5.10 GCD curves of CNW, PCNW1, PCNW2 and PCNW3

To further study the capacitive behavior samples, EIS was used to measure the charge transport and ion diffusion. The Nyquist plots of the samples are demonstrated in Fig. 5.11a. Except for CNW, the other samples present similar shapes, and are composed of three parts: a semi-circular line in the high frequency region, corresponding to charge transfer resistance; a nearly  $45^\circ$  diagonal line in the medium frequency region, corresponding to diffusion resistance; a nearly vertical line in the low frequency region, corresponding to capacitive behavior [45]. We can find that PCNW1 and PCNW3 exhibit high charge transfer resistance due to the fact that they have large diameter of semi-circular at the high frequency region. For CNW, the Nyquist plot does not show semicircle regions, probably due to its low faradaic resistance [46]. Moreover, the equivalent series resistance (ESC) of the sample can be obtained from the x intercept on the Nyquist plot, corresponding to the conductivity of both material and electrolyte [47]. Fig. 5.11a inset shows that the ESC of CNW, PCNW1, 2 and 3 are 1.43, 1.25, 1.06 and 1.42  $\Omega$ , respectively, which indicates that the KOH activation benefits for the decrease of the ESC, and the ESC of PCNW decreases with the increase of KOH/CNW mass ratio. At the same time, the equivalent circuit for Nyquist plots of PCNW2 is shown as the inset in Fig. 5.11a. The EIS data are fitted by the internal resistance ( $R_s$ ), the charge transfer resistance ( $R_{ct}$ ),

the diffusion resistance ( $Z_w$ ), the electrochemical double layer capacitance ( $C_{dl}$ ), and the  $C_L$  to attribute to the limited pseudocapacitance [48, 49]. The Nyquist plots and fitting estimations (as shown in table 5.3) reveal obviously lowest  $R_s$  and  $R_{ct}$  values for PCNW2, indicating that KOH activation could effectively facilitate ion transfer, compared to the CNW.

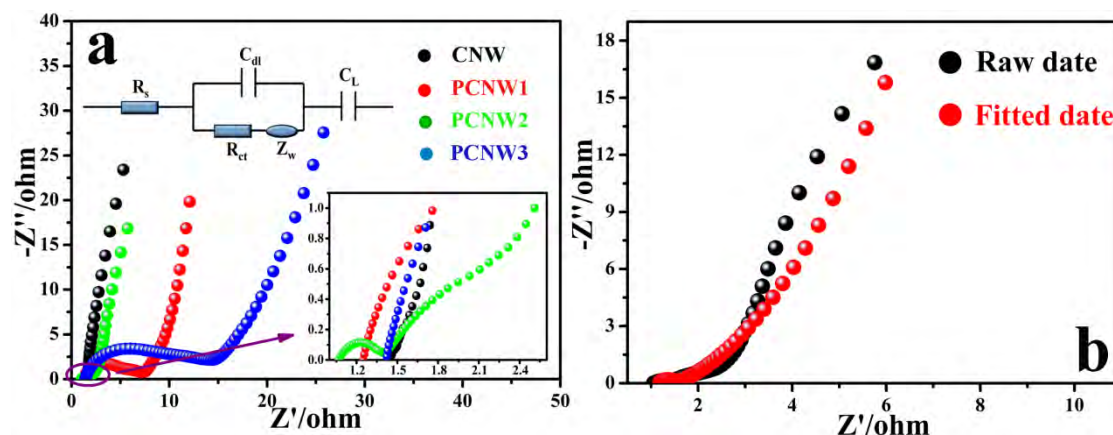


Fig. 5.11 (a) EIS curves of CNW, PCNW1, PCNW2 and PCNW3; (b) the Nyquist plots of PCNW2 for raw and fitted data.

Table 5.3 Equivalent circuit parameters fitted from Nyquist plots for PCNW1, 2 and 3.

Sample	$R_s$ (ohm $\text{cm}^2$ )	$R_{ct}$ (ohm $\text{cm}^2$ )	$Z_w$ ( $\text{Ss}^{-0.5} \text{cm}^{-2}$ )
PCNW1	1.37	4.603	0.3236
PCNW2	1.19	0.338	0.5224
PCNW3	1.55	9.135	0.1386

Fig. 5.12a shows the CV curves of PCNW2 at different scan rates (0.01-0.1  $\text{V s}^{-1}$ ). With the increase of the scan rate, the response current of PCNW2 increases clearly, suggesting its good rate ability. Need to pay attention to is that the pair of peaks attributed to pseudocapacitance disappears at the scan rate of 0.05  $\text{V s}^{-1}$  (as shown the inset of Fig. 5.12a), which is due to the fact that there is not enough time for redox reaction, and the specific capacitance of PCNW2 will decline by the contribution of

pseudocapacitance decrease. Fig. 5.12b shows the GCD curves of PCNW2 at different current densities (1-10 A g<sup>-1</sup>). Basically, the shapes of the GCD curves are closely linear and symmetrical, even when the current density reaches to 10 A g<sup>-1</sup>. The GCD curve still remains the nearly linear-like shape, indicating an excellent capacitive performance. Compared with PCNW2, the GCD curves of PCNW1 and 3 at current densities of from 1 to 5 A g<sup>-1</sup> (as shown in Fig. 5.12c and d) are far from the linear and symmetrical shape, and exhibit the large IR drop with the increase of current density, suggesting that PCNW1 and 3 lose the fast charge-discharge performance.

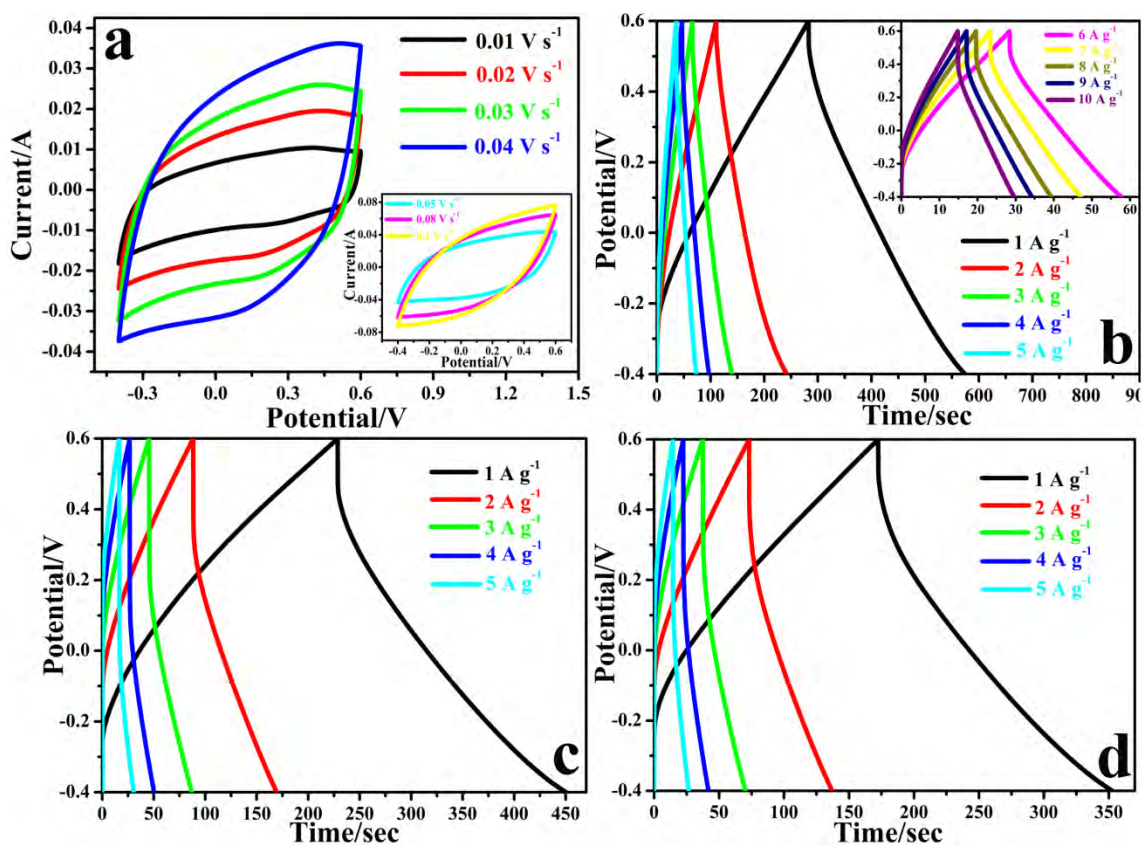


Fig. 5.12 CV (a) and GCD (b) curves of PCNW2 at different scan rate and current density; GCD curves of PCNW1 (c) and PCNW3 (d) at different current densities.

Fig. 5.13 shows the specific capacitance as a function of current density for all samples. It is clear that the specific capacitance of all samples decreases with the increase of current density. However, PCNW1 and 3 almost linearly decrease, which further evidences the conclusions from Fig. 5.12b. Some studies have shown that,

there are four conditions if porous carbon materials exhibit excellent capacitive performance [50-53]: (1) some macroporous cores can serve as ion buffering reservoirs; (2) a certain number of mesoporous walls guarantee a smaller ion transfer resistance; (3) prolific micropores accommodate charge; (4) localized graphitic structure enhance the electrical conductivity. The fast charge-discharge performance is mainly depended on the abundant macropores [53], and IR drop is closely related to the inner resistance of ion diffusion in micropores and the electrical conductivity of materials [43]. However, with the increase of KOH/CNW mass ratio, though the specific surface area of PCNW significantly increases, the macroporous volume and area both decrease (as shown in table 5.1). This means the collapse of macropores; also, the graphitic structure of CNW is possibly damaged by the KOH activation. Therefore, with the increase of KOH/CNW mass ratio, PCNW samples gradually lose the fast charge-discharge performance, and exhibit obvious IR drop.

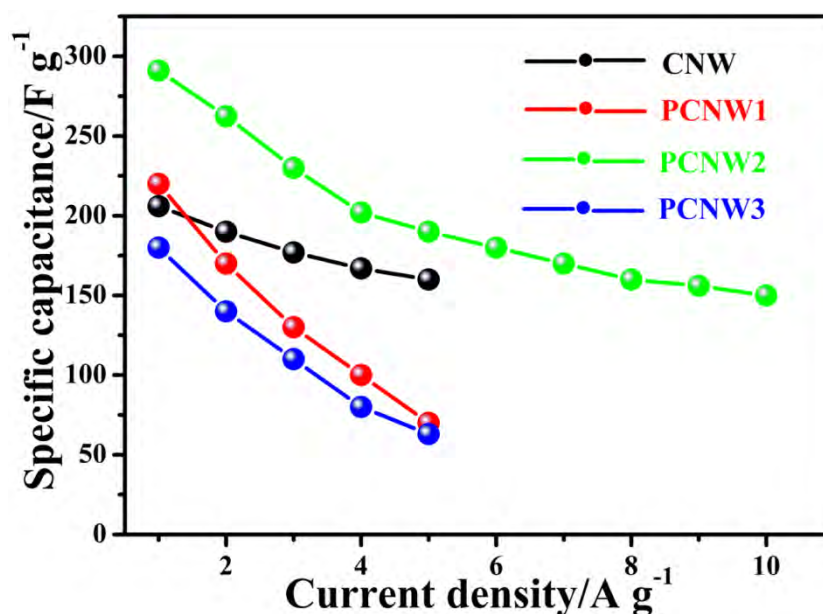


Fig. 5.13 Specific capacitance versus current density of CNW, PCNW1, PCNW2 and PCNW3.

Fig. 5.14a shows that the cycling performance of PCNW2 is dependent on the current density. During the first 100 cycles with a GCD current density of 1 A g<sup>-1</sup>, the specific capacitance is stabilized at 290 F g<sup>-1</sup>. In the following 500 cycles, although the current density continues to increase, PCNW2 always shows a stable specific capacitance. When the current density returns to 1 A g<sup>-1</sup>, the specific capacitance (285

$\text{F g}^{-1}$ ) is almost unchanged compared with the first 100 cycles, suggesting that the PCNW2 has an excellent rate capability. Its GCD test was measured at a current density of  $3 \text{ A g}^{-1}$  for 5000 cycles. The result also shows its cycle stability (Fig. 5.14b). The specific capacitance of PCNW2 has a slight decline of about 5.2 % after 5000 cycles, suggesting excellent cycle stability. It is noteworthy that, the pair of peaks on the CV curve disappears after 5000 cycles (as shown the inset of Fig. 5.14b). This means that the pseudocapacitance is contributed to the total specific capacitance decrease, and this is the reason why the specific capacitance decreases after 5000 cycles.

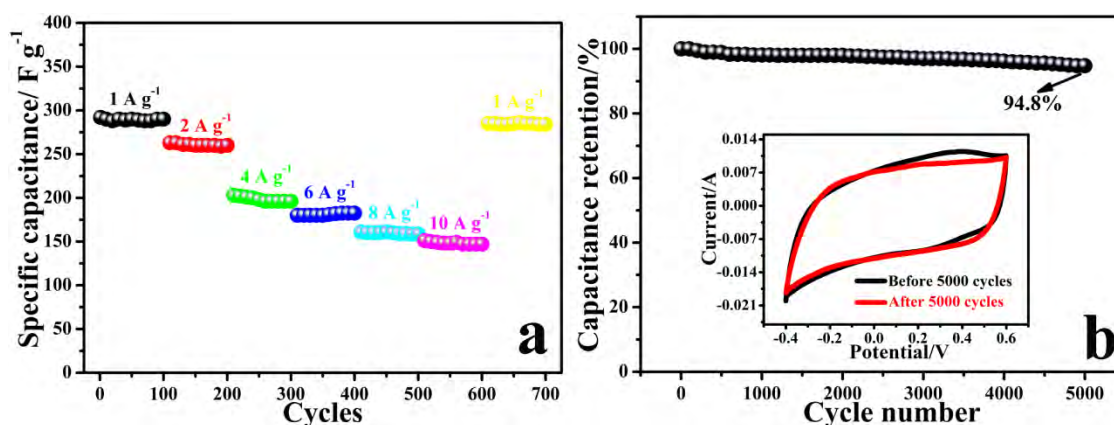


Fig. 5.14 (a) Dependence of cycle stability in the current density of PCNW2; (b) cycle stability of PCNW2 at a current density of  $3 \text{ A g}^{-1}$ .

A two-electrode system is often used to evaluate the applicability potential of supercapacitors materials, because it can show the most exact results. In order to further confirm the excellent capacitive performance of PCNW2 from the three-electrode system, we also carried out the CV and GCD tests in two-electrode systems, and the results are shown in Fig. 5.15. The voltage window is a key factor for two-electrode systems, for it can directly impact the energy density and specific capacitance of supercapacitors [54]. CV and GCD tests were performed in different voltage windows to define the best operating voltage window. As shown in Fig. 5.15a, all CV curves exhibits a quasi-rectangular shape even at the voltage window is 0-1.6

V. These results reflect an ideal capacitive behavior. Furthermore, the current response of CV curves gradually increases with the voltage window increase. This phenomenon means that the specific capacitance of symmetric capacitor gradually increases. The CNW CV curve in the voltage window of 0-1.6 V in two-electrode systems is also shown in Fig. 5.16. Its current response is significantly smaller than that of PCNW2. This result further proves that the capacitive performance of PCNW2 is better than that of CNW. Fig. 5.15b shows the GCD curves of PCNW2 in two-electrode at different voltage windows. All GCD curves show the equilateral triangle shape, which still means the ideal capacitive behavior. We can obtain specific capacitances of different voltage windows by Eq. 2.2 [55]. From Eq. 2.2, the specific capacitances are 42.4, 47.1, 51.9 and 56.1  $\text{F g}^{-1}$  at 0-1.0, 0-1.2, 0-1.4 and 0-1.6 V, respectively. These results also evidence the inference of CV curves.

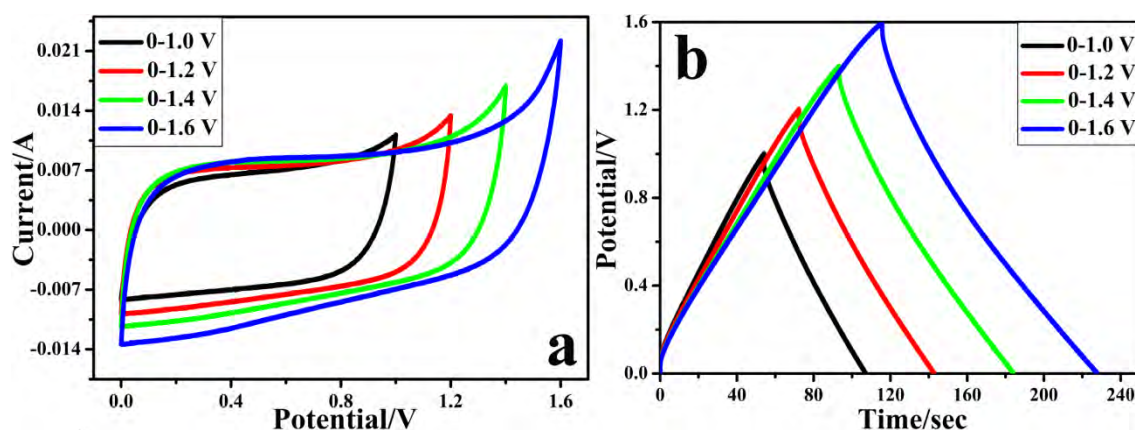


Fig. 5.15 CV (a, scan rate is  $0.01 \text{ V s}^{-1}$ ) and GCD (b, current density is  $0.8 \text{ A g}^{-1}$ ) curves of PCNW2 in two-electrode system at different voltage windows

For supercapacitors with excellent performance, the high power and energy density are expected. The energy density ( $E$ ,  $\text{Wh kg}^{-1}$ ) and power density ( $P$ ,  $\text{W kg}^{-1}$ ) were calculated from the GCD curves according to Eq. 2.3 and 2.4 [56, 57]. The relationship between power and energy density (Ragone plot) of different voltage windows at a series of charge-discharge rates for PCNW2 is shown in Fig. 5.17a. In general, the energy density gradually decreases with the increase of power density; at the same charge-discharge rate, the power and energy density gradually increase with the voltage window increase. The maximum energy density ( $21.9 \text{ Wh kg}^{-1}$ , as shown

in table 5.4) achieved at the current density of  $0.4 \text{ A g}^{-1}$  with a voltage window of 0-1.6 V. At the current density of  $3.2 \text{ A g}^{-1}$  and voltage window of 0-1.6 V, the power density reaches to  $2560 \text{ W kg}^{-1}$ , and the corresponding energy density is  $14.9 \text{ Wh kg}^{-1}$ . Compared with the current density of  $0.4 \text{ A g}^{-1}$ , the energy density retention is 68.0 %.

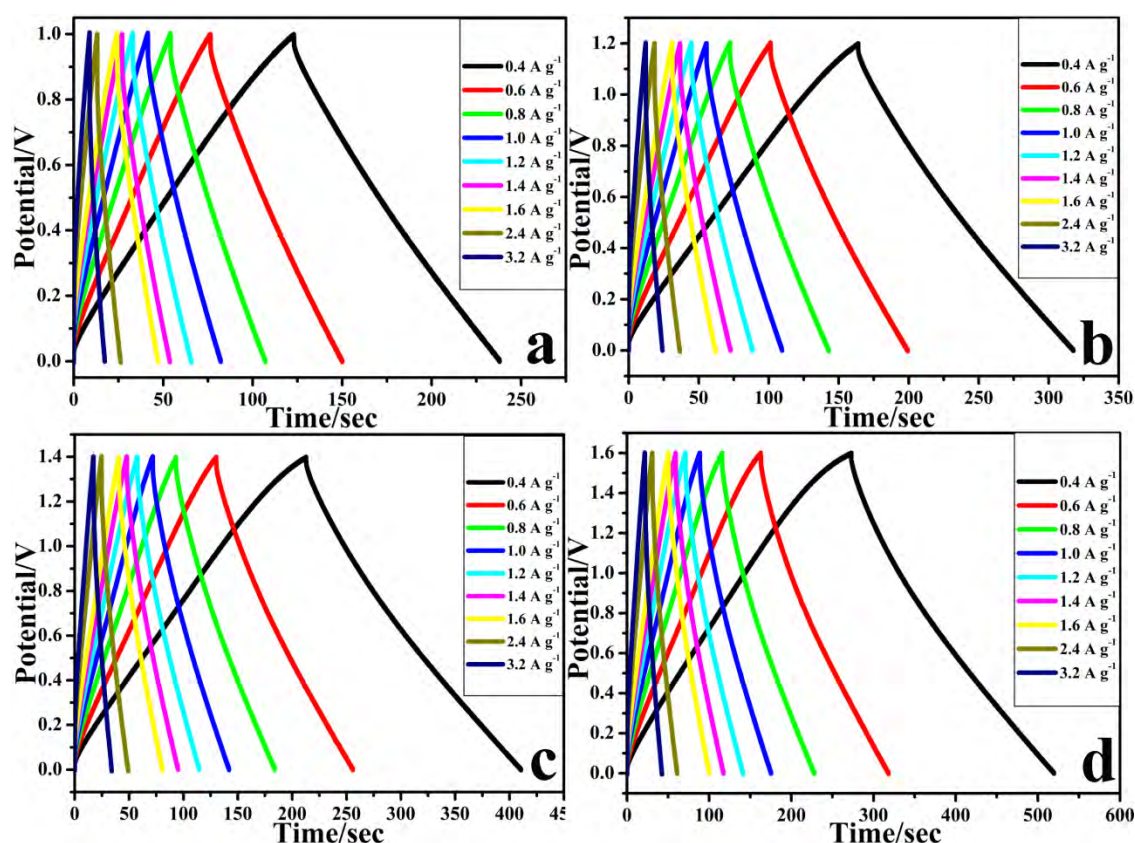


Fig. 5.16 GCD curves of PCNW2 in two-electrode systems at voltage windows of 0-1.0 V (a), 0-1.2 V (b), 0-1.4 V (c) and 0-1.6 V (d).

In the same condition, the energy density retention is 59.4 %, 62.1 % and 67.5 % at voltage windows of 0-1.0 V, 0-1.2 V and 0-1.4 V, respectively (as shown in table 5.4). The energy density retention of 0-1.6 V is higher than those of the other voltage windows, and this further suggests that the voltage window is a key factor for supercapacitors. PCNW2 shows the significant advantage, compared with the previous reports energy density of carbon materials ( $< 10 \text{ Wh kg}^{-1}$ ) [58-61]. In addition, the Ragone plot of CNW in 0-1.6 V was obtained by GCD test at different current densities (as shown in Fig. 5.17c, d, e and f), and the results are shown in Fig.

5.17b. The energy density of CNW is much smaller than that of PCNW2, and the energy density retentions of CNW and PCNW2 are 77.9 % and 81.7 %, respectively. These results further suggest that the capacitive performance of CNW has been greatly improved after KOH activation. To sum up, these above results indicate that the optimal voltage window of PCNW2 samples in two-electrode systems is 0-1.6 V, and this window is very suitable for supercapacitors.

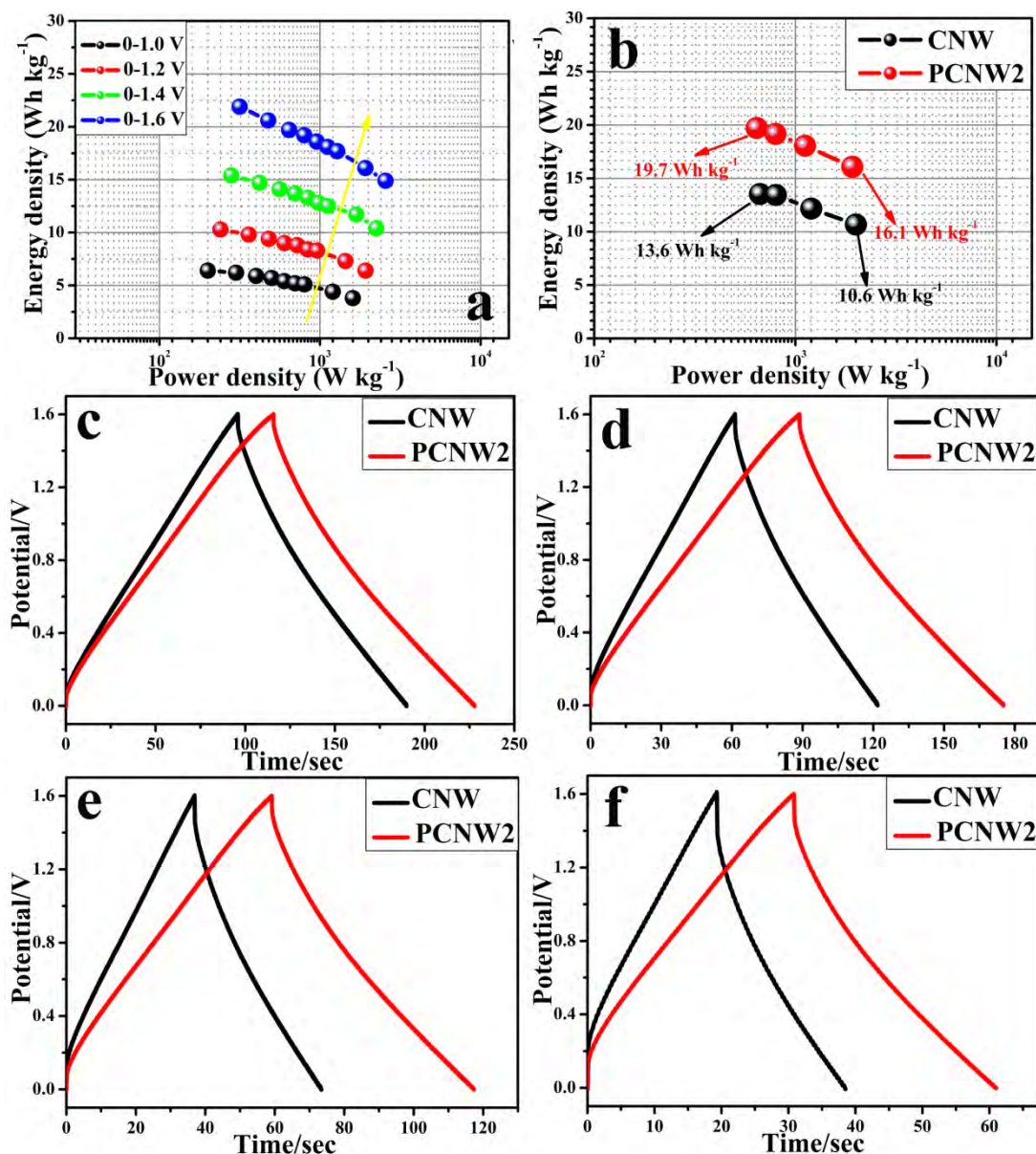


Fig. 5.17 (a) Ragone plot of PCNW2 in two-electrode system at different voltage windows; (b) Ragone plot of CNW and PCNW2 in symmetric two-electrode systems; GCD curves of CNW and PCNW2 in two-electrode systems at current density of 0.8 (c), 1.0 (d), 1.4 (e) and 2.4 (f) A g<sup>-1</sup>.

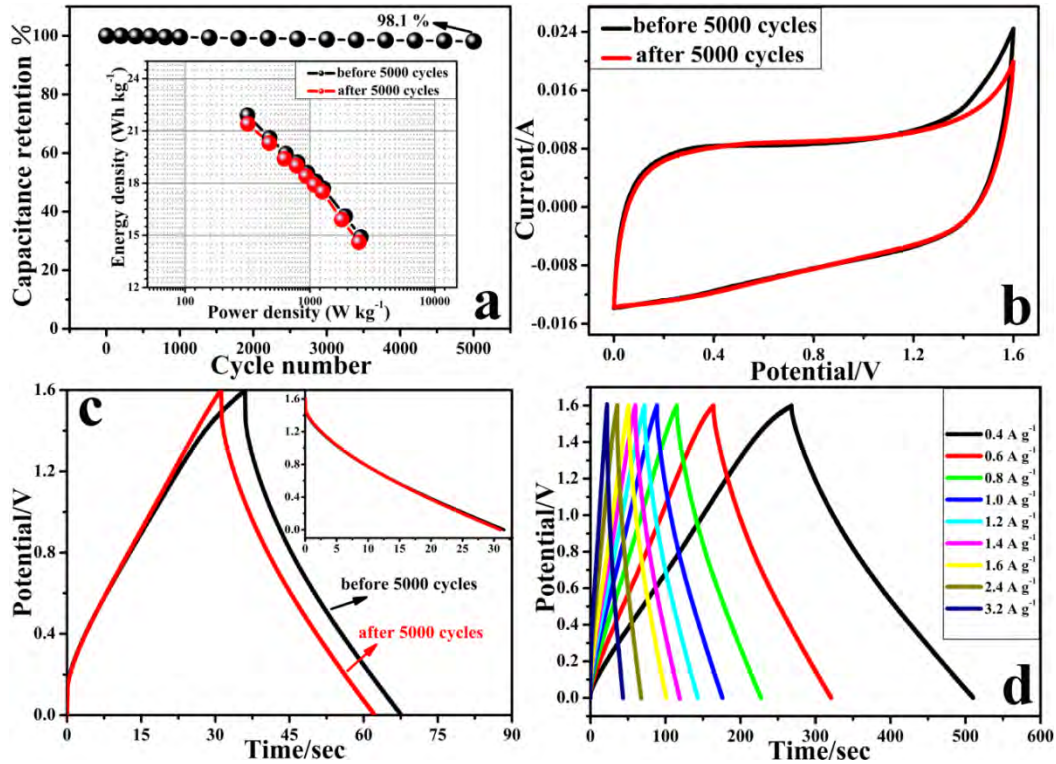


Fig. 5.18 (a) Cycle stability of PCNW2 in two-electrode system at a current density is  $2.4 \text{ A g}^{-1}$ , the inset is a Ragone plot of PCNW2 before and after 5000 cycles; CV (b, scan ratio is  $0.01 \text{ V s}^{-1}$ ) and GCD (c, current density is  $2.4 \text{ A g}^{-1}$ ) curves of PCNW2 in two-electrode systems before and after 5000 cycles; (d) GCD curves of PCNW2 at different current density in two-electrode systems after 5000 cycles.

We also evaluated the cycle stability of PCNW2 in two-electrode systems by repeating the GCD test at the current density of  $2.4 \text{ A g}^{-1}$  in 0-1.6 V and the result is shown in Fig. 5.18a. The specific capacitance of PCNW2 in two-electrode systems shows a 1.9 % variation after 5000 cycles, indicating the excellent cycle stability. We compared Ragone plot of PCNW2 before and after 5000 cycles to further understand the excellent electrochemical stability of the sample, and the results are shown in the inset of Fig. 5.18a. PCNW2 also exhibits a high energy density ( $21.4 \text{ Wh kg}^{-1}$ ) at a current density of  $0.4 \text{ A g}^{-1}$  after 5000 cycles, and compared with before cycle, the energy density retention is 97.7 % (as shown in table 5.5). Even at the current density of  $3.2 \text{ A g}^{-1}$ , the energy density is still as high as  $14.6 \text{ Wh kg}^{-1}$  after 5000 cycles, and the energy density retention is 98.0 % compared with that before cycle. These results further evidence the excellent cycle stability of PCNW2.

Table 5.4 The specific capacitance and energy density of PCNW2 in two-electrode systems

Voltage windows/V	0.4		0.6		0.8		1.0		1.2		1.4		1.6		2.4		3.2		EDR (%) <sup>c</sup>
	C <sup>a</sup>	E <sup>b</sup>	C	E	C	E	C	E	C	E	C	E	C	E	C	E	C	E	
0-1.0	46.0	6.4	44.2	6.2	42.4	5.9	40.7	5.7	39.2	5.4	37.4	5.2	36.5	5.1	31.7	4.4	27.2	3.8	59.4
0-1.2	51.2	10.3	49.0	9.8	47.1	9.4	45.0	9.0	43.9	8.8	42.0	8.4	41.3	8.3	36.2	7.3	32.0	6.4	62.1
0-1.4	56.5	15.4	53.9	14.7	51.9	14.1	50.1	13.7	48.8	13.3	47.1	12.8	45.9	12.5	42.0	11.7	38.4	10.4	67.5
0-1.6	61.7	21.9	58.3	20.6	56.1	19.7	54.1	19.2	52.7	18.6	50.9	18.1	49.7	17.7	45.3	16.1	41.8	14.9	68.0

<sup>a</sup> The specific capacitance (F g<sup>-1</sup>) of PCNW2 sample in two-electrode systems.

<sup>b</sup> The energy density (Wh kg<sup>-1</sup>) of PCNW2 sample in two-electrode systems.

<sup>c</sup> The energy density retention, the energy density at current density of 3.2 A g<sup>-1</sup> divided by that of current density of 0.4 A g<sup>-1</sup>.

Table 5.5 The specific capacitance and energy density of PCNW2 before and after 5000 cycles in two-electrode systems

Current density (A g <sup>-1</sup> )	Before 5000 cycles		After 5000 cycles		EDR (%) <sup>c</sup>
	C <sup>a</sup>	E <sup>b</sup>	C	E	
0.4	61.7	21.9	60.5	21.4	97.7
0.6	58.3	20.6	58.0	20.3	98.5
0.8	56.1	19.7	55.0	19.4	98.5
1.0	54.1	19.2	53.5	19.0	99.0
1.2	52.7	18.6	52.0	18.4	99.0
1.4	50.9	18.1	50.3	17.9	98.9
1.6	49.7	17.7	49.2	17.5	98.9
2.4	45.3	16.1	44.8	15.9	98.8
3.2	41.8	14.9	41.2	14.6	98.0

<sup>a</sup> The specific capacitance (F g<sup>-1</sup>) of PCNW2 sample in two-electrode systems at voltage window of 0-1.6 V.

<sup>b</sup> The energy density (Wh kg<sup>-1</sup>) of PCNW2 sample in two-electrode systems at voltage window of 0-1.6 V.

<sup>c</sup> The energy density retention, the energy density of after 5000 cycles divided by that of before 5000 cycles.

## 5.4 Conclusions

In conclusion, nitrogen doped porous carbon nanowires with high specific surface area and adequate nitrogen content are prepared by KOH activation of nonporous nitrogen doped carbon nanowires. The specific surface area of PCNW2 is  $1642 \text{ m}^2 \text{ g}^{-1}$  with a nitrogen content of 2.41 at. %. The co-contribution of EDLC and pseudocapacitance makes PCNW2 high capacitance of  $291 \text{ F g}^{-1}$  at the current density of  $1 \text{ A g}^{-1}$ . The PCNW2 also shows excellent rate capability and good cycle stability (94.8 % capacitance retention after 5000 cycles). Moreover, the results in symmetric two-electrode systems suggest that PCNW2 possesses high energy density ( $21.9 \text{ Wh kg}^{-1}$  at the current density of  $0.4 \text{ A g}^{-1}$ ), and high the energy density retention of 68.0 % at the current density of  $3.2 \text{ A g}^{-1}$ . Overall, these features indicate a promising electrode material for supercapacitors application.

## References:

- [1] L.L. Zhang, X.S. Zhao, *Chem. Soc. Rev.* 38 (2009) 2520-2531.
- [2] G.A. Snook, P. Kao, A.S. Best, *J. Power Sources* 196 (2011) 1-12.
- [3] G. Zhao, F.G. Zhao, J.Q. Sun, W. Wang, Y. Lu, W.S. Li, Q.Y. Chen, *Carbon* 94 (2015) 114-119.
- [4] Y. Huang, J.J. Liang, Y.S. Chen, *Small* 8 (2012) 1805-1834.
- [5] Y.Y. Lv, F. Zhang, Y.Q. Dou, Y.P. Zhai, J.X. Wang, H.J. Liu, Y.Y. Xia, B. Tu, D.Y. Zhao, *J. Mater. Chem.* 22 (2012) 93-99.
- [6] M. Zhou, F. Pu, Z. Wang, S.Y. Guan, *Carbon* 68 (2014) 185-194.
- [7] Z.S. Wu, D.W. Wang, W.C. Ren, J.P. Zhao, G.M. Zhou, F. Li, H.M. Cheng, *Adv. Funct. Mater.* 20 (2010) 3595-602.
- [8] H. Zhao, K.S. Hui, K.N. Hui, *Carbon* 76 (2014) 1-9.
- [9] D.Y. Zhang, Y.Hao, L.W. Zheng, Y. Ma, H.X. Feng, H.M. Luo, *J. Mater. Chem.* 1 (2013) 7584-7591.
- [10] Q.L. Hao, X.F. Xia, W.Lei, W.J. Wang, J.S. Qiu, *Carbon* 81 (2015) 552-563.
- [11] Y.P. Zhai, Y.Q. Dou, D.Y. Zhao, P.F. Fulvio, R.T. Mayes, S. Dai, *Adv. Mater.* 23 (2011) 4828-4850.
- [12] H. Chen, M. Zhou, Z. Wang, S.Y. Zhao, S.Y. Guan, *Electrochim. Acta.* 148 (2014) 187-194.
- [13] B. Xu, S. Hou, G. Cao, F. Wu, Y. Yang, *J. Mater. Chem.* 22 (2012) 19088-19093.
- [14] D.Y. Zhai, B.H. Li, F.Y. Kang, H.D. Du, C.J. Xu, *Micropor. Mesopor. Mat.* 130 (2010) 224-228.
- [15] V. Ruiz, R. Santamaría, M. Granda, C. Blanco, *Electrochim. Acta.* 54 (2009) 4481-4486.
- [16] M.X. Wang, C.Y. Wang, M.M. Chen, Y.S. Wang, Z.Q. Shi, X. Du, T.Q. Li, Z.J. Hu, *New Carbon Mater.* 25 (2010) 285-290.
- [17] L. Mao, Y. Zhang, Y.T. Hu, K.H. Ho, Q.Q. Ke, H.J. Liu, Z.G. Hu, D. Zhao, J. Wang, *RSC Adv.* 5 (2015) 9307-9313.
- [18] C.M. Yang, C. Weidenthaler, B. Spliethoff, M. Mayanna, F. Schuth, *Chem. Mater.*

17 (2005) 355-358.

[19] L. Qie, W.M. Chen, Z.H. Wang, Q.G. Shao, X. Li, L.X. Yuan, X.L. Hu, W.X. Zhang, Y.H. Huang, *Adv. Mater.* 24 (2012) 2047-2050.

[20] Z.H. Wang, X.Q. Xiong, L. Qie, Y.H. Huang, *Electrochim. Acta.* 106 (2013) 320-326.

[21] X.Y. Zhou, J.J. Tang, J. Yang, J. Xie, B. Huang, *J. Mater. Chem.* 1 (2013) 5037-5044.

[22] L.M. Dai, D.W. Chang, J.B. Baek, W. Lu, *small* 8 (2012) 1130-1166.

[23] J. Yan, T. Wei, B. Shao, F.Q. Ma, Z.J. Fan, M.L. Zhang, C. Zheng, Y.C. Shang, W.Z. Qian, F. Wei, *Carbon* 48 (2010) 1731-1737.

[24] J.C. Wang, S. Kaskel, *J. Mater. Chem.* 22 (2012) 23710-23725.

[25] T. Otowa, R. Tanibata, M. Itoh, *Gas Separation & Purification* 7 (1993) 241-245.

[26] D. Lozano-Castello, J.M. Calo, D. Cazorla-Amoros, A. Linares-Solano, *Carbon* 45 (2007) 2529-2536.

[27] E. Raymundo-Pinero, P. Azais, T. Cacciaguerra, D. Cazorla-Amoros, A. Linares-Solano, F. Beguin, *Carbon* 43 (2005) 786-795.

[28] H.L. Wang, Q.M. Gao, J. Hu, *J. Am. Chem. Soc.* 131 (2009) 7016-7022.

[29] Y. Fan, P.F. Liu, Z.Y. Huang, T.W. Jiang, K.L. Yao, R. Han, *J. Power Sources* 280 (2015) 30-38.

[30] Y.W. Ma, S.J. Jiang, G.Q. Jian, H.S. Tao, L.S. Yu, X.B. Wang, X.Z. Wang, J.M. Zhu, Z. Hu, Y. Chen, *Energy Environ. Sci.* 2 (2009) 224-229.

[31] L. Zhao, L.Z. Fan, M.Q. Zhou, H. Guan, S.Y. Qiao, M. Antonietti, M. Titirici, *Adv. Mater.* 22 (2010) 5202-5206.

[32] S.N. Talapaneni, G.P. Mane, A. Mano, C. Anand, D.S. Dhawale, T. Mori, A. Vinu, *ChemSusChem* 5 (2012) 700-708.

[33] A. Vinu, *Adv. Funct. Mater.* 18 (2008) 816-827.

[34] C.X. Guo, N. Li, L.L. Ji, Y.W. Li, X.M. Yang, Y. Lu, Y.F. Tu, *J. Power Sources* 247 (2014) 660-666.

[35] X.M. Fan, C. Yu, J. Yang, Z. Ling, J.S. Qiu, *Carbon* 70 (2014) 130-141.

[36] V. Datsyuk, M. Kalyva, K. Papagelis, J. Parthenios, D. Tasis, A. Siokou, I.

- Kallitsis, C. Galiotis, Carbon 46 (2008) 833-840.
- [37] Z.B. Zulamita, C.M. Francisco, M.C. Carlos, J. Power Sources 219 (2012) 80-88.
- [38] C. Merino, P. Soto, E. Vilaplana-Ortego, J.M.G.D. Salazar, F. Pico, J.M. Rojo, Carbon 43 (2005) 551-557.
- [39] C. Vagner , G. Fingueneisel , T. Zimny , P. Burg , B. Grzyb , J. Machnikowski , J.V. Weber, Carbon 41 (2003) 2847-2853.
- [40] X.L. Ma, G.Q. Ning, Y.F. Kan, Y.M. Ma, C.L. Qi, B. Chen, Y.F. Li, X.Y. Lan, J.S. Gao, Electrochim. Acta. 150 (2014) 108-113.
- [41] Y.Y. Peng, Y.M. Liu, J.K. Chang, C.H. Wu, M.D. Ger, N.W. Pu, C.L. Chang, Carbon 81 (2015) 347-356.
- [42] R. Ramya, R. Sivasubramanian, M.V. Sangaranarayanan, Electrochim. Acta. 101 (2013) 109-129.
- [43] W.M. Qiao, S.H. Yoon, I. Mochida, Energ. Fuel. 20 (2006)1680-1684.
- [44] H. Teng, Y.J. Chang, C.T. Hsieh, Carbon 39 (2001) 1981-1987.
- [45] J.G. Wang, Y. Yang, Z.H. Huang, F.Y. Kang, Carbon 61 (2013) 190-199.
- [46] Q. Wu, Y.X. Xu, Z.Y. Yao, A. Liu, G.Q. Shi, Acs Nano 4 (2010) 1963-1970.
- [47] X.J. He, P.H. Ling, J.S. Qiu, M.X. Yu, X.Y. Zhang, C. Yu, M.D. Zheng, J. Power Sources 240 (2013) 109-113.
- [48] M. Huang, X.L. Zhao, F. Li, W. Li, B. Zhang, Y.X. Zhang, J. Mater. Chem. 3 (2015) 12852-12857.
- [49] H.F. Yen, Y.Y. Horng, M.S. Hu, W.H. Yang, J.R. Wen, A. Ganguly, Y. Tai, K.H. Chen, L.C. Chen, Carbon 82 (2015) 124-134.
- [50] D.W. Wang, F. Li, M. Liu, G.Q. Lu, H.M. Cheng, Angew. Chem. Int. Ed. 47 (2008) 373-376.
- [51] J.B. Wang, X.Q. Yang, D.C. Wu, R.W. Fu, M.S. Dresselhaus, G. Dresselhaus, J. Power Sources 185 (2008) 589-594.
- [52] D.C. Wu, R.W. Fu, M.S. Dresselhaus, G. Dresselhaus, Carbon 44 (2006) 675-681.
- [53] D.S. Su, R. Schlegel, ChemSusChem 3 (2010) 136-168.
- [54] K. Fic, G. Lota, M. Meller, E. Frackowiak, Energy Environ. Sci. 5 (2012)

5842-5850.

[55] C. Johne, R. Fritzsche, A. Ignaszak, *Electroanal.* 26 (2014) 1560-1572.

[56] S.A. El-Khodary, G.M. El-Enany, M. El-Okr, M. Ibrahim, *Electrochim. Acta.* 150 (2014) 269-278.

[57] B. Ma, X. Zhou, H. Bao, X.W. Li, G.C. Wang, *J. Power Sources* 215 (2012) 36-42.

[58] Q. Wang, J. Yan, Y.B. Wang, G.Q. Ning, Z.J. Fan, T. Wei, *Carbon* 52 (2013) 209-218.

[59] C.W. Huang, C.T. Hsieh, P.L. Kuo, H. Teng, *J. Mater. Chem.* 22 (2012) 7314-7322.

[60] K.H. An, W.S. Kim, Y.S. Park, J.M. Moon, D.J. Bae, S.C. Lim, Y.S. Lee, Y.H. Lee, *Adv. Funct. Mater.* 11 (2001) 387-392.

[61] J.T. Zhang, J.W. Jiang, H.L. Li, X.S. Zhao, *Energy Environ. Sci.* 4 (2011) 4009-4015.

# Chapter 6 Preparation of MnO<sub>2</sub>/carbon nanowires composites for supercapacitors

## 6.1 Introduction

The above studies focused on the development of negative electrode materials. In order to assemble the full supercapacitor, the study was transferred to the development of positive electrode material. Till now, many transition metal oxides nanomaterials, such as Co<sub>3</sub>O<sub>4</sub> [1-3], NiO [4-6] and MnO<sub>2</sub> [7-10], have been widely used in positive electrode of supercapacitors due to their multiple oxidation states at the charge/discharge process. Especially, MnO<sub>2</sub> as one of the most promising materials for energy storage owing to its low cost, high energy density, nature abundance and low environmental pollution [11], has been favored by researchers [12, 13]. Unfortunately, MnO<sub>2</sub>-based materials exhibit poor conductivity and cycling performance, these defects limit their development into supercapacitors [14]. In order to solve these problems, some research focused on preparation of MnO<sub>2</sub>/special type carbon composites, which was shown an effective method [15-17]. Currently, carbon nanotube (CNT) [18], graphene (GS) [19] and active carbon [20] are often used as the carbon content in the composites due to their remarkable properties, such as high surface area, excellent electronic conductivity, unique internal structures, reasonable chemical stability, superior thermal stability, low mass density and outstanding intrinsic strength [6, 21]. However, the preparation processes of these special type carbon materials are often complex [22, 23], and these carbon materials usually need a pretreatment process for improving agglomeration and insolubility in water before preparation of MnO<sub>2</sub>/carbon composites, which will further increase the cost and cause severe environmental problems [24-26].

MnO<sub>2</sub>, as we all know, differences in its morphology can cause different specific surface area and surface to volume ratio, which can further lead to different electrochemical performance [6]. MnO<sub>2</sub> has much morphology attributed to its

crystallographic structure, and the effect of MnO<sub>2</sub> morphology on its capacitive performance has been studied. For example, Devaraj [27] and Yin [28] showed that the specific capacitance (SC) of MnO<sub>2</sub> depends strongly on the crystallographic structure, and the  $\alpha$ -MnO<sub>2</sub> achieved the highest SC. Especially, Sun et al. prepared various crystallographic structures of MnO<sub>2</sub> by a hydrothermal method under different reaction times [29], and the results further showed that the above phenomenon mainly due to the fact that  $\alpha$ -MnO<sub>2</sub> possesses large tunnel size, the insertion of electrolyte cations. Therefore, Mn centers located both in the bulk and at the surface can contribute to the faradaic charge storage. Although researchers already have conducted an in-depth study for MnO<sub>2</sub> itself, the relationship between MnO<sub>2</sub>/carbon composites crystallographic structure and their capacitive performance is rarely reported.

In this paper, we report an efficient preparation of MnO<sub>2</sub>/carbon nanowire composites (CNWMn) as the electrode materials for supercapacitors. The carbon nanowires (CNW) were produced with a simple method (based on our previous study [30]). Polypyrrole (PPy) nanowires are prepared by chemical oxidation method, and then CNW were obtained by direct carbonization of PPy nanowires. The preparation process of CNW is simpler than that of the other special carbon materials (CNT, GS). However, it still has problems such as the energy consumption and environmental impact of carbonization process, which we believe will be gradually overcome with the development of the technique. Moreover, the CNW contains many oxygen or nitrogen-containing functional groups (as shown in Table 1 and SI 5), and these functional groups can greatly improve the dispersion of CNW in water [31, 32] (the dispersion result as shown in SI 1, compared with commercially available multi-walled CNT, the CNW exhibited more excellent dispersion in water) These CNW with these advantages are then used to prepare MnO<sub>2</sub>/carbon composites. In the current study, we prepared various morphologies of CNWMn through a redox reaction between KMnO<sub>4</sub> and CNW by hydrothermal method under different reaction times, and we find that the morphologies of CNWMn have a profound effect on their electrochemical performance by three-electrode systems. We also assembled a

two-electrode asymmetric system using CNW/Mn<sub>2</sub> and porous carbon nanowires (PCNW, preparation method based on our previous study [30]) as the positive and negative electrode, respectively. We find that the composites in asymmetric systems possess the high energy density, excellent rate capability, and high cycle stability.

## 6.2 Experimental section

### 6.2.1 Materials

Pyrrole (Py) monomer was purified by distillation under reduced pressure before use. Multi-walled carbon nanotube (MWCNT) powder was purchased from Institute of Chemical Physics (Chengdu, China). The other reagents, such as KOH, ammonium persulphate (APS), cetyltrimethylammonium bromide (CTAB), KMnO<sub>4</sub> and hydrochloric acid (HCl), all were locally commercially available and of analytical grade, and were used without further purification. All solutions were prepared with distilled water.

### 6.2.2 Preparation of porous carbon nanowires (PCNW)

PCNW samples were obtained by KOH activation method based on our previous study [30]. A typical process as follows: first, we prepared PPy nanowires. 0.757 g CTAB, 0.5 mL Py and 10.5 mL HCl (12 mol L<sup>-1</sup>) were added in 52 mL deionized water and stirred for 2 h; 10 mL 0.83 M APS solution was added into the above mixture and the reaction was performed under room temperature for 1 h. The product was removed from solution and washed with deionized water, dried in vacuum at 50 °C for 12 h to obtain the PPy nanowires. Second, PPy nanowires were carbonized under flowing N<sub>2</sub> at 750 °C for 2 h, and obtained the carbon nanowires (CNW). Third, a mixture of the KOH and CNW in the weight ratio of 2/1 was heated in a tube furnace in N<sub>2</sub> atmosphere at 800 °C for 1 h, and the product was washed with HCl solution and deionized water till the filtrate became neutral and drying at 80 °C for 12 h. Then the PCNW sample was obtained. In addition, in order to show the dispersion of CNW in water, a certain amount of CNW and MWCNT was dispersed in deionized water

(0.275 mg mL<sup>-1</sup>) with 0.5 h sonication, respectively, followed by standing for 8 h.

### 6.2.3 Preparation of CNW/MnO<sub>2</sub> composites (CNWMn)

The CNWMn composites were prepared by directly reacting KMnO<sub>4</sub> with CNW. Briefly, 0.110 g KMnO<sub>4</sub> dissolved in 200 mL deionized water, and then 0.055 g CNW added the above solution under sonication. After 1 h for sonication, the solution was transferred to a Teflon-lined stainless steel autoclave (capacity of 200 mL) and heated at 140 °C in an electric oven for a certain time (see below). Based on the reaction time, the samples are denoted CNWMn1 (1 h), CNWMn2 (2 h), CNWMn3 (4h) and CNWMn4 (8 h). The autoclave was cooled naturally to room temperature, and the products were filtered, washed by water to remove the residual reactants. Finally, the products were dried in an oven at 80 °C. For comparison, we also prepared MnO<sub>2</sub>X (X=1, 2, 3, 4, where the X stands for the reaction time 1, 2, 4 and 8 h, respectively) at the same conditions except CNW replaced by HCl (37 %, 0.5 mL). Moreover, CNW was still carried out hydrothermal treatment for 2 h (HCNW) for comparison with CNW.

### 6.2.4 Characterizations

The morphology of samples was characterized by scanning electron microscopy (SEM, s-4300, Hitachi Co., Ltd. Tokyo. Japan). The crystallographic structure of samples was tested by X-ray diffraction system (XRD, XRD-600, Shimadzu Co., Ltd. Kyoto, Japan). Surface area and pore size distribution measurement (ASAP 2020, surface area and pore size analyzer, Micromeritics) was carried out by nitrogen adsorption-desorption at bath temperature of -196 °C. The X-ray photoelectron spectroscopy (XPS) analysis was performed on PHI Quantum 5000 equipped with an Al K $\alpha$  radiation source.

### 6.2.5 Electrochemical measurement

The fabrication of working electrodes was carried out as follows. The samples,

acetylene blank and polytetrafluoroethylene (PTFE) were mixed at a mass ration of 90:5:5. In the Following, ethanol (50  $\mu$ L) added the mixture and grinding adequately to obtain a paste. Then the paste was coated onto the nickel foam substrate and dried in a vacuum oven at 80  $^{\circ}$ C for 12 h. Finally, the nickel foam substrate compressed at 10 MPa for 5 min.

The electrochemical properties of samples were studied in three and two-electrode systems in 6 M KOH electrolyte with electrochemical workstation (CHI 660D, Shanghai Chenhua, China). In three-electrode systems, saturated calomel electrode was used as the reference electrode and platinum foil as the counter electrode; in asymmetric two-electrode systems, the active materials of positive and negative electrode were CNWMn and PCNW, respectively. Cyclic voltammetry (CV), galvanostatic charge/discharge (GCD) and electrochemical impedance spectroscopy (EIS) tests were respectively performed in three and two-electrode systems. The EIS was measured with frequency range between  $10^5$  to  $10^{-2}$  Hz. The SC of electrode based on GCD curves was evaluated according to Eq. 2.2 [33].

## 6.3 Results and discussion

### 6.3.1 Microstructural characterization

In this study, CNW was used as the both reducing agents and scaffolds for  $\text{MnO}_2$  growth.  $\text{MnO}_2$  nanostructures grew on the surface of CNW based on the self-limiting reaction between  $\text{KMnO}_4$  and carbon in neutral aqueous solution through the hydrothermal method [34]. The redox reaction (Re. 6.1) can be expressed as follows [35, 36]:



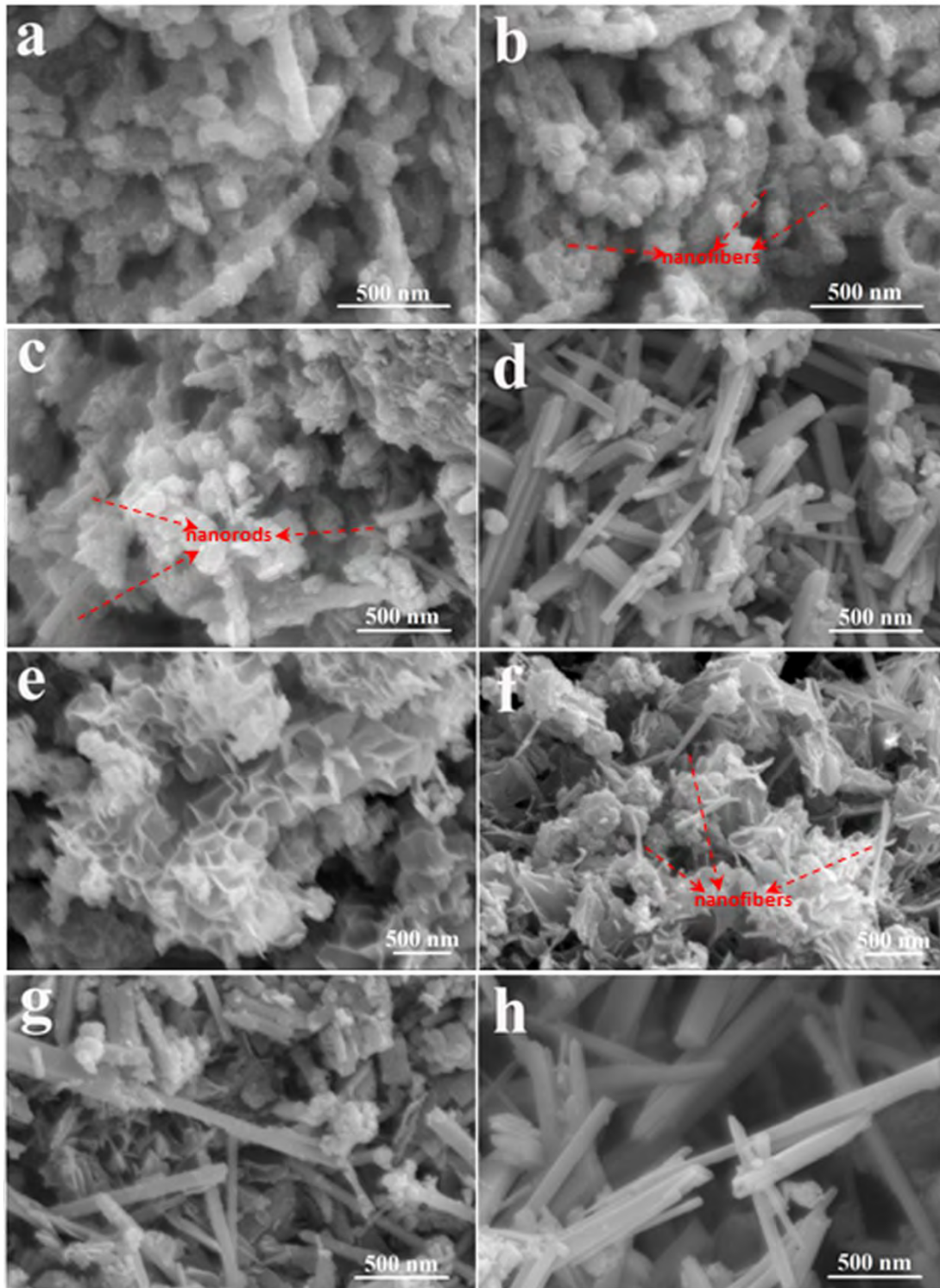


Fig. 6.1 SEM image of CNWMn1 (a), CNWMn2 (b), CNWMn3 (c), CNWMn4 (d), MnO<sub>2</sub>1 (e), MnO<sub>2</sub>2 (f), MnO<sub>2</sub>3 (g), and MnO<sub>2</sub>4 (h).

SEM was used to examine the morphology of prepared CNWMn and pure MnO<sub>2</sub> samples, and the results were shown in Fig. 6.1. Compared with pristine CNW, the clean surface and net nanowires structure of CNW (as shown in Fig. 6.2a) were

coated by thin nanosheets  $\text{MnO}_2$  (formed the core/shell structure) in sample CNWMn1 and 2 (as shown in Fig. 6.1a and b, respectively), and no aggregations of  $\text{MnO}_2$  nanoparticles were observed. Moreover, it is interesting to note that a few of nanofibers  $\text{MnO}_2$  were also observed in CNWMn2. For pure  $\text{MnO}_2$ , after a reaction of

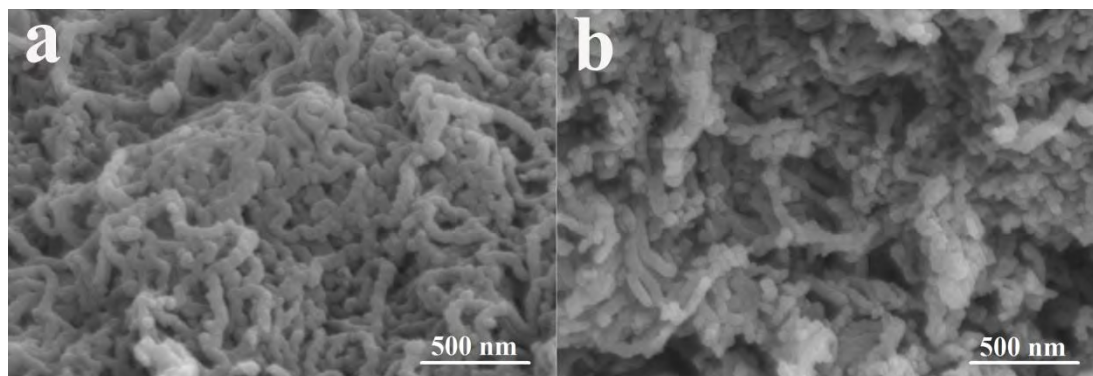


Fig. 6.2 SEM image of CNW (a) and PCNW (b).

1 h ( $\text{MnO}_2$ 1, as shown in Fig. 6.1e), the mixed solution of  $\text{KMnO}_4$  and  $\text{HCl}$  aqueous resulted in the nucleation and growth of nanoflowers, and the nanoflowers were comprised of many wrinkled nanosheets, which were self-assembled perpendicular to the outer surface of the nanoflowers. When the reaction time was increased to 2 h ( $\text{MnO}_2$ 2, as shown in Fig. 6.1f), similar to CNWMn2, short nanofibers began to emerge between nanosheets, but the flower-like morphology persisted. The above phenomena suggest that the nucleation of  $\text{MnO}_2$  is inhibited due to the intervention of CNW. When the reaction time was further prolonged to 4 h, for CNWMn3 sample (as shown in Fig. 6.1c), more nanofibers  $\text{MnO}_2$  were observed, and a little of nanofibers  $\text{MnO}_2$  changed into nanorods  $\text{MnO}_2$ . Furthermore, lots of aggregations of  $\text{MnO}_2$  nanoparticles were observed; on the contrary, the core/shell structure of CNW coated by nanosheets  $\text{MnO}_2$  was hard to observe. Different to CNWMn3, some nanorods and a little of aggregations were observed in  $\text{MnO}_2$ 3 (as shown in Fig. 6.1g), and the flower-like morphology disappeared. Finally, after reaction time of 8 h, many nanorods and a little of aggregations were observed in CNWMn4 (as shown in Fig. 6.1d). However, for  $\text{MnO}_2$ 4 (as shown in Fig. 6.1h), the aggregations disappeared completely, moreover, a large number of nanorods formed and the diameter of the nanorods also increased, compared to the CNWMn3. These morphology differences

between CNWMn and pure MnO<sub>2</sub> further indicate that CNW inhibits the space growth of MnO<sub>2</sub>. The growth process of CNWMn and pure MnO<sub>2</sub> based on the reaction time will be described later in the paper.

XRD was carried out to investigate the phase and crystallinity of the CNWMn samples with different reaction times, as shown in Fig. 6.3a. For CNW sample (as shown in Fig. 6.3b), there are two broad peaks (24° and 43°), resulted from the (002) and (101) plane of graphite, respectively [37, 38]. For CNWMn1 and 2 samples, except the signals of CNW, several new broad diffraction peaks can be observed with 2θ around 12°, 25°, 37° and 66°, corresponding to the (001), (002), (006) and (119) diffraction of δ-MnO<sub>2</sub> crystalline phase, respectively (JCPDS no. 18-0802) [39, 27]; the broad and low intensity peaks suggest a poor or polycrystalline feature of the δ-MnO<sub>2</sub>. Meanwhile, three weak peaks appeared in the CNWMn2 sample, the peaks at 26° and 34° attributed to (120) and (031) plane of γ-MnO<sub>2</sub>, respectively [40], and the peak at 54° attributed to (600) plane of α-MnO<sub>2</sub> [41]. This discovery corresponds the nanofibers MnO<sub>2</sub> in SEM image of CNWMn2. However, for the CNWMn obtained at hydrothermal reaction of more than 2 h (CNWMn3 and 4), many sharp and high intensity peaks corresponding to α-MnO<sub>2</sub> (JCPDS no. 44-0141) [12] and γ-MnO<sub>2</sub> (JCPDS no. 14-644) [40] appeared, indicating the high crystallinity of MnO<sub>2</sub> prepared by the hydrothermal method [42]. Moreover, the α- and γ-MnO<sub>2</sub> correspond to the nanorods and aggregations MnO<sub>2</sub> in SEM images of CNWMn3 and 4. For comparison, we also tested the XRD spectrum of MnO<sub>2</sub> samples with different reaction times, and the results are shown in SI 6. From Fig. 6.3c, we also found four broad diffraction peaks corresponding to δ-MnO<sub>2</sub> when the reaction time was less than 2 h (MnO<sub>2</sub>1 and 2). However, the crystalline structures of MnO<sub>2</sub>3 and 4 (the reaction time is 4 and 8 h, respectively) are different with CNWMn3 and 4. They exhibited the complete crystalline structure of α-MnO<sub>2</sub>, suggesting the difference of the formation process of pure MnO<sub>2</sub> and CNWMn composites. The growth process of MnO<sub>2</sub> when CNW participation will be further explained in following content.

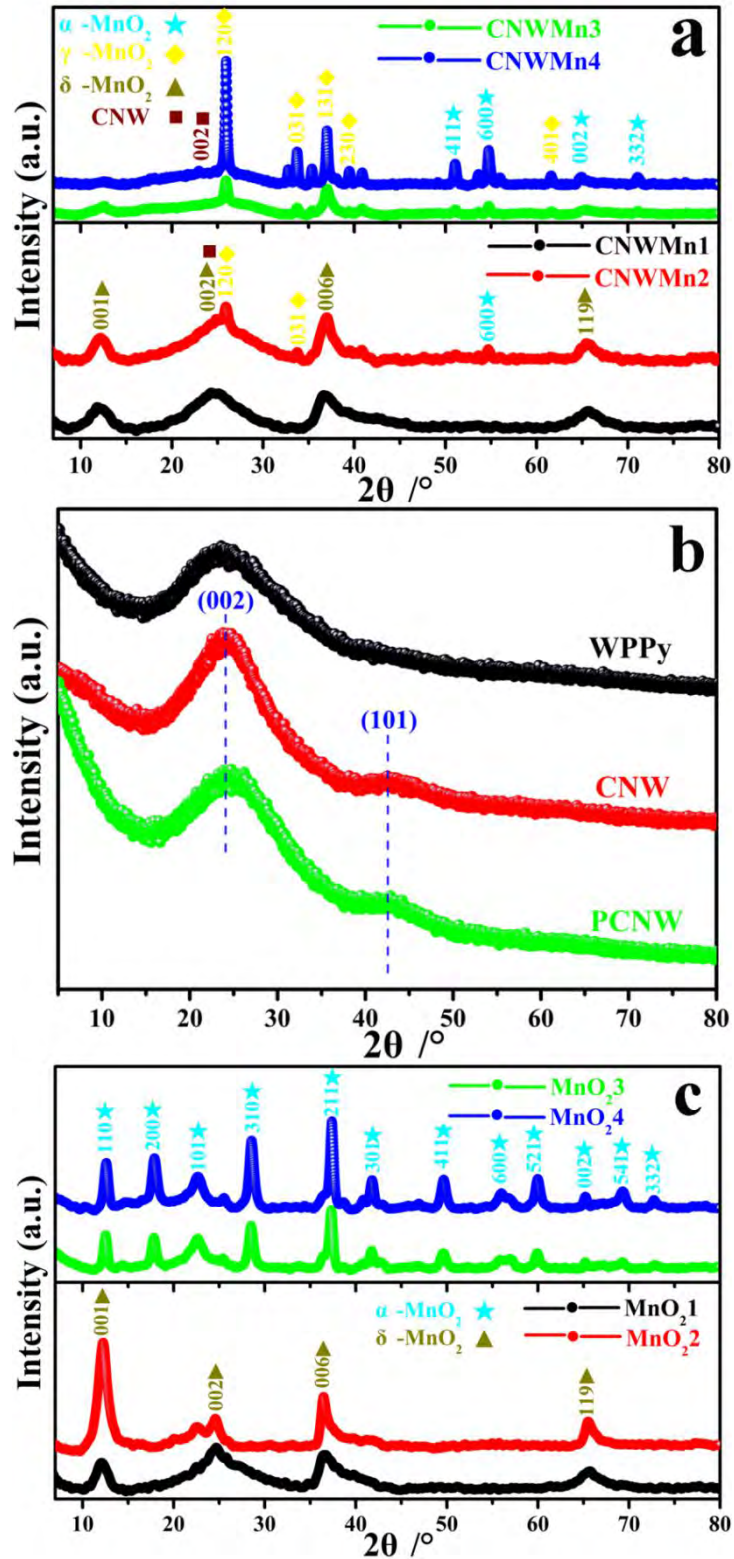


Fig. 6.3 (a) XRD patterns of CNWMn1, CNWMn2, CNWMn3 and CNWMn4; (b) XRD patterns of WPPy, CNW and PCNW; (c) XRD patterns of MnO<sub>2</sub>1, MnO<sub>2</sub>2, MnO<sub>2</sub>3 and MnO<sub>2</sub>4.

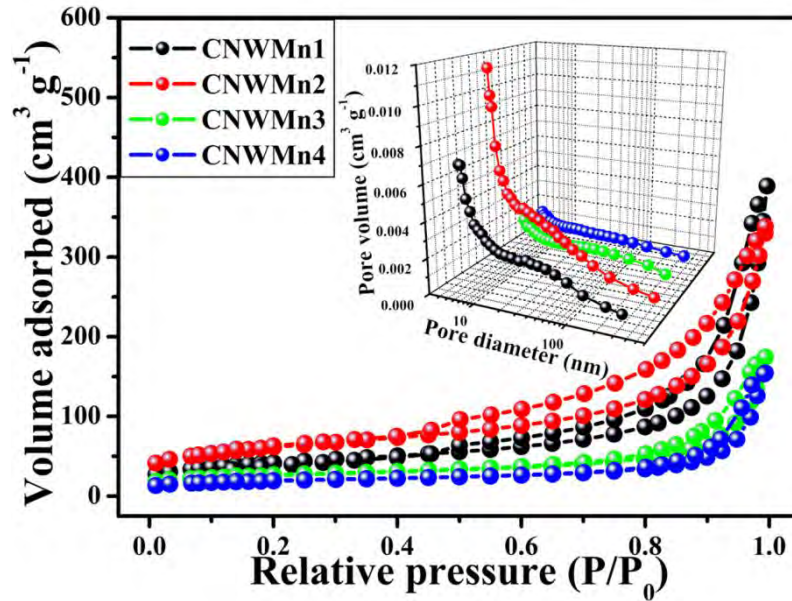


Fig. 6.4 N<sub>2</sub> adsorption-desorption isotherms of CNWMn1, CNWMn2, CNWMn3 and CNWMn4 (the inset of b is pore size distribution plots).

The nitrogen adsorption/desorption isotherm for the CNWMn samples and their corresponding pore size distribution are shown in Fig. 6.4. For CNWMn1 and 2, they show a distinct hysteresis in the large range from 0.45 to 1.0 P/P<sub>0</sub>, and the isotherm can be classified as a type IV isotherm with a type H2 hysteresis [43, 44]. These results suggest that these samples possess mesopores formed by nanoflakes MnO<sub>2</sub> on the surface of CNW or CNWMn nanowires stack. However, when the reaction time was more than 2 h, the hysteresis in the range of 0.45 to 1.0 P/P<sub>0</sub> gradually disappeared (for CNWMn3 and 4, as shown in Fig. 2b), indicating that the mesopores structure gradually disappeared. This is owing to more and more nanorods MnO<sub>2</sub> is generated with the increase of reaction time (as shown in Fig. 6.1). The inset of Fig. 6.4 shows the pore size distribution curves recorded by the adsorption process of the isotherms. From the inset, we can find that CNWMn1 and 2 possess the prolific mesopores structure in a narrow range of the pore size from 4 to 10 nm. Similar to isotherms, the prolific mesopores structure gradually disappeared with the increase of reaction time. In comparison, the isotherm of CNW (as shown in Fig. 6.5a) shows the type-II sorption isotherm, suggesting the non-porous structure [45]. Moreover, a distinct H3 hysteresis was observed at a range of 0.9 to 1.0 P/P<sub>0</sub>, reflecting the

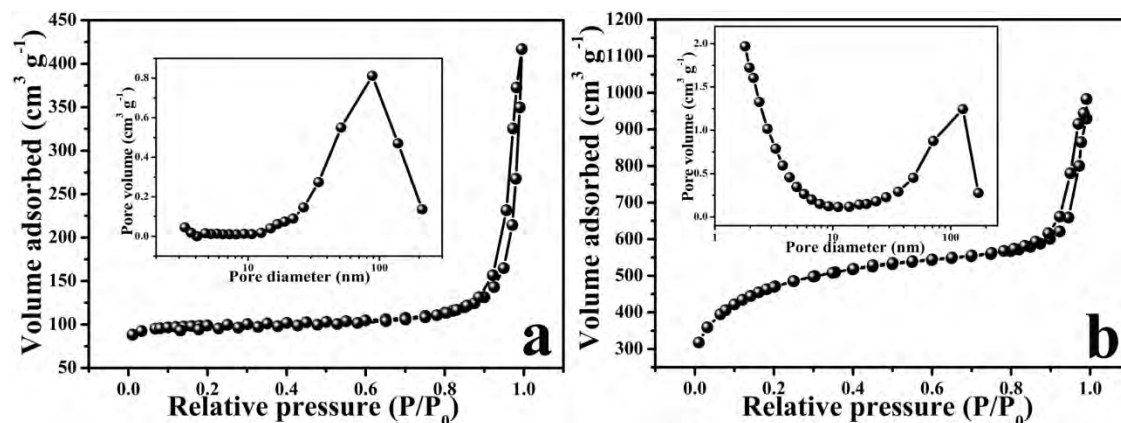


Fig. 6.5 N<sub>2</sub> adsorption-desorption isotherms of CNW (a) and PCNW (b), and the inset is pore size distribution plots.

existence of stacking macroporous structure by CNW nanowires. The BET specific surface area ( $S_{\text{BET}}$ ) and total pore volume of samples are shown in Table 6.1. The  $S_{\text{BET}}$  and pore volume of CNW remarkably decreased when CNW reacted with  $\text{KMnO}_4$  by hydrothermal reaction. Furthermore, it is noted that the  $S_{\text{BET}}$  and pore volume of CNWMn increased first and then decreased with the reaction time, and the highest  $S_{\text{BET}}$  ( $213 \text{ m}^2 \text{ g}^{-1}$ ) of CNWMn was achieved at the reaction time of 2 h (CNWMn2). This phenomenon is consistent with the literature [46] and can be explained as following: the  $S_{\text{BET}}$  mainly depend on the pore structure where the N<sub>2</sub> adsorption/desorption takes place [47]; here, CNWMn2 exhibits a few of nanofibers structures, which leads to the increase in pore structure for N<sub>2</sub> adsorption/desorption by associating with the nanoflakes structure (it was confirmed by the inset of Fig. 6.4) [47], though XRD showed a more amorphous structure at reaction time of 1 h.

Table 6.1 Pore volume, specific surface area and pore size of samples

Sample	Pore Volume (cm <sup>3</sup> g <sup>-1</sup> )	$S_{\text{BET}}$ (m <sup>2</sup> g <sup>-1</sup> )	Average pore size (nm)
CNW	0.75	406	40.10
CNWMn1	0.34	182	60.8
CNWMn2	0.39	213	50.7
CNWMn3	0.26	131	98.0
CNWMn4	0.22	97	122.2

These results further indicate that the nanoflakes  $\text{MnO}_2$  were successfully and homogeneously coated on the surface of CNW as reaction time less than 2 h, and this phenomenal would have a profound impact on electrochemical performance of CNWMn samples.

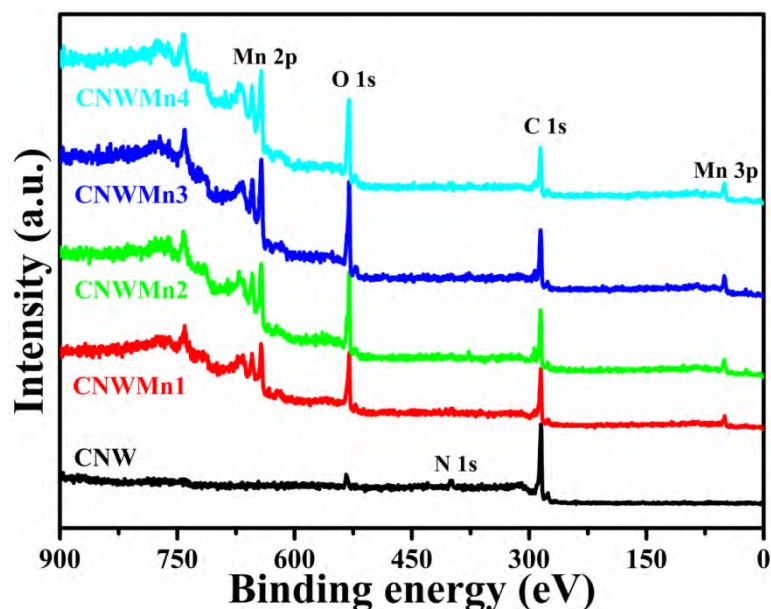


Fig. 6.6 XPS survey spectra of CNWMn1, CNWMn2, CNWMn3 and CNWMn4;

XPS was conducted for a better understanding of the chemical composition and the valence states of Mn, C and O in CNWMn composites. The survey of XPS spectra of CNW shows the signals of C, O and N elements. Compared with CNW, the XPS spectrum of CNWMn added a signal of Mn element (as shown in Fig. 6.6). As shown in Table 6.2, the content of C and N obviously decreased, just the opposite, and the content of Mn and O obviously increased after CNW went through the hydrothermal reaction. In addition, it is also found that the content of Mn and O gradually increased in CNWMn composites with the reaction time increase. This result suggests that the hydrothermal reaction has been conducted with the increase of reaction time.

Table 6.2 XPS spectrum analysis of samples

Sample	C/at. %	N/at. %	O/at. %	Mn/at. %	O/C	Mn/C	O-Mn (%)	O-C (%)
CNW	89.06	5.33	5.61	--	0.063	--	--	--
CNWMn1	56.46	3.23	26.17	14.14	0.464	0.250	43.3	56.7
CNWMn2	51.29	2.57	28.79	17.35	0.561	0.338	56.3	43.7
CNWMn3	47.86	1.77	31.23	19.14	0.653	0.400	59.3	40.7
CNWMn4	42.37	1.67	33.59	22.37	0.793	0.528	60.5	39.5

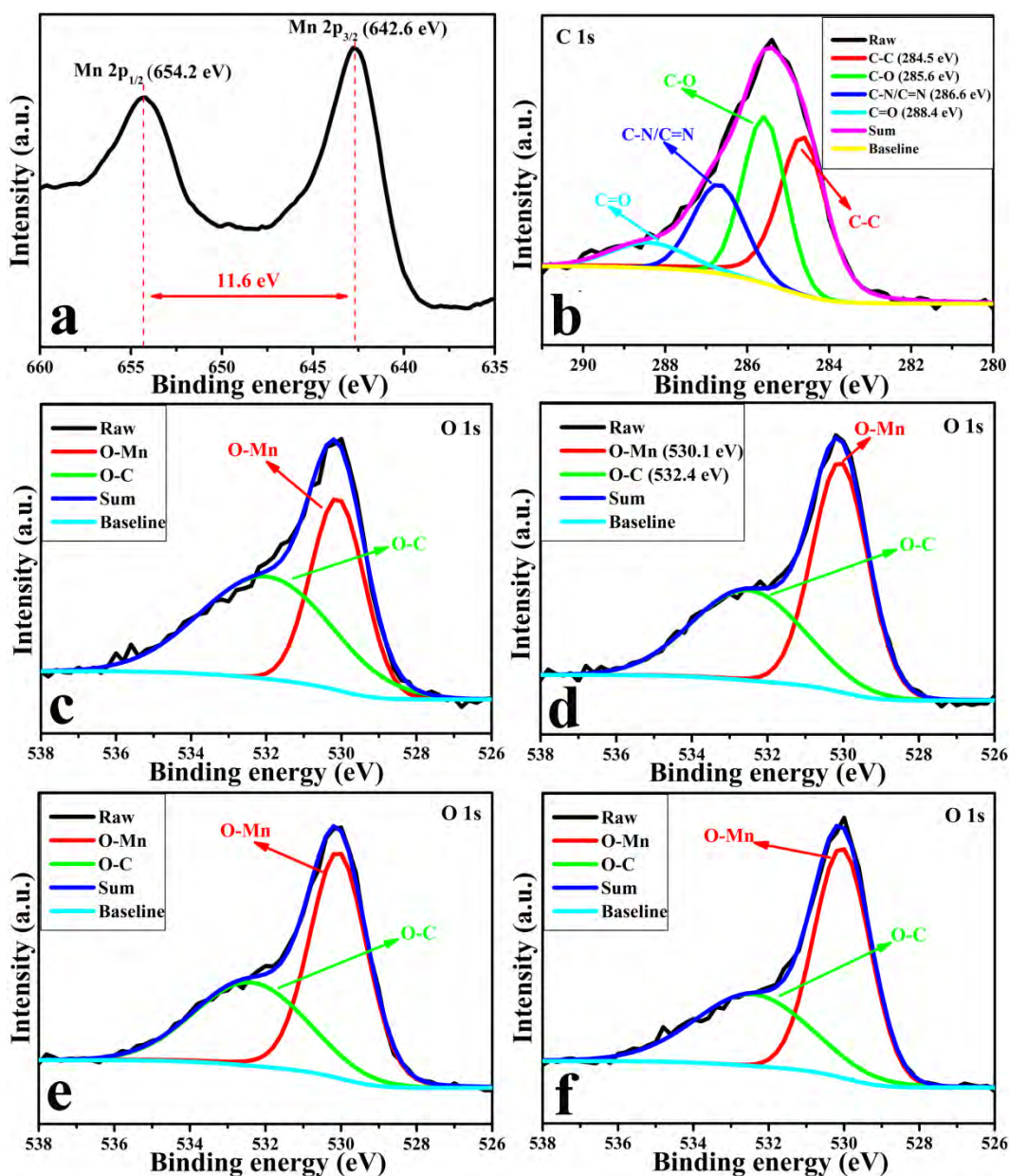


Fig. 6.7 (a) High resolution Mn 2p XPS spectra of CNWMn2; (b) high resolution of C 1s XPS spectra of CNWMn2; High resolution O 1s XPS spectra of CNWMn1 (c), CNWMn2 (d), CNWMn3 (e) and CNWMn4 (f).

The high resolution Mn 2p spectra (as shown in Fig. 6.7a) of CNWMn2 show a Mn 2p<sub>1/2</sub> peak at 654.2 eV and a Mn 2p<sub>3/2</sub> peak at 642.6 eV. The binding energies of Mn 2p with a spin energy separation of 11.6 eV are consistent with literatures reported previously, confirming the formation of MnO<sub>2</sub> [48, 49]. Fig. 6.7b shows the high resolution C 1s spectra of CNWMn2, which can be fitted as four peaks at binding energies of 284.5, 285.6, 286.6 and 288.4 eV, corresponding to C-C, C-O, C-N/C=N

and C=O, respectively [44, 50]. Fig. 6.7c, d, e and f show the high resolution O 1s spectra of CNWMn composites. Compared with high resolution O 1s spectra of CNW (as shown in Fig. 6.8, it can be fitted by three types of oxygen containing functional groups on the surface of CNW), they can be deconvoluted into two different peaks, at 530.1 and 532.4 eV, attributed to oxygen bonded with manganese (O-Mn) in MnO<sub>2</sub> crystal lattice [51] and the oxygen complexes on the surface of CNW (O-C/O=C) [52], respectively. The content of two types of oxygen atoms are also listed in Table 6.2. It is easy to find that the content of O-Mn significantly increased and the O-C/O=C significantly decreased with the reaction time increase. These transformations further evidence that the hydrothermal reaction has never been interrupted, and they will have an interesting impact in the electrochemistry performance of CNWMn composites.

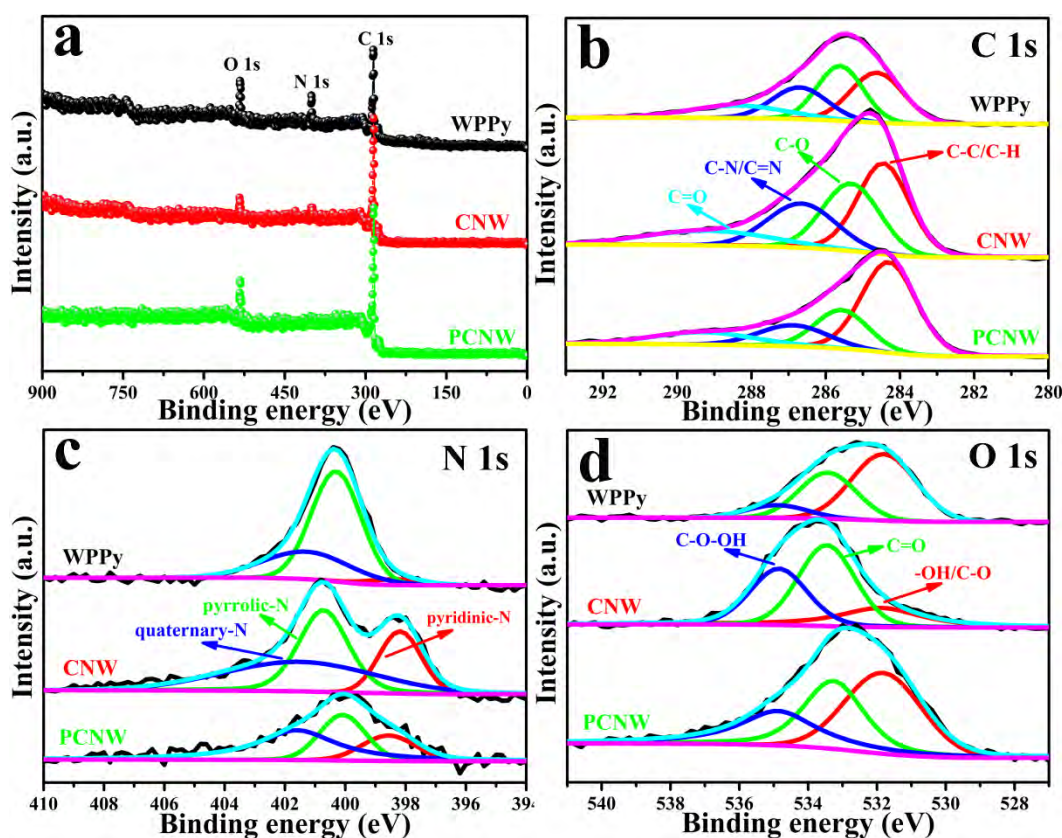


Fig. 6.8 (a) XPS survey spectra of WPPy, CNW and PCNW; high resolution C 1s (b), N 1s (c) and O 1s (d) XPS spectra of WPPy, CNW and PCNW.

### 6.3.2 Growth process of the CNWMn nanostructures

In order to get the desired morphology and crystal phase for excellent

electrochemical performance of CNWMn composites, it is important to understand the formation process of the CNWMn composites nanostructures. Some growth processes of the hydrothermally synthesized  $\text{MnO}_2$  have been proposed by researchers. Truong et al. proposed that the  $\delta$ - $\text{MnO}_2$  nanosheets can be formed once the reaction is initiated regardless of the reaction conditions, followed the  $\delta$ - $\text{MnO}_2$  nanosheets tend to transform into  $\alpha$ - $\text{MnO}_2$  nanodomains undergo an Ostwald ripening process [53]. Li et al. reported that the  $\alpha$ - $\text{MnO}_2$  nanowires or nanorods tended to assemble along lateral surface and form thick nanorods through an “oriented attachment” process under the hydrothermal condition due to the formation of bundles could reduce the surface-to-volume ratio and the surface energy [54]. However, the formation process of  $\text{MnO}_2$ /carbon composites has rarely been reported. We infer that the formation process of pure  $\text{MnO}_2$  and CNWMn composites is different by the SEM and XRD analysis, and Fig. 6.9 summarizes our view of the formation process of CNWMn composites nanostructure based on the hydrothermal reaction time.

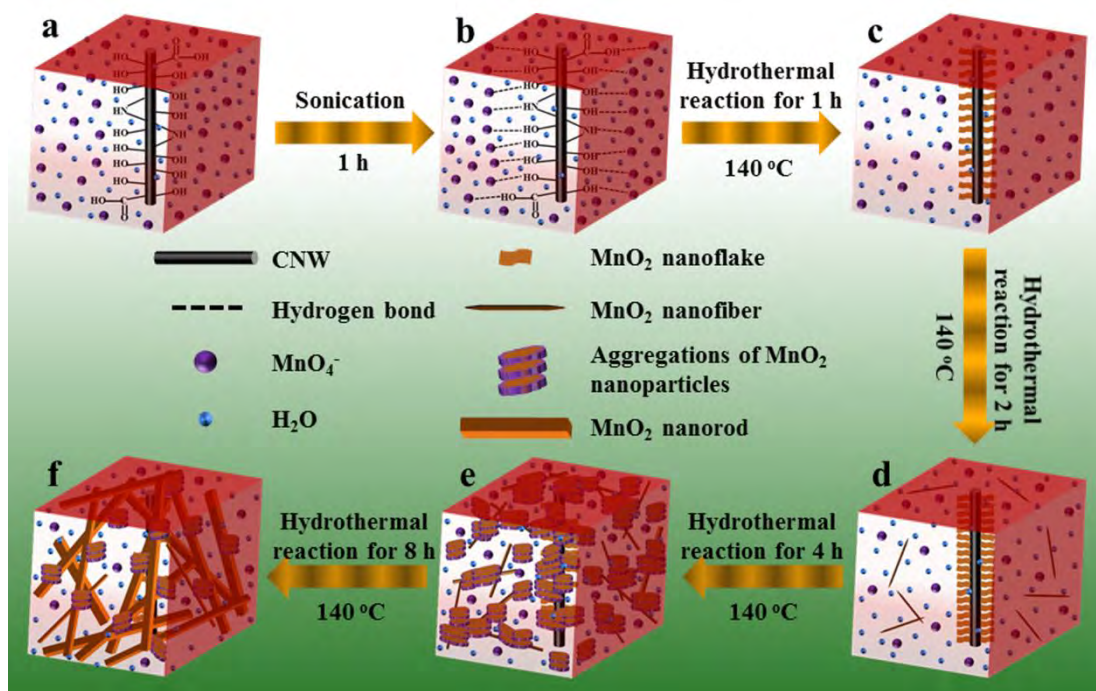
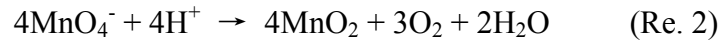


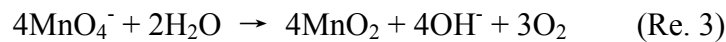
Fig. 6.9 Schematic illustrations of the growth process of CNWMn composites controlled by the hydrothermal reaction time.

As shown in Fig. 6.9a, CNW nanowires dispersed into the  $\text{KMnO}_4$  solution and sonicated for 1 h, many  $\text{MnO}_4^-$  ions combined with electroactive functional groups of

CNW via hydrogen bond (as shown in Fig. 6.9b). After hydrothermal reaction for 1 h, as shown in Fig. 6.9c, the CNW nanowires were coated by MnO<sub>2</sub> nanosheets (determined to be δ-MnO<sub>2</sub> by XRD and SEM) according to Re. 1. For preparation of pure MnO<sub>2</sub>, the nanoflower-like MnO<sub>2</sub> (as shown in Fig. 6.10) made of δ-MnO<sub>2</sub> nanosheets is also confirmed (revealed by XRD and SEM) and the reaction mechanism is according to reaction (2) (Re. 2) [42]



As we all know, the δ-MnO<sub>2</sub> nanosheets are in a metastable state and tend to be diffused to stable α-MnO<sub>2</sub> at high temperature and pressure [53]. In addition, some researchers [55] have proposed that preparation of MnO<sub>2</sub>/carbon composites through hydrothermal reaction. Besides Re.1, the reaction mechanism including the fact that the MnO<sub>2</sub> nanosheets grow from the preformed nanocrystalline due to the decomposition of KMnO<sub>4</sub> in water according to reaction (3) (Re. 3), when the solution is further treated by the hydrothermal reaction:



Therefore, as shown in Fig. 6.9d (hydrothermal reaction for 2 h), the CNW nanowires were further coated by more δ-MnO<sub>2</sub> nanosheets according to Re. 1; moreover, some MnO<sub>2</sub> nanofibers have formed according to Re. 3 due to pursuing the stable state. The similar phenomenon appears in the preparation of pure MnO<sub>2</sub> at the reaction time of 2 h (as shown in Fig. 6.10). Subsequently, when the hydrothermal reaction time reached to 4 h, some MnO<sub>2</sub> nanofibers started to undergo the Ostwald ripening process. For preparation of pure MnO<sub>2</sub>, many α-MnO<sub>2</sub> nanorods have been formed by the Ostwald ripening process (as shown in Fig. 6.10d, and revealed by XRD and SEM), and this phenomenon agreed well with the previous reports [53, 56]. However, compared with preparation of pure MnO<sub>2</sub>, there are obviously different in preparation of CNWMn composites at the reaction time of 4 h (as shown in Fig. 6.9e). Except some α-MnO<sub>2</sub> nanorods, many aggregations MnO<sub>2</sub> (determined to be γ-MnO<sub>2</sub> by XRD and SEM) have been formed, and this is due to the fact that CNW nanowires impede the Ostwald ripening process of nanofibers MnO<sub>2</sub> transform into nanorods MnO<sub>2</sub>. This difference will further impact the specific surface area and electrochemical performance of

CNWMn composites. Finally, when the hydrothermal reaction time reached to 8 h, all of MnO<sub>2</sub> nanofibers transformed into the nanorods  $\alpha$ -MnO<sub>2</sub> and all of nanoflower-like MnO<sub>2</sub> completely disappeared in preparation of pure MnO<sub>2</sub> process (as shown in Fig. 6.10e, revealed by XRD and SEM). But, in preparation of CNWMn process, the aggregations MnO<sub>2</sub> still had a certain reservations, though the nanorods MnO<sub>2</sub> formed significantly (as shown in Fig. 6.9f, revealed by XRD and SEM).

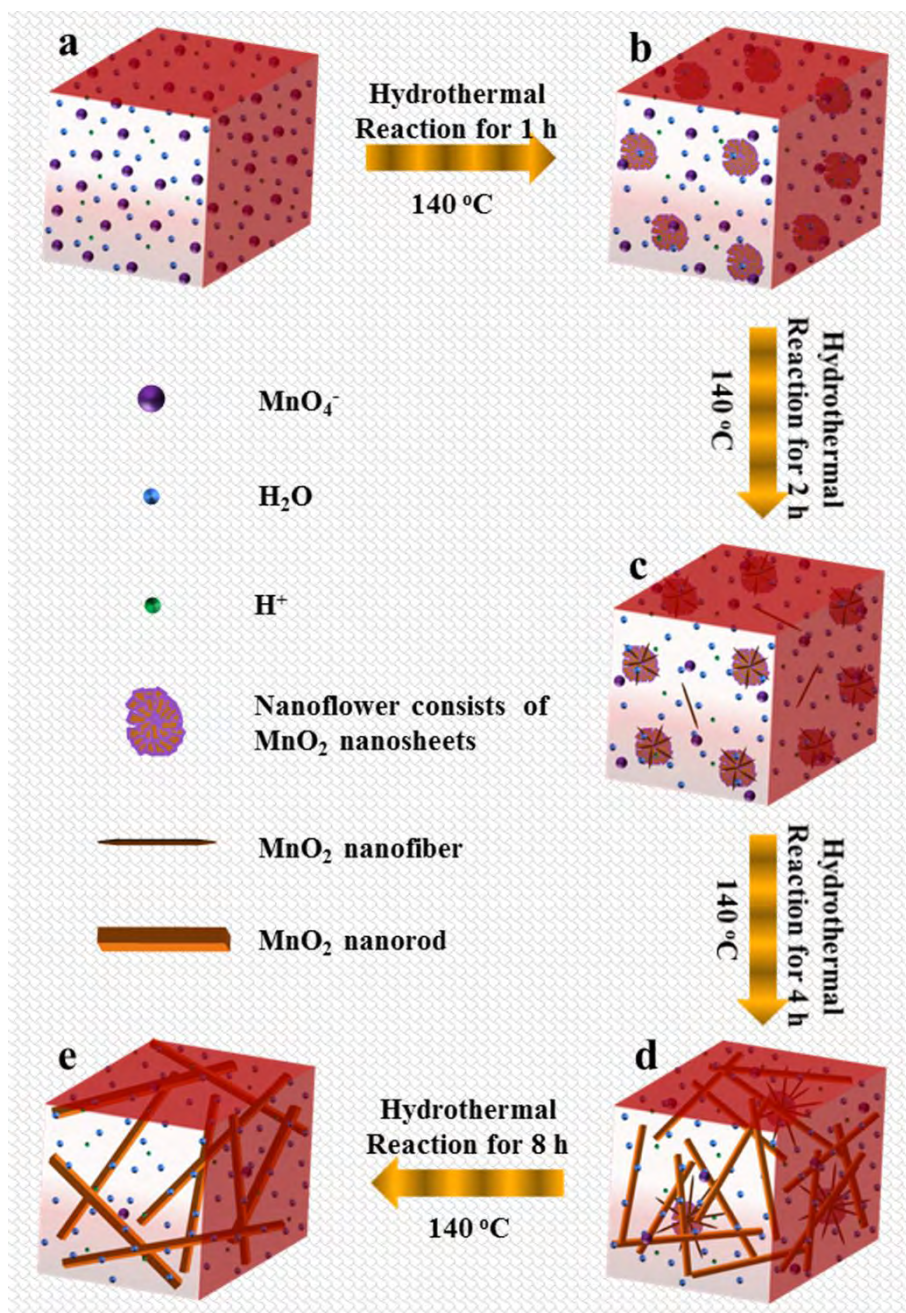


Fig. 6.10 Schematic illustrations of the growth process of pure MnO<sub>2</sub> controlled by the hydrothermal reaction time.

### 6.3.3 Electrochemical performance of CNWMn composites

The electrochemical performances of the as-prepared CNWMn composites were first investigated by CV, GCD and EIS in a three-electrode configuration. Fig. 6.11 shows the CV curves of CNWMn composites at a scan rate of  $0.01 \text{ V s}^{-1}$ . Compared with CV curve of PCNW (as shown in Fig. 6.12), all the CV curves of CNWMn composites deviate from the rectangular shape because of the intervention of  $\text{MnO}_2$  content. Generally, the shape of CV curve for  $\text{MnO}_2$  electrode is close to square in mild aqueous electrolyte (such as  $\text{K}_2\text{SO}_4$  or  $\text{Na}_2\text{SO}_4$  aqueous solution) [57].

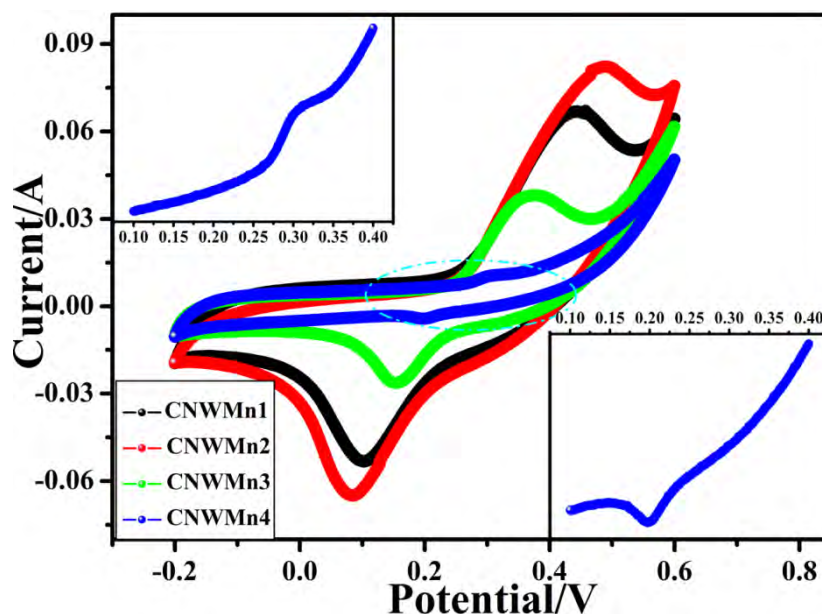
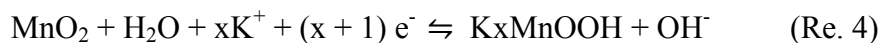


Fig. 6.11 CV (scan rate of  $0.01 \text{ V s}^{-1}$ ) curves of CNWMn composites in three-electrode system.

However, CNWMn electrodes are an exception in KOH electrolyte and possess a pair of peaks. The same phenomenon is also reported in the literatures [28] and [58]. Redox peaks of CV curves can be attributed to the intercalation and de-intercalation of hydrated  $\text{K}^+$  from the electrolyte into the pores of the  $\text{MnO}_2$  [58]. These results further reveal that the CNWMn composites have been successfully prepared. Furthermore, we also find that the peak current and potential increase first and then decrease with the increase of the reaction time. Some researchers have proposed two mechanisms of charge storage by  $\text{MnO}_2$ . The first mechanism involves the

intercalation/extraction of protons ( $\text{H}_3\text{O}^+$ ) or alkali cations such as  $\text{Li}^+$ ,  $\text{Na}^+$  and  $\text{K}^+$  into the bulk of the nanoparticles with the concomitant reduction/oxidation of Mn ions, as shown in reaction (4) (Re. 4) [27, 59, 60]:



The second mechanism is a surface process, and which involves the adsorption/desorption of alkali cations, as shown in reaction (5) (Re. 5) [28, 13]:

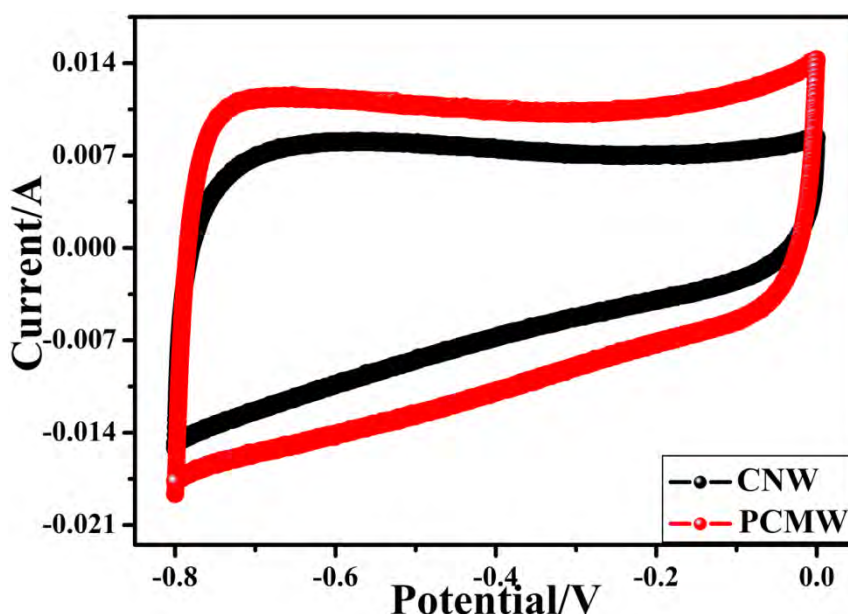


Fig. 6.12 CV (scan rate of  $0.01 \text{ V s}^{-1}$ ) curves of CNW and PCNW in three-electrode system.

Generally, the bulk process (Re. 4) occurs in crystalline  $\text{MnO}_2$ , and the surface process (Re. 5) occurs in amorphous  $\text{MnO}_2$  [27, 61]. In this study, when the reaction time was less than 2 h, the CNW nanowires were coated by amorphous  $\text{MnO}_2$ , and the Re. 5 was in the dominant position. Moreover, the content of amorphous  $\text{MnO}_2$  in CNWMn2 is higher than that of CNWMn1 (revealed by XPS analyses), and this leads to that the peak current and potential of CNWMn2 is higher that of CNWMn1. However, when the reaction time was more than 2 h, the crystalline  $\text{MnO}_2$  gradually formed and the structure of CNW coated by amorphous  $\text{MnO}_2$  gradually decreased (revealed by SEM and XRD). These results lead to the Re. 4 gradually becoming dominant in the reaction, which further affects the peak current and potential of

CNWMn3 and 4 in CV curves. Finally, the area enclosed by the CV curves of CNWMn, which is proportional to the SC [62], increases first and then decreases with the increase of the reaction time. These analyses suggest that CNWMn2 sample possesses an excellent capacitive performance.

The capacitive performance of CNWMn composites was further investigated by GCD method and the results are shown in Fig. 6.13. All the GCD curves deviate from symmetrical behavior and the corresponding CV curves deviate from the rectangular shape. Simultaneously, all the GCD curves show two knees at 0.3 and -0.1 V, respectively. We can further observe that the knee at 0.3 V does not significant change with the increase of reaction time; on the contrary, the platform range of knee at -0.1 V significant decreases with the increase of reaction time. This phenomenon indicates that the knee at 0.3 and -0.1 V corresponding to the Re. 4 and Re. 5, respectively. The discharge time of CNWMn2 is markedly longer than those of other samples, indicating that the CNWMn2 possesses the more superior capacitive performance than the other samples, and we can get the SC by Eq. 2.2. The SC of CNWMn1, 2, 3 and 4 are 362, 465, 198 and 137 F g<sup>-1</sup>, respectively, at a current density of 1 A g<sup>-1</sup>. The SC of CNWMn increases first and then decreases with the increase of the reaction time, and this result further evidences the inference from CV curves.

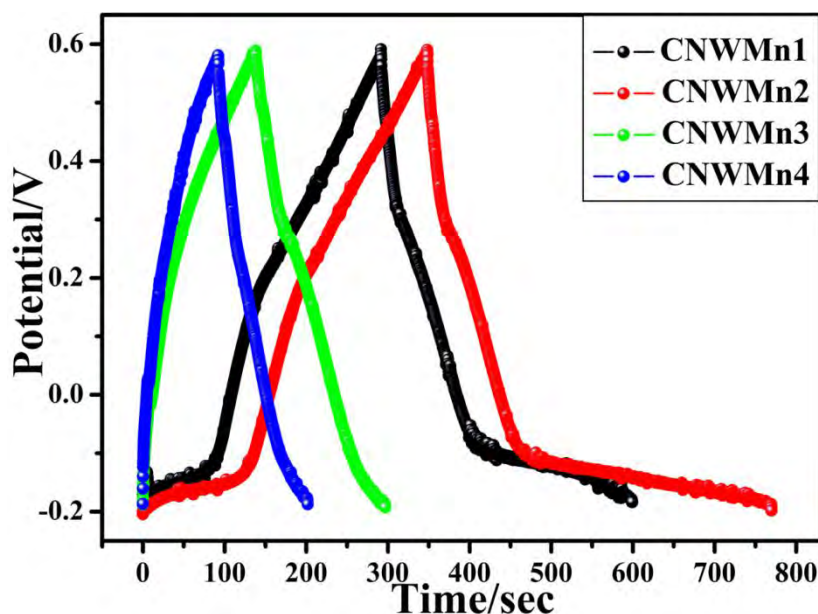


Fig. 6.13 GCD curves (current density of 1 A g<sup>-1</sup>) of CNWMn composites in three-electrode system.

The EIS measurements were performed in order to further evaluate the capacitive performance of CNWMn composites. The Nyquist plots of the samples are showed in Fig. 6.14. All samples present similar shapes, and each EIS curve has a short arc located at high frequency region, followed by an inclined line with a slope about  $45^\circ$  in the medium frequency region, and a nearly vertical line in the low frequency region.

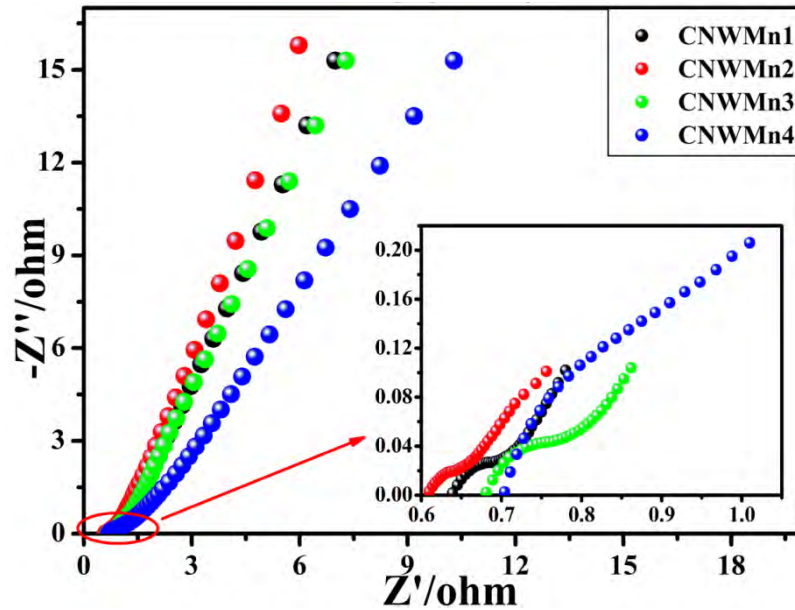


Fig. 6.14 EIS curves of CNWMn composites in three-electrode system.

The diameter of the arc is revealing the charge transfer resistance, the  $45^\circ$  diagonal line corresponding to diffusion resistance, and the nearly vertical line related to the capacitive behavior [63, 64]. We can find that CNWMn2 exhibits the lowest charge transfer resistance own to the fact that it has the least diameter of arc at the high frequency region (as shown in the inset of Fig. 6.14). Meanwhile, CNWMn2 also possesses the lowest diffusion resistance and best outstanding capacitive performance than those of the other samples, which is attributed to the fact that it shows the shortest  $45^\circ$  diagonal line and the largest slope of the straight line at the medium frequency region and low frequency region, respectively. In addition, the point intersecting of EIS curve with the real axis at the high frequency region indicates the internal resistance ( $R_s$ ) [65]. The  $R_s$  is a combination of the ionic resistance of the electrolyte, the intrinsic resistance of the active material and the contact resistance at

the active material/current collector interface [66]. The inset of Fig. 6c shows that the  $R_s$  of CNWMn1, 2, 3 and 4 are 0.64, 0.61, 0.68 and 0.70  $\Omega$ , respectively, which indicates that the  $R_s$  of CNWMn2 is lower than those of the other samples. In short, the analyses of EIS indicate that CNWMn2 sample possesses an excellent capacitive performance, and this result agrees with the analyses of CV and GCD.

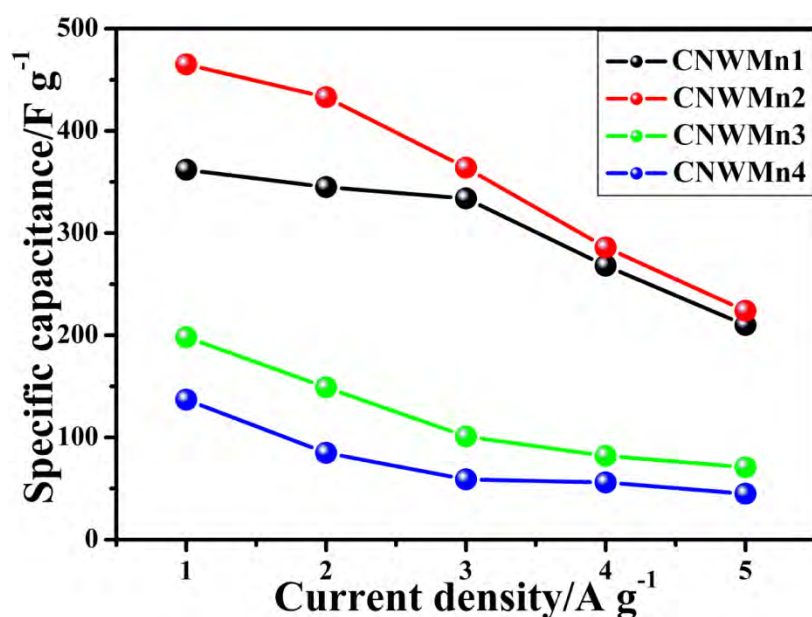


Fig. 6.15 Specific capacitance versus current density of CNWMn composites in three-electrode system.

Fig. 6.15 shows the SC as a function of current density for CNWMn composites. Overall, the SC of all samples decreases with the increase of current density. It is noteworthy that the SC downtrend of CNWMn1 and 2 are larger than that of CNWMn3 and 4 at the current density of more than 3  $A g^{-1}$ . This is mainly due to the fact that the contribution of Re. 5 to capacitive performance of CNWMn1 and 2 gradually weakens with the increase of current density (revealed by Fig. 6.16a and b, the potential of knee caused by Re. 5 gradually decreases with the increase of current density). In addition, the contribution of Re. 4 to capacitive performance of CNWMn composites also gradually decreases with the increase of current density. This leads to the SC of all samples decrease with the increase of current density, though the contribution of Re. 4 to capacitive performance of CNWMn composites is less than that of Re. 5. However, the SC of CNWMn2 could reach to 224  $F g^{-1}$  at the current

density of  $5 \text{ A g}^{-1}$ , and this value is much larger than that of  $\text{MnO}_2$  at the current density of  $1 \text{ A g}^{-1}$  ( $123 \text{ F g}^{-1}$ , obtained from GCD curve of  $\text{MnO}_2$ , as shown in Fig. 6.17b), and this result suggest that the CNWMn2 composite possesses a more excellent fast charge/discharge performance than pure  $\text{MnO}_2$ .

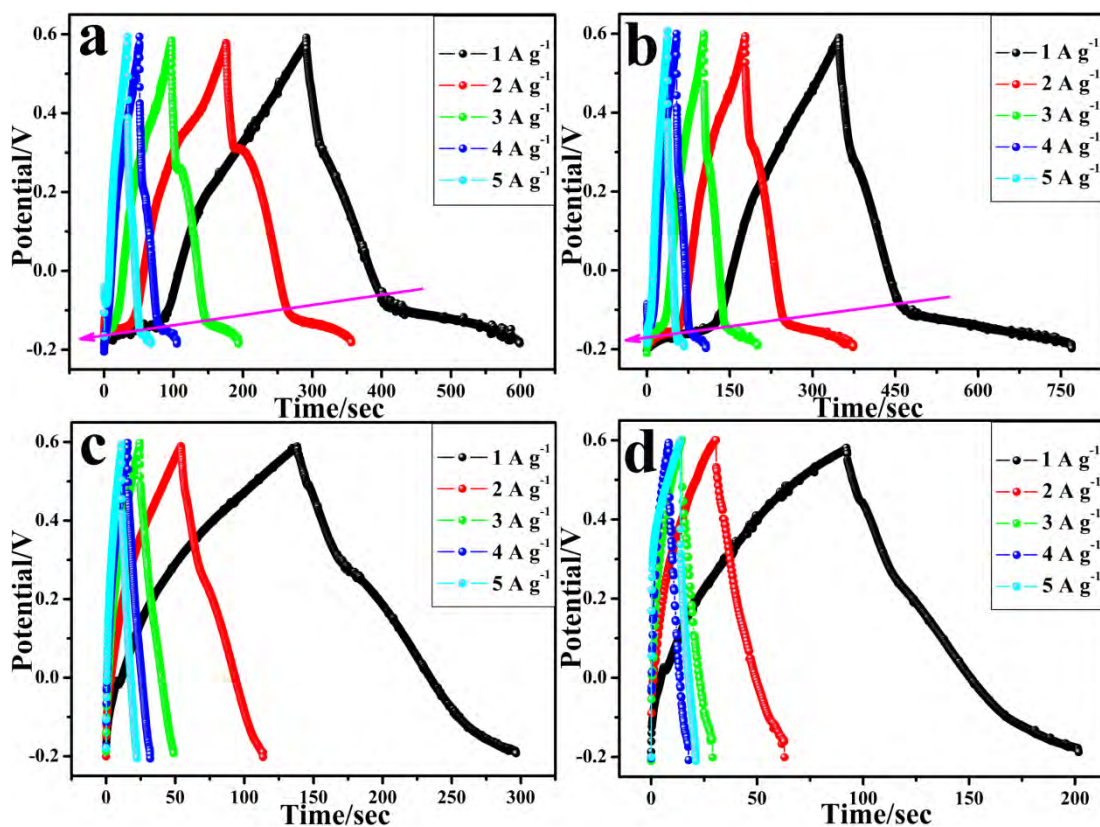


Fig. 6.16 GCD curves of CNWMn1 (a), CNWMn2 (b), CNWMn3 (c) and CNWMn4 (d) at different current densities in three-electrode system.

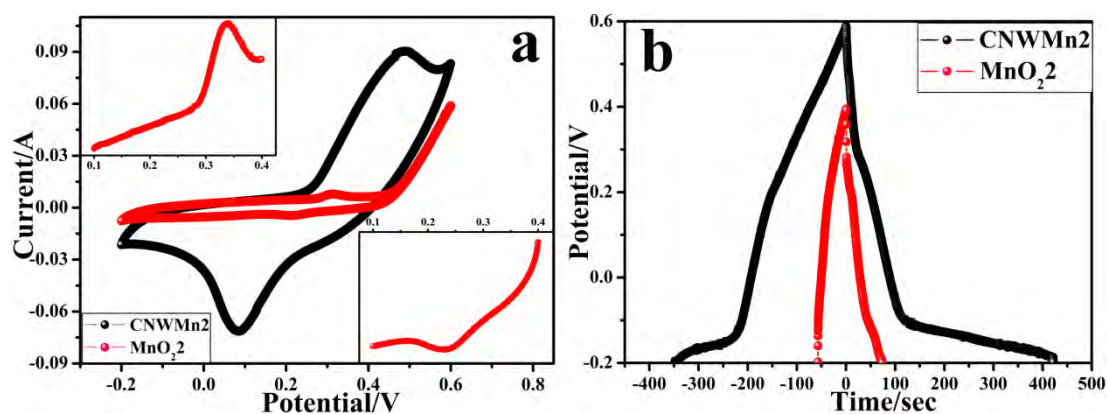


Fig. 6.17 CV (a, scan rate of  $0.01 \text{ V s}^{-1}$ ) and GCD (b, current density of  $1 \text{ A g}^{-1}$ ) curves of CNWMn2 and  $\text{MnO}_2$  in three-electrode system.

Fig. 6.18 shows that the cycling performance of CNWMn2 is dependent on the

current density. Overall, the SC of CNWMn2 decreased with the increased of current density, but, at the same current density, the CNWMn2 showed a stable SC. During the first 100 cycles with the current density of  $1 \text{ A g}^{-1}$ , the SC is stabilized at  $465 \text{ F g}^{-1}$ . And then, after 400 cycles with the different current densities, when the current density returns to  $1 \text{ A g}^{-1}$ , the SC ( $463 \text{ F g}^{-1}$ ) is almost unchanged compared with the first 100 cycles, suggesting that the CNWMn2 has an excellent rate capability.

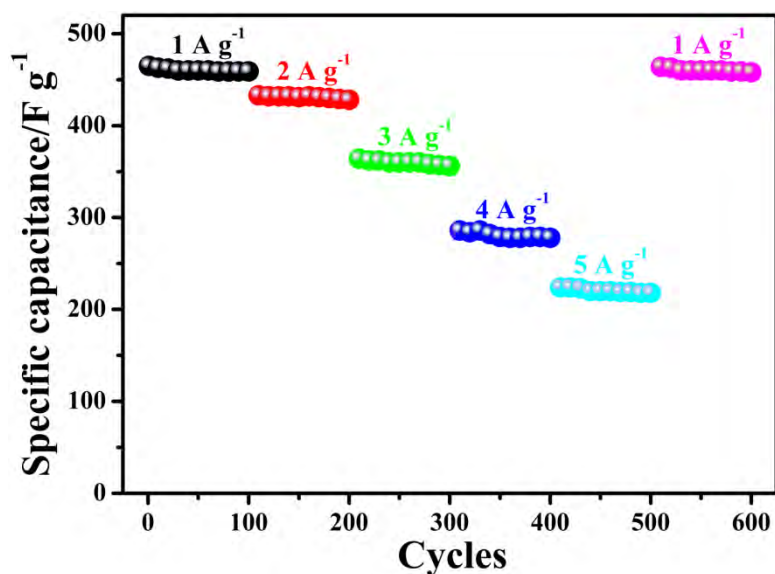


Fig. 6.18 Dependence of cycle stability in the current density of CNWMn2.

To further evaluate the capacitive performance of CNWMn2 composite, we also performed the CV, GCD and EIS measurements in two-electrode asymmetric systems (positive and negative electrodes material were CNMWN2 and PCNW, respectively, denoted as CNWMn2//PCNW). For confirming the potential window of CNWMn2//PCNW, CNWMn2 and PCNW were first performed by CV measurements in three-electrode system, and the results as shown in Fig. 6.19. The PCNW and CNWMn2 electrodes were measured within potential window of  $-0.8\sim 0 \text{ V}$  and  $-0.2\sim 0.6 \text{ V}$  at a scan rate of  $0.01 \text{ V s}^{-1}$ , respectively, and CV curve of PCNW showed an ideal rectangular shape, indicating a typical characteristic of EDLC behavior [67]. Accordingly, the sum of the potential window of the CNWMn2//PCNW is about  $1.4 \text{ V}$ . Fig. 6.20a shows the CV curves of CNWMn2//PCNW in different voltage windows to define the best potential window. It can be obviously found that all CV curves exhibit a rectangular shape when the voltages are below  $1.5 \text{ V}$ ; moreover, a

pair of weak redox peaks also appears in all CV curves, indicating that the EDLC capacitance and pseudocapacitance are simultaneously exist. Furthermore, there is no significant increase of anodic current even when voltage is 1.5 V, which means that the electrolyte is not being decomposed due to the storage of nascent hydrogen on the electrode below the thermodynamic potential for water decomposition [68, 69].

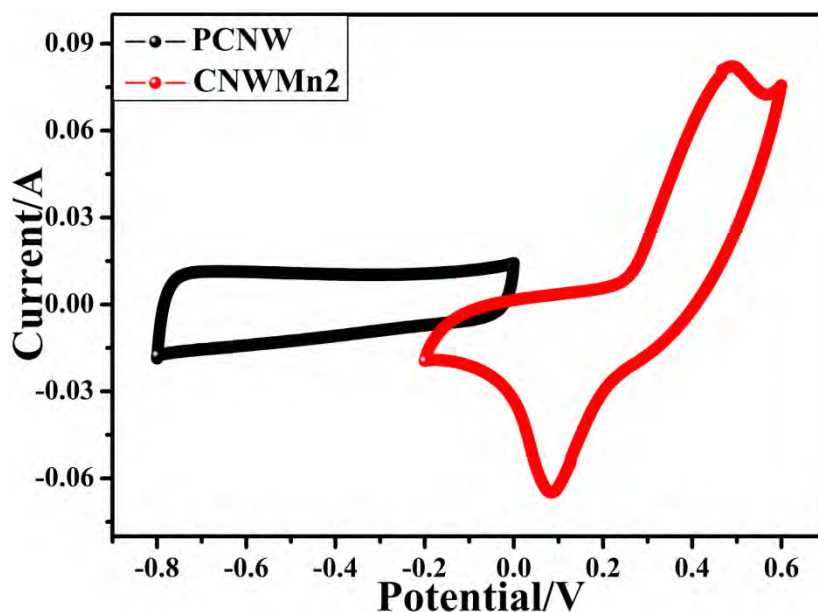


Fig. 6.19 CV curves of PCNW and CNWMn2 in three-electrode system at  $0.01 \text{ V s}^{-1}$ .

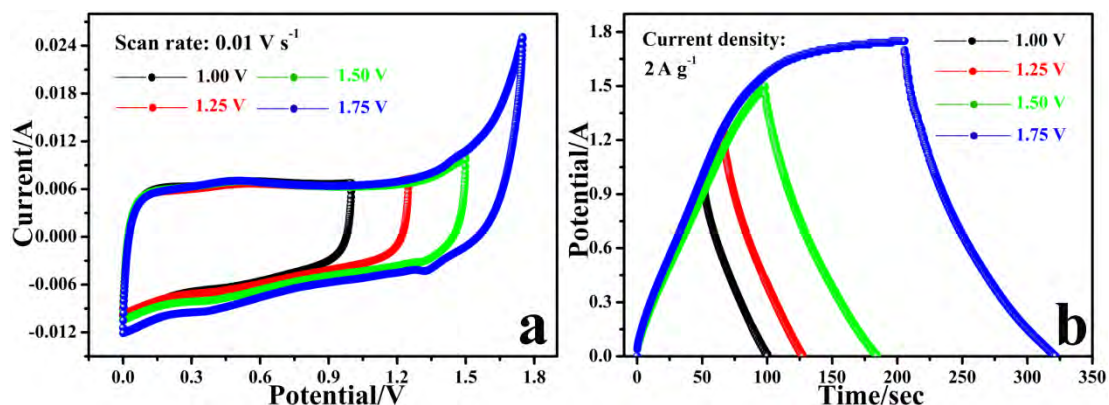


Fig. 6.20 CV (a, scan rate of  $0.01 \text{ V s}^{-1}$ ) and GCD (b, current density of  $2 \text{ A g}^{-1}$ ) curves of two-electrode asymmetric system (using CNWMn2 and PCNW as the positive and negative electrode, respectively) at different potential windows.

However, the anodic current dramatically increases when the potential window is increased to 1.75 V, which indicate that the electrolyte is being decomposed with hydrogen and/or oxygen evolution [70]. Fig. 6.20b shows the GCD curves of

CNWMn2//PCNW at different potential windows. Similar to CV curves, we still find that all GCD curves show the isosceles triangle shape except when potential window is increased to 1.75 V, which still means the ideal capacitive behavior. Therefore, these above data analyses suggest that the best potential window of CNWMn2//PCNW is 0~1.5 V.

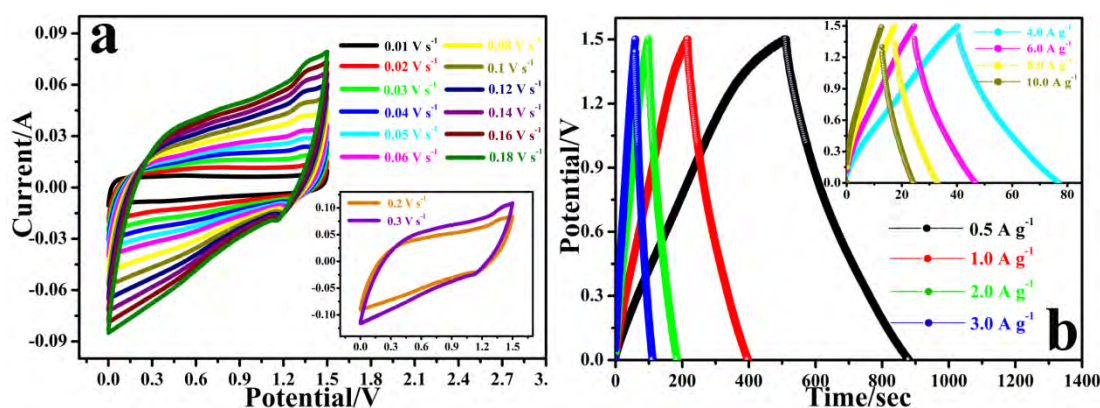


Fig. 6.21 CV (a) and GCD (b) curves of asymmetric system measured at different scan rates and current densities in a potential window of 1.5 V, respectively.

The CV curves of CNWMn2//PCNW at different scan rates ( $0.01\sim 0.3\text{ V s}^{-1}$ ) measured between  $0\sim 1.5\text{ V}$  are displayed in Fig. 6.21a. The CV curves gradually deviate from the rectangular shape with the increase of scan rate, which means that the CNWMn2//PCNW gradually deviate from the ideal capacitive behavior with the scan rate increase. In addition, a pair of redox peaks can be observed even when scan rate reaches to  $0.3\text{ V s}^{-1}$ . This indicates that the contribution of pseudocapacitance to the whole capacitance has no significant change with the increase of the scan rate, and further suggests the CNWMn2//PCNW possesses excellent rate capability desirable for high-power supercapacitors. GCD measurements were made at various current densities ( $0.5\sim 10\text{ A g}^{-1}$ ) to evaluate the capacitive performance and determine the SC of the CNWMn2//PCNW at the voltage of  $1.5\text{ V}$ , as shown in Fig. 6.21b. These typical triangular shape and the charge curves are nearly symmetrical with the corresponding discharge curves, again demonstrating the ideal capacitive behavior. The SC of the CNWMn2//PCNW is also obtained from GCD curves by Eq. 2.2. The SC is  $125\text{ F g}^{-1}$  at a current density of  $0.5\text{ A g}^{-1}$ , and still maintains at  $77\text{ F g}^{-1}$  when

the current density increases to  $10 \text{ A g}^{-1}$ , further indicating that the CNWMn2//PCNW has excellent capacitive performance.

EIS analysis was used to gain a deep insight into the capacitive behaviors of CNWMn2//PCNW. The Nyquist plot of CNWMn2//PCNW is shown in Fig. 6.22a. The EIS curve is also composed of a short arc,  $45^\circ$  diagonal line (as shown in the inset of Fig. 6.22a) and a nearly vertical line. The EIS was fitted by the software of ZSimpWin based on the electrical equivalent circuit (as shown in the inset of Fig. 6.22a), and the fitted results are showed in Fig. 6.22b. The EIS data is fitted by the internal resistance ( $R_s$ ), the electrochemical double layer capacitance ( $C_{dl}$ ), the charge transfer resistance ( $R_{ct}$ ), the diffusion resistance ( $Z_w$ ) and pseudocapacitance ( $C_L$ ) [3, 71]. The  $R_s$  is  $1.47 \Omega$  obtained from raw Nyquist plots, and same as the  $R_s$  of fitted Nyquist plots (as shown in the table of Fig. 6.22b). Moreover, the  $R_s$  is smaller than that of the previous reports about  $\text{MnO}_2$  composites (Ref. 32 and Ref. 70 are  $1.8$  and  $2.2 \Omega$ , respectively) [34, 72]. In addition, we can obtain the  $R_{ct}$  ( $0.13 \Omega$ , as shown in the table of Fig. 6.22b) from the fitted Nyquist plots, and the value is far less than that of the previous reports about  $\text{MnO}_2$  composites (Ref. 32 and Ref. 3 are  $2.5$  and  $9.73 \Omega$ , respectively) [34, 3]. The lower  $R_s$  and  $R_{ct}$  of CNWMn2//PCNW favor high-rate power delivery.

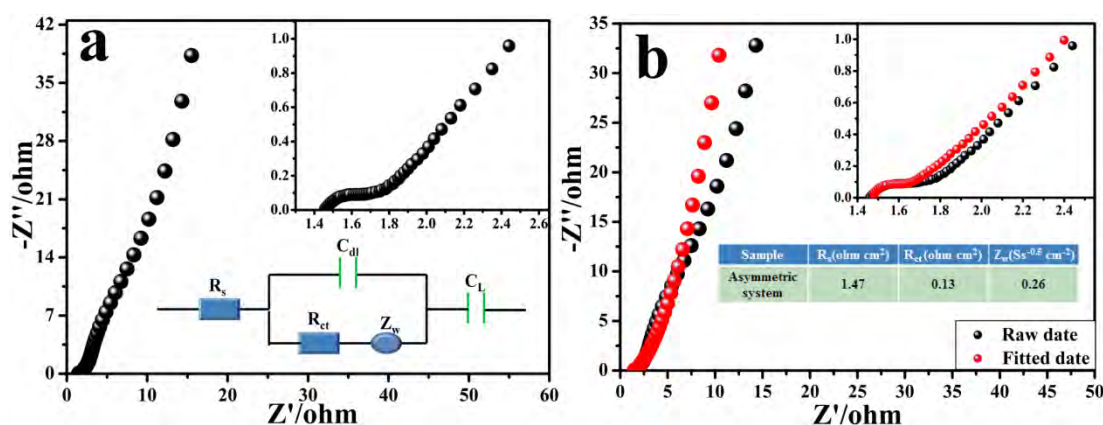


Fig. 6.22 (a) EIS curve of asymmetric system (the inset is electrical equivalent circuit); (b) EIS curves of two-electrode asymmetric system for raw and fitted data (the table is equivalent circuit parameters).

Cycle stability at a high current density is an essential property of supercapacitors.

The cycle stability of CNWMn<sub>2</sub>//PCNW by repeating the GCD test at the current density of 4 A g<sup>-1</sup> was performed and the results are shown in Fig. 6.23. The CNWMn<sub>2</sub>//PCNW exhibits excellent cycle stability with 93% (the SC of first and last cycle are 98.4 and 91.6 F g<sup>-1</sup>, respectively) SC retention after 2000 cycles. Obviously, its cycle stability is comparable to those of other MnO<sub>2</sub> composites in asymmetric system, such as MnO<sub>2</sub>//active carbon (the retention is less than 90% after 1000 cycles) [73, 74], MnO<sub>2</sub>//carbon nanotube (CNT) (90% retention after 1000 cycles) [75], CNT/MnO<sub>2</sub>//CNT/SnO<sub>2</sub> (92% retention after 1000 cycles) [76], MnO<sub>2</sub>//graphene//graphene (79% retention after 1000 cycles) [77], MnO<sub>2</sub>//graphene (87% retention after 2000 cycles) [78].

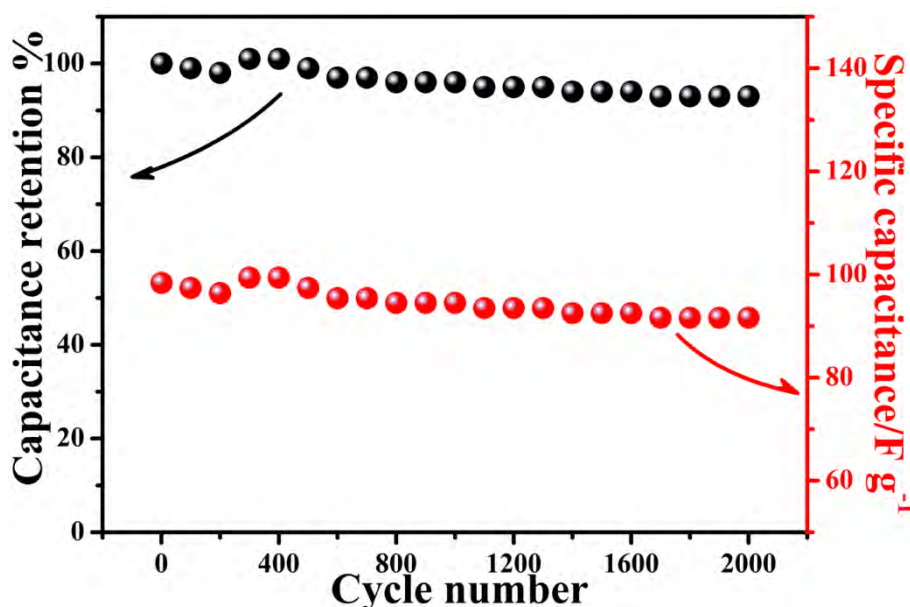


Fig. 6.23 Cycle stability of asymmetric system.

Ragone plot, acting as a performance indicator of power density against energy density, is usually used to characterize the electrochemical properties of a supercapacitor. The energy density ( $E$ , Wh kg<sup>-1</sup>) and power density ( $P$ , W kg<sup>-1</sup>) were calculated from the GCD curves at different current densities according to Eq. 2.3 and 2.4 [34]. Fig. 6.24 shows the Ragone plots of CNWMn<sub>2</sub>//PCNW. The maximum energy density (39.2 Wh kg<sup>-1</sup>) is achieved at the current density of 0.5 A g<sup>-1</sup>. At the current density of 10 A g<sup>-1</sup>, the power density reaches to 7500 W kg<sup>-1</sup>, and the corresponding energy density is 24.2 Wh kg<sup>-1</sup>. Compared with the current density of

0.5 A g<sup>-1</sup>, the energy density retention is 61.7 %. In addition, it is obviously that the CNWMn2//PCNW exhibits much higher energy density than that of traditional sense supercapacitors (the range of energy density 1~10 Wh kg<sup>-1</sup> [79]). More significantly, the maximum energy density greatly surpasses that of previous reports, such as MnO<sub>2</sub>/CNT//CNT (15.3 Wh kg<sup>-1</sup>) [80], MnO<sub>2</sub>/graphite hollow carbon spheres (GHCS)//GHCS (22.1 Wh kg<sup>-1</sup>) [81], graphene/MnO<sub>2</sub>//CNT (12.5 Wh kg<sup>-1</sup>) [82], MnO<sub>2</sub> nanowire/graphene// graphene (30.4 Wh kg<sup>-1</sup>) [64], MnO<sub>2</sub> nanowires//CNT (25.5 Wh kg<sup>-1</sup>) [83], MnO<sub>2</sub> nanoplates// graphene hydrogel (23.2 Wh kg<sup>-1</sup>) [67], MnO<sub>2</sub>//PPy (7.4 Wh kg<sup>-1</sup>) [84], and MnO<sub>2</sub>//active carbon (10-21 Wh kg<sup>-1</sup>) [85-87]. These findings indicate the CNWMn2//PCNW holds a great promise in the practical applications.

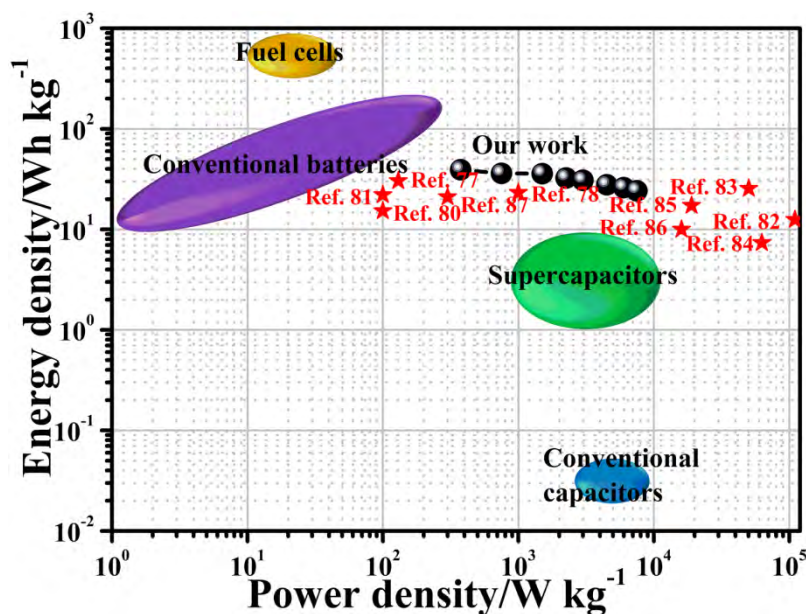


Fig. 6.24 Ragone plot of asymmetric system.

## 6.4. Conclusions

In this paper, CNMWn composites were synthesized via hydrothermal method. In the synthesis process, CNW not only act as the reducing agents but also act as the scaffolds for MnO<sub>2</sub> growth. The electrochemical performance of CNWMn composites is closely related to the hydrothermal reaction time, and the maximum SC of CNWMn composites is 465 F g<sup>-1</sup> (at the current density is 1 A g<sup>-1</sup>) when the reaction time is 2 h

(CNWMn<sub>2</sub>) in three-electrode system. Moreover, we have assembled a two-electrode asymmetric system using CNWMn<sub>2</sub> as the positive electrode and PCNW as the negative electrode. The asymmetric system possesses high energy density (39.2 Wh kg<sup>-1</sup> at the current density of 0.5 A g<sup>-1</sup>), excellent rate capability (high energy density of 24.2 Wh Kg<sup>-1</sup> at the current density of 10 A g<sup>-1</sup>), and high cycle stability (the SC retention is 93% after 2000 cycles). Overall, these features suggest a promising electrode material for supercapacitors application.

## References:

- [1] L.L Zhang, X.S. Zhao, *Chem. Soc. Rev.* 38 (2009) 2520-2531.
- [2] G.A. Snook, P. Kao, A.S. Best, *J. Power Sources* 196 (2011) 1-12.
- [3] M. Huang, X.L. Zhao, F. Li, W. Li, B. Zhang, Y.X. Zhang, *J. Mater. Chem. A* 3 (2015) 12852-12857.
- [4] Y. Huang, J.J. Liang, Y.S. Chen, *Small* 8 (2012) 1805-1834.
- [5] W.T. Gu, G. Yushin, *WIREs Energy and Environment* 3 (2014) 424-473.
- [6] M. Huang, F. Li, F. Dong, Y.X. Zhang, L.L. Zhang, *J. Mater. Chem. A* 3 (2015) 21380-21423.
- [7] X.H. Xia, J.P. Tu, Y.J. Mai, X.L. Wang, C.D. Gao, X.B. Zhao, *J. Mater. Chem.* 21 (2011) 9319-9325.
- [8] J.W. Lee, T. Ahn, J.H. Kim, J.M. Ko, J.D. Kim, *Electrochim. Acta.* 56 (2011) 4849-4857.
- [9] W. Xiao, H. Xia, J.Y.H. Fuh, L. Lu, *J. Power Sources* 193 (2009) 935-938.
- [10] J.F. Zang, X.D. Li, *J. Mater. Chem.* 21 (2011) 10965-10969.
- [11] Y. Chen, B.Q. Xie, S.Y. Luo, Y. Zhang, *Appl. Surf. Sci.* 285 (2013) 425-430.
- [12] R. Ranjusha, A.S. Nair, S. Ramakrishna, P. Anjali, K. Sujith, K.R.V. Subramanian, N. Sivakumar, T.N. Kim, V.S. Nair, A. Balakrishnan, *J. Mater. Chem.* 22 (2012) 20465-20471.
- [13] M. Toupin, T. Brousse, D. Bélanger, *Chem. Mater.* 16 (2004) 3184-3190.
- [14] L.F. Chen, Z.H. Huang, H.W. Liang, Q.F. Guan, S.H. Yu, *Adv. Mater.* 25 (2013) 4746-4752.
- [15] Y.S. Luo, J. Jiang, W.W. Zhou, H.P. Yang, J.S. Luo, X.Y. Qi, H. Zhang, D.Y.W. Yu, C.M. Li, T. Yu, *J. Mater. Chem.* 22 (2012) 8634-8640.
- [16] C.L. Long, D.P. Qi, T. Wei, J. Yan, L.L. Jiang, Z.J. Fan, *Adv. Funct. Mater.* 24 (2014) 3953-3961.
- [17] S. Hassan, M. Suzuki, S. Mori, A.A. El-Moneim, *J. Power Sources* 249 (2014) 21-27.
- [18] H.J. Huang, W.Y. Zhang, Y.S. Fu, X. Wang, *Electrochim. Acta* 152 (2015)

480-488.

- [19] D.Y. Zhai, B.H. Li, H.D. Du, G.Y. Gao, L. Gan, Y.B. He, Q.H. Yang, F.Y. Kang, *Carbon* 50 (2012) 5034-5043.
- [20] P.C. Gao, A.H. Lu, W.C. Li, *J. Power Sources* 196 (2011) 4095-4101.
- [21] S. Bose, T. Kuila, A.K. Mishra, R. Rajasekar, N.H. Kim, J.H. Lee, *J. Mater. Chem.* 22 (2012) 767-784.
- [22] A. Ameli, M. Arjmand, P. Pötschke, B. Krause, U. Sundararaj, *Carbon* 106 (2016) 260-278.
- [23] B. Wang, J.H. Qiu, H.X. Feng, E. Sakai, *Electrochimica Acta* 151 (2015) 230-239.
- [24] Z. Spitalsky, D. Tasis, K. Papagelis, C. Galiotis, *Progr. Polym. Sci.* 35 (2010) 357-401.
- [25] X.B. Jin, W.Z. Zhou, S.W. Zhang, G.Z. Chen, *small*, 3 (2007) 1513-1517.
- [26] M. Kim, Y. Hwang, K. Min, J. Kim, *Electrochim. Acta.* 113 (2013) 322-331.
- [27] S. Devaraj, N. Munichandraiah, *J. Phys. Chem. C* 112 (2008) 4406-4417.
- [28] B. Yin, S.W. Zhang, H. Jiang, F.Y. Qu, X. Wu, *J. Mater. Chem. A* 3 (2015) 5722-5729.
- [29] C.T. Sun, Y.J. Zhang, S.Y. Song, D.F. Xue, *J. Appl. Cryst.* 46 (2013) 1128-1135.
- [30] B. Wang, J.H. Qiu, H.X. Feng, E. Sakai, T. Komiyama, *Electrochim. Acta.* 190 (2016) 229-239.
- [31] Z.B. Zulamita, C.M. Francisco, M.C. Carlos, *J. Power Sources* 219 (2012) 80-88.
- [32] Y.P. Zhai, Y.Q. Dou, D.Y. Zhao, P.F. Fulvio, R.T. Mayes, S. Dai, *Adv. Mater.* 23 (2011) 4828-4850.
- [33] X. Wang, C. Yang, H.D. Li, P. Liu, *Electrochim. Acta.* 111 (2013) 729-737.
- [34] J.G. Wang, Y. Yang, Z.H. Huang, F.Y. Kang, *Carbon* 61 (2013) 190-199.
- [35] J.H. Zhang, Y.H. Wang, J.B. Zang, G.X. Xin, Y.G. Yuan, X.H. Qu, *Carbon* 50 (2012) 5196-5202.
- [36] C.Z. Yang, M. Zhou, Q. Xu, *Phys. Chem. Chem. Phys.* 15 (2013) 19730-19740.
- [37] Y. Fan, P.F. Liu, Z.Y. Huang, T.W. Jiang, K.L. Yao, R. Han, *J. Power Sources* 280 (2015) 30-38.

- [38] Y.W. Ma, S.J. Jiang, G.Q. Jian, H.S. Tao, L.S. Yu, X.B. Wang, X.Z. Wang, J.M. Zhu, Z. Hu, Y. Chen, *Energy Environ. Sci.* 2 (2009) 224-229.
- [39] S.J. He, W. Chen, *J. Power Sources* 262 (2014) 391-400.
- [40] C.Z. Wu, W. Xie, M. Zhang, L.F. Bai, J.L. Yang, Y. Xie, *Chem. Eur. J.* 15 (2009) 492-500.
- [41] A.K. Sinha, M. Pradhan, T. Pal, *J. Phys. Chem. C* 117 (2013) 23976-23986.
- [42] W. Chen, R.B. Rakhi, Q.X. Wang, M.N. Hedhili, H.N. Alshareef, *Adv. Funct. Mater.* 24 (2014) 3130-3143.
- [43] X.Y. Xie, C. Zhang, M.B. Wu, Y. Tao, W. Lv, Q.H. Yang, *Chem. Commun.* 49 (2013) 11092-11094.
- [44] K. Dai, L.H. Lu, C.H. Liang, J.M. Dai, Q.Z. Liu, Y.X. Zhang, G.P. Zhu, Z.L. Liu, *Electrochim. Acta.* 116 (2014) 111-117.
- [45] M. Zhou, F. Pu, Z. Wang, S.Y. Guan, *Carbon* 68 (2014) 185-194.
- [46] Y. Zhao, Y.N. Meng, P. Jiang, *J. Power Sources* 259 (2014) 219-226.
- [47] V. Subramanian, H.W. Zhu, R. Vajtai, P. M. Ajayan, B.Q. Wei, *J. Phys. Chem. B* 109 (2005) 20207-20214.
- [48] X.L. Wang, X.Y. Fan, G. Li, M. Li, X.C. Xiao, A.P. Yu, Z.W. Chen, *Carbon* 93 (2015) 258-265.
- [49] J.G. Wang, Y. Yang, Z.H. Huang, F. Kang, *J. Mater. Chem.* 22 (2012) 16943-16949.
- [50] T. Ramanathan, F.T. Fisher, R.S. Ruoff, L.C. Brinson, *Chem. Mater.* 17 (2005) 1290-1295.
- [51] Q. Qu, P. Zhang, B. Wang, Y. Chen, S. Tian, Y.P. Wu, R. Holze, *J. Phys. Chem. C.* 113 (2009) 14020-14027.
- [52] B. Wei, L.D. Wang, Q.H. Miao, Y.A. Yuan, P. Dong, R. Vajtai, W.D. Fei, *Carbon* 85 (2015) 249-260.
- [53] T.T. Truong, Y.Z. Liu, Y. Ren, L. Trahey, Y.G. Sun, *ACS Nano* 6 (2012) 8067-8077.
- [54] Y.L. Li, J.J. Wang, Y. Zhang, M.N. Banis, J. Liu, D.S. Geng, R.Y. Li, X.L. Sun, *J. Colloid Interf. Sci.* 369 (2012) 123-128.

- [55] Y. Wang, Z.J. Han, S.F. Yu, R.R. Song, H.H. Song, K.K. Ostrikov, H.Y. Yang, *Carbon* 64 (2013) 230-236.
- [56] W. Xiao, D.L. Wang, X.W. Lou, *J. Phys. Chem. C* 114 (2010) 1694-1700.
- [57] P. Simon, Y. Gogotsi, *Nat. Mater.* 7 (2008) 845-854.
- [58] R. Ranjusha, A.S. Nair, S. Ramakrishna, P. Anjali, K. Sujith, K.R.V. Subramanian, N. Sivakumar, T.N. Kim, S.V. Nair, A. Balakrishnan, *J. Mater. Chem.* 22 (2012) 20465-20471.
- [59] S.L. Kuo, N.L. Wu, *J. Electrochem. Soc.* 153 (2006) A1317-A1324.
- [60] L. Benhaddad, L. Makhloufi, B. Messaoudi, K. Rahmouni, H. Takenouti, *J. Mater. Sci. Technol.* 27 (2011) 585-593.
- [61] P. Ragupathy, H.N. Vasan, N. Munichandraiah, *J. Electrochem. Soc.* 155 (2008) A34-A40.
- [62] X.L. Ma, G.Q. Ning, Y.F. Kan, Y.M. Ma, C.L. Qi, B. Chen, Y.F. Li, X.Y. Lan, J.S. Gao, *Electrochim. Acta.* 150 (2014) 108-113.
- [63] S.X. Deng, D. Sun, C.H. Wua, H. Wang, J.B. Liu, Y.X. Sun, H. Yan, *Electrochim. Acta.* 111 (2013) 707-712.
- [64] J.G. Wang, Y. Yang, Z.H. Huang, F.Y. Kang, *Carbon* 61 (2013) 190-199.
- [65] J.P. Liu, J. Jiang, M. Bosman, H.J. Fan, *J. Mater. Chem.* 22 (2012) 2419-2426.
- [66] J. Zhang, Y. Yu, L. Liu, Y. Wu, *Nanoscale* 5 (2013) 3052-3057.
- [67] M.D. Stoller, S. Park, Y. Zhu, J. An, R.S. Ruoff, *Nano Lett.* 8 (2008) 3498-3502.
- [68] Q. Wang, J. Yan, Y.B. Wang, G.Q. Ning, Z.J. Fan, T. Wei, J. Cheng, M.L. Zhang, X.Y. Jing, *Carbon* 52 (2013) 209-218.
- [69] X. Yang, Y.S. He, G. Jiang, X.Z. Liao, Z.F. Ma, *Electrochem. Commun.* 13 (2011) 1166-1169.
- [70] K. Fic, G. Lota, M. Meller, E. Frackowiak, *Energy Environ. Sci.* 5 (2012) 5842-5850.
- [71] J.G. Wang, Y. Yang, Z.H. Huang, F. Kang, *J. Power Sources* 204 (2012) 236-243.
- [72] Q. Cheng, J. Tang, J. Ma, H. Zhang, N. Shinya, L.C. Qin, *Carbon* 49 (2011) 2917-2925.
- [73] V. Khomenko, E. Raymundo-Piñero, F. Béguin, *J. Power Sources* 153 (2006)

183-190.

- [74] X. Zhang, X.Z. Sun, H.T. Zhang, D.C. Zhang, Y.W. Ma, *Mater. Chem. Phys.* 137 (2012) 290-296.
- [75] H. Jiang, C.Z. Li, T. Sun, J. Ma, *Nanoscale* 4 (2012) 807-812.
- [76] C.J. Yu, C. Masarapu, J.P. Rong, B.Q. Wei, H.Q. Jiang, *Adv. Mater.* 21 (2009) 4793-4797.
- [77] Z.S. Wu, W.C. Ren, D.W. Wang, F. Li, B.L. Liu, H.M. Cheng, *ACS Nano* 4 (2010) 5835-5842.
- [78] H.C. Gao, F. Xiao, C.B. Ching, H.W. Duan, *ACS Appl. Mater. Interfaces* 4 (2012) 2801-2810.
- [79] M. Huang, Y.X. Zhang, F. Li, L.L. Zhang, R.S. Ruoff, Z.Y. Wen, Q. Liu, *Sci. Rep.* 4 (2014) 3878.
- [80] H. Zhang, Y.Q. Huang, B. Xu, G.P. Cao, *ECS Solid State Lett.* 1 (2012) M1-M3.
- [81] Z.B. Lei, J.T. Zhang, X.S. Zhao, *J. Mater. Chem.* 22 (2012) 153-160.
- [82] G.H. Yu, L.B. Hu, M. Vosgueritchian, H.L. Wang, X. Xie, J.R. McDonough, X. Cui, Y. Cui, Z.A. Bao, *Nano Lett.* 11 (2011) 2905-2911.
- [83] P.C. Chen, G.Z. Shen, Y. Shi, H.T. Chen, C.W. Zhou, *ACS Nano* 4 (2010) 4403-4411.
- [84] V. Khomenko, E. Raymundo-Pinero, E. Frackowiak, F. Beguin, *Appl. Phys. A*, 82 (2006) 567-573.
- [85] T. Cottineau, M. Toupin, T. Delahaye, T. Brousse, D. Belanger, *Appl. Phys. A* 82 (2006) 599-606.
- [86] T. Brousse, P.L. Taberna, O. Crosnier, R. Dugas, P. Guillemet, Y. Scudeller, Y. Zhou, F. Favier, D. Belanger, P. Simon, *J. Power Sources* 173 (2007) 633-641.
- [87] C.J. Xu, H.D. Du, B.H. Li, F.Y. Kang, Y.Q. Zeng, *J. Electrochem. Soc.* 156 (2009) A435-A441.

# Chapter 7 Summary and outlook

## 7.1. Summary of thesis results

This thesis has demonstrated the successful design, preparation and testing of carbon materials and carbon-based composites for supercapacitors.

In chapter 3, a novel three-component composite, graphene oxide/polypyrrole/chlorinated multi-wall carbon nanotube composite were synthesized by in-suit polymerization method. In which, the effect of three componets' mass ratio on the property of electrochemical performance and chemical structure of composites was explored. For composites, the polypyrrole chains acted as the "bridge" between multi-wall carbon nanotube and graphene through the amide group and  $\pi$ - $\pi$  stacking, respectively. The most outstanding electrochemical performance of composite was achieved when the mass ratio of graphene oxide and multi-wall carbon nanotube is 1, and the mass ratio of carbon materials (the sum of graphene and multi-wall carbon nanotube) and pyrrole is 0.04. However, the preparation method of composites is complexity, and is difficulty to apply to reality.

In chapter 4, we used a simple and low cost method to prepare nitrogen doped carbon nanowires. For this method, first, the polypyrrole nanowires were prepared when CTAB as soft template, and then obtained the nitrogen doped carbon nanowires by direct carbonization method when polypyrrole nanowires as the carbon precursor. The preparation conditions of sample which achieved the most excellent electrochemical performance are the molar ratio of pyrrole and CTAB is 3.4, and the carbonization temperature is 750 °C. For further improve the electrochemical performance of carbon nanowires, in chapter 5, porous carbon nanowires were prepared by KOH activation of nonporous carbon nanowires. The most outstanding electrochemical performance of sample with specific surface area is 1642 m<sup>2</sup> g<sup>-1</sup> and a nitrogen content of 2.41 at. % was prepared when the mass ratio of KOH and nonporous carbon nanowires is 2.

The above studies focused on the development of negative electrode materials of supercapacitors. In chapter 6, based on chapter 4, a kind of positive electrode material of supercapacitor—MnO<sub>2</sub>/carbon nanowires composites were prepared by hydrothermal reaction. The electrochemical performance of sample is closely related to the micromorphology of itself. When the mass ratio of KMnO<sub>4</sub> and carbon nanowires is 2 and hydrothermal reaction time is 2h, the preparation composite possesses the most excellent electrochemical performance. Moreover, the two-electrode asymmetric system (using the composite as the positive electrode and porous carbon nanowires as the negative electrode) possesses high energy density (39.2 Wh kg<sup>-1</sup>), excellent rate capability and high cycle stability (the specific capacitance retention is 93 % after 2000 cycles). These features suggest a promising electrode material for supercapacitors application.

## 7.2. Outlook

In view of the electrical double layer storage mechanism of carbon materials, the capacitance and energy density is still unsatisfactory whereas the pseudo-capacitive materials, such as metal oxide and conductive polymers. Therefore, high energy storage could be achieved by combining electrical double layer capacitance together with highly reversible pseudo-capacitance utilizing their synergistic effects. A key limitation of metal oxide is their poor conductivity while conductive polymers suffer from the swelling and shrinking of structure during the charge-discharge process. Thus far, the best ideal method is preparation of carbon-based composites. At present, although a lot of progress has been made, the complete understanding of the relationship between carbon-based nanostructure and enhanced electrochemical performance are still in their primary stage.

For improve the energy density of supercapacitors, the other effective method is using organic electrolyte. The organic electrolyte can offer a large voltage stability of up to 2.7-2.8 V resulting in high energy density. Recently, room temperature ionic liquids proved to be the most promising electrolyte to enhance the voltage of

supercapacitors to values reach to 3.0 V. However, their high viscosity and low ionic conductivity limit its application in supercapacitors. How to solve the above problems and extend the application of organic electrolyte? This problem is a recently research hotspot.

Supercapacitors are promised to complement and even replace batteries to some extent in certain applications. For example, in hybrid electric vehicles, it remains a challenge to supercapacitors and other components in the hood due to limited space. For mitigate the problem, preparation of thin and flexible supercapacitors is an effective method. Preparation of thin and flexible supercapacitors and which can fit anywhere have been a research hotspot.

# Publication

## I. 審査付投稿論文

- [1] **Bin Wang**, Jianhui Qiu, Huixia Feng, Eiichi Sakai. Preparation of graphene oxide/polypyrrole/multi-walled carbon nanotube composite and its application in supercapacitors. **Electrochimica Acta**, 2015, 151, pp230-239. (IF=4.803)
- [2] **Bin Wang**, Jianhui Qiu, Huixia Feng, Eiichi Sakai, Takao Komiyama. KOH-activated nitrogen doped porous carbon nanowires with superior performance in supercapacitors. **Electrochimica Acta**, 2016, 190, pp229-239. (IF=4.803)
- [3] **Bin Wang**, Jianhui Qiu, Huixia Feng, Eiichi Sakai, Takao Komiyama. Nitrogen doped carbon nanowires prepared from polypyrrole nanowires for potential application in supercapacitors. **J. Electroanal. Chem.** 2016, 775, pp219-227. (IF=2.822)
- [4] **Bin Wang**, Jianhui Qiu, Huixia Feng, Nuoxin Wang, Eiichi Sakai, Takao Komiyama, Preparation of MnO<sub>2</sub>/carbon nanowires composites for supercapacitors, **Electrochimica Acta**, 2016, 212, pp710-721. (IF=4.803)
- [5] Huixia Feng, **Bin Wang**, Nuoxin Wang, Jianhui Qiu, Lin Tan, Nali Chen. Synthesis and characterization of secondary doped polypyrrole/organic modified attapulgite conductive composites. **J. Appl. Polym. Sci.**, 2014, 132, DOI: 10.1002/app.41407. (IF=1.866)
- [6] Lin Tan, Yong-Chen Zhang, **Bin Wang**, He-Ming Luo, Hui-Xia Feng. Reduced Graphene Oxide as a Metal-Free Carbocatalyst for Polymerization of 1-Naphthylamine. **ChemPlusChem**, 2014, 79, pp929-935. (IF=2.836)

注: 博士論文テーマ関連: 4 編 ((1) ~ (4)), その他: 2 編 ((5) ~ (6))

## II. 国際会議発表論文

- [1] **Bin Wang**, Jianhui Qiu, Eiichi Sakai. Nitrogen doped carbon nanowires for high-performance supercapacitors electrode materials. 2<sup>nd</sup> China International Congress on Composite Materials (CCCM-2).

注：博士論文テーマ関連：1件

### III. 国内学会発表

- [1] 王濱、邱建輝、境英一、伊藤一志、陳姣、馮輝霞、尾藤輝夫. カーボンナノワイヤ/二酸化マンガン複合材料の創製およびスーパーキャパシタの適用. 2016年9月日本機械学会東北支部第52期秋季講演会、秋田市.
- [2] 王濱、邱建輝、境英一. ポリピロールナノワイヤからの窒素ドーパドカーボンナノワイヤの創製およびスーパーキャパシタの潜在的なアプリケーション. 2015年9月日本機械学会東北支部第51期秋季講演会、福島市.
- [3] 王濱、邱建輝、境英一. 酸化黒鉛/ポリピロール/カーボンナノチューブ複合材料の創製及び性能評価. 2014年9月第39回複合材料シンポジウム講演、秋田市.

注：博士論文テーマ関連：3編（(1)～(3)）.

# Acknowledgements

I would like to thank the following individuals for the support and the help they have provided:

First, Professor Jianhui Qiu, my research advisor for all the support, trust and encouragement throughout the course of my graduate studies. He has been and always be my inspiration scientist and human decency.

And then, my deepest appreciation goes to the professors in Department of Machine Intelligence and Systems Engineering, Faculty of Systems Science and Technology at Akita Prefectural University, Prof. Mamoru Mizuno, Prof. Nobuhiro Kanazawa and Professor in Department of Bioscience and Textile Technology, Faculty of Textile Science and Technology at Shinshu University, Prof. Qingqing Ni for the comments and suggestions, whose advices have inestimable value for my research.

Third, Prof. Eiichi Sakai and Prof. Kazushi Ito, I am grateful for his kind help and assistance in my work.

Finally, Professor Huixia Feng, I am grateful for her continuing support and generous access to all electrochemical instruments in her lab.

I also appreciate the technical support from Prof. Takao Komiyama, Prof. Teruo Bitoh, Prof. Ruilu Liang.

In addition, I wish to express my sincere thanks to my friends in Professor Jianhui Qiu group members, Prof. Yanlin Yu, Dr. Limin Zang, Mr. Liqiang Gu, Mr. Longxiang Zhu, Ms. Jiao Chen, Mr. Haodao Mo, Dr. Xueli Wu for their valuable discussion on my project.

At last, I would like to express my gratitude to my parents and other relevant for their moral support and warm encouragements.